Development and Fabrication of Room Temperature Mixed Metal Oxide Based Ozone Sensing Elements for Health and Safety Applications

Ger Hickey

Submitted for the degree of Doctorate of Philosophy

Department of Electronic & Computer Engineering,
University of Limerick,
Limerick,
Ireland

Supervisor: Prof. Khalil Arshak

Declaration

"I hereby declare that this thesis is entirely my own work and has not been submitted to any other University or higher education institution, or for any other academic award in this University"

_____

Ger Hickey

Acknowledgements

I wish to express my gratitude and appreciation to my supervisor Prof. Khalil Arshak for the opportunity to undertake this research and for all his guidance and advice throughout this work.

Thanks to all of my colleagues and friends who helped me greatly during this work, particularly Eddie, Niall, Deirdre, Kelly, Colm, Marie, Marie, Leon, Ivor, Olga and John.

Finally, thanks to Helen and my family, who have endured this long process with me always offering their support and love.

Abstract

Atmospheric pollution is defined as a status containing gases, offensive odours and particles that are harmful to humans, animals, vegetation or living environments above the regulation limits specified by regulatory bodies in the specific areas.

Atmospheric pollution has become particularly serious since the Industrial Revolution. Furthermore due to the recent dramatic growth in population and industrial development, coupled with an intensified usage of fossil fuels, the natural atmospheric environment has become severely polluted and is rapidly deteriorating. As the level of public concern related to living and working in a healthy environment has now increased, the demand for monitoring and controlling the atmospheric environment in the house and workplace has also increased. As a result, intensive research efforts have been made in various fields in an attempt to resolve such environmental problems or dangers.

Indoor sources of ozone are more common than they were in the past due to the introduction of electronic equipment. Some of the most significant ozone generating equipment includes photocopiers, laser printers, air purifiers, ozone generators and electrostatic precipitators.

Exposure to ozone at extremely low concentrations (Table 2.2 – World Health Organisation, 43-85ppb) constitutes a human health hazard. Exposure is known to decrease the short-term lung function and adversely affect the respiratory system. Prolonged exposure to relatively low levels has been linked to increases in morbidity and mortality rates.

This work undertakes to develop easily producible, cost effective and novel metal oxide based gas sensors capable of operating at room temperature for the detection of environmentally relevant ozone.

Fabrication techniques of novel metal oxide mixtures are explored and these sensing layers are further developed/optimized and analysed. Room temperature ozone sensors have been shown to be sensitive to low ppb levels of ozone. Operation of these sensor

types at room temperature has the added advantages of reduced fabrication costs, reduced operating costs, low power consumption and ease of implementation into other portable/handheld devices.

In this work, mixed In_2O_3, ZnO, SnO_2 and sole NbO_2 oxide sensing layers were fabricated and studied. Optimization of the composition and concentration of the mixtures was undertaken in an attempt to discover the best sensor performance. It was found that mixing of the above oxide materials and simultaneous evaporation from a molybdenum boat yielded workable room temperature ozone sensors.

Optimization of the fabrication process was also studied in detail and the effect of changing the various fabrication parameters was documented and analysed. It is shown that decreasing the sensing layer thickness of these devices, while increasing the deposition rate of the material from the molybdenum boat yields to a significant improvement in overall sensor performance.

To understand the nature of the sensing films, the surfaces of the sensing layers were examined via SEM analysis. For these SEM images it can be seen that higher deposition rates result in more porous sensing layers. XPS analysis of the sensor samples (wide and narrow scans) was carried out in an attempt to better understand the increases in sensor performance. From these results it was seen that there are slight shifts in the binding energies of the metal oxide components which is known to have an effect on the sensitivity of the devices. Also of particular interest from these results is the presence and shape of the O 1s peaks and the corresponding performance of the sensing layer with respect to oxygen vacancies present.

This work has led to the successful use of the vacuum thermal evaporation process to fabricate room temperature ozone sensing elements based on a mixture of In_2O_3, ZnO and SnO_2 as well as an NbO_2 based ozone sensor, both of which are capable of detecting ozone levels as low as 50ppb.

TABLE OF CONTENTS

List of Tables

List of Figures

List of Equations

Chapter 1: Introduction

1.1. Introduction

Many industrial and commercial activities involve the monitoring and control of the environment, with applications ranging from domestic gas alarm sensors [1-3] to industrial plant instrumentation [4-6]. The greatest obstacle to achieving improved monitoring lies at the interface between the measuring device and environment to be monitored.

Ever increasing industrialisation makes it necessary to constantly monitor and control air pollution in the environment, in factories, laboratories, hospitals and general technical installations. The following is a list of desirable characteristics for an ideal sensor: high sensitivity, high selectivity, fast response, portable (small size), low power consumption, simple operation, simple fabrication, robust, durable and low fabrication costs [7-11].

Gases are materials constituted by atoms or molecules in continuous motion with random orientation. The average distance between particles in gas phase is much wider than the typical interatomic distances inside a molecule, so that the interactions with each other are much reduced. In an ideal gas, these interactions are perfectly elastic collisions. The

pressure, P, the number of particles, N, the temperature, T, and the volume, of an ideal gas are related by a simple formula known as the ideal gas equation:

$$PV = NkT \qquad \textit{(Eq. 1.1)}$$

Where k is the Boltzmann constant. Real gases show deviations from this law, mainly due to the non-elastic character of the interactions [12].

Air is a mixture of several gases whose main components are nitrogen and oxygen. Other components of air usually present in smaller concentrations are argon, other inert gases, carbon dioxide and hydrogen [12]. The composition of air is constantly varying due to the interchange of atoms and molecules between air and the surrounding bodies and also, because of the diffusion and interaction of the particles in the gas phase. This makes the atmosphere a fully open system, spatially in–homogeneous and with rich internal dynamics [12]. One of the compounds whose concentration shows a higher variation in air is water vapour. Other substances usually detected in varying concentrations are ozone, carbon monoxide, sulphur or nitrogen oxides and several organic volatile compounds. Also important is noting that very small solid (smoke, dust) or liquid particles (clouds, fog) can be carried in suspension by air [12].

Since air acts as a source of substances for biological processes, the absence of some of its components or the presence of unusual compounds can severely disturb the processes that depend upon it. That is the case when concentration of oxygen has been highly reduced locally in a combustion process or when a toxic compound is carried in air. Since oxygen is odourless, its shortage in atmosphere can only be perceived by the side effects on the respiratory processes. Other gaseous compounds can sometimes be perceived by smell, but in many cases they are odourless [12].

1.2. Sensor Overview

It has long been human endeavour to mimic nature's creations. Nature has endowed humans and animals with 5 primary sensory organs, eyes, ears, nose, tongue and skin [13]. Efforts to recreate/improve on these sensors are briefly summarised in Table 1.1.

Table 1.1 Summary of Recreations

Nature's Sensors	**Recreations**
Eyes	Camera
Ears	Microphone/Recorder
Nose/Tongue	Chemical/Gas Sensors
Skin	Tactile Sensors

Sensors can be thought of as extensions of our sensing capabilities. Sensors usually generate electrical signals that can be processed and transmitted by suitable electronic processes. In recent years, the area of sensing technology has undergone an explosive growth due to the availability of processing devices to manipulate the output signals and the progress in communication technology [13]. A very basic schematic representation of a sensor system is illustrated in Figure 1.1.

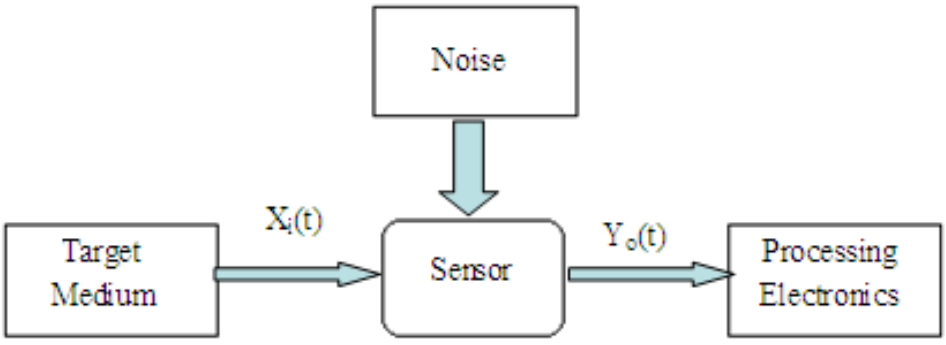

Figure 1.1. Basic Schematic of a sensor system

The output signal $Y_O(t)$ is produced in response to the input signal $X_i(t)$, thus characterising the state of the target medium. For an ideal sensor system the relation between the system input and output can be expressed as follows:

$$Y_O(t) = f(X_i(t)) \qquad \textit{(Eq. 1.2)}$$

Recently much of the current research in the area of sensing technology has been focussed on the area of gas sensors [13-17] this is due to the increasing awareness and concern of personal health and safety. Gases are key targets in many industrial and domestic activities requiring improved levels of environmental measurement and control. This has been stimulated by a series of clean air laws, which have or are being legislated on the international, national and local levels. These often require in-situ continuous monitoring of air quality and the emission rates of specific chemical species and equipment.

1.3. Regulations

In Ireland, for example, the Environmental Protection Agency (EPA) carries out detailed studies of air quality and compare measured concentrations of pollutants with current and future air quality standards for a suite of air pollutants [18]. The Air Quality Standards Regulations (DELG, 2002) and Ozone Regulations (DEHLG, 2004) correspond to limit values laid down in a number of recent EC directives, which began to take effect from 2005.

Below is a table of some of the pollutants under continuous monitoring in Ireland from 26 bases around the country. Also included in Table 1.2 is an explanation of the formation of the pollutants, a summary of the health effects as well as the recommended limits of exposure.

Table 1.2. Review of Some Typical Pollutants

Pollutant	Source	Health Effects	Limit ($\mu g/m^3$)
SO_2	Formed when fuel containing sulphur (coal, oil) is burned at power plants, factories, homes, etc.	High concentration can result in temporary breathing impairment for asthmatics, especially when active out doors. Long term exposure can result in aggravation of existing cardiovascular disease, respiratory illness and alterations in the lungs' defences.	350 hourly mean 125 daily mean
NO_x	Power generation plants and motor vehicles are the principal sources of NO_x, through high temperature combustion. NO_x contributes to the formation of acid rain and is also an ozone precursor.	Short term exposure can result in reduced lung function, airway responsiveness and increased reactivity to allergens. Long term exposure has been associated with increased risk of respiratory infections in children.	NO_2 200 hourly limit NO_2 Annual mean
PM_{10}	Main sources of PM_{10} are the combustion of solid fuels and road traffic, in particular emissions from diesel engines. Other particulates include industrial emissions.	Inhalation of these particles can increase the risk, frequency and severity of respiratory and cardiopulmonary disorders.	50 Daily limit 40 Annual limit
Pb	Airborne lead levels have dramatically reduced since the introduction of lead-free petrol.	Exposure can lead to neurological impairments such as seizures, behavioural disorders, nervous system damage, high blood pressure and heart disease.	0.5 Annual mean
C_6H_6	Benzene is found in the emissions from burning coal, oil, from motor vehicle exhaust and cigarette smoke.	Short term exposure can cause drowsiness, headaches, as well as eye, skin and respiratory tract irritation. Long term exposure can cause reduced numbers of red blood cells and anaemia. Benzene is also a recognised carcinogen.	5 Annual mean
CO	Formed when carbon in fuel is not burned completely.	Can reduce oxygen delivery to the body's organs and tissue. At high concentrations can be poisonous.	10 over 8hour period
O_3	Ozone is a secondary pollutant formed from the interaction of NO_x, CO and various VOCs in the presence of sunlight.	Small concentrations can cause damage to the respiratory system. High concentrations can result in death	120 over 8hour 240 hourly limit

1.4. Classification of Approaches

Some common classification schemes group the sensors by their applications, input, conversion mechanism or materials, etc. Here the sensors are grouped according to their input stimuli. According to this approach the sensors may be divided unto seven different classes as seen in Table 1.3.

Table 1.3. Classification of Sensors

Sensor Type	**Detected Properties**
Electrical	Current, Voltage, Resistance, Capacitance, Inductance, Charge, etc.
Mechanical	Pressure, Force, Length, Acceleration, Flow, etc.
Magnetic	Magnetic Flux Density, Magnetic Moment, etc.
Thermal	Temperature, Specific Heat, Heat Flow, etc.
Chemical	Composition, Concentration, pH, etc.
Optical	Light Intensity, Absorption, Wavelength, Polarization, etc.
Radiation	Radiation Type, Number of radiation particles, etc.

The sensors characteristics may also be used to classify the sensors. This approach is often used in data sheets and catalogues and is very useful when seeking sensors to meet specific demands. For example sensors for outdoors use need to be less influenced by environmental conditions than the indoor counterparts, where there is little change in the environmental conditions. Sensors used for continuous monitoring should have long-term stability but may have lower resolution than a sensor used for accurate periodic measurements. Another important consideration and one, which should not be overlooked, is that sensors intended for domestic applications should be much simpler and cheaper than those used for scientific applications. The fact that a sensor being developed shows lower sensitivity than previously studied ones does not mean that it is not a worthwhile study, since it might show characteristics other than sensitivity that may be advantageous in some applications where a high sensitivity is not of fundamental concern [12].

1.5. Gas Sensors

Unlike control electronics, sensors must interact with the changing environment which they are in contact with. Even apparently benign atmospheres may contain corrosive, toxic or hazardous species that can seriously interfere with the operation of the sensing device. For this reason sensor technology has continued to lag and constantly strives for better performance in sensitivity, selectivity and reliability.

Among the various types of gas sensors, semiconducting gas sensors are promising candidates for sensor development given their sensitivity to many gases of interest and the ability to fabricate them readily in many configurations (single crystals, thick films and thin films). Thin film technology in particular is being actively applied in the development of semiconducting gas sensor devices given that such sensors depend largely on gas-surface interactions (Chapter 4). Thin film gas sensors have potential advantages of fast response times and importantly the potential for miniaturization and low power consumption.

In 1962, porous semiconducting ceramics, ZnO and SnO_2, were first demonstrated [5] as gas sensing devices. From this first conception ZnO [19-23], SnO_2 [24-28] and In_2O_3 [29-34] have received the majority of attention in recent years for various gas detectors and monitors.

When considering the semiconducting oxide sensor, the principally measured parameter is resistance/conductance. This can be viewed as either strength or a weakness of semiconducting sensors. It is viewed as an advantage in the fact that the resistance is a simple and easily measured parameter, but on the other hand the weakness is that the resistance is a second-order parameter and therefore not an ideal indicator of the exact process/reaction taking place (See Chapter 4: Fundamentals of Metal Oxide Sensors).

These sensors perform the important task of sensing the chemical analytes and also giving quantitive information of the concentration of the analyte in the environment. Today there is a great deal of interest in developing sensors for applications of air pollution monitoring, detection of harmful gases in populated environments, exhaust gas

monitoring, hand-held breath analyzers etc. Table 1.4 gives some common applications of gas sensors.

Table 1.4. Common Gas Sensor Applications

Automobiles	Car ventilation protection, Filter Control, Gasoline vapour protection, Alcohol breath testing
Safety	Fire detection, Leak detection, Toxic gas detection, Flammable gas detectors, Explosive gas detectors, Boiler control, Personal gas monitor
Indoor Air quality	Air purifiers, ventilation control, cooking control
Environmental Control	Weather Stations, Pollution monitoring
Food	Food quality control, Process control, Packaging quality control (off-odours)
Industrial Production	Fermentation Control, Process Control
Medical	Breath Analysis, Disease Detection

1.6. The basis of work in this Thesis

In this study, among various semiconducting oxide materials, ZnO, SnO_2 and In_2O_3 have been chosen as the key gas sensing materials since they have been widely studied and can be fabricated as high quality films by vacuum evaporation. The widespread applicability of wide band semiconducting oxides such as SnO_2, ZnO and In_2O_3 as gas sensors is due to the variable range of conductance possible and to the fact that they respond to both oxidizing and reducing gases [35].

This research project investigates the fabrication, development and optimisation of thin film metal oxide based gas sensors for the detection of ozone in the low ppb region. Investigations were carried out on the effect of oxide thickness, oxide particle size, percentage metal oxide and effect of contaminants on the overall operation of the gas sensor. This information was then used for the optimisation of the sensors for the detection of ozone.

1.7. Thesis Outline

Chapter 1: This chapter provides an insight into the definition of a sensor, focussing in particular on gas sensor. A brief history of the most type of gas sensors and their applications is shown. Also included is a review of some of the most common gases that cause pollution and danger to the health and safety of the public.

Chapter 2: This chapter gives a brief introduction to the history of ozone gas, when it was discovered where it may be found (Naturally Occurring Ozone) and how it may be formed. Also included are some of the applications and uses of ozone gas. The limits and recommendations for exposure are also provided as well as some of the health effects associated with various concentrations and exposure times of ozone. Also discussed are some techniques and equipment used for the decomposition of ozone.

Chapter 3: Chapter 3 is a review of various gas sensor technologies, ozone sensors and it concentrates on metal oxide based ozone sensors, comparing the advantages and disadvantages of different materials and technologies and process techniques.

Chapter 4: Chapter 4 deals with the fundamentals of metal oxide based gas sensors, discussed in detail is the principles of operation, the response mechanisms towards oxidising and reducing gases. Also discussed in this chapter is the operation temperature and its effect on the sensitivity, selectivity and reliability of the devices.

Chapter 5: Electrical and optical properties of semiconductors are dealt with in this chapter. Optical absorption of metal oxides, absorption spectra is explained along with amorphous solids. Also included in this chapter is an explanation and an in depth look at the conduction mechanisms present in the semiconducting materials.

Chapter 6: Chapter 6 deals with the Experimental and Equipment utilised throughout this work. Included are substrate preparation, Electrode design and fabrication, fabrication processes, Experimental set up and experimental procedure. Also included in this chapter is a outline and explanation of the analysis equipment used, such as SEM and XPS.

Chapter 7

This chapter is dedicated to the results and discussions obtained in this work. Response characteristics for each individual sensing device are detailed and graphed, also included are comparisons of important properties of the various sensor types. Extensive analysis is detailed to understand and explain the sensor devices performance as well as the effect the fabrication parameters have on the final operation of the device. Numerous analysis techniques were utilised in characterising the various sensing layers including SEM, XRD and XPS. The chapter is summarized in the flowchart below.

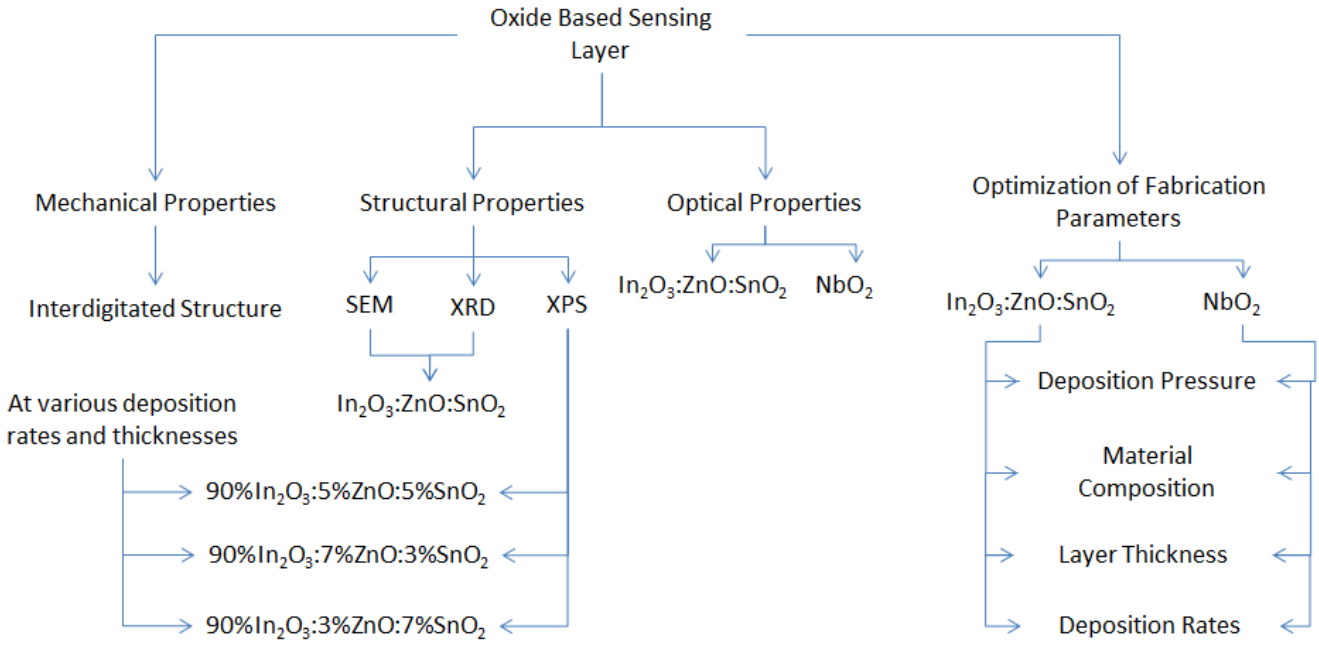

Figure 1.2. Flowchart of structure of Chapter 7

Chapter 8

Summarises and concludes the results of the conducted studies and offers a number of recommendations for future work.

Chapter 2: Overview of ozone

2.1. Introduction

Ozone was first identified as a distinct chemical compound in 1828 by Christian Schonbein at the University of Basel [36]. He noted that ozone had been an accompaniment of electrical storms and reproduced the effect by producing arcing between two electrodes in the presence of oxygen [36]. In 1839 Schonbein reported that the electrolysis of water produced an odour at the positive electrode which was the same as the odour produced by an arc between two electrodes [36]. Three volumes of oxygen produce two volumes of ozone (Equation 2.1). The formation of ozone is endothermic.

$$3O_2 \rightarrow 2O_3 \qquad \textit{(Eq. 2.1)}$$

Ozone is thermodynamically unstable and spontaneously reverts back into oxygen (Equation 2.2) [37]:

$$2O_3 \rightarrow 3O_2 \qquad \textit{(Eq. 2.2)}$$

Ozone is a colourless gas which can have either a beneficial or detrimental affect on human health or the environment [38]. Naturally occurring ozone in the upper atmosphere protects the earth against harmful radiation from the sun which can result in skin cancer [38]. It is also a strong oxidizing agent and is widely used as a disinfectant and deodorizing agent [1]. However, ozone occurring from activities at or near ground level is the principal constituent of smog which adversely affects the respiratory system, agricultural crops and plant life [38]. (See later for sections on respiratory health effects). Ozone gas is also used in large volumes in several large scale industries such as water purification [39-43] and paper and pulp processing [44, 45]. Many electronic devices such as photocopiers and laser printers produce ozone [46].

2.2. Physical properties of ozone

As mentioned previously, in gaseous form ozone is colourless, whereas liquid ozone is bluish-black and its crystals are violet-blue [3]. Olfactory organs are extremely sensitive to ozone; it has been known to be detected by humans at a dilution of 1 parts per million (ppm) of air. The half-life in air is approximately 15 minutes in open areas and increases with lower temperature and lower humidity [3]. It is important also to note that the half-life may be greatly extended to several hours in enclosed areas. Ozone is about 50% heavier than air and has a low vapour pressure; therefore it tends to sink to the ground and does not disperse well where there is little circulation [3].

Maximum ozone concentration in water varies directly with the concentration of the gas in the sparging air and inversely with temperature. Doubling the concentrations of ozone in the feed gas will double the concentration in the water at any given temperature [3]. Due to the unstable nature of ozone it cannot be stored and transported it must be

generated “in situ”. Olfactory organs are very sensitive to ozone, humans cannot detect ozone in the air at a concentration of less than 1 part per million (ppm).

By analysis of the electronic structure, the ozone molecule is considered to have the following resonant structure (Figure 2.1), characterised by end oxygen atoms with only six electrons [46].

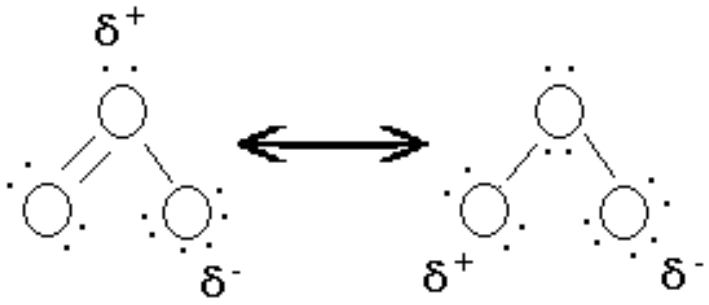

Figure 2.1. Resonant structure of ozone

The half – life of ozone in air is typically 15 minutes in open areas, however it can extend to several hours in enclosed spaces [38]. The half – life may be further increased by lowering both temperature and humidity [38]. Ozone is roughly 50% heavier than air and has a low vapour pressure; therefore it tends to sink to the floor and does not disperse if there is no circulation [38].

2.3. Formation of ozone

Ozone is formed from oxygen molecules as a result of electrical discharge or ultraviolet (UV) radiation. Oxygen atoms are formed by the splitting of diatomic oxygen molecules into two atoms (Equation 2.3), which then recombine with other oxygen molecules to produces ozone molecules (Equation 2.4) [38] [47]. Ozone (O_3) reverts back to oxygen (O_2) (Equation 2.5) [48].

$$O_2 \rightarrow O + O \qquad \textit{(Eq. 2.3)}$$

$$O + O_2 \rightarrow O_3 \qquad \textit{(Eq. 2.4)}$$

$$O + O_3 \rightarrow 2O_2 \qquad \textit{(Eq. 2.5)}$$

Table 2.1. Physical Properties of Ozone

Physical Properties	**Value**
Molecular Weight	48
Boiling point (101 kPa)	-111.9
Melting Point	-192.7
Critical Temperature	-12.1
Critical Pressure	5.53MPa
Density, gas (0°C, 101kPa)	2.144 $kg.m^{-3}$
Density, liquid (-112°C)	1358 $kg.m^{-3}$
Surface tension (-183°C)	3.84 x 10^{-2} $N.mm^{-1}$
Viscosity, liquid (-183°C)	1.57 x 10^{-3} Pa.s
Heat capacity, liquid (-183 to -145°C)	1884 $J.kg^{-1}.K^{-1}$
Heat capacity, gas (25°C)	818 $J.kg^{-1}.K^{-1}$
Heat of Vaporization	15.2 $kJ.mol^{-1}$

2.4. Naturally occurring ozone

Ozone occurs naturally in the atmosphere, constituting about 27% by weight at altitudes of 15 – 25km. It is formed from molecular oxygen by the absorption of solar UV radiation in the range 240nm – 300 nm via the reactions (Eq. 2.3 and 2.4).

Ozone absorbs UV radiation in the range 200nm – 600nm. This leads to a reversal of the formation reaction and the establishment of a steady-state concentration. A consequence of these processes is absorption of considerable UV radiation and its conversion into heat. This protects the Earth's surface from the harmful effects of UV light [46].

Ozone (O_3) is a naturally occurring gas; it contains three atoms of oxygen, rather than the usual two in oxygen (O_2). In the atmosphere ozone is created by ultraviolet radiation from the sun reacting with oxygen atoms.

At ground level ozone is created by lighting discharge reacting with oxygen atoms. Ozone has a characteristic smell, which can sometimes be detected by people with a keen sense of smell after a lightning storm.

Ozone close to the ground constitutes a serious air pollution problem. At ground level, ozone may be formed from the photochemical interactions of Volatile Organic Compounds (VOCs) and nitrogen oxides. The reactions involved are initiated by the photolysis of NO_2 and are summarized as follows:

$$NO_2 + h\nu \rightarrow NO + O \qquad \textit{(Eq. 2.6)}$$

The ozone formation reaction is balanced by the reaction:

$$NO + O_3 \rightarrow NO_2 + O_2 \qquad \textit{(Eq. 2.7)}$$

Ozone oxidizes NO to NO_2, resulting normally in low levels of ozone. However, in the presence of VOCs, radicals are formed which consume NO or convert NO to NO_2, and this can lead to an increase in the O_3 levels. The major processes can be summarized by the following non-elementary reactions:

$$VOC + OH \rightarrow RO_2 + products \qquad \textit{(Eq. 2.8)}$$

$$RO_2 + NO \rightarrow NO_2 + radicals \qquad \textit{(Eq. 2.9)}$$

$$Radicals \rightarrow OH + products \qquad \textit{(Eq. 2.10)}$$

Many types of VOCs are released into the atmosphere, which react in the above manner at different rates by a variety of mechanisms [46].

Ozone is created artificially by mimicking the above natural process; the two main methods of commercial ozone generators are Corona discharge and UV radiation.

2.5. Ozone generation

All processes that can dissociate molecular oxygen into oxygen radicals are potential ozone generation reactions. Energy sources that make this action possible are electrons or photo quantum energy. Electrons can be used from high-voltage sources in the silent coronal discharge, from chemi-nuclear sources, and from electrolytic processes. Suitable photon quantum energy includes UV light of wavelengths of 240nm and γ-rays.

2.5.1. Corona Discharge

In a corona discharge ozone generator the feed gas (oxygen), passes between closely spaced electrodes, one of which is coated with a dielectric material, under a nominal applied voltage potential of ~10kV [46]. A barrier discharge occurs when the gas becomes partially ionized, resulting in a characteristic glow. Efficiency of ozone production by corona discharge depends on the strength of micro discharges that depend on a number of parameters, such as, gap width, gas pressure, properties of the dielectric and metal electrodes, power supply and the presence of moisture.

Ozone has been an accompaniment to electrical storms during all the history of mankind. Figure 2.2 illustrates how oxygen (O_2) is transformed into ozone (O_3). Ozone can be easily created from oxygen and high electrical discharge. High voltage discharge breaks the two oxygen atoms (O_2) apart, creating two oxygen radicals O and O, as can be seen from Equation (2.3). These oxygen radicals are extremely reactive and they combine with oxygen molecules with the resulting molecule being called ozone (O_3) or trivalent oxygen, demonstrated in Equation (2.4).

Commercially available corona discharge ozone generators can produce ozone concentrations in excess of that possible by the UV radiation technique. This process is better suited to applications where large concentrations of ozone are required.

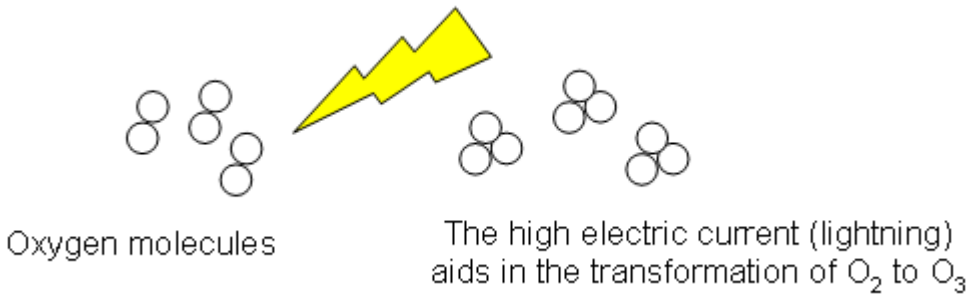

Figure 2.2. Formation of ozone from electrical current

2.5.2. Ultraviolet (UV) Radiation

The mechanism of photochemical production of ozone is similar to that which takes place in the stratosphere, where oxygen atoms, which are formed by the photo – dissociation of oxygen by short wavelength UV radiation (240 nm) react with oxygen molecules to form ozone.

In the UV radiation technique the feed gas (air, oxygen) is passed over a UV lamp, oxygen atoms formed by the photo dissociation of oxygen by short wavelength UV radiation (240nm) react with oxygen molecules to form ozone (Figure 2.3).

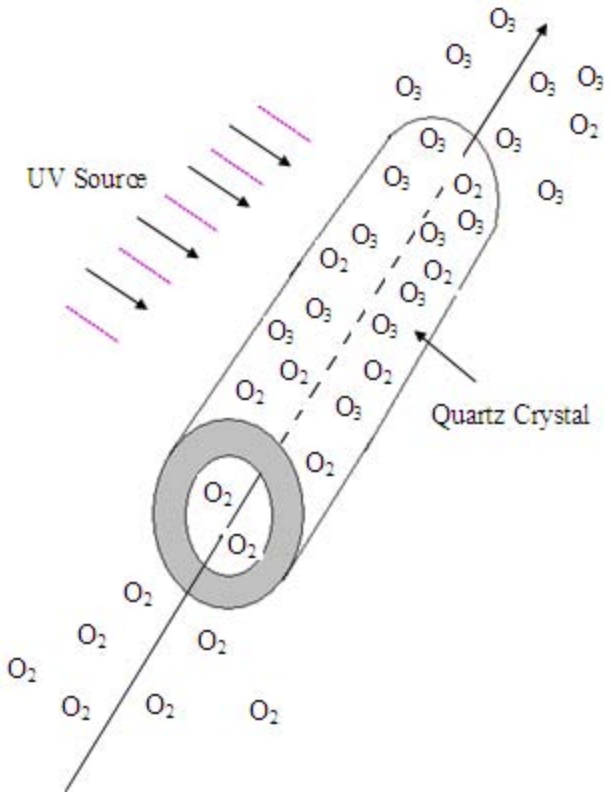

Figure 2.3. UV radiation

2.5.3. Electrolysis

High current density electrolysis of aqueous phosphate solutions at room temperature produces ozone and oxygen in the anodic gas. Electrolysis of sulphuric acid can produce very high ozone concentrations in oxygen when a well cooled cell is used. Although electrolysis of water can produce high concentrations of ozone, the output is low, and the cost is several times more than that of the corona discharge or UV radiation processes.

2.5.4. Review of Methods

Ozone gas produce by corona discharge method has a higher ozone concentration but is difficult to compress, dry, produce and then dilute the produced ozone in comparison to ozone produced by the UV radiation method.

Air treatment usually required large volumes of low ozone concentration. Ozone produced by UV, in comparison, generally needs no air pre-treatment and is produced at concentrations capable of destroying airborne bioaerosols and volatile organic compounds. Reduced gas flow rate in the UV radiation-based ozone generator gives higher ozone concentration due to longer retention time of oxygen molecules in the presence of UV light.

The factors that can influence the production yield of ozone are chemical composition (percentage of oxygen) and physical properties and process conditions such as, pressure, temperature, impurities, moisture of the feed gas, dielectric material, thickness and discharge gap of the generator, type of the UV bulbs (wavelength, frequency, energy consumption) used in the generator. The most obvious source for producing ozone gas is atmospheric air but it does not posses high purity oxygen. High purity oxygen does not require further drying. It gives much higher ozone concentration at lower energy consumption, reduces the size of the generator and eliminates the by products of nitrous oxides from the nitrogen contained in the dry air.

2.6. Useful Ozone

Ozone is one of the most powerful oxidants (Table 2.1) known and the naturally occurring level protects all life from the harmful effects of solar ultraviolet radiation. When ozone is present in the air one of the atoms from the O_3 molecule attaches itself to a pollutant molecule and destroys it. For example, ozone may be used to destroy bacteria [49-52], viruses [53-57] and odour [58, 59].

Table 2.2. Oxidizing potentials of various reagents

Oxidizing Reagent	Oxidizing Potential
Ozone	2.07
Hydrogen Peroxide	1.77
Permanganate	1.67
Chlorine Dioxide	1.57
Hypochlorous acid	1.49
Chlorine Gas	1.36
Hypobromous acid	1.33
Oxygen	1.23
Bromine	1.09
Hypoiodous acid	0.99
Hypochlorite	0.94
Chlorite	0.76
Iodine	0.54

Bacteria are microscopically small, single-cell creatures having a primitive structure. A relatively solid-cell membrane seals the bacteria body. Ozone interferes with the metabolism of the bacterium-cells through inhibiting and blocking the operation of the enzymatic control system. A sufficient amount of ozone breaks through the cell membrane, and this leads to the destruction of the bacteria [60].

Viruses are small, independent particles, built of crystals and macromolecules. Unlike bacteria, they multiply only within the host cell. They transform protein of the host cell into proteins of their own. Ozone destroys viruses by diffusing through the protein coat into the nucleic acid core, resulting in damage of the viral RNA. At higher concentrations, ozone destroys the exterior protein shell by oxidation, so DNA (deoxyribonucleic acid), or RNA (ribonucleic acid) structures of the microorganism are affected. Ozone destroys bad odours in the environment rather than merely filtering out some of the visible particles like “air cleaners”. For example, it eliminates the irradiation caused by phenol gasses, by oxidizing them. Phenol gasses are the invisible parts of

tobacco smoke that cause offensive odours and discomfort to the eyes and nasal passages. Figure 2.4 demonstrates how ozone destroys pollutants. The extra oxygen atom attaches to pollutants causing it to break down into a benign substance – Oxidizing, deodorizing and disinfecting [60].

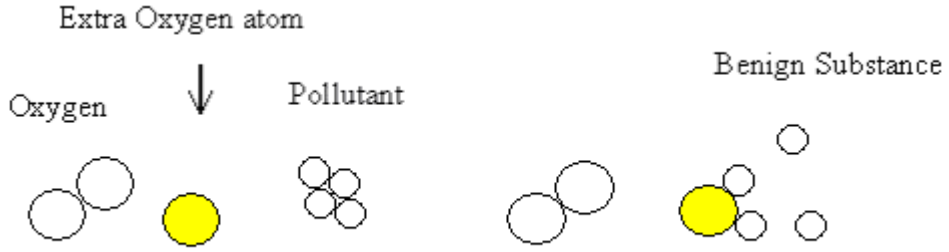

Figure 2.4. Ozone destroying pollutant

Ozone has been shown by extensive laboratory trials to be effective at reducing bacteria and odour when used at high levels no higher than 0.05ppm (50ppb). These levels are considered safe to breathe 24 hours per day (Tables 2.3 and 2.4). Tests have also shown that at these levels there are not harmful effects on plants. Therefore, by accurately generating and controlling artificial ozone, it can be used safely and effectively to destroy pollutants such as unpleasant odours, bacteria, viruses and molds.

Table 2.3. List of specific bacteria, viruses and molds susceptible to ozone

Aspergillus Niger (Black Mount)	Enteric Virus	Penicillium Bacterium
Bacillus Bacteria	Escherichia Coli Bacteria	Phytophthora Parasitica
Bacillus Anthracis	Enterovirus Virus	Poliovirus Type 1
Botrytis cinerea	Hepatitus A Virus	Rhabdovirus Virus
Candida Bacteria	Herpes Virus	Salmonella Bacteria
Cladosporium	Influenza Virus	Staph epidemidis
Clostridium Bacteria	Klebs-Loffer Bacillus	Stomatitis Virus
Diphtheria Pathogen	Mucor piriformis	Vesicular Virus
Eberth Bacillus	Mycobacterium Avium	Virbrio Cholera Bacteria

2.7. Harmful Ozone

One of the most important properties of ozone is that it has a very short half-life of approximately 5-30minutes, depending on (a) the amount of contaminants present in the air or on surfaces that the ozone can counteract with, (b) temperature and (c) humidity. If ozone cannot find a contaminant to work on it simply reverts to oxygen, Equation (2.5). Despite this short half-life, ozone is extremely dangerous to human health, and can have major adverse effects at relatively low concentrations. Table 2.2 and Table 2.3 represents the allowed safety limits proposed by the (WHO) World Health Organization (Table 2.2) and the actual ozone concentration thresholds within the (EU) European Union (Table 2.3). Ozone is usually found or generated in human environments (aircraft cabins, offices with photocopiers, laser printers, sterilizers).

2.8. Ozone Thresholds

Exposure to ozone constitutes a human health hazard. Exposure is known to decrease short-term lung function [61]. Ozone exposure has also been shown to be a mitigating factor in the development rates of asthma-like symptoms among children and adults [62-67]. Prolonged exposure is linked to increases in morbidity and mortality rates [68-75]. Outdoor ozone concentrations are considered to be the dominant source of indoor ozone concentrations [76]. In addition to these outdoor ozone sources, there are a number of indoor sources that need to be controlled and reduced; it is a well known fact that laser printers, photocopiers, ion generators and some sterilisation equipment produce ozone [77-84].

Table 2.4. Ozone Concentration Thresholds in the EU (adapted data from EU)

Threshold	μg/m^3	PPB	Max Exposure Time
Protection of Health	110	47	8hours
Protection of Vegetation	200	85	1hour
Protection of Vegetation	65	28	24hours
Provision of Info. to the Population	180	77	1hour
Alert to General Public	360	155	1hour

Table 2.5. Ozone Concentration Thresholds Proposed by the WHO (adapted data from WHO)

Threshold	μg/m^3	PPB	Max. Exposure Time
Protection of Health	150-200	64-85	1hour
Protection of Health	100-120	43-51	8hours
Protection of Vegetation	200	85	1hour
Protection of Vegetation	65	28	8hours

2.9. Outdoor Ozone

The ozone that is present in outdoor air at ground level reflects a combination of photochemical production and destruction coupled with injection from the stratosphere [76]. The photochemical production of ozone results from a complex set of reactions involving vapour phase organic compounds, nitrogen oxides, carbon monoxide and sunlight [76].

Many studies have reported on the associations between outdoor ozone concentrations and morbidity and mortality rates. Hubbell et al. have produced a review article which

describes monitored ozone levels over a three year period and then assess the human health benefits of attaining the 8-hr ozone threshold [75]. This article also includes summaries of the links between ozone and respiratory-related hospital admissions, lost school days, restricted activity days, asthma-related emergency department visits and premature mortality rates [75].

The outdoor concentration of ozone has increased over the years. The increase in outdoor ozone levels has tempered by the average reduction in ventilation rates and concomitant decrease in the transport of ozone from outdoors to indoors [81]. Ozone can be present at a concentration of up to 70% of outdoor concentration [83]. A study reviewing the activity pattern of people revealed that most time is spent indoors, whether it be work or home, as a result many people receive their highest and most dangerous exposures in indoor environments [85].

2.10. Indoor Ozone

Indoor sources of ozone are more common than they were in the past due to the introduction of electronic and office equipment. Some of the most significant ozone generating equipment include photocopiers, laser printers, air purifiers, ozone generators and electrostatic precipitators [81].

Although indoor ozone concentrations tend to be lower than concentrations found in the corresponding outdoor environments, this is somewhat counterbalanced by the much larger fraction of time the majority of people spend indoors. Some studies have shown that as much as 60% of harmful ozone exposure occurs indoors [74]

Although there are indoor ozone sources, a considerable percentage of indoor ozone has been transported from the outdoor environment [83]. Indoor ozone concentrations track outdoor concentrations with a slight time lag that is dependent on the air exchange rate. In the absence of indoor ozone sources, the ratio of indoor to outdoor ozone concentrations $(I:O)$ may be estimated using the simple expression below [74]:

$$I : O = \lambda / (\lambda + k_{SR}) \qquad \textit{(Eq. 2.11)}$$

Where λ is the air exchange rate and k_{SR} is the first-order rate constant for surface removal (both are in units of reciprocal time). This equation assumes that the penetration coefficient for ozone is unity (an assumption that remains largely untested), and ignores gas-phase reaction, which tend to be smaller sinks than surface reactions.

It has long been known that photocopiers emit ozone along with a number of stable VOCs, such as formaldehyde and other aldehydes [84]. The ozone exposure to people working with photocopiers depends on the ozone emission rate (and therefore the copy frequency), and the local ventilation [84]. This, in turn, depends on the indoor climatic parameters (fresh air exchange rate, outside weather conditions, traffic density, etc.), on building surfaces, the level of indoor VOCs and penetration of outdoor ozone [84].

Electronic equipment is present in almost every office worldwide, in particular photocopiers and other printing equipment in addition to computers, laptops and visual display units (VDUs) [84]. Determining the contribution from any one type of equipment is a complex task. In the case of dry-process photocopiers, measurements of the emissions of primary pollutants such as ozone, VOCs and particles can be carried out in the laboratory. In addition to these primary pollutants, secondary pollutants are also important such as, radicals and other unstable products that may be produced in reactions between ozone and unsaturated VOCs. The latter may either originate from the photocopier itself or from other sources present, such as processed copier paper, indoor furnishings, cleaning products and even human exhalation [84].

Office workers have reported specific symptoms including eye, airway and throat irritation as well as more general symptoms of headaches, fatigue and nausea [84]. Symptom reporting has been related to exposure parameters such as ozone concentration, or the frequency of use of photocopiers.

Exposure to high ozone levels may eventually cause injury to the lungs. This injury may depend on daily exposures to smaller amounts of ozone rather than peak exposures.

Exposures to air contaminants in a given enclosed environment has been defined as the concentration of the pollutant in that enclosed environment times the amount of time and individual spends there.

2.11. Health Effects of Ozone

2.11.1 Respiratory Effects (Asthma)

While there are several possible risk factors associated with asthma and other respiratory conditions, such as family history, demographics and management practices, ambient air pollution has been extensively investigated as a potential risk factor for acute asthma episodes [62]. Several studies have suggested that hospitalisations due to respiratory issues increase during periods of poor air quality and particularly with increases in ozone levels [62]. Additionally, ozone has been associated with respiratory symptoms and the use of asthma medication for asthmatic school children using maintenance medicine [65]. There are a number of factors responsible for the increase in the number of cases of asthma and other respiratory complaints, such as, exposure to dust mites or other antigens, changing patterns of viral infections, measles, changes in diet and increasing levels of pollution [66]. Ozone has been treated as exacerbating asthma, however there is also evidence linking long term exposure to ozone to the development of asthma in adult males [66].

2.11.2. Mortality Effects

There have been a number of studies carried out at various locations around the world which provide a range of estimates for the association of a single day increase of 10ppb of ozone concentration with increases of premature mortality ranging from 0.78 – 1.28% [69, 73, 86, 87].

Also, a study in Genoa, Italy, found an increase of 4.0% in mortality per 25 ppb increase in ozone [68] while a study in Shanghai found an increase of 0.45% mortality per 5 ppb

increase in 2 – day average ozone [88]. Significantly, when data used only included with average ozone levels lower than 15 ppb [89], outdoor ozone was significantly associated with premature mortality.

An increase in the concentration of outdoor ozone concomitantly produces an increase in the indoor concentrations of ozone and its reaction products [74, 76]. Thus, some of the associations between outdoor ozone concentrations and the morbidity and mortality rates are likely due to ozone transported into various indoor environments (residences, work places, hospitals, schools, etc.) where subsequent exposures occur [74].

2.12. Decomposition of Ozone

Surface deposition dominates indoor ozone removal and is typically modelled by the following equation [76]:

$$R = v_d C A \qquad \textit{(Eq. 2.12)}$$

where R is the removal rate of ozone to a surface (μg h^{-1}), v_d is the deposition velocity for ozone to a surface (m h^{-1}), C is the concentration of ozone in air above a surface (μg m^{-3}) and A is the area of surface on which ozone is depositing (m^2).

The ozone deposition velocity to a surface encompasses the transport of ozone to the surface and the reactivity of that surface with ozone. The overall resistance to ozone removal at a surface is typically modelled as the sum of a transport resistance and a surface reaction resistance, as described by the following equation [90]:

$$\frac{1}{v_d} = \frac{1}{v_t} + \frac{4}{\gamma \langle v_B \rangle} \qquad \textit{(Eq. 2.13)}$$

where v_t is the transport limited deposition velocity (m h^{-1}), γ is the reaction probability, and v_B = Boltzmann velocity (m h^{-1}) for a depositing gas (ozone in this case).

As indicated by the above two equations (Eq. 2.12. and Eq. 2.13.), there are three parameters that have a significant effect on the degree of ozone removal to a surface:

1) The surface area of the reactive material.
2) The fluid mechanics of the room and boundary layer adjacent to the material.
3) The reactivity of the material.

Fluid mechanic conditions determine the transport limited deposition velocity, which encompasses both transport from the source to the reactive material as well as boundary layer effects. The reaction probability is defined as the number of reactions that occur on a surface normalised by the number of collisions of molecules with that surface, and is used to characterise the reactivity of the surface. Ozone reaction probabilities for common building materials generally range from about 10^{-7} to 10^{-5}, with some highly reactive materials approaching 10^{-4} [77, 78, 91].

Homogeneous and heterogeneous ozone reactions with unsaturated organic compounds form a range of by products such as, carbonyls, carboxylic acids, oxidised secondary organic aerosols and other oxidised products [74]. Many of these reaction products may be as harmful to human health as ozone itself [74]. Therefore, any strategy to remove ozone by using reactive materials should strive for materials of high reactivity that produce negligible formation and release of harmful by-products. Further, the material should be strategically placed to enhance the transport limited deposition velocity (v_t) [90].

2.12.1. Determination of v_d

A well-mixed environment was assumed for both O_3 and CO_2. Equation below is based on a mass balance for either gas, assuming there are no emission sources of the gas, and homogeneous gas phase reactions are negligible.

$$\frac{dC}{dt} = -\lambda C + \lambda C_{OUT} - \frac{1}{V}\sum_i v_{di} A_i C \qquad \textit{(Eq. 2.14)}$$

where C is the concentration of gas in the test environment air (ppb), t is the time (hours), λ is the air exchange rate (h^{-1}), C_{OUT} is the concentration of gas entering chamber (ppb), V = volume (m^3), v_{di} is the deposition velocity of the ith material (mh^{-1}), and A_i is the surface area of the ith material (mh^{-1}).

Irreversible deposition does not occur for CO_2, allowing for the solution of air exchange rate in accordance with the following equation:

$$\lambda t = -\ln\left(\frac{C - C_{OUT}}{C_0 - C_{OUT}}\right) \qquad \textit{(Eq. 2.15)}$$

where C_0 is the initial concentration of CO_2 in the chamber air (ppb).

The ozone decay rate β, is defined as the sum of deposition losses to the test environment background and Passive Removal Material (PRM) in the following equation [90]:

$$\beta = \frac{v_{dPRM} A_{PRM}}{V} + \frac{v_{dc} A_c}{V} \qquad \textit{(Eq. 2.16)}$$

where β is the ozone decay rate (h^{-1}), v_{dc} is the deposition velocity to the chamber surfaces (mh^{-1}), A_C is the surface area of the chamber (m^2), v_{dPRM} is the deposition velocity of the PRM (mh^{-1}), and A_{PRM} is the horizontally projected area of the PRM (m^2).

The deposition velocity for the PRM is set to zero in the absence of a PRM in the chamber. To determine the ozone deposition velocities for the test environment and PRM, Eq. 2.14 was solved for ozone concentration, yielding Eq. 2.17 below. Experimental data were fitted to Eq. 2.17 for each scenario. Knowing the horizontally projected surface area of each material and the volume of the room allowed for deposition velocities to be calculated in accordance with Eq. 2.16,

$$C = \frac{\lambda p C_{OUT}}{\lambda + \beta}\left[1 - e^{-(\lambda+\beta)t}\right] + C_0 e^{-(\lambda+\beta)t} \qquad \textit{(Eq. 2.17)}$$

where p is the penetration factor for ozone (generally assumed to be 1). Uncertainties in the measured ozone decay rates for the background were based on a propagation of error analysis using the maximum of instrument error. The uncertainties in the ozone decay rate for the PRMs were based on a propagation of error from the background error and the maximum of instrument error or standard error.

In order to put PRMs in the context of building occupant exposure to ozone, we calculated the effectiveness of removing ozone in a typical residence. Ratios of indoor ozone to outdoor ozone were calculated by rearranging Eq. 2.14 for C/C_0. The ratio was calculated for two scenarios: a hypothetical home with and without the presence of a PRM. The ratio of C/C_0 with a PRM to C/C_0 without a PRM can be used to determine an effective ozone removal which is independent of outdoor ozone concentration. This calculation was repeated while varying air exchange rates and area of

experimental material. Based on the effectiveness for portable air cleaners defined by Miller-Leiden et al, we define an effectiveness, H, using the following equation:

$$H = 1 - \frac{C^*}{C} \qquad \textit{(Eq. 2.18)}$$

where C^* is the steady state indoor concentration of ozone with PRM present (ppb) and C is the steady state indoor concentration of ozone with no PRM present (ppb).

2.13. Methods of Decomposition

The problem of ozone decomposition is very important because of ozone's toxic properties and the need to remove it from human surroundings. The decomposition of ozone is necessary in many situations. In airplane cabins, exterior air must be purged before being circulated in the cabin [59]. In office environments, cooling air from photocopiers and laser printers carries large amounts of ozone generated by the corona discharge process must be reduced before being emitted into the workspace. Similarly, discharges from sterilization [92, 93], deodorization [94] and wastewater treatment units [40, 95] must also have ozone levels reduced before being emitted.

Although the decomposition of ozone to dioxygen is a thermodynamically favoured process, ozone is thermally stable up to 523 K and catalysts are needed to decompose it at lower temperatures [96].

There are several options available to effectively control and destroy ozone with varying levels of efficiency and cost. The three most common methods to control ozone emissions are: Thermal Destruction, Carbon Destruction and Catalytic Conversion.

2.13.1. Thermal Destruction

Ozone can be thermally destroyed at >320°C with a contact time of approximately 3 seconds. This method of ozone destruction is very effective. However, the capital expenditure and operational cost of the thermal destruct unit are both very high [46].

2.13.2. Carbon Decomposition

Activated carbon can be used to efficiently decompose ozone. The reaction between the ozone and the activated carbon is chemical in nature and carbon is consumed in the process, this makes the process less cost effective. Another disadvantage of this method is that the use of carbon is usually limited to applications where the ozone concentration is relatively low. It is critical to note that a fire can start in activated carbon in higher concentration applications [46].

2.13.3. Catalytic Conversion

Ozone can also be destroyed catalytically. In this process, a catalyst is used to convert ozone into oxygen. A catalyst is a substance that increases the rate of chemical reaction without being consumed in the reaction. Unlike carbon, a catalyst is not consumed in the reaction, therefore the catalysts lifetime is extensive (usually several years) [61].

2.13.3a. Precious Metal Catalysts

Precious metal catalysts such as platinum/palladium can be used to decompose ozone at room temperature. The draw back of using these precious metals is that a residence time of approximately 3 seconds is required for effective decomposition of ozone. The cost of

the precious metal catalyst required for an effective system makes this type of catalyst cost prohibitive in its application.

2.13.3b. Metal Oxide Based Catalysts

The use of manganese oxide based catalysts appears to be the benchmark technology for ozone destruction. This technique can operate effectively at room temperature. Manganese dioxide based catalysts show very high ozone destruction efficiencies. These catalysts also require a residence time of only 0.36 seconds, which means relatively small catalyst volumes are needed, making the catalytic system with manganese dioxide based catalyst very cost effective. Another advantage of using this process is that the inlet concentration of ozone does not affect the amount of catalyst required or the design of the system [97].

2.14. Manganese Dioxide

There are generally three available physical forms of catalysts: monoliths, foams and pellets (Figure 3.5(a), (b) and (c)).

Monoliths are unitary structures (often referred to as honeycombs), which provide parallel straight through pore shapes. Foams are unitary structures composed of open cells that form a three-dimensional network of passages. Pellets are usually obtained by extrusion and come in a variety of forms, including spherical, cylindrical and ring shapes [59].

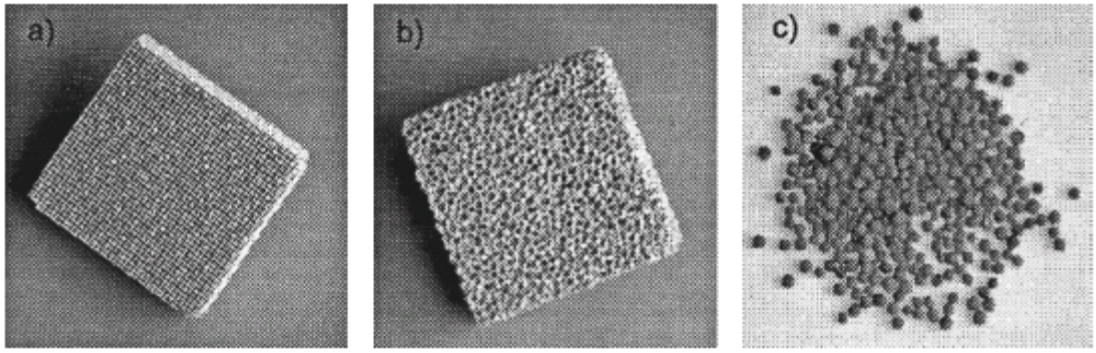

Figure 2.5. Typical geometric shapes for catalysts: (a) monolith, (b) foam and (c) pellets.

The use of pellets result in a substantial pressure build-up at high flow rates, whereas the corrugated structures, monoliths and foams are able to accommodate high gas throughput with little resistance [59]. In a comparative study of pellets and monolith structures[59], it was found that the important parameters in the comparison were mass-transfer, heat-transfer and pressure drop effects. It was found that for the same bed height and flow rate, the pressure drop for a monolith structure was two or three orders of magnitude lower than pellets [59]. Because of these reasons monolithic structures have been the predominant geometry employed in many commercial products.

Chapter 3: Literature Review of Gas Detection

3.1. Introduction

Gases are the key measurands in many industrial or domestic activities. In the last decade the specific demand for gas detection and monitoring has emerged particularly as the awareness of the need to protect the environment has grown alongside our own need for unpolluted air. Gas sensors find applications in many fields, such as automotive industry [98-100], food industry [101-103], medical industry [104-106] and environmental monitoring [107-110]. The environmental gas sensing industry covers a huge area, including gas sensors for use as fire detectors [111-113], leakage detectors [114, 115], detection of harmful gases, alarm devices warning the overcoming of threshold concentration values of hazardous gases [116, 117]. The detection of volatile organic compounds or odours generated from food or household products has also become increasingly important in the food industry and in indoor air in general. Table below gives a list of some of the most common applications and the associated industries.

Table 3.1. Gas Sensor Applications

Automotive	Ventilation control (indoor) Lambda sensors
Domestic	Fire detection Leak detection Toxic/Flammable Gas detection Ventilation Control
Industrial	Process Control Off gas Emission Control Fire detection Leak detection Toxic/Flammable Gas detection Ventilation Control
Food	Food Quality Control Odour Detection Bacteria Detection
Medical	Breath Analysis Disease Detection
Air Pollution	Harmful gas monitor

3.2. Current Gas Sensor Technology

Some of the more common analytical gas sensing instruments such as mass spectrometry and chromatography are expensive, complex, bulky and require specific sample preparation, thereby making real time monitoring difficult.

Much research has been carried out to design smaller and inexpensive gas sensors possessing good characteristics such as high sensitivity, selectivity and stability. Based on different sensing principles a large variety of sensors, such as semiconducting gas sensors, optical sensors, thermal conductivity sensors, mass sensitive devices such as

quartz microbalance sensors catalytic sensors, dielectric sensors, electrochemical sensors and electrolyte sensors have been developed. Typically the target gas interacts or adsorbs on the surface of the gas sensitive material, thereby inducing a change in the electrical characteristics of the material, which is a direct relation to the target gas concentration [35]. The electrical parameters extracted can be of a wide variety including DC resistance, AC resistance, AC impedance, Field Effect Transistor (FET), threshold voltage, phase change of a wave propagated across the surface, resonant frequency of cantilever beams etc. The methodological applications of some of these technologies are described in the following sections.

3.2.1. Capacitive Based Gas Sensors

Capacitive based gas sensors measure the change in dielectric constant of films between the electrodes as a function of the gas concentration. Capacitance changes in the sensors are typically of the order of Pico farads (pF) and are dependent on the operating frequency and surrounding conditions, like humidity and temperature [118, 119]. The capacitive sensors rely on the inter-digitated electrode structures (IDS), which correspond to the two plates of a standard capacitor, to monitor changes of the dielectric coefficient of the film [120]. If the dielectric constant of the film is lower than that of the analyte, the capacitance will increase, and if the film dielectric constant is larger the capacitance will reduce [120].

Capacitive sensors have good prospects given that the capacitor structure is simple, thereby enabling miniaturisation and achieving high reliability and fabrication costs [121]. Another advantage of this sensor type is that amplification of capacitance is easily achieved by oscillator circuits, therefore sensitive detection of target gas may be easily obtained [121].

Capacitance is expressed as:

$$C = \frac{\varepsilon_0 \varepsilon_r A}{d} \qquad \textit{(Eq. 3.1)}$$

where ε_0 is the permittivity in vacuum, ε_r is the relative permittivity, A is the electrode area and d is the distance between the electrodes (i.e. the thickness of the dielectric layer) [121]. For detection, the target molecules of interest must induce a change in ε_r, A or d.

3.2.2. Piezoelectric Sensors

As mentioned above there are many types of piezoelectric sensors. In general there are two types of piezoelectric sensors used in gas sensing technologies, Quartz Crystal Microbalance (Bulk Acoustic Wave device, BAW) and the Surface Acoustic Wave (SAW) device. The SAW device produces a surface wave that travels along the surface of the sensor while the QCM produces a wave that travels through the bulk of the sensor. Both types of devices work on the principle that a change in the mass of piezoelectric layer is a result of exposure to the target gas. Piezoelectric materials produce a change in voltage when mechanical stress is applied, and will deform if a voltage is applied across them [122]. Applying a similar oscillating frequency to that of the resonant frequency of the piezoelectric crystal produces a stable oscillating circuit [122].

3.2.2.1. Quartz Crystal Microbalance Sensor

A QCM sensor comprises of a slice of a single crystal of quartz material, typically sensors are circular in shape with a diameter of approximately 10mm [123]. Thin coatings (10nm - 1μm) are deposited on the crystal by spin coating, airbrushing or inkjet printing. Gold electrodes are attached to either side of the crystal [123]. Applying an alternating electrical potential across the crystal at room temperature causes the crystal to vibrate at a resonant frequency of 10 – 30MHz [124]. The thickness of the crystal determines the wavelength (λ) of the fundamental harmonics of oscillation [123]. The

three dimensional wave produced, travels through the entire bulk of the crystal. Upon exposure to the target gas the deposited layer adsorbs gas molecules, which results in an increase in mass on the crystal surface. This increase in mass alters the resonant frequency of the crystal. This recorded frequency variation is used for the detection of gas concentration [122].

The resonant frequency of the QCM can be related to the change of the mass of QCM loading by Eq. 3.2 below (Sauerbrey equation) [123]:

$$\Delta f = -2 f_0^2 m_f / A(\rho_q \mu_q)^{1/2} \qquad \textit{(Eq. 3.2)}$$

where Δf is the change in resonant frequency, f_0 is the resonant frequency, m_f is the mass change due the adsorption of gas molecules on the crystal, A is the electrode area, ρ_q is the density of the quartz and μ_q is the shear modulus of the quartz [123].

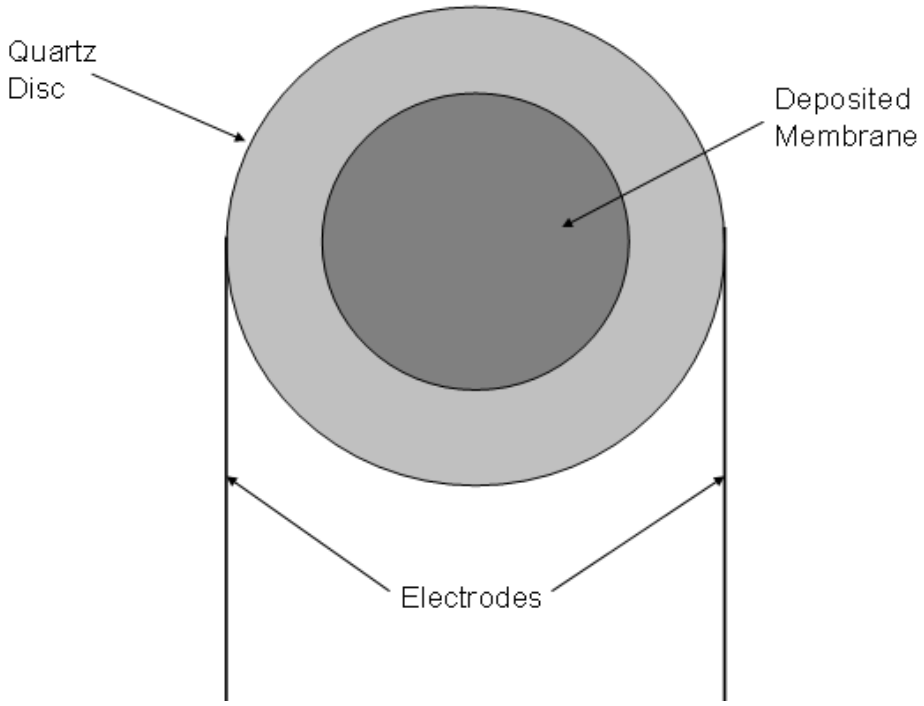

Figure 3.1. Quartz Crystal Microbalance (QCM)

3.2.2.2. Acoustic wave based gas sensors

Acoustic wave sensors are so named because they utilize a mechanical or acoustic wave as the sensing mechanism. As the acoustic wave propagates through the material or on the surface of the material and any changes to the characteristics of the propagation path will have an affect on the velocity and/or amplitude of the wave [125]. Velocity deviations may be monitored by measuring the frequency or phase characteristics of the sensor, which then may be used to determine the physical quantity being measured [125]. Due to the high sensitivity of the acoustic waves to surface mass changes, they have many applications as gas sensors [126, 127], biological sensors [128, 129] and tactile sensors [130, 131]. There are numerous types of acoustic wave sensors such as Thickness Shear Mode (TSM) sensor, Surface Acoustic Wave (SAW) sensor, Flexural Plate Wave (FPW) sensor and Acoustic Plate Mode (APM) sensors. All these sensors use piezoelectric material either in the thin film form or in bulk form to launch the acoustic waves.

There is a lot of literature dedicated to these devices for gas sensor applications [10 – 14]. An analytical comparison between the various acoustic sensors has been reported by [22, 23].

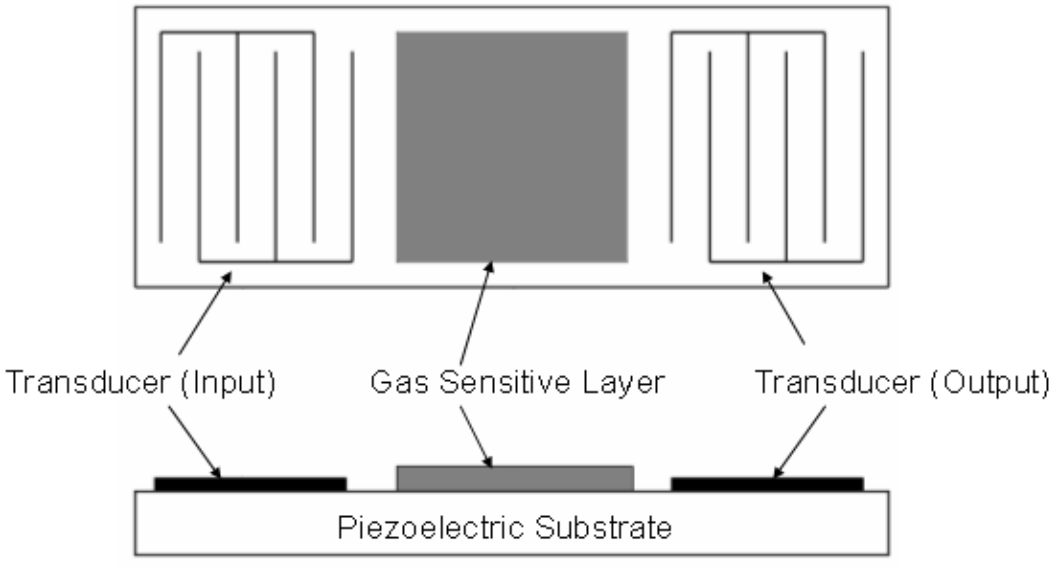

Figure 3.2 Surface Acoustic Wave (SAW) sensor

The SAW device consists of a relatively thick substrate plate made of piezoelectric material (ZnO or lithium niobate) with an input and output transducer deposited on the substrate surface [132]. The sensitive layer is fabricated between the two interdigitated structures (IDS) as shown in the above figure. An AC signal is applied across the input transducer creating a 2 dimensional acoustic wave which propagates along the surface of the device at a depth of one wavelength at operating frequencies between 100 – 400 MHz, this wave is then picked up after a certain distance by an identical pair of IDS (output transducer). It is important that the electrode pairs are separated by an integer number of wave lengths for accurate measurements. The mass of the gas sensitive membrane of the SAW device is changed on interaction with a compatible analyte and causes the frequency of the wave to be altered. This change in frequency is given by Eq. 3.3.

$$\Delta f = \Delta f_P c_g K_P / \rho_P \qquad \textit{(Eq. 3.3)}$$

Where Δf_P is the change in the frequency caused by the gas sensitive layer, c_g is the gas concentration, K_P is the partition coefficient, ρ_P is the density of the membrane used [123].

Acoustic wave based sensors require higher frequencies of operation at smaller sizes, thereby complicating the read out electronic circuitry and incurring stringent constraint on impedance matching and noise control at these high frequencies [133]

Another important acoustic wave based sensor is a FPW sensor, in which, the device plate thickness is only a few percent of the acoustic wavelength as opposed to SAW devices where the device thickness is greater than the wavelength. This offers an improved behaviour over SAW devices in terms of sensitivity, response time and also allowing complete isolation of the electronic from the medium under investigation [35].

3.2.3. Field Effect Transistor (FET) Based Gas Sensor

The development of semiconductor technology has led to the emergence of many semiconductor chemical sensors. The semiconductor chemical sensor is based on the metal oxide semiconductor (MOS) junction principle. MOSFET based gas sensors are complex solid-state gas sensors and are inherently more difficult to fabricate and require more extensive control and measurement electronics [35]. The MOSFET sensor as shown in Figure 3.3 is a metal-insulator-semiconductor (MIS) device as shown in the figure below [35, 134]. The structure of the MOSFET consists of a metal layer on top of an oxide layer (SiO_2), and a p-type silicon base substrate with two n-doped channels on either side of the gate [122]. Conduction between the source and drain of the transistor is controlled by the potential on the gate electrode. Charge at the gate leads to a reflected charge induced in the channel and this in turn modifies the conductance between the source and drain of the device [135].

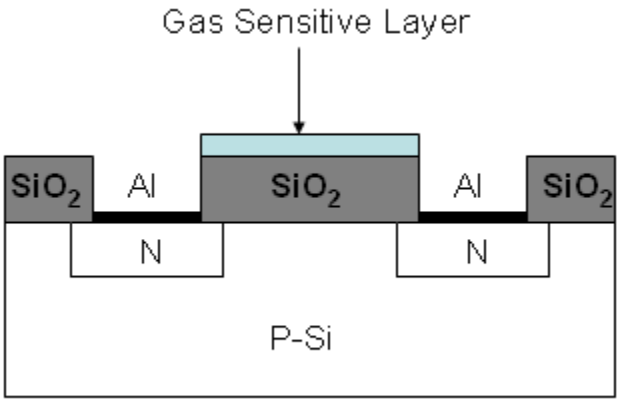

Figure 3.3. MOSFET gas sensor [135]

This sensor works on the principle that the threshold voltage of the MOSFET sensor changes on interaction of the gate material (catalytic metal) with certain types of gases due to corresponding changes in the work functions of the metal and oxide layers [122, 136] (Figure 3.3). The changes in the work function occur due to the polarization of the surface and the interface of the catalytic metal and oxide layer when the gas interacts

with the catalytically active surface [134]. In order for the physical changes in the sensor to occur the metal-insulator interface must be accessible to the gas. Hence a porous gate material must be used to facilitate diffusion of the gas into the material [134]. The change in the threshold voltage is proportional to the concentration of the analyte and is used as the response mechanism for the gas. Changes in the drain-source current and the gate voltage have also been used as the response mechanisms for the MOSFET gas sensors as they are also affected by the changes in the work function [134].

Apart form the standard MOSFET gas sensor architecture a hybrid suspended gate FET (HSGFET) gas sensor can also be fabricated by micromachining. The HSGFET is a metal air-gap insulator device. The air-gap allows easy access to both the gate material and the insulator so diffusion is not necessary and therefore a wider choice of gas sensitive materials may be used [134] (Figure 3.4)

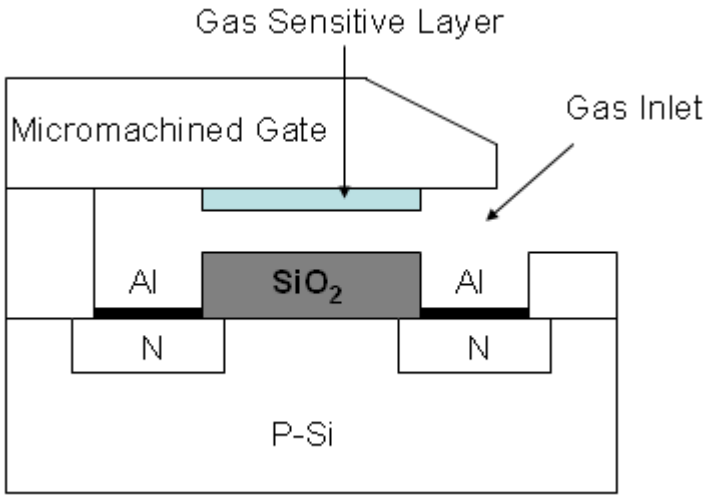

Figure 3.4. HSGFET gas sensor [135]

Gas sensing MOSFETs are produced by microfabrication techniques. Therefore, reproducibility is relatively good compared to other sensor technologies discussed. However, these sensors can suffer from baseline drift and instability depending on the sensing materials used [135]. Some limiting factors are that the gas must flow directly across the sensing material and the operating temperature are very important and

seriously affect the sensitivity of the device, control of the surrounding environment is important [135].

3.2.4. Optical Gas Sensors

In conventional gas sensors, the detection methods are based on the change in the electrical properties of the sensing material on exposure to the target gas [137]. For optical gas sensors the detection method is based on the reversible changes of optical properties of the sensor materials in a chemically active environment [137]. Examples of modulation in light property for gas detection are; changes in absorbance, fluorescence, polarization, refractive index, interference, scattering and reflectance [123]. In general optical sensors are comprised of four basic components: a) light source (laser), b) optics to direct the laser to and from the sensor housing, c) the sensing element and d) the detector for interpreting the light signal [123]. Figure 3.5 below shows a basic schematic diagram of the optical sensor elements. Optical gas sensors play an important role in the sensing field for the measurement of environmental and biological quantities. At present a large variety of optical methods are used in chemical sensors and biosensors, including ellipsometry, spectroscopy (luminescence, phosphorescence, fluorescence, raman), interferometry (white light interferometry, modal interferometry, in optical waveguide structures), spectroscopy of guided modes in optical waveguide structures (grating, coupler, resonant mirror) and a surface plasmon resonance (SPR). In these sensors a desired quantity is determined by measuring the refractive index, absorbance and fluorescence properties of the analyte molecules or a chemical-optical transducing element [138].

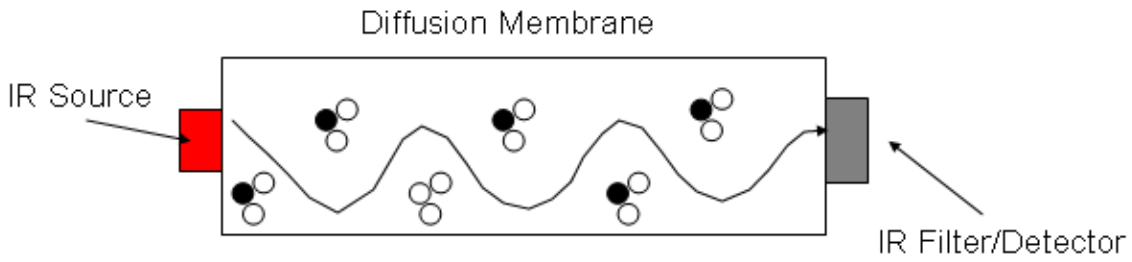

Figure 3.5. Optical Gas Sensor Schematic

3.2.5. Electrochemical Gas Sensors

Electrochemical gas sensors employ an electrochemical cell consisting of a casing that contains a collection of chemical reactants (electrolytes or gels) in contact with the surroundings through two terminals (anode and cathode) of identical composition. For gas sensors, the top of the casing has a membrane which can be permeated by the gas sample. Oxidation takes place at the anode and reduction occurs at the cathode. A current is created as the positive ions flow to the cathode and the negative ions flow to the anode [139]. Gases such as oxygen, nitrogen oxides and chlorine which are electrochemically reducible are sensed at the cathode, while electrochemically oxidizable gases such as carbon monoxide, nitrogen dioxide, ozone and hydrogen sulphide are sensed at the anode [139]. The output of the electrochemical cell is directly related to the concentration of the target gas present in the atmosphere. Depending on whether the output is an electromotive force (open circuit) or an electrical current, the electrochemical cell can be classified as potentiometric or amperometric [138]. Potentiometric measurements are performed under conditions of near-zero current. Amperometric sensors are usually operated by imposing an external cell voltage that is sufficiently high to maintain a zero oxygen concentration at the cathodic surface: therefore the sensor current response is diffusion controlled [138]. The different types of gas sensing technologies are summarised in Table 3.1.

3.2.6. Metal Oxide Based Gas Sensors

The detection principle of resistive gas sensors is based on changes in the resistance of a metal oxide layer upon exposure to the target gas molecules. The gas-solid interactions influence the density of electronic species in the film and thereby the overall resistance of the film. These are the simplest type of sensors among the various technologies and hence the most attractive type for portable applications. They posses the advantages of compact size, simple fabrication, low cost and simple measurement electronics. Simplicity of fabrication in these sensors is sometimes offset by inherent limitations in selectivity and sensitivity. The sensing properties are related to the surface reactions between the target gas and the oxygen ionosorbed. The measured physical quantity is normally the resistance, which depends on the adsorbed species through the height of the energy barriers between the grains. The applications of semiconducting gas sensors range from environmental monitoring to domestic and industrial applications. The benefits offered by semiconductor gas sensors are related to low dimensions and low fabrication and operating costs.

Metal oxide sensors can be either n-type or p-type. The n-type sensors include oxides such as, In_2O_3 [29], SnO_2 [24], ZnO [23] and WO_3 [140]. The n-type oxides are used for the detection of oxidising gases. Some common oxides used in p-type sensors include NiO [141] and CoO [142]. These sensors respond to reducing gases. Excitation of an n-type (negative or donor type) semiconductor results in an excess of electrons in the conduction band thereby increasing the reactivity with oxidizing molecules present in the atmosphere [135]. Excitation of a p-type (positive, hole, acceptor type) semiconductor gives rise to an electron deficiency in the valence band which promotes reaction with reducing compounds present [135].

For n-type semiconductor sensors, oxygen in the atmosphere reacts with the surface of the sensor and traps the free electrons present on the surface of the film or at the grain boundaries of the oxide grains. This produces an increase in resistance due to the lack of carriers and the resulting potential barriers produced between the grains inhibit the carrier mobility [135]. Exposing the sensor to a reducing gas decreases the resistance of the

sensitive layer as the gas reacts with the oxygen releasing an electron. The consequent increase in free electrons results in an increase in conductivity [123]. The mechanism is similar for p-type semiconductors but is of opposite sign. The mechanism of the increase in carrier concentration by reacting with the reducible gases as described above can be understood from the following equations [122]:

$$e + \frac{1}{2}O_2 \rightarrow O^-(s) \qquad \textit{(Eq. 3.4(a))}$$

$$R(g) + O^-(s) \rightarrow RO(g) + e \qquad \textit{(Eq. 3.4(b))}$$

where e is an electron from the conduction band of the oxide layer, R(g) is the reducible gas, and s and g imply surface and gas respectively [123].

3.2.7. Summary of Sensor Technology

The sensors discussed above can be used to detect many oxidizing and reducing gases. The endeavour of the research community is to increase the sensitivity, selectivity and stability of such devices, while providing a simple cost effective method of fabrication. Volatile organic components (acetone, benzene, propanol) and harmful gases (nitrogen dioxide, ozone) are known to have adverse effect on the quality of the environment and its inhabitants. Hence it is critical to develop methods of early and inexpensive detection of their presence in the environment. Table below illustrates sensor types along with the corresponding measurable physical change used for gas detection [35].

Table 3.2. Review of Gas Sensor Technology

Device	Physical Change
Semiconductor gas sensor	Electrical Conductivity/Resistivity
Field Effect Gas Sensors: Diodes, Transistors, Capacitors	Work Function (electrical polarisation)
Piezoelectric gas sensors: Quartz Crystal Microbalance (QCM), Surface Acoustic Waves (SAW)	Mass
Optical Sensors	Optical Parameters: SPR, Reflection, Interferometry, absorption, fluorescence, refractive index or optical path length
Catalytic Gas Sensors	Heat/Temperature
Electrochemical Gas Sensors (Amperometric, Potentiometric)	Electromotive Force, Electrical Current

3.3. Overview of Ozone Gas Sensors

As can be seen from the above sections there are numerous methods of gas and ozone detection. However, ozone sensing requires a typical set of parameters which need to be met in order to produce a practical ozone sensor. UV absorption method may be the most widely used technique for the detection of ozone. This method is very reliable and stable as the ozone gas is contained within an optical cell. However, a major disadvantage of this method is the cost due the complexity of the equipment and operation.

Metal oxide based semiconductor gas sensors have extremely high sensitivities with the added advantages of low fabrication costs, low operating costs, lower power consumption and portable. Metal oxide gas sensors are frequently used in gas leakage detection and ambient air quality monitoring in traffic [143]. The latter application utilizes a metal oxide sensor to close the air intake in the presence of high concentration of noxious gases [143].

Today there are numerous companies offering this type of sensor such as Figaro, FIS, MICS, UST, CityTech, Applied Sensors, NewCosmos, etc, with applications ranging from harmful, toxic or explosive gas detection to air intake control in automobiles [144].

The following sections focus on metal oxide semiconductor sensors as they are ideally suited to low concentration ozone detection.

In general a metal oxide based sensing device comprises of the following parts [144]:

1) Substrate material
2) Electrodes (deposited on the surface of the substrate used to measure the electrical characteristics of the sensitive layer)
3) Heater (deposited on the underside of the substrate, used to raise the operation temperature of the device
4) Sensitive layer (deposited on top of electrodes)

Each of these elements is discussed in detail in the following sections.

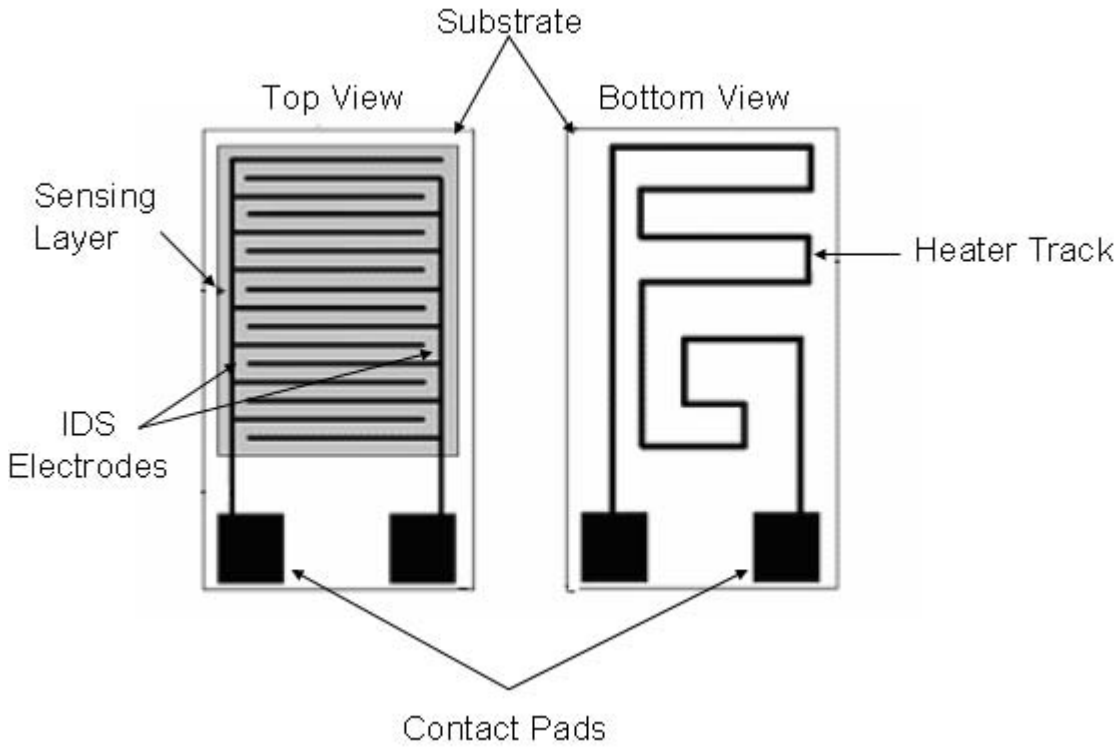

Figure 3.6. Sensor Structure

3.4. Sensor Structure

While it is true that the gas sensitive material is the most important element of the sensor device, the substrate material on which the electrodes and sensing layer are based on is of critical importance. For example, when the sensor is being operated at several hundred degrees Celsius, the influence of the substrate becomes important [145]. Other important aspects to consider when choosing a substrate material include mechanical, thermal and chemical stability in various harsh environments as well as a good surface finish to aid the fabrication process [146]. In many cases, sapphire was selected as the substrate material due to its excellent mechanical, thermal and chemical stability in harsh environments as well as a good surface finish for thin-film deposition [18]. Other important criteria to consider when choosing substrate material is the size and shape of the device required. Other common materials used as the substrate material in this type of sensor are alumina and silicon as defined in Table 3.4.

Electrodes deposited on top of the substrate material allow measurement of the characteristic changes in the metal oxide layer. In general the electrodes are thereby located underneath the sensing films, however the deposition of so-called top electrodes on thin film metal oxide layers have been utilised [147]. As a further possibility it has been suggested that the application of a traverse electric field to the sensing layer by using the upper interdigitated electrode as a gate electrode and the heater as a counter electrode [147]. This additional electric field can influence the effective signal values caused by desorption and adsorption of the gas specimen, thereby enhancing the selectivity of the resistive gas sensor [147].

There are various electrode types and designs, but the interdigitated structure is the most common approach used in the literature [135], [148], [149], [150]. Interdigitated structures (IDSs) are commonly used as a basis for gas sensitive layers (Figure 3.7). The transducer principle can be either resistive or capacitive in nature [151].

The purpose of interdigitated electrodes is to maximise the electrical admittance between the conducting structures in order to exploit the properties of the gas sensitive material deposited on top of them.

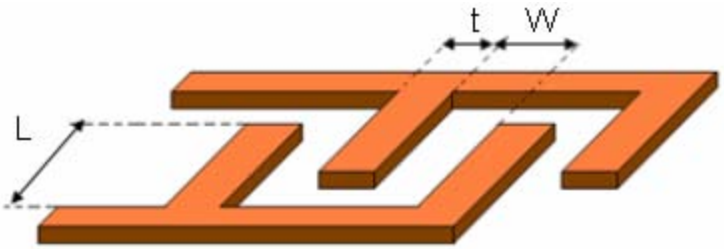

Figure 3.7. Interdigitated Structure (IDS) of Electrodes

There are other important parameters to consider for electrode fabrication such as, the diffusion of the electrode material in the sensing film is a source of long-term drift [12]. To prevent this diffusion, a barrier layer may be deposited between the electric contact and the sensing material.

The heating element is fabricated in a meandering type shape usually on the reverse side of the substrate material (an electrically insulating layer) to reduce interference with the measurement. While there is a slight variation in the materials used for the substrate, there is almost universal use of platinum as the sensor electrodes and heater. This is because of the required thermodynamic stability and the need for temperature measurement [146].

Also of great consideration when fabricating these sensor types, is the method of deposition of each of the required layers. It is possible that two different contact types can be seen for the same material. From Figure 3.8 it can be seen that there is the possibility of a near perfect contact as depicted in Figure 3.8(a) or a more irregular contact type as shown in Figure 3.8(b) [12].

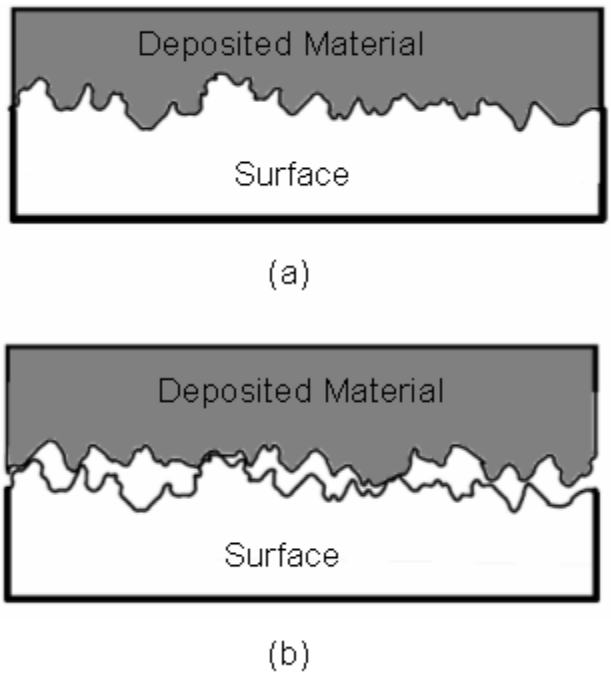

Figure 3.8. Contact microstructure (a) good contact (b) poor contact

3.5. Thick & Thin Film Technologies

Thick film metal oxides were the first type used as semiconducting sensors [152]. The first sensors consisted of a heater coil and an electrode wire pressed into the oxide powder material [152]. It has been reported that thick film sensors are not suitable for the detection of ozone [153]. In the case of thin film sensor, the increase in film thickness has induced considerable decrease in ozone sensitivity, and in particular, the thin film sensor with an In_2O_3 fine particle layer had very low ozone sensitivity [154].

Kim et al. [153] have investigated In_2O_3 thick film sensor technology for the detection of O_3. The results show good linearity between the ozone concentration and the sensor resistance and good reproducibility in repeated measurements. The addition of Fe_2O_3 into In_2O_3 yields slight improvement in response time and sensitivity. The sensor was successfully applied to ozone detection in the low ppb range [153].

It has been shown that thin film sensors respond very easily towards strongly oxidizing gases such as NO_2 and O_3 i.e. species which are hard to detect using conventional thick film technology [155]. Thick film sensors are more suited to reducing gases such as NO [155]. These differences can be explained by the different geometries of these devices. For example, in a thin film sensor the outer surface on which the interaction between the target gas and the sensing layer takes place and the actual current transport path between the electrodes beneath the sensing layer are very close together when compared with thick film devices. In contrast, in a thick film device, the current transport path between both bottom electrodes is relatively far removed from the outer sensor surface [155]. This is illustrated in Figure 3.9.

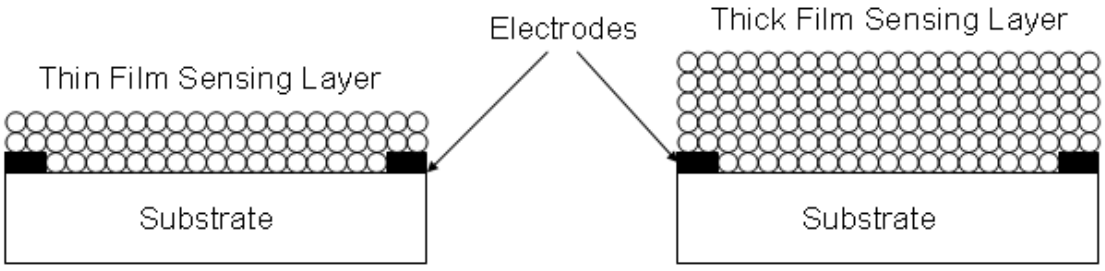

Figure 3.9. Thin Film Vs Thick Film Sensors

Considering the strength of the ozone and NO_2 detection reactions, it is suggested that these strongly oxidizing gases immediately interact with the outermost layers of the sensing film, producing a resistivity change. Clearly, this effect will influence the conductance of a thin film device more than that of a thick film sensor [155]. Thin-films are best suited for O_3 detection as a large part of O_3 is thermally decomposed on the fine particle surface and cannot reach the sensing film inner bulk parts [156].

Since Ozone is a strongly oxidizing gas, and it is generally accepted that thin film sensors are best suited to the detection of oxidizing gasses, in this regards the focus will concentrate on thin-film devices.

3.6. Deposition Methods

The synthesis and deposition of the sensing layer is obviously the most crucial part in the preparation of gas sensors. There are various deposition methods available to deposit the sensing layer onto the substrate. Three main groups can be distinguished: powder/slurry deposition, Chemical Vapour Deposition (CVD) and Physical Vapour Deposition (PVD).

Table 3.3. Deposition Methods

Powder/Slurry	**CVD**	**PVD**
Sol-gel	Thermal CVD	Sputtering
Precipitation	Plasma CVD	Thermal evaporation
Screen Printing	Laser induced CVD	Reactive evaporation
Dip coating	Electroless plating	Ion plating
Drop coating		Laser evaporation
Spin coating		Reactive ion plating
Pulverisation coating		

The main difference between powder/slurry based films and CVD or PVD has been attributed to their different film thickness. While the former lead to sensitive layers of several microns of thickness (thick films), the layer thickness of the latter varies between 20 and 1000nm. Spin-coating techniques, which are actually slurry, can produce thin films in the sense of thickness (and the slurry can be obtained by a sol-gel process, for instance), being actually thick films in terms of porosity. Thin films are usually very compact (non porous), so the interaction with gas is limited to the external surface of the sensitive layer. Conversely, gas can penetrate through most thick films and so the interaction can occur throughout the whole layer [157].

The selection of the technique to be used for a specific application depends on the properties desired from the resulting film. Each deposition technique, with its associated process parameters yields fields of varying quality and properties. For good gas sensing films, thickness, uniformity and high conductivity are the most desirable properties [157].

Compared to the fabrication methods associated with thick film sensors, the fabrication of thin film devices are based on a number of well-defined evaporation or sputtering processes, usually under clean room conditions [152].

CVD techniques generally require elevated substrate temperatures to bring the precursor material to reaction, while PVD techniques need low partial pressures to have a long enough mean free path [152]. Sberveglieri et al. introduced a preparation technique for the fabrication of porous thin films named Rheotaxial Growth and Thermal Oxidation (RGTO) [158].

For CVD techniques, the film is formed by thermal decomposition of gaseous molecules on the heated substrates. This process is controlled by mass transport and by the reaction constants.

The following sections will detail some of the methods most often used in the deposition of metal oxide based gas sensitive layers for the detection ozone. The most common fabrication methods for thin film sensors is the vapour deposition which are clean and easily controlled methods [152]. Each method has its own advantages and disadvantages as discussed in the following sections.

The film deposition technique further divides each sensor type in to thin film (5 – 1000nm) or thick film (1 - 300μm) metal oxide sensors [124]. Film deposition methods include screen printing, spin coating, sputtering and evaporation techniques. These methods have been utilized to fabricate ozone gas sensors with various fabrication parameters and differing levels of success. Table 3.4 illustrates a sample of metal oxide based ozone sensors (focussing on In_2O_3, as it is the most common oxide used for metal oxide ozone sensors). In general the metal oxide films are deposited onto a flat substrate made of alumina, glass, silicon or sapphire containing gold or platinum electrodes.

3.6.1. Physical Vapour Deposition (PVD)

PVD is a process by which a thin film of some material is deposited onto a substrate according to the following steps:

- The source material is converted into vapour phase via some physical means.
- The converted vapour is transported across a low pressure atmosphere from source to substrate.
- The vapour under condensation on the substrate to form the thin film.

In gas sensor fabrication, the primary PVD methods used are evaporation and sputtering. The other methods used include laser deposition, spin coating and RGTO.

3.6.1.1. Sputtering Techniques

Sputtering is an electro-physical process where by the substrate and target material to be deposited is placed in a vacuum chamber. The target (rendered cathodic) is bombarded with highly energetic positive ions, which, by transferring their energy, cause atoms from the target to be propelled towards and bond with the substrate, which has been placed on an anodic or grounded holder [159].

The simplest variant of sputtering is D.C. (Direct Current) sputtering. A plasma (glow discharge) is generated between the two plates by first evacuating to remove air, moisture and extraneous gases, then backfilling with argon gas and applying a negative bias of 1-2kV to the cathode. A plasma discharge is created in which the argon is electronically activated, loses an electron, and becomes an argon cation (positively charged ion). These ions are attracted and accelerated toward the cathode where they bombard the target with sufficient energy, the effect is a transfer of momentum and cause particles of the material to be sputtered [159]. D.C. sputtering is limited to electrically conductive targets (metals and metal alloys) [160]. The deposited thin films show stable and repeatable gas sensing characteristics towards O_3 and NO_2 [160]. Suchea et al have also shown that the stoichiometry role on film sensing properties as well as the fact that the sensing surface phenomenon is strongly connected with film surface parameters [160].

Radio-Frequency (RF) sputtering, in addition to depositing metals and metal alloys can be used to deposit many other materials such as, oxides, glasses, alumina and some plastics. The equipment is essentially the same as for DC sputtering except that an RF generator is added [159].

Reactive Sputtering is yet another variation of sputtering technique. A reactive gas is introduced along with argon to form the plasma. The reactive gas becomes activated and chemically combines with the atoms that are sputtered from the target to form a new compound [159].

In sputtering deposition as in other common vacuum deposition techniques, the material arrives at the substrate mostly in an atomic or molecular form. Using the kinetic theory of gases it is possible to estimate the frequency with which gas particles impinge on a surface [12]:

$$s = \frac{P}{\sqrt{2\pi mkT}} \qquad \textit{(Eq. 3.5)}$$

where s refers to the surface, P is the gas phase pressure, m is the mass of the gas particles, k is the Boltzmann constant and T is the measured temperature [12].

Sputtering has many advantages over other PVD techniques used in thin film sensors such as:

- Sputtering can be achieved from large targets, thereby simplifying the deposition of thin films with uniform thickness [35, 161]
- Film thickness is easily controlled by fixing the operating parameters and simply by adjusting the deposition time [35]
- Deposited material composition is easily controlled [35, 161].

The sputtering process also has the following disadvantages:

- Sputtering equipment is very expensive [35]
- Sputtering has a greater tendency to introduce impurities in the substrate than deposition by evaporation due to the lesser vacuum range required for sputtering [162].

3.6.1.2. Evaporation Techniques

Thin films may be evaporated from a hot source material onto a substrate [35]. The source material to be deposited is placed in a crucible which is encapsulated in a high vacuum environment to ensure that the vaporized atoms or molecules will be transported to the substrate with minimal collision interference from other gas atoms or molecules. The material can be evaporated via resistive evaporation or via an electron beam (e^- beam evaporation). Another possible method involves heating the source material with RF energy, an RF induction heating coil surrounds the crucible containing the source material, and this method of evaporation is known as inductive heating evaporation.

Some of the advantages of the evaporation method include [35]:

- High film deposition rates.
- Less substrate damage from impinging atoms as the film is being formed.
- Excellent purity of the film because of the high vacuum condition used by evaporation [163].
- Less tendency for unintentional substrate heating.

The disadvantages of using the evaporation include [35]:

- Difficult to control film composition and thickness of the deposited film.
- Step coverage is more difficult to improve by evaporation than by sputtering.
- X-ray damage caused by the electron beam evaporation may occur [164].

3.6.1.3. Sol-Gel Technique

A sol is a dispersion of the solid particles in a liquid where only Brownian motions suspend the particles. A gel is a state where both liquid and solid are dispersed in each other. The sol-gel coating process usually consists of the following steps:

- Desired particles are dispersed in a liquid to form a sol mixture.
- The prepared solution is then spun onto the substrate platform, film thickness is reduced by increasing the spinning speed [165].
- The deposited thin film is then annealed.

- A thicker layer may be obtained by repeating the previous two steps

Jimenez et al. provide a detailed account of the deposition process of In_2O_3 by this technique [165]. From this study novel ozone sensors were fabricated with enhanced ozone sensitivity by optimising the age time of the solutions and lowering the annealing temperature [165].

Some of the advantages of this fabrication technique include:

- Ease of control of film thickness.
- Produces a porous structure (The extensive porosity enhances the interaction with ozone molecules and as a result substantially improves ozone sensitivity [166].
- Production of fine grain size [167].

Some of disadvantages include weak bonding to the substrate platform and difficulty in reproducing samples.

3.6.1.4. Spray Pyrolysis

Pyrolysis refers to the thermal decomposition of gaseous species at a hot surface. The major advantage of this technique is that it has a relatively fast deposition rate (> 1000Å/min) and it does not require a vacuum [168]. The actual spraying process is carried out in a furnace at approximately 400ºC. Critical parameters include positioning of the substrate and the chemical composition of the spray solution [168].

Deposition Technique	Sensing Material	Sensor Structure	Notes	Ref
Rf magnetron sputtering from an oxide target	In_2O_3	Alumina structure, Pt IDS, Pt heating structure	Operating Temp = RT - 130ºC Response measured 20 - 150ppb Work function and conductivity sensors fabricated Layer thickness of 77nm	[169]
Rf magnetron sputtering, through RGTO technique (substrate at 250ºC)	In_2O_3	Si micromachined and Alumina substrates, Au electrodes	Operating Temp = 200 - 400ºC Ozone measured 5 – 200ppb Layer thickness of between 50 – 200nm	[170
Sol-gel based technique	In_2O_3 $In_2O_3 – MoO_3$	Sapphire substrate, Pt electrodes	Operating Temp = 150 - 400ºC Ozone measured 400 – 800ppb Layer thickness of 100nm	[171]
Reactive evaporation of Indium in oxygen environment	In_2O_3	No info. Provided in paper	Substrate temperature of 250ºC during deposition	[172]
Sol-gel based technique RF sputtering	In_2O_3	Sapphire substrate, Pt IDS, Pt heating structure	Operating Temp = 200ºC Ozone measured 20 – 85ppb Sol-gel method has higher sensitivity	[167]
Modified RGTO technique	In_2O_3-Fe_2O_3	Alumina substrate, Pt IDS, Pt heating structure	Operating Temp = 200 - 250ºC Ozone measured 60 – 350ppb Layer thickness of 50nm	[173]
Sol-gel based technique	In_2O_3 $In_2O_3 – MoO_3$	Alumina substrate, Pt IDS, Pt heating structure	Operating Temp = 400ºC Ozone measured 200 - 400ppb	[174]
RF magnetron sputtering	MgO -In_2O_3 ZnO – In_2O_3 $ZnIn_2O_5$ – $MgIn_2O_4$	Corning glass substrate, Au parallel electrodes	Operating Temp = 200 - 350ºC Ozone measured 1.4ppb Layer thickness of 300 – 500nm	[175]
Sol–gel based technique	In_2O_3 $In_2O_3 – Fe_2O_3$	Alumina substrate, Pt IDS, Pt heating	Operating Temp 300 -620ºC Ozone measured 100ppb	[153]

		structure		
DC magnetron sputtering (pure metallic target)	In_2O_3 (InO_x)	Corning 7059 glass substrate, NiCr electrodes	Operating Temp = RT - 350ºC Layer thickness of 10 - 1100nm	[161]
Reactive sputtering (modified RGTO)	In_2O_3 Ga_2O_3 $In_2O_3 – Ga_2O_3$	Alumina substrate, Pt IDS, Pt heating structure	Operating Temp 25 - 600ºC Ozone measured 100ppb	[176]
Dip Coating technique	Sn doped In_2O_3	Alumina substrate, gold electrodes, ruthenium oxide glass frits resistive heater	Operating Temp 300 - 400ºC Sensor dimensions 1.5*3*0.38mm Ozone measured 0.1ppm	[177]
Sol–gel based technique	In_2O_3	Sapphire substrate, Pt IDS, Pt heating structure	Operating Temp =200ºC Layer thickness 50nm Ozone measured 20 – 85ppb	[165]
Sol-gel based technique	In_2O_3	Sapphire substrate, Pt IDS, Pt heating structure	Operating Temp 200ºC Layer thickness 20 - 50nm Ozone measured 20 – 85ppb	[166]
Spray Pyrolysis	In_2O_3	Alumina and Si substrates	Operating Temp 100 - 450ºC Layer thickness of 20 – 40nm	[32]
Dip Coating	TiO_2	Alumina substrate of 10mm*5mm, Au IDS, Response measured 0.5ppm – 2.5ppm	T_{RES} = 75s, T_{REC} = 145s	[178]
	SnO_2		T_{RES} = 3275, T_{REC} = 260s	
	$ZnO – SnO_2$ (1:4)		T_{RES} = 110, T_{REC} = 420s	
	$TiO_2 – SnO_2$ (1:4)		T_{RES} = 185s, T_{REC} = 15s	
	$TiO_2 – SnO_2$ (1:1)		T_{RES} = 230s, T_{REC} = 205s	
	$Cu/TiO_2 – SnO_2$		T_{RES} = 1325s, T_{REC} = 35s	
	$Ag/TiO_2 – SnO_2$		T_{RES} = 820s, T_{REC} = 25s	
	$Pt/TiO_2 – SnO_2$		T_{RES} = 160s, T_{REC} = 20s	
	Pt/SnO_2		T_{RES} = 357s, T_{REC} = 70s	

Sputtering	SnO_2	Si Substrate, embedded thin film heater	Operating Temp 350ºC Layer thickness = 260nm Ozone measured 50 – 135ppb Sensing layer dimensions of 150µm*150 µm	[179]
Spray Pyrolysis	SnO_2	Au based electrodes	Layer Thickness = 30 – 200nm Ozone measured 1ppm Sensing Layer dimensions 2mm*2mm	[180]
RGTO Technique	SnO_2	Si Substrate, Pt IDS, Pt heating structure	Operating Temp 400ºC Ozone measured 50 – 400ppb Layer Thickness 300nm	[155]
Thermal Evaporation	WO_3	Sapphire substrate 4.3*6*o.25mm, Pt IDS, Pt heating structure	Layer Thickness 150nm Ozone measured 175ppb Operating Temp >200ºC	[156]
RF magnetron sputtering	WO_3	Si Substrate, Pt IDS, Pt heating structure	Ozone measured 30 – 800ppb Operating Temp 200ºC	[181]
RF reactive magnetron sputtering	WO_3	Si Substrate, Pt IDS, Pt heating structure	Operating Temp 200 – 400ºC	[182]
Sol – gel Thermal Evaporation Sputtering	WO_3	Alumina substrate, Pt IDS	Operating Temp 200 – 400ºC Ozone measured 10 – 160ppb	[183]
DC magnetron sputtering	ZnO	Corning 7059 glass substrate, NiCr electrodes	Room temperature + photoreduction	[184]
Aqueous Chemical Growth (ACG)	ZnO	Glass substrate	Room temperature + photoreduction, 1ppm ozone.	[185]

Table 3.4. Review of some of the more common materials and techniques for the fabrication of metal oxide based ozone sensors

Chapter 4: Fundamentals of Metal Oxide Sensors

4.1. Introduction

For many decades gas detection was used solely for industrial applications. These applications would have been of a critical nature and cost insensitive [186]. Therefore, they were not designed with minimisation, bulk manufacturing and cost in mind. In recent years gas sensing has become interesting to the public for health and safety reasons. Hence gas sensing has been integrated into consumer and commercial applications. For example, carbon monoxide gas detection for home safety and carbon dioxide gas sensing for building ventilation monitoring. With this increasing trend has come a larger demand for a reliable, sensitive, accurate and miniaturised cost effective sensing device.

One of the most promising types of gas sensors is the metal oxide gas sensor [186]. Previous research in the 1950's on a single germanium crystal lead to the discovery that changing the composition of the surrounding gas changed the semiconductors resistance [186]. This discovery leads to the conclusion that gas sensing based on semiconductors was possible.

However, there are a number of problems associated with metal oxide gas sensors. The difficulty in reproducibility of results is one issue. Non-reproducibility is manifest in sensors using identical materials and of identical construction having significantly different sensing characteristics. The most likely causes of this are sintering and other physical effects and the possible presence of uncontrolled trace impurities [162].

In early semiconductor devices there was a problem with instability, both of the conductance in the air and of the sensitivity to gas over long periods of time. This may have been due to the slow oxidation of the oxide, hydration of the oxide and other irreversible reactions [162]. Nowadays, this problem is minimised by using semiconducting oxides as the sensor active elements. This approach greatly reduces the oxidation problem. However, instability in these devices still exists to a certain extent.

4.2. Sensor Characteristics

The key characteristics of gas sensor performance are sensitivity, selectivity and response time.

4.2.1. Sensitivity

Sensitivity is the device characteristics of perceiving a variation in physical and/or chemical properties of the sensing material under gas exposure [35]. The term has also been used to refer to the lowest level of chemical concentration that can be detected or to the smallest increment of concentration that can be detected in the sensing environment [35]. In general the sensitivity, in the case of resistive gas sensors is defined as the ratio of the resistance of the sample measured in air or reference gas (R_{REF}) to the resistance of the sample when exposed to the target gas R_{TAR} [35]. Equations below relate to sensitivity of oxidizing (Eq. 4.1) and reducing gases (Eq. 4.2)

$$S = \frac{R_{TAR}}{R_{REF}} \qquad \textit{(Eq. 4.1)}$$

$$S = \frac{R_{REF}}{R_{TAR}} \qquad \textit{(Eq. 4.2)}$$

Various calculation methods have been used to determine the sensitivity (S) and the overall performance of metal – oxide semiconductor gas sensors. Choi et al [187] determined the H_2 gas – sensing characteristics of samples by;

$$S(\%) = ((R_{AIR} - R_{HYDROGEN}) / R_{AIR}) \bullet 100 \qquad \textit{(Eq. 4.3)}$$

The sensitivity (S) of SnO_2 towards NO_2 has been calculated by equation 4.8 [170].

$$S = (R_{NO2} - R_{AIR}) / R_{AIR} \qquad \textit{(Eq. 4.4)}$$

The sensitivity of a device is a measure of the change in the output (electrical signal) for a change in the input (target gas concentration).

4.2.2. Selectivity

Selectivity is related to the discrimination capacity of the gas sensor in the presence of multiple gases. It is the ratio of the sensor's ability to detect the target gas over the sensors ability to detect other gases that may be present in the surrounding atmosphere. Catalytic additives can lead to an improvement of the sensor performance by means of a selective promotion of the target gas molecules [35]. The introduction of a catalytic element also modifies the operating temperature, sensitivity and response and recovery times [35].

4.2.3. Sensor Response

The response of metal oxide gas sensors can be regarded as a first order time response. The first step is to flush a reference gas (i.e. air) over the sensor in order to obtain a baseline resistance. Once a baseline has been established, the target gas is introduced. When a steady state reading is reached for the target gas, the sensor may again be flushed with the reference gas and return to the original baseline resistance (Figure 4.1).

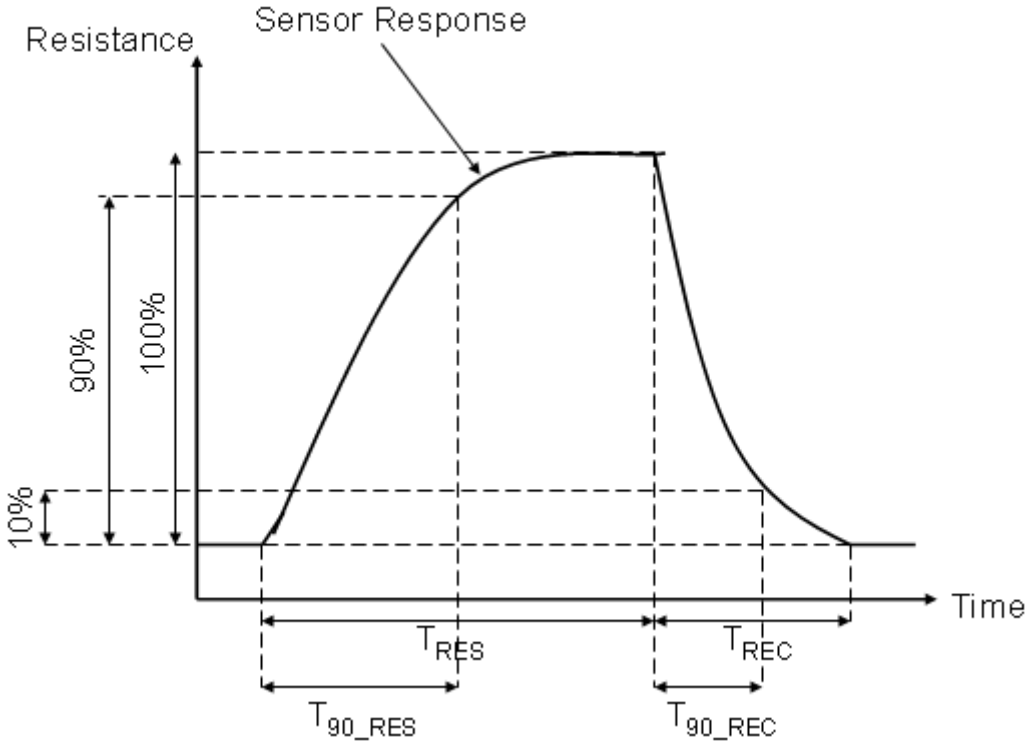

Figure 4.1. Typical Gas response curve

The time, which the sensor is exposed to the target gas, is referred to as the response time (T_{90_RES}) while the time taken for the sensor to return to baseline resistance after reference gas is applied is referred to as the recovery time (T_{90_REC}).

In general the response time is referred to as the time taken to reach 90% of the maximum saturated conductance value following a change in gas concentration over the

sensor. The recovery time is referred to as the time taken to return to 10% of the saturated value.

4.2.4. Baseline Manipulation

The next stage in analysing the gas concentration is response manipulation with respect to the baseline resistance. This process compensates for noise, drift and also inherently large or small changes [123]. The three most widely used methods are shown below:

Differential: The baseline $X_S(0)$ is subtracted from the sensor response $X_S(t)$ to remove any noise or drift δ_A present. The baseline manipulated response $y_S(t)$ is determined by:

$$y_S(t) = (X_S(t) + \delta_A) - (X_S(0) + \delta_A) = X_S(t) - X_S(0) \qquad \textit{(Eq. 4.5)}$$

Relative: The sensor response is divided by the baseline. This process eliminates multiplicative drift δ_M and a dimensionless response $y_S(t)$ is obtained:

$$y_S(t) = \frac{X_S(t)(1+\delta_M)}{X_S(0)(1+\delta_M)} \qquad \textit{(Eq. 4.6)}$$

Fractional: The baseline is subtracted from the response $X_S(t)$ and then divided by the baseline $X_S(0)$ from the sensor response which provides a dimensionless, normalised response $y_S(t)$ that can compensate for inherently large or small responses:

$$y_S(t) = \frac{(X_S(t) - X_S(0))}{X_S(0)} \qquad \textit{(Eq. 4.7)}$$

The choice of baseline manipulation depends on the particular sensor type and application. Certain manipulation techniques have been shown to be more suitable to certain sensor types and also variations in the manipulation techniques can occur in the literature [136].

4.3. The Kinetic of Gas Sensing for Semiconducting Metal Oxides

Metal oxide semiconductor gas sensors are used to monitor the content of reducing or oxidising gas molecules in the atmosphere. This device operates by transforming the value of adsorption and desorption of oxygen into an electrical signal. The electrical signal is the conductivity of the sensing layer, measured by the IDS, which changes due to the presence of different target gases.

Semiconducting oxides have been shown to exhibit sensitivity to various oxidising and reducing gases. The principle manner in which these sensors operate is summarised as follows:

There is a finite density of electron donors (e.g. adsorbed hydrogen) and/or acceptors (e.g. adsorbed oxygen) bound to the surface of a wide band gap semiconducting oxide, such as Indium oxide (band gap: 3.6eV). The electron donors or acceptors cause the formation of surface states followed by an exchange of electrons within the interior of the semiconductor thus forming a space charge layer close to the surface. By changing the surface concentration of the donors/acceptors, the conductivity/resistance of the space charge region is modulated.

The resistance change is caused by a loss or gain of surface electrons because of adsorbed oxygen reacting with the target gas. If the oxide is an n – type (i.e. SnO_2, WO_3, etc.) there is a donation of electrons when reducing gases are present and a subtraction of electrons

when oxidizing gases are present. The result is that n – type oxides increase their resistance when oxidizing gases are present and decrease resistance when reducing gases are present. In contrast to n–type, p–type oxides decrease their resistance when oxidizing gases are present and increase resistance when reducing gases are present.

Thin films of metal oxides such as In_2O_3, SnO_2, and ZnO respond to a wide range of oxidizing and reducing gases. In general the process involved in gas detection is [35]:

- Diffusion of reactants to the active region.
- Adsorption of reactants on to the active region.
- Surface reactions.
- Desorption of production from the active region.
- Diffusion of products away from the active region.

When the target gas molecules diffuse into the active layer, they adhere to the sensing surface, this process is known as adsorption. There are two types of adsorption of physisorption and chemisorption. In the case of physisorption, the species are bonded only be weak physical forces (van der Waals-type forces) to the surface. Chemisorption bonds have a re-arrangement of the electron density between the adsorbed gas and the surface. When a solid is terminated by a surface, the surface atoms are incompletely coordinated. One or two nearest neighbours are missing and there are "dangling bonds" which are said to be unsatisfied (unshared with neighbours) [35].

Despite the disadvantages associated with semiconducting sensors, they offer the advantages including small size, simple operation, high sensitivity and simple circuitry. One of the main advantages, however, is that they are sensitive to some gases at sub-ppm levels enabling detection at concentrations below toxic levels [186].

The main sensing applications of semiconducting oxide is, firstly, in the detection of oxygen, e.g. in the monitoring of exhaust gases from internal combustion engines, and secondly, in the detection of toxic gases in air.

4.3.1. Oxygen Gas Response Mechanism

Much of the impetus for the development of rugged, low cost sensors for oxygen stems from the need to monitor the exhaust gases from internal combustion engines. In such environments there are simultaneous changes in partial pressure of oxygen and of a number of other gases as the ratio of air to fuel in the ignition mixture (the lambda ratio) is altered. Oxygen sensors used in this application are sometimes referred to as lambda sensors [188], [189].

Semiconducting oxides that have been explored as lambda sensors generally respond to changes in oxygen partial pressure at high temperatures by exploiting the equilibrium between the composition of the atmosphere and the bulk stoichiometry. In general the relationship between oxygen partial pressure and the electrical conductivity of a mixed valence oxide sensor may be represented by Eq. 4.8 below:

$$\sigma = A\exp(-E_A / kT)\rho(O_2)^{1/N} \qquad \textit{(Eq. 4.8)}$$

where σ is the electrical conductivity, A is a constant, E_A is the activation energy for conduction, $\rho(O_2)$ is the oxygen partial pressure, N is a constant determined by the dominant type of bulk defect involved in the equilibrium between oxygen and the sensor and T is the absolute temperature [188].

4.3.2. Target Gas in Air

The other major category of gas detection utilizing metal oxide semiconductor involves their use in an atmosphere of constant partial pressure (air) to detect minor concentrations of specific gases [188]. Bulk changes in stoichiometry are not relevant to this type of application and the materials are usually held at elevated temperatures (200 – 600°C), at which temperature useful surface reactions occur at a sufficient rate.

At elevated temperatures (>100°C) oxygen molecules are dissociated via a chemisorption process. Firstly, oxygen is connected via a dipole binding to the semiconductor surface atoms. Under this condition, electrons are removed from the semiconductor surface via a charge transfer mechanism. This is followed by the formation of chemical bonds with the semiconductor surface atoms. The band and activation energy of the surface reaction depends on the lattice and defect structure of the surface [188].

The most important requirement for the efficient detection of ozone at low temperatures is the suitable catalytic activity of an oxide reaction of ozone decomposition [173].

The atomic oxygen is adsorbed on the semiconductor surface as O^{2-} or O^{-} and the resistivity of the semiconductor increases. At temperatures below 100°C, the oxygen molecules are adsorbed via physisorption process. The coverage of physisorbed molecules is less than one monolayer. This process is accomplished by weak van der Waals forces. The binding forces are very small (20kJ/mol ~ 0.2eV per molecule) and the molecules are mobile on the surface of the semiconductor without changing their electrical properties [188]. The low value of the physisorption enthalpy of about 20kJ/molcauses physisorption to disappear almost completely at elevated temperatures. The activation energy of diffusion jumps of physisorbed molecules is smaller than the adsorbed energy. Consequently the probability that a molecule jumps to neighbouring site is greater than the desorption process [188].

4.4. Gas Sensing Mechanism

There are many models to explain the mechanisms of interaction between metal oxides and the gas phase, the two most important models are the Wolkenstein model and the boundary layer theory [189].

4.4.1. The Wolkenstein Adsorption Theory

In the Wolkenstein model, the adsorption of an oxidizing gas species requires two successive steps, firstly, weak (neutral) chemisorption and secondly strong (ionised) chemisorption [191]. During the neutral chemisorption stage the bond between the adsorbate and the substrate is weak and does not involve any electronic transfer; the electrons of the atom or molecule remain located in the vicinity of the adsorbate involving a simple deformation of the orbitals [192]. The binding energy of the adsorbate E_W corresponds to the loss of free energy of the system during the adsorption process. This neutral chemisorption does not change the electrical properties of the material but the perturbation created by the adsorbate induces surface state E_{SS} in the band gap. This surface state acts as a trap for the electrons [192].

The second stage, ionised chemisorption, occurs when an electron from the conduction band, with energy E_C , is transferred from the semiconductor to the adsorbed species, which causes the electronic properties of the material to change. The binding energy of the adsorbate is increased by the loss of energy from the system during the ionisation process [192]:

$$E_S = E_C - E_{SS} \qquad \textit{(Eq. 4.9)}$$

This process involves the creation of a negative superficial charge and a chemisorption induced surface potential barrier, V_S , $(V_S < 0)$ [186].

The surface of the conduction band level is represented by the equation below:

$$E_{CS} = E_C - qV_S \qquad \textit{(Eq. 4.10)}$$

Therefore,

$$E_S = E_{CS} - E_{SS} + qV_S \qquad \textit{(Eq. 4.11)}$$

The energy difference $(E_{CS} - E_{SS})$ can also be represented by the difference between the electronic affinities of the neutral adsorbate (χ_{ads}) and the semiconductor (χ_{sc}). Hence,

$$E_S = \chi_{ads} - \chi_{SC} + qV_S \qquad \textit{(Eq. 4.12)}$$

The expression representing the binding energy of the strongly adsorbed species decreases when the covering rate increases, which facilitates the desorption. (Eq. 4.13);

$$E_W + E_S = E_W + \chi_{ads} - \chi_{SC} + qV_S \qquad \textit{(Eq. 4.13)}$$

The neutral chemisorption mechanism is limited by the number of adsorption sites at the surface of the material, while the strong adsorption is limited by the upper band bending. For oxygen (diatomic gas) the adsorption may be either non–dissociative (lower temperatures) or dissociative (higher temperatures). Eq. 4.14(a) and (b) shows the reaction of an O_2 molecule and a free adsorption site, S, for non–dissociative kinetics [192].

$$S + O_2 \rightarrow (\mathrm{S} — \mathrm{O_2}) \qquad \textit{(Eq. 4.14(a))}$$

$$(\mathrm{S} — \mathrm{O_2}) + e^- \rightarrow (\mathrm{S} — \mathrm{O_2})^- \qquad \textit{(Eq. 4.14(b))}$$

For dissociative kinetics and two free adsorption sites, $2S$ (Eq. 4.15(a) and (b)):

$$2S + O_2 \rightarrow 2(\mathrm{S} — \mathrm{O}) \qquad \textit{(Eq. 4.15(a))}$$

$$(S — O) + e^- \rightarrow (S — O)^- \qquad \textit{(Eq. 4.15(b))}$$

For triatomic gases (O_3) there is only one possibility (Eq. 4.16(a) and (b)):

$$S + O_3 \rightarrow (S — O) + O_2 \qquad \textit{(Eq. 4.16(a))}$$

$$(S — O) + e^- \rightarrow (S — O)^- \qquad \textit{(Eq. 4.16(b))}$$

4.4.1.1. Non – dissociate adsorption

In stationary conditions, the value of the covering rate $(\theta = N_{ads} / N^*)$ is determined by the adsorption and desorption balance [192]:

$$\frac{p(1-\theta)}{N\sqrt{2\pi mkT}} = \nu \exp\left(\frac{-E_W}{kT}\right)\left[\theta_0 + \theta\_ \exp\left(\frac{-E_S}{kT}\right)\right] \qquad \textit{(Eq. 4.17)}$$

Where p is the gas partial pressure, m is the molecular mass, N^* is the total density of adsorption sites, k is the Boltzmann constant and T is the thermodynamic temperature. In the second term, ν is the typical phonon frequency of the lattice θ_0 and $\theta\_$ are the covering rates of the neutral and ionised species respectively. This equation means that a strongly chemisorbed species must give again its trapped electron to the bulk and return to the neutral state before desorbing and a neutral chemisorbed species must release its bonding energy E_W before desorbing [192].

4.4.1.2. Dissociative adsorption

The presence of two free close sites is necessary so that the reaction of adsorption occurs, conversely the reaction of desorption requires the presence of two close atoms, the relation of balance is this modified in the following way [192]:

$$\frac{p(1-\theta)^2}{N\sqrt{2\pi mkT}} = \nu \exp\left(\frac{-E_W}{kT}\right)\left[\theta_0^2 + \theta_-^2 \exp\left(\frac{-E_S}{kT}\right)\right] \quad \textit{(Eq. 4.18)}$$

The adsorption kinetics of a triatomic gas (ozone) (Eq. 4.16) which utilises only one adsorption site has the same behaviour as non dissociative kinetics.

θ_- and θ_0 are related to the total covering rate θ by the Fermi-Dirac statistics [192]:

$$\eta_- = \frac{\theta_-}{\theta} = \frac{1}{1+2\exp\frac{E_{SS}-E_F}{kT}} \quad \textit{(Eq. 4.19)}$$

$$\eta_0 = \frac{\theta_0}{\theta} = 1-\eta_- \quad \textit{(Eq. 4.20)}$$

Equations 4.17 - 4.20 depend on the band bending, qV_S. This quantity must be calculated from Poisson's Equation:

$$\Delta V = \frac{q}{\varepsilon}(n - p - N_d^+) \quad \textit{(Eq. 4.21)}$$

Where V is the intrinsic potential, n and p are the electron and hole densities, N_{d^+} is the density of ionised oxygen vacancies and ε is the permittivity. (Note: n, p and N_{d^+} are

calculated by the set of classical drift diffusion equations using the Fermi-Dirac statistics). Thus, the computation of the solution of Equations 4.17, 4.19 and 4.20 or 4.18 and 4.20 must be performed simultaneously with Poisson's equation. The boundary condition is given by Gauss' law at the surface of each individual grain [192]:

$$E_n = \frac{\sigma}{\varepsilon} = \frac{-qN\theta_-}{\varepsilon} \qquad \textit{(Eq. 4.22)}$$

Where E_n is the normal electric field and σ is the superficial density of charge.

When two species of oxidising adsorbates are simultaneously in the atmosphere, it is assumed that no interaction between these two species takes place in the gaseous phase and Equation 4.17 is replaced by two coupled equations:

$$k_1 p_1 (1-\theta_1-\theta_2) = \nu_1 \exp\left(\frac{-E_{W1}}{kT}\right)\left[\theta_{10} + \theta_{1\_} \exp\left(\frac{-E_{S1}}{kT}\right)\right]$$

(Eq. 4.23)

$$k_2 p_2 (1-\theta_1-\theta_2) = \nu_2 \exp\left(\frac{-E_{W2}}{kT}\right)\left[\theta_{20} + \theta_{2\_} \exp\left(\frac{-E_{S2}}{kT}\right)\right]$$

(Eq. 4.24)

And the total covering rate writes;

$$\theta = \theta_1 + \theta_2 = \frac{k_1 A_1(\eta_{20},\eta_{2-}) p_1 + k_2 A_2(\eta_{10},\eta_{1-}) p_2}{k_1 A_1(\eta_{20},\eta_{2-}) p_1 + k_2 A_2(\eta_{10},\eta_{1-}) p_2} + A_1(\eta_{20},\eta_{2-}) A_2(\eta_{10},\eta_{1-})$$

(Eq. 4.25)

With,

$$A_i(\eta_{i0},\eta_{i-}) = \nu_i \exp\left(\frac{E_{Wi}}{kT}\right)\left[\eta_{i0} + \eta_{i-}\exp\left(\frac{-E_{Si}}{kT}\right)\right] \qquad \textit{(Eq. 4.26)}$$

In the dissociative adsorption case (Eq. 4.18) related to oxygen must be modified in the same way:

$$k_1 p_1 (1-\theta_1-\theta_2)^2 = \nu_1 \exp\left(\frac{-E_{W1}}{kT}\right)\left[\theta_{10}^2 + \theta_{1-}^2\exp\left(\frac{-E_{S1}}{kT}\right)\right] \qquad \textit{(Eq. 4.27)}$$

Where as Eq. 4.24 remains valid for ozone.

In this case the total covering rate writes:

$$\theta = \theta_1 + \theta_2 = \frac{1}{k_2 p_2 + A_1(\eta_{20},\eta_{2-})} \times \left\{ k_2 p_2 + \frac{\sqrt{k_1 p_1}\left[A_1(\eta_{20},\eta_{2-})\right]^2}{\sqrt{k_1 p_1}A_1(\eta_{20},\eta_{2-}) + \left[k_2 p_2 + A_1(\eta_{20},\eta_{2-})\right]\sqrt{A_1(\eta_{20}^2,\eta_{2-}^2)}} \right\}$$

(Eq. 4.28)

The previous set of Equations cannot be analytically solved, but a numerical resolution is possible if one chooses grains of simple geometric form [183]. By supposing that the film consists of an homogeneous stacking of identical spherical grains, each of known properties, the resistivity of the layer can be determined as the properties of a single grain.

The Wolkenstein model takes into account the electronic coupling between the semiconductor and the adsorbate species but is rather complex to implement because it requires the simultaneous resolution with Poisson's equation [192] as seen from the above calculations.

4.4.2. The Boundary Layer Theory

The boundary layer theory is a widely accepted description of the processes and the prediction of the sign of the change in conductivity of metal oxide semiconductors in the presence of the target gas (oxidizing or reducing). As shown below, for an n-type metal oxide surface exposed to an oxidizing gas (Figure 4.2), chemisorbed particles cause a localized energy level within the band gap of the metal oxide, acting as electron acceptors [190]. This results in a charged layer of electron depletion at the surface leading to a compensating boundary layer and to the formation of a surface potential V_S [190]. The electrons must overcome the electronic barrier to cross grain boundaries. The conduction of the sensing layer is approximated via the Shottky model [190]:

$$\sigma = \sigma_0(T)e^{\frac{-eV_S}{kT}} \qquad \textit{(Eq. 4.29)}$$

where σ is the conductivity of the semiconductor material and σ_0 is the bulk conductivity which is dependent on the temperature and geometric properties of the sensing layer [190].

N-type metal oxide surface exposed to a reducing gas (Figure 4.3), chemisorbed particles cause a localized energy level within the band gap of the metal oxide, acting as electron donors.

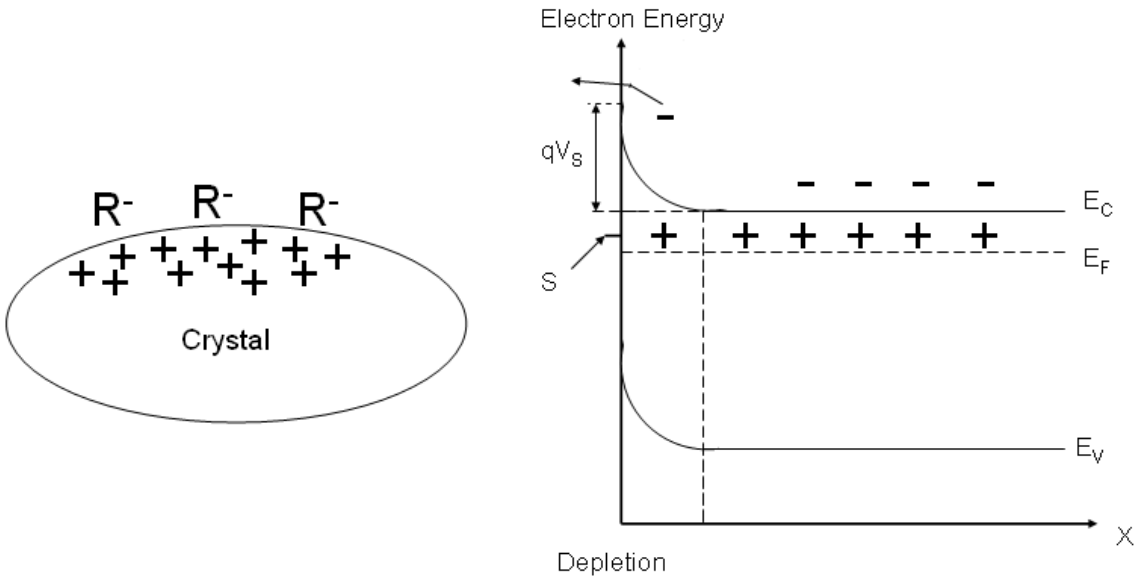

Figure 4.2. Boundary layer theory and surface charge of an n-type metal oxide in the presence of an oxidizing gas

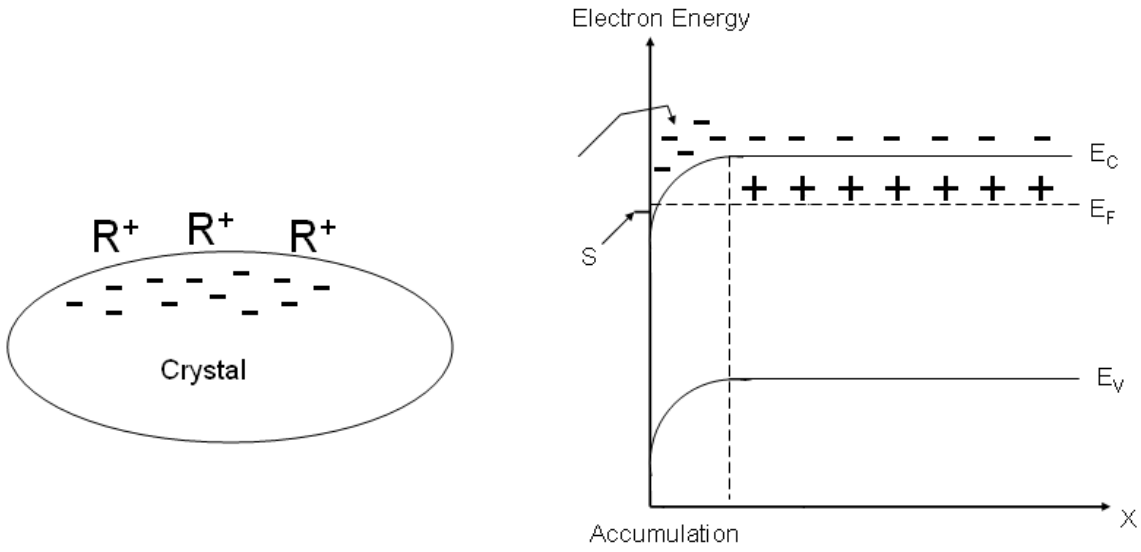

Figure 4.3. Boundary layer theory and surface charge of an n-type metal oxide in the presence of a reducing gas

4.5. Thickness Dependence for Compact Films

The sensitivity of the layers depends strongly on the layer thickness (as discussed previously). For example if the thickness of the electron-depleted region is about the size of film then high gas sensitivity can be expected. Therefore, sensitivity of the metal oxide sensor is directly influenced by the size of the oxygen induced depletion layer at the surface of the film relative to the thickness of the bulk semiconductor as shown in Figure 4.4 [35] [194].

Figure 4.4 (a) below shows the depletion region in the atmosphere ambient whereas Figure 4.4 (b) shows the reduction in the depletion depth upon exposing to the reducing gas.

Thin SnO_2 layer, (50 – 300 nm) mainly responds to oxidizing gases such as ozone and NO_2, whereas thick films (15 – 80 μm) respond better to reducing gases such as CO and CH_4.

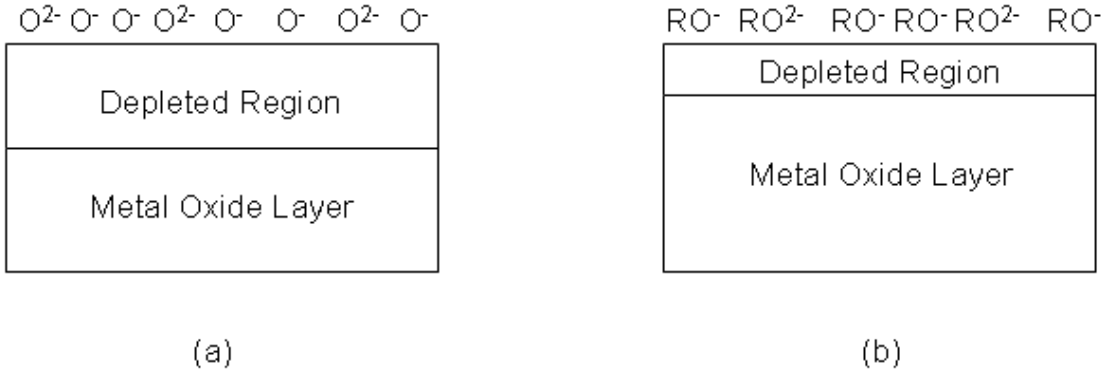

Figure 4.4, Sensitivity dependence on the depletion layer depth in the metal oxide. (a) Adsorption of the atmospheric oxygen on the surface of the sensing film, resulting in an increase of the film resistance. (b) Reduction in the depletion area upon exposing to a reducing gas, thus decreasing the film resistance.

4.6. Compact and Porous Morphology

In compact sensing layers, gases cannot penetrate into the layer and the gas sensing reaction is confined to the surface of the sensing layer. This compact layer is usually obtained with one of a number of thin film deposition methods. For the porous layer, gases can access all of the volume of the sensing layer and the gas sensing reaction can therefore take place at the surface of individual grains, at grain-grain boundaries and interface between grains and electrodes. Figure 4.5 below shows a basic gas interaction in the two layers.

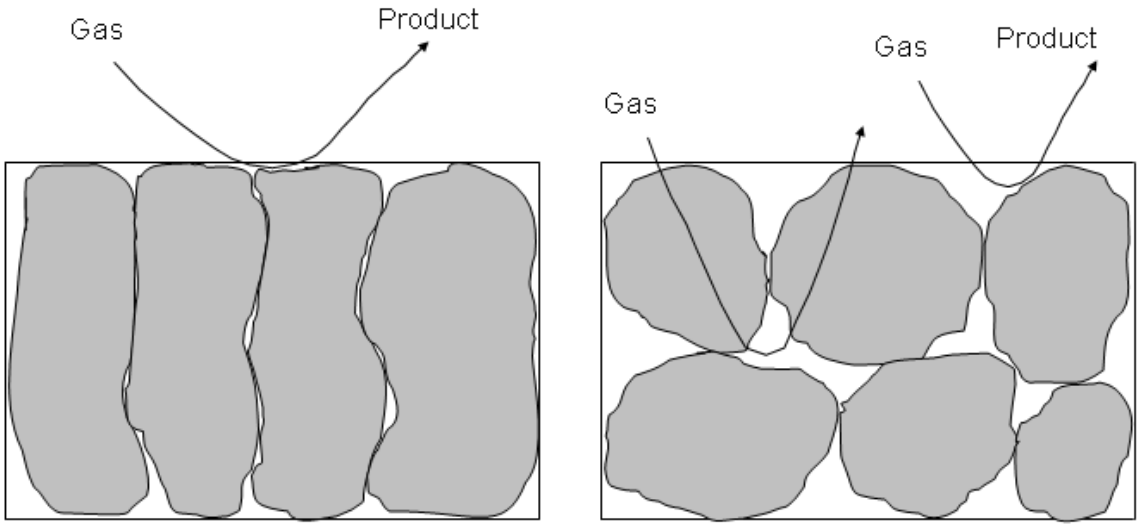

Figure 4.5. Gas sensing reaction of compact and porous layers

For compact layers, the sensitivity layer can be completely or partly depleted depending on the relation between film thickness and depletion layer as shown in Figure 4.6 [195]. When the film thickness, Z_g, is smaller than the depletion layer thickness, Z_0, the compact sensing layer will be completely depleted. When the film thickness is larger than the depleted layer $(Z_g > Z_0)$, the sensing layer will be partly depleted and two resistances occur in parallel. One is influenced by the surface reaction with the higher resistance value (Z_0) and the other one has the bulk resistance value $(Z_g - Z_0)$.

Thus, the partly depleted layer can be treated as a conductive layer with a gas reaction dependent thickness. For the completed depleted later, the exposure to reducing gases can act as a switch to the partly depleted layer. It is also possible that exposure to oxidizing gases acts as a switch from partly completed depleted layer. From Figure 4.6 below, Z_0 is the thickness of the depleted region, Z_g is the layer thickness and eV_S is the band bending. Top right shows the schematic of a partly depleted compact layer. Bottom right represents a completely depleted region.

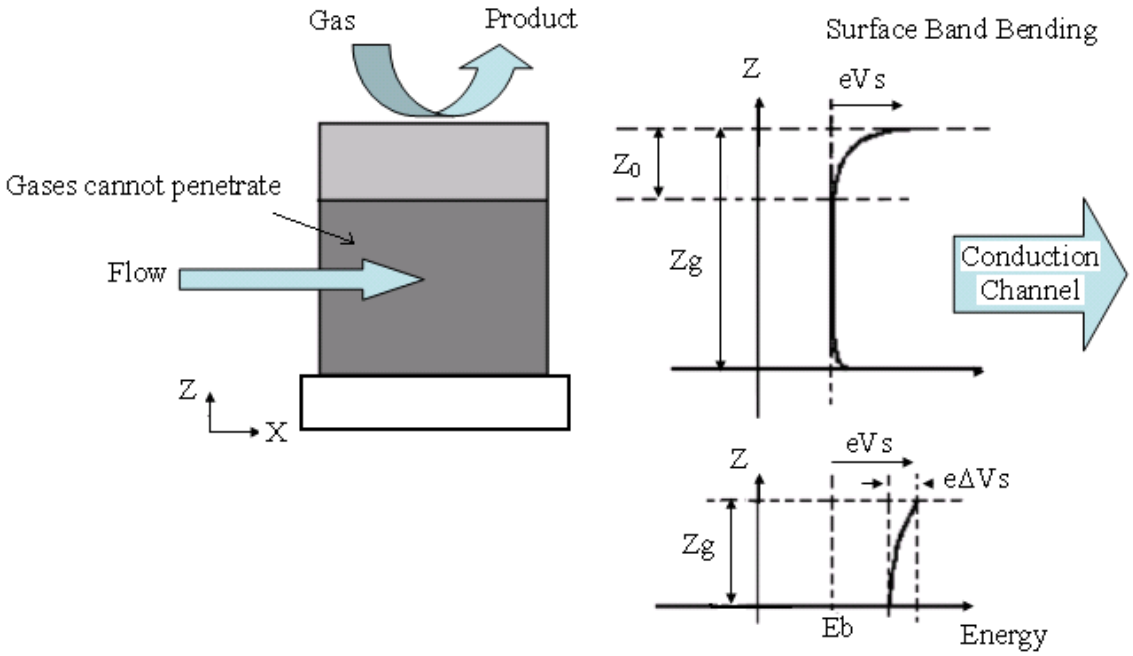

Figure 4.6. Schematic representation of a compact sensing layer with geometry and energy band representations; Z_0 is the thickness of the depleted surface layer; Z_g is the layer thickness and qV_S the band bending. (a) Partly depleted compact layer (b) completely depleted layer [195]

In the case of compact layers, the active surface is the geometric one and the electrical conduction is taking place in a direction parallel to the maximum effect on the band bending. When discussing the conductance, G, one has to start with the microscopic conductivity σ.

The electronic conductivity in a homogenous ideal single crystal is given by Eq. 4.30 [195]:

$$\sigma_b = qn_b\mu_b \qquad \textit{(Eq. 4.30)}$$

Where $_b$ indicates the bulk values, q represents the elementary charge, and the charge carrier/electron concentration and μ represents the electron mobility. In the case of an n-type semiconductor the relation between the conductivity σ and the conductance G is given by a simple relation (keeping in mind that one is still omitting the surface phenomena) shown in the following equation [195]:

$$G = const(qn_b\mu_b) \qquad \textit{(Eq. 4.31)}$$

The constant, const, includes the geometry of the sample. By including the surface effects as shown in Figure 4.6, the situation gets a little bit more complicated, the conductivity now depends on the depth, z :

$$\sigma(z) = qn(z)\mu(z) \qquad \textit{(Eq. 4.32)}$$

For the conductance, one has to integrate over the entire thickness z_g [195]:

$$G = const\frac{q}{z_g}\int_0^{z_g} n(z)\mu(z)dz \qquad \textit{(Eq. 4.33)}$$

Equation 4.33 above describes the general case of a single crystal or compact layer.

4.7. Debye Length

Nanotechnology can be applied to create sensors of minuscule size. The reduction in sensor size can result in lower materials and fabrication costs, reduced weight, lower power consumption, all of which are key factors driving opportunities in the marketplace. Nanosensors of highly reduced power consumption are very suitable for integration into wireless communication devices to enable widespread distributed monitoring and control. Very low power nanosensors would also be beneficial for use as battery operated handheld or wearable sensors. Logical and promising sensing application areas for nanosensors include medical (blood gas monitoring/blood analysis, patient monitoring, diagnostic testing), biowarfare detection, genetic analysis, drug screening or discovery, food inspection/testing, environmental monitoring, and industrial chemical process monitoring/leak detection.

Conductivity, which is a product of the carrier concentration and mobility has been shown to be highly sensitive to target gas concentration [196]. An increase in carrier concentration and mobility was reported with an increase in the concentration of the target gas. From these results it was concluded that ultrafine particles are highly sensitive to gases. An electrical conduction model based on particle size and Debye length or the depth of the space charge layer was also proposed [196]. The mathematical definition of the Debye length (L_D) is give by Eq. 4.34 below:

$$L_D = (\varepsilon kT / q^2 n_C)^{\frac{1}{2}} \qquad \textit{(Eq. 4.34)}$$

Where ε is the static dielectric constant of the sensing material (SnO_2, in this case), k is Boltzmann's constant, T is the absolute temperature in Kelvin, q is the electron charge and n_C is the carrier concentration of the ultra fine particle films. According to this model, the width of the channel for electrons to move without any disturbance from the surface oxygen ions is given by:

$$L_C = D - 2L_D \qquad \textit{(Eq. 4.35)}$$

Where D is the grain size and L_D is the Debye length.

As the grain size approaches twice the Debye length, the mobility modulation becomes remarkable because of electron depletion in the whole crystallite, resulting in high sensitivity to gases.

In 1991 the effect of grain size on gas sensitivity of porous tin oxide based devices was reported [197]. Using metal additives they were able to control the crystallite size of the tin oxide in the range of 5 – 32 nm. The reason for the addition of metal into the lattice is to affect an increase or decrease in carrier concentration. Thereby the Debye length equation, a trivalent metal such as aluminium in tin oxide lattice should decrease the carrier concentration and therefore increase the Debye length. The case is reversed for a pentavalent metal such as antimony, where a decrease in the Debye length is expected. By theory, if grain size is assumed constant, a decrease in Debye length should correspond to lower sensitivity and an increase in Debye length should correspond to higher sensitivity. It was proposed that [197]:

- $D >> 2L_D \rightarrow$ the sensing mechanism is grain boundary controlled.
- $D \sim 2L_D \rightarrow$ the sensing mechanism is neck controlled.
- $D << 2L_D \rightarrow$ the sensing mechanism is grain controlled.

In general, the response to the target gas increases dramatically with the decreasing grain size of the sensing materials. It has been shown the gas response increases abruptly when the particle size becomes comparable to or smaller than the Debye length [198]. As the grain size is reduced to the Debye length the carrier is depleted in the whole grain and the sensor response can be improved according to the grain control model [199].

4.8. Grain Size Effects

One of the most important factors which affect the sensing property of semiconducting gas sensors is the microstructure of the sensing layer. Each crystallite of semiconductor oxide in the element has an electron depleted surface to a depth of L in air, L is determined by the Debye length and the strength of chemisorptions. If the diameter D of the crystallite is comparable to $2L$, the whole crystallite is depleted of electrons and this would cause gas sensitivity to change with D. The crystallites in the gas sensing elements are connected to the neighbouring crystallites either by grain boundary contacts or by necks. In the case of grain boundary contacts, the electrons should move across the potential barrier, the height of which changes with the surrounding atmosphere. The gas sensitivity in this case is independent of the grain size. In the case of conduction through necks, electrons move through the channel penetrating through each neck. The aperture of the channel is attenuated by the surface space charge layer. This model is related to the grain size through the neck size [197]. For $D >> 2L$, conduction of electrons in the sensing layer is dominated by conduction through grain boundary contacts. For $D \geq 2L$, neck control forms the primary mechanism for conductivity modulation. For $D < 2L$, the electrical resistance of the grain dominates the complete resistance of the sensor and thus the sensitivity is controlled by the grains themselves. The grain size effects are illustrated in Figure 4.7.

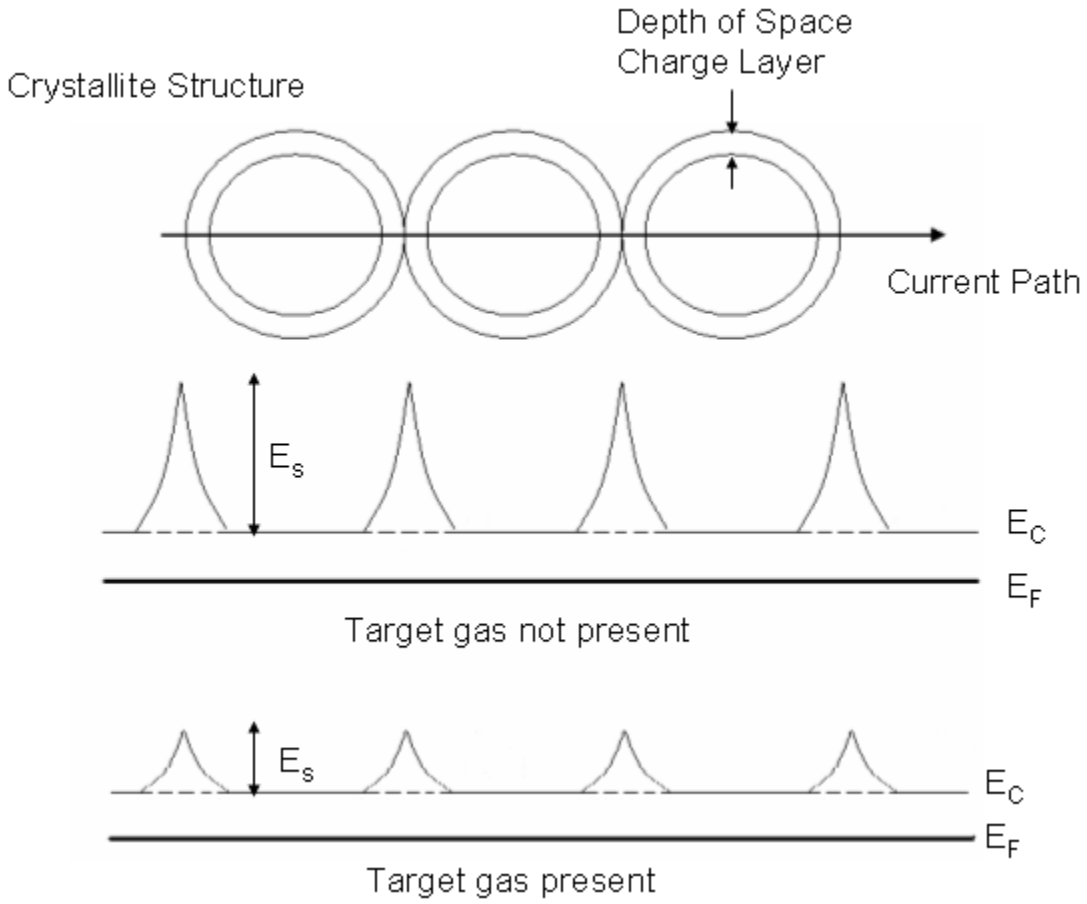

Figure 4.7. The crystallite size of the sensing film is more than the depletion width, resulting in incomplete depletion of grain. Figure also shows the energy barrier for electron in both the presence and absence of the target gas.

Figure 4.7 explains the conductivity increase due to the carrier mobility of the metal oxide sensors for a reducing target gas. Before the target gas is introduced to the sensing material, oxygen atoms (present in the atmosphere) are adsorbed onto the particle surface, forming a potential barrier in the grain boundaries [123]. This potential barrier restricts the flow of electrons, causing the electrical conductivity to decrease. When the sensor is exposed to an atmosphere containing a reducible gas such as CO, the oxide surface adsorbs the gas molecules and causes oxidation to occur [123]. This lowers the potential

barrier, allowing electrons to flow more easily, thereby increasing the conductivity of the sensing layer.

The reaction between the target gas and the surface oxygen varies depending on many factors such as, operating temperature and the activity of the sensor materials [123]. The sensitivity and selectivity of the sensor may be altered by adding impurities and catalytic metal additives such as palladium (Pd) or platinum (Pt). The impurities act as extrinsic donors (or acceptors) and consequently, controlling the doped amount of impurities can change the conductivity of the sensors. Doping of the catalytic metal to the sensor or coating with thin catalytic metal film of the sensor surface changes the selectivity of the sensor [123].

4.9. Some Techniques to improve sensor performance

4.9.1. Catalysts

A catalyst is a material which increases the rate of chemical reactions between the target gas and the sensing layer. It does not change the free energy of the reaction but lowers the activation energy. Small amounts of noble metal additives, such as Pd or Pt are commonly dispersed on the semi-conducting surface as activators or sensitizers to improve the gas selectivity and lower the operating temperature [200, 201]. The addition of a catalyst can affect the inter-granular contact region and film resistance in two ways. One is the spill-over mechanism and the other is the Fermi energy control mechanism.

Catalytic theory proposed as spill-over and Fermi energy control have not led to a widely accepted catalyst mechanism that predicts or explains sensor behaviour in different environments [202]. In spite of all the work reported, a deep analysis of the material-gas interaction and its influence on the sensor electrical response is still lacking to completely understand the role played by the additives on the gas sensing mechanism. A model for increase in sensitivity using nano particles has been explained by activated charge carrier creation and tunnelling through potential barrier.

4.9.2. Spill – Over Mechanism

The spill over mechanism takes effect when the metal catalysts dissociates the target gas molecule allowing the atom to "spill-over" onto the semiconductor sensing layer surface [35]. The term spill-over refers to the process illustrated in Figure 4.8, namely the process where the metal catalysts dissociate the molecule, and then the atom can 'spill-over' onto the surface of the semiconductor support. At appropriate temperatures, reactants are first adsorbed onto the surface of the additive particles and then migrate to the oxide surface to react there with surface oxygen species, thereby changing the resistance of the oxide layer [35].

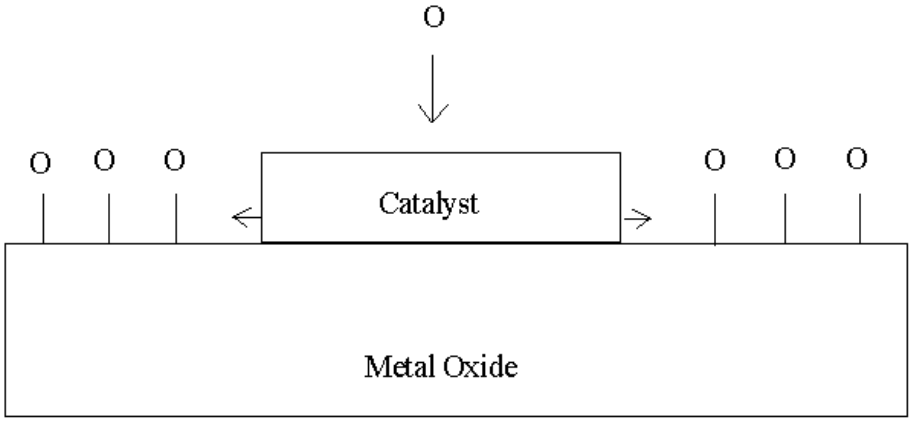

Figure 4.8. Schematic of spill-over mechanism

For the above processes to dominate the film resistance, the spiller-over species must be able to migrate to the inter-granular contact as shown below. For a catalyst to be effective there must be a good dispersion of the catalysts as shown in Figure 4.9 (Fermi Energy control), so that the catalyst particles are available near all inter-granular contacts.

The inverse effect may also occur, when a nascent oxygen or gas atom is newly formed from a reaction on a metal oxide site. The nascent atom may migrate to a metal site and desorb into a gas molecule. This is called reverse spill-over or the porthole effect [203].

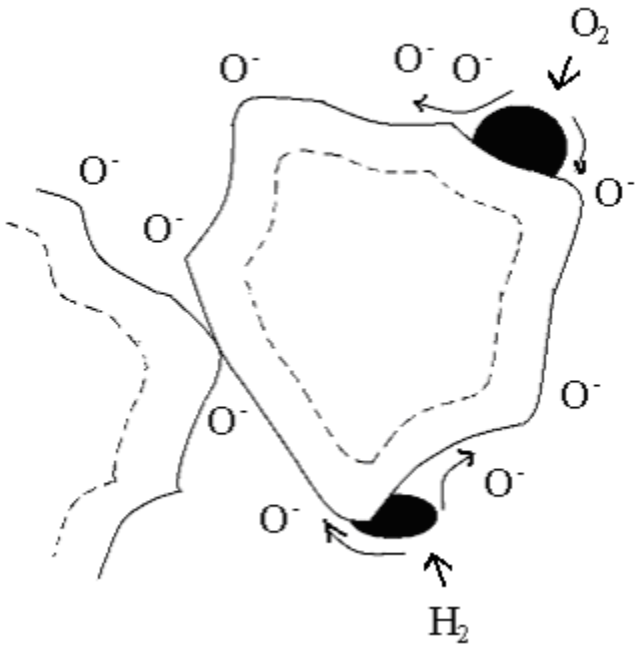

Figure 4.9. Illustration of spill-over caused by catalyst particles on the surface of grains

4.9.3. Fermi Energy Control

Fermi energy control is an electronic interaction whereby additives interact electronically with the metal oxide as a sort of electron donor or acceptor. For example, changes in the work function of the additive due to the presence of a gas will cause a change in the Schottky barrier between the metal and the oxide and thus, a change in the conductivity of the layer [35]. The oxygen adsorption on the catalyst removes electrons from the catalyst and the catalyst in turn removes electrons from the semiconductor, as shown in the Figure 4.10.

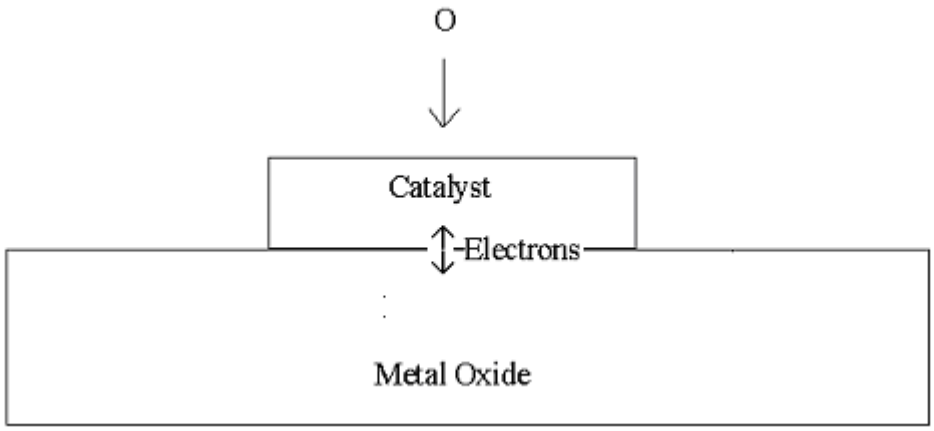

Figure 4.10. Fermi Energy Control

Figure 4.10 shows the catalyst, by Fermi energy control, dominates the depletion of electrons from the semiconductor surface, but the poor catalyst dispersion precludes any influence on the inter-granular contact resistance. In other words, oxygen adsorbing on the catalyst removes electrons from the catalyst and the catalyst then removes electrons from the nearby surface of the semiconductor [35]. However, if only a few catalyst particles are on each semiconductor particle, then only a small portion of the semiconductor surface has a barrier controlled by the catalyst (Figure 4.11). Then the chances of a catalyst particle being near enough to the inter-granular contact to control its surface barrier is rather small [35].

Figure 4.12 shows the more desired situation where one has a good dispersion of catalyst particles such that the depleted regions at the surface of a metal oxide overlap and the influence of the catalyst extends to the inter-granular contact [35].

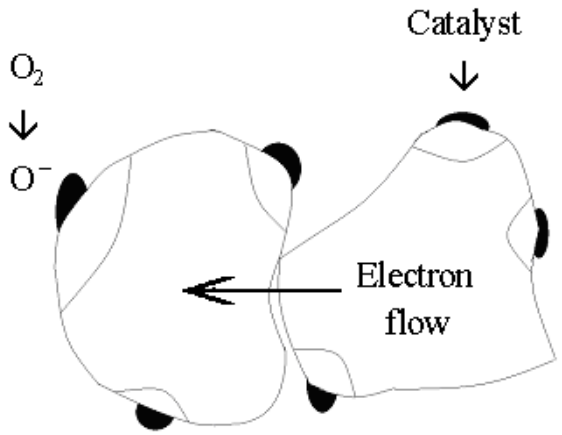

Figure 4.11. Example of poor catalyst dispersion

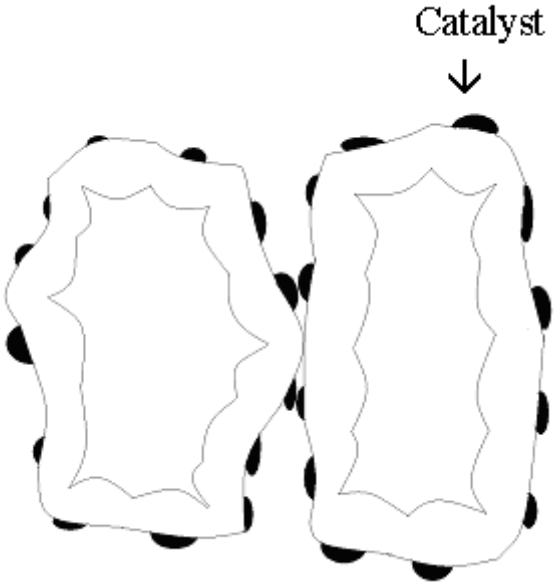

Figure 4.12. Example of adequate catalyst dispersion

4.10. Photoreduction (UV Illumination)

When a metal oxide gas sensor is used at low temperatures (<100°C), it has been demonstrated that UV light illumination can be used to enhance the sensitivity of the metal oxide gas sensor to oxidising gases such as nitrogen dioxide (NO_2) and ozone (O_3) [161]. Photo excitation can effect the charge carrier transport across grain boundaries by

increasing the density of free carriers throughout the material and decreasing the inter grain barrier height. This method is suitable as an alternative to high temperature operation, in situations where temperature and power consumption of the device are important [161].

Photoreduction causes a change in the chemical composition of the sensing layer, the charged carriers remains in the layer and do not disappear completely. The radiation does not change the chemical composition of material, but causes structural defects. It has been reported that photoexcitation can affect the electron transport across grain boundaries in the semiconductor sensing layer by [204]:

- Increasing the density of the free carriers throughout the semiconductor material.
- Decreasing the intergrain barrier height by changing the intergrain states charge.
- Increasing the probability if tunnelling through the intergrain barriers by decreasing the depletion layer thickness in the adjacent grains.

The photoreduction and oxidation treatments only affect the surface conductivity, while the bulk material of the sensing layer remains largely unchanged because the diffusion of absorbed species is highly suppressed at room temperature.

Illumination, changing the occupancy of the defects by electrons and holes, changes the concentration of the adsorption centres of each given type and the capacity of adsorption on the surface of the semiconductor [205].

4.10.1. Explanation of the Photoreduction Mechanism

UV light of 366nm is used as the excitation source for the sensing material, $^{*}-e^{-}$ is generated from the valence band to the conduction band on the surface vacancy sites $^{*}-O^{-}$ of the sensing material [178]. Simultaneously, $^{*}-h^{+}$ is generated in the valence band, this process is described below (Eq 4.36). The generated electrons have the affect of increasing the electron density in the conduction band, thereby decreasing the overall resistance of the material.

The recombination of $*-e^-$ and $*-h^+$ is highlighted by Eq. 4.37. Ozone gas adsorbs on the $*-e^-$ site of the sensing material and produces the surface adsorbed oxygen ion $*-O^-$ and oxygen gas (O_2), as shown in Eq. 4.38. This is the ozone oxidation reaction and it increases the resistance of the surface. Processes stated in equations 4.37 and 4.38 are competitive reactions. Reaction from equations 4.36 to 4.39 can be summarized as the total reaction in equation 4.40 [178].

$$2*-O^- \xrightarrow{h\nu(366nm)} *-e^- + *-h^+ + O_2 \qquad \textit{(Eq. 4.36)}$$

$$*-e^- + *-h^+ \rightarrow 2* \qquad \textit{(Eq. 4.37)}$$

$$2*-e^- + 2O_3 \rightarrow 2*-O^- + 2O_2 \qquad \textit{(Eq. 4.38)}$$

$$2*-O^- + 2* \rightarrow 2*-O + 2*-e^- \qquad \textit{(Eq. 4.39)}$$

$$2O_3 \xrightarrow{h\nu} 3O_2 \qquad \textit{(Eq. 4.40)}$$

4.11. Defects Chemistry

Electrical properties and characteristics of crystalline structures are determined by imperfections or the detects in the crystals [206]. Point defects are described as deviations from the ideal atomic arrangement of the structure, such as, missing ions, replaced ions,

interstitial ions and their associated valence electrons as shown in Figure 4.13. A principal difference between point defects in ionic solids and those in metals is that in the former, these defects may be electrically charged. Ionic defects are point defects that occupy lattice atomic positions, such as, vacancies, interstitial and substitutional solutes [206].

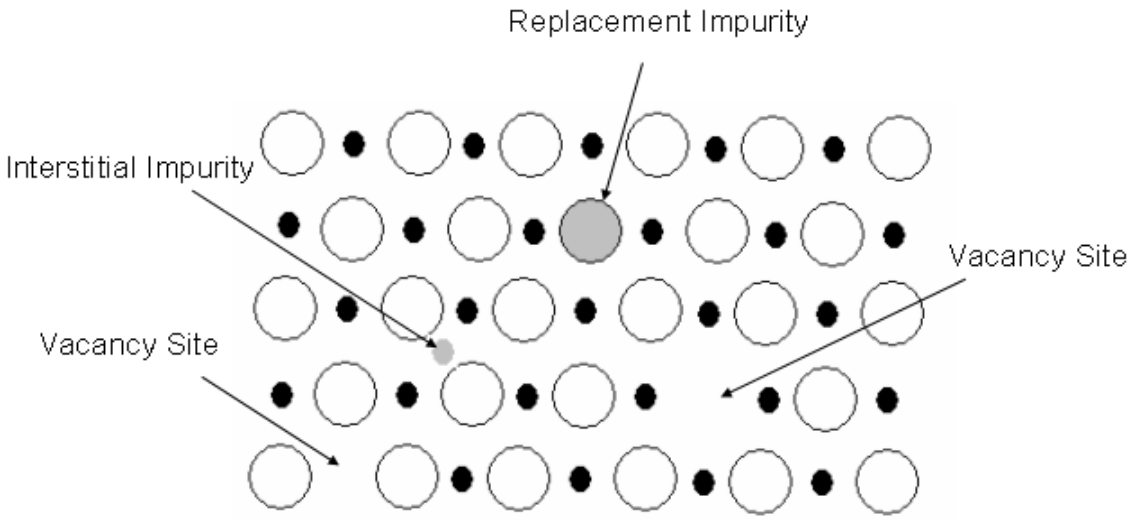

Figure 4.13. Types of point defects in crystalline structure

Electronic defects are deviations from the ground state electron orbital configuration of a crystal, formed when valence electrons are excited into higher orbital energy levels. Such an excitation may create an electron in the conduction band and/or an electron hole in the valence band of the crystal. In terms of spatial positioning, these defects may be localised near atom sites, in which case they represent changes in the ionization state of an atom, or may be delocalised and move freely through the crystal [206].

Chapter 5: Thin Film Technology (Vacuum Thermal Evaporation) - Electrical and Optical Properties

5.1. Introduction

As discussed in the previous chapters, there are numerous techniques used for the fabrication of thin films of metal oxide materials for gas sensing applications. In this study the fabrication of the thin sensing films was performed via the vacuum thermal evaporation (VTE) technique. Vacuum evaporation uses the atomic cloud formed by the evaporation of the source material in a vacuum environment to coat all surfaces in the line of sight of the evaporant. The theory of vacuum evaporation includes the thermodynamics of phase transitions from the equilibrium vapour pressure of materials may be derived as well as the kinetic, which provides models of the atomistic processes.

An evaporation event in solids is the release of an atom from the confining structure [207]. Atoms with different lattice positions cannot possess the same binding energy because they have a different number of nearest neighbours attached to them. VTE consists of vaporising the source material (evaporant) by applying sufficiently high temperatures and then re-condensing the vaporised material onto a cooler substrate to form a thin layer [208]. The application of heat is carried out by passing a large current through a filament support (basket, boat or crucible) with a finite electrical resistance.

The evaporation temperature and the inertness of the support material to alloying/chemical reaction with the evaporant dictate the choice of the filament support material [208]. The rate of evaporation, G is given by Langmuir's equation [209]:

$$G = p\left(\frac{M}{2\pi RT}\right)^{\frac{1}{2}} \qquad \textit{(Eq. 5.1)}$$

where p is the vapour pressure of the material at a temperature T, M is the molecular weight of the material and R is the gas constant per mole.

This technique is also known as "indirect" thermal evaporation since a supporting material is used to hold the evaporant. Once the metal is evaporated, the vapour undergoes collisions with the surrounding gas molecules inside the evaporation chamber. As a result a fraction is scattered within a given distance during their transfer through the ambient gas. The mean free path for air at 298K is approximately 45cm and 4500cm at pressures of 10^{-4} and 10^{-6} torr respectively. Therefore, pressures lower than 10^{-5} torr are necessary to ensure a straight-line path for most of the evaporated species and for substrate-to-source distance of approximately 10cm to 50cm in a vacuum chamber. The lower the pressure in the chamber the less chance of the material colliding or bonding with other molecules that may be present in the environment. If the pressure is not low enough a contaminated layer may be deposited on the substrate [210]. The rate of arrival, n of the evaporated molecules at the substrate is given by the following equation:

$$n = \left(\frac{tN}{M}\right) \qquad \textit{(Eq. 5.2)}$$

M is the molecular of the evaporated atoms of molecules, t is the deposited thickness and N is Avogadro's constant.

The following is a brief summary of the major steps involved in VTE of thin films onto a substrate material [209] (Figure 5.1):

- The transition of a solid or a liquid into a gaseous state.
- Transportation of the vapour along the space between the source and the substrate.
- Condensation of the vapour on the substrate surface.

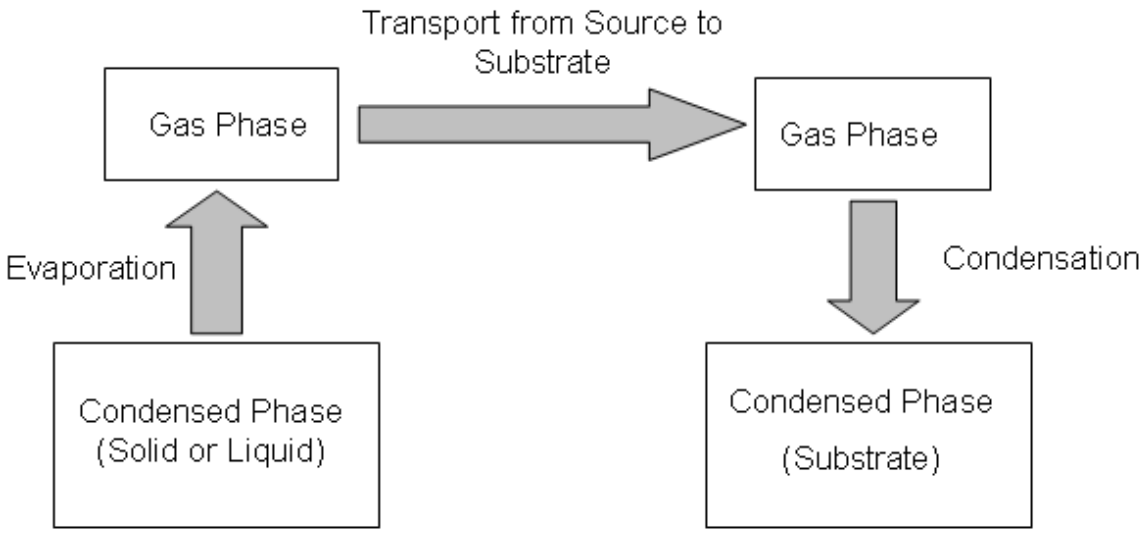

Figure 5.1. Evaporation Process

5.2. Theory of Evaporation of Solids

In order to understand the evaporation mechanism of solids, it is essential to determine the structure (atomic pattern) of the end phase material. There are three types of solid structures:

- Amorphous
- Poly-crystalline
- Crystalline

The amorphous structure has no recognizable short or long range order atomic patterns [162] (Figure 5.2(a)). In contrast, for the crystalline structure, the entire solid is made of atoms in an orderly array as shown in Figure 5.2 (c). The poly-crystalline structure is considered as a middle ground between amorphous and crystalline, it may consist of short ranges of repeated patterns (Figure 5.2(b).

Many solid materials are crystalline in structure, with atoms arranged in a three-dimensional array that repeats in space. This three-dimensional framework of atoms is known as a crystal lattice. Thus, a lattice may be defined as an indefinitely extended and periodic arrangement of atoms, or points. An identical grouping of neighbouring points therefore surrounds each point in a lattice [208].

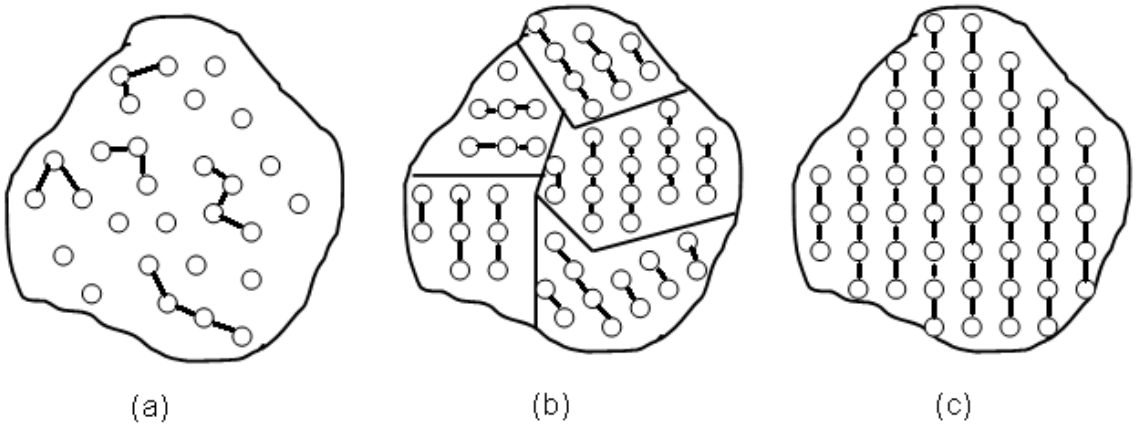

Figure 5.2. Structure of solids (a) Amorphous, (b) Poly-crystalline and (c) Crystalline

5.2.1. The Evaporation Event

An evaporation event in solids is the release of an atom from the confining structure. Atoms with different lattice positions cannot posses the same binding energy because they have a different number of nearest neighbours attached to them. Consequently, the liberation of an atom occurs in certain sequences [162]. Modelling this sequence, the crystal surface is divided into a number of sites. Each site consists of a number of atoms

of nearest neighbours and next nearest neighbours. From this model, there are three types of atoms in the site [162]:

- A primary ledge atom with a few nearest neighbours attached to it (this atom is weakly bound and can be easily removed from the site).
- A secondary ledge atom with a maximum number of nearest neighbours (this atom is tightly bound and requires high energy to dissociate).
- A kink atom is intermediate in the site (this atom requires average site energy to be released).

This model was further enhanced with the introduction of the stepwise concept [162]. The primary ledge is released first since it requires the least energy to disassociate. The last atom to escape is the secondary ledge. This process is continuous throughout the site and the whole surface. Consequently, the entire crystal melts and evaporates [162].

5.2.2. Congruent Evaporation

Relatively few inorganic compounds, alloys or mixtures evaporate congruently, because the constituents which are present in the solid state usually differ in their vapour pressures [162]. As a result, the composition of the vapour is not equal to that of the source material. There are various methods employed to control the vapour composition such as, reactive, two-source and flash evaporation [162].

For the evaporation of compounds, transition from solid to gas phase rarely occurs without changes to the molecular species. Dissociation or association usually accompany vaporisation of compounds. Association does not affect the stoichiometry of the constituents, whereas dissociation often does, namely, if one of the dissociation products is not volatile. Thus, deposition of compound films from single vapour source requires that the material enter the gaseous phases either in the form of complete molecules, or if dissociation occurs, that the constituents are equally volatile [162].

5.2.3. Film Formation

Condensation is initiated by the formation of small clusters through combination of several adsorbed atoms. These clusters are called nuclei and the process is known as nucleation. Vapour molecules arriving at the substrate are easily adsorbed. If the adsorbed atom has energy equal to the adsorption energy of the site then it may re-evaporate or 'hop' to an adjacent site. The mobility of atoms depends on the temperature of the substrate during the deposition process. Collision probability is high, as there are lots of atoms present at the deposition site. Bonding between colliding atoms becomes a possibility as more collisions occur. Atoms come together, forming islands, which grow, pending on island size and temperature (Figure 5.3(a)). Clusters coalesce and form a new island, occupying a smaller area than the sum of the original two, revealing fresh substrate surface where secondary nucleation occurs. Eventually a single continuous film is formed [162] (Figure 5.3(b) and (c)).

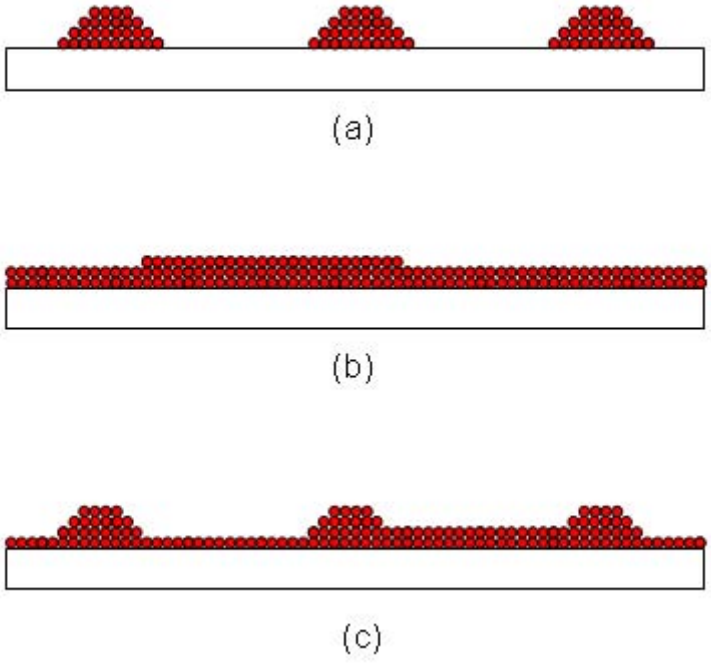

Figure 5.3. (a) Island Growth, (b) Layer Growth and (c) Layers and Islands

5.2.4. Thin Film Structure

Vacuum thermal evaporation (VTE) produces films with structural defects within the film. Controlling the deposition parameters such as, pressure, deposition rate, thickness, substrate temperature and surface nature may limit these defects. Despite the amorphous nature of thin films, the experimental and theoretical investigations have indicated that they can still share the crystalline structure models and theories. Since amorphous solids contain relatively rigid chemical bonds in terms of both direction and length, deviation from the crystalline state is limited. Therefore excessive energy would be required to bend or distort this rigidity. Consequently, assumptions made for short-range order within an amorphous thin film are possible and the fundamentals of crystalline band structure remains applicable to amorphous films [211]. There is no quantitative measure of the degree of 'amorphicity' in a solid. It is noted that the amorphous state to some extent can be considered metastable and generally an amorphous film exhibits a drift in electrical properties [211].

In a solitary atom, electrons are restricted to specific energy levels. Any transition of an electron can only be in the form of a quantum leap from one allowed energy level to another by either absorbing or emitting an amount of energy equivalent to the difference between the states. The atomic system is further governed by the Pauli exclusion principle, which states that in a closed system no two electrons can occupy the same state [211].

5.2.5. Thin Film Structural Defects

Vacuum thermal evaporation (VTE) produces films with structural defects within the film such as grain boundaries or lattice imperfections. The most frequently encountered defects in evaporated thin films are dislocations [162]. Dislocations may be formed by the following mechanisms:

- Since nuclei form at random points on the substrate surface, misfit displacements of the lattices of nuclei or islands exist. On coalescence, dislocations are

incorporated at the boundary of the two islands. If the islands are small, they rotate and translate to accommodate small misfits. Consequently, dislocations are permanently incorporated only when the islands become too large to move and minimise the misfit. Thus, the dislocation density rises rapidly when the final – stage coalescence of large islands takes place to make the film continuous [162].

- If coalescence of more than two islands takes place simultaneously so as to minimise the elastic strain at each interface, the islands may join to leave a hole between them. Stresses in the film may generate incipient dislocations in the hole. It is geometrically necessary that real dislocations are formed as these holes fill in, since the incipient dislocations are effectively dislocations with a hollow core [162].
- Dislocations may be formed because of point – defect aggregation during growth provided that the vacancies are relatively immobile. Deposition at very high rates and sufficiently low temperatures might cause many vacancies to become trapped, and these could aggregate slowly [162].
- The extension of the substrate imperfections into the deposited film is another possible mechanism. Surface impurities can have a significant effect in introducing dislocations and other defects in the deposited thin film [162].

Controlling the deposition parameters such as, pressure, deposition rate, thickness, substrate temperature and surface nature may limit these defects [162].

5.3. Crystalline Band Structure

In the crystal lattice, atoms are periodically arranged. The outer electrons of an atom in the crystal are shared and altered by neighbouring atoms so that the whole crystal becomes a single system in which the Pauli Exclusion Principle still holds [211]. As a result the discrete energy states split in the crystal to form a band of allowed energy levels around E_0 as shown in Figure 5.4 [211]. Furthermore, since the electron states of a given atom are of two types, inner and outer, the resulting allowed energy bands split

into two bands of higher and lower energies. The conduction and valence bands represent the higher and lower energy bands respectively [211]. These bands are separated by a forbidden energy gap, the size and nature of which determines the physical properties of the crystalline structure. The width and the nature of the band gap are the main determinant of the physical properties of any crystalline or amorphous structures ranging from conductors to insulators [208]. Therefore band structure and the existence of an energy gap are believed to be dependent on the arrangement of nearest atomic neighbours and the existence of local or short-range order [211].

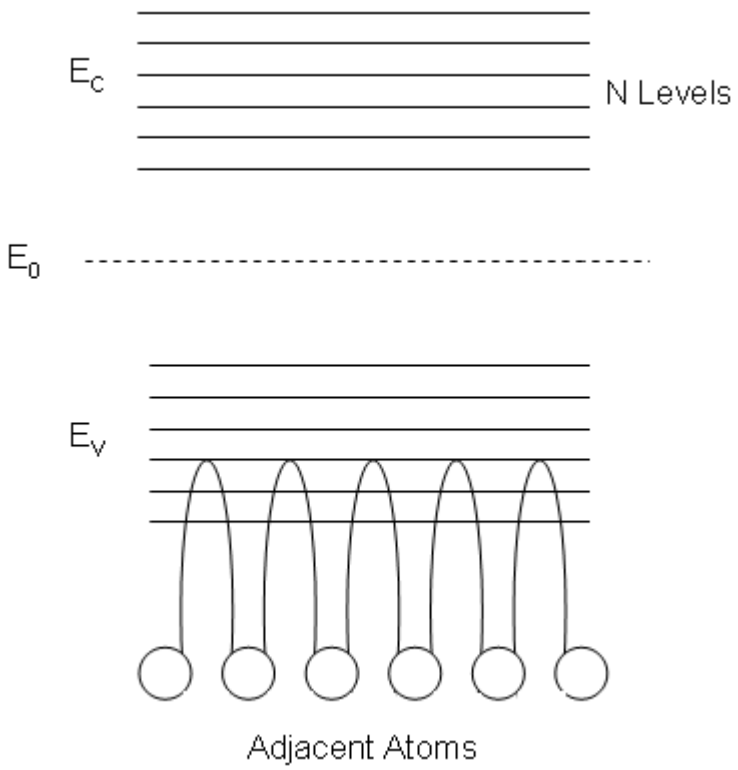

Figure 5.4. Crystalline Band Structure

5.4. Band Structure of Amorphous Semiconducting Materials

In this section the differences between the band structure of amorphous solids and that of crystalline materials will be examined. It has been stated that the interaction of electrons

with atomic cores in a lattice can determine the nature of the band structure. In amorphous materials, the structural disorder causes local electric fields to be generated within the materials matrix [211]. The interaction of electrons with these local fields gives rise to the phenomena known as localisation. Therefore in a disordered material the electron states are classed as localised and delocalised states, these states describing the extent to which a charge carrier is bound [211].

5.4.1. Anderson Localisation

Since localisation was first proposed by Anderson in 1958, it has proved to be invaluable for understanding the electronic processes occurring in amorphous solids. This analysis was applicable to a three dimensional crystalline array of potential wells. Each well has a depth H as shown in Figure 5.5(a), such that for each well an electron can occupy an S-state at a depth w. The three dimensional array is broadened into a band of width J, according to the tight binding approximation:

$$J = 2ZI \qquad \textit{(Eq. 5.3(a))}$$

where Z is the coordination number and I may be expressed as:

$$I = \omega \exp(-\alpha R_0) \qquad \textit{(Eq. 5.3(b))}$$

$$\omega = \frac{C}{R_0 (H \alpha v)} \qquad \textit{(Eq. 5.3(c))}$$

where R_0 is the distance between nearest neighbours, v is the volume occupied by each well, C is a constant of order unity, and α is the rate of electron wave function decay. It is assumed that $J << w$, which is a condition of the tight binding approximation. The random potential energy v is added to the potential energy of each well as shown in Figure 5.5(b), so that v may have values of $\pm\frac{V_0}{2}$, where $w >> V_0 >> J$. Therefore the density of states $N_0(E)$ in the middle of the band is given by:

$$N_0(E) = \frac{N}{V_0} \qquad \textit{(Eq. 5.4)}$$

where N is the number of wells per unit volume [211].

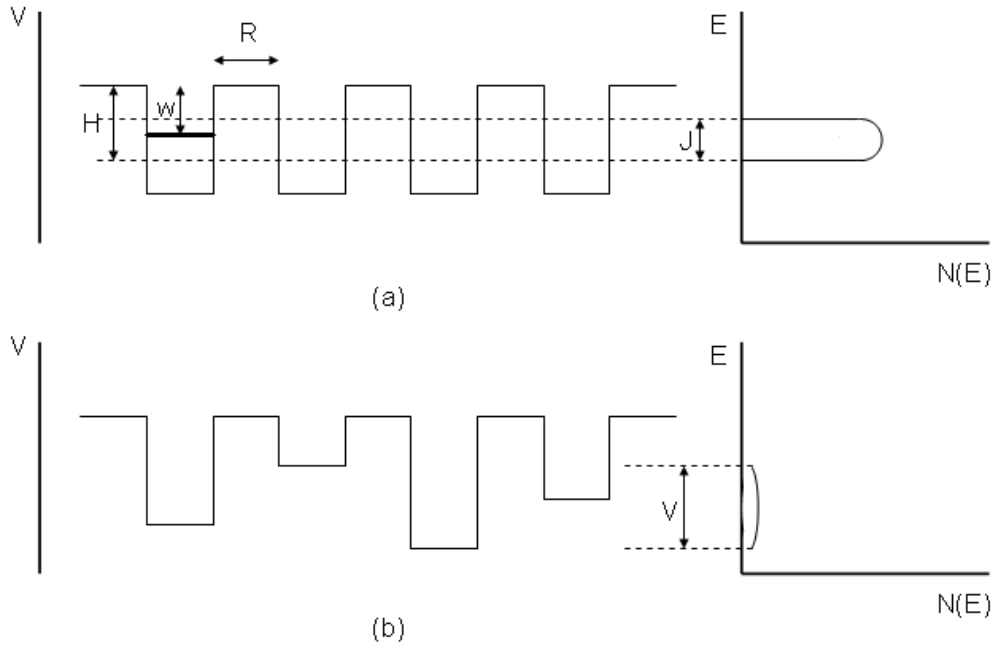

Figure 5.5. Anderson Localisation

On the basis of Anderson's theory, Mott [213] argued that the spatial fluctuations in potential experienced by an electron in a disordered system should lead to the formation of a tail of localised states above and below the normal band edges as shown in Figure 5.6 [213]. The existence of these localised states smears out the band edges at E_C and E_V, the edges of the conduction and valence bands, thus they are no longer well defined [211]. This can be understood in terms of a lack of long-range order, deviations from stoichiometry and incorporated impurities, all of which may be produced by vacuum thermal evaporation (VTE) [211]. Although the band edges are no longer sharp, carrier mobilities close to the band edges drop by many orders of magnitude. This observation gave rise to the concept of a mobility edge [211]. Therefore, it is more appropriate to speak of a mobility gap rather than a crystalline density of states gap, which for amorphous materials is not so well defined [211].

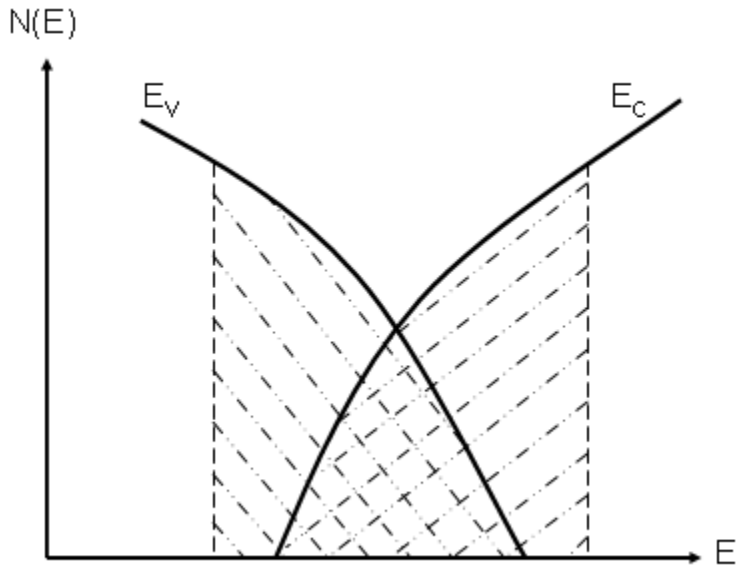

Figure 5.6. Cohen, Fritzsche and Ovhinsky (CFO) Model [203]

A number of theoretical models have been postulated to describe the bandgap states of amorphous solids. The most appropriate model which may be considered for any given system depends on the extent and nature of the defects which produce the localised states.

Two models of disordered solids are discussed in this thesis, these are the Cohen, Fritzsche and Ovhinsky model (CFO) [212] and the Davis and Mott model [213].

5.4.2. The CFO Model

Figure 5.6 shows a representation of the model proposed by Cohen, Fritzsche and Ovhinsky [212], for the density of states in the band-gap of an amorphous solid. This is considered as an appropriate model for amorphous covalent semiconductor alloys which contain a high density of both compositional and structural defects resulting in a continuous range of localised states between E_C and E_V. It is known that the structural deformation produces broken or dangling bonds which introduce deep trapping levels in the bandgap [211]. If the concentration of spatial and compositional defects is great enough, the band-tails may broaden until overlapping occurs. This model supports the idea of self compensation, and pins the Fermi level near the middle of the energy gap. In support of this argument it may be noted that for many amorphous semiconductors the Fermi level is located near the mid-gap and appears to be pinned over a range of temperatures [211].

5.4.3. The Davis and Mott Model

An alternative to the C.F.O model for the density of states distribution is the Davis and Mott model (Figure 5.7.), it can be seen that the tails of the valence and conduction bands are narrow and non–overlapping. These tails may extend only a few tenths of an electron-volt into the forbidden energy gap. The two deep levels of localised states in the band gap represented by E_X and E_Y are the acceptor and donor states respectfully and are due to dangling bonds that may be positively or negatively charged [211, 213].

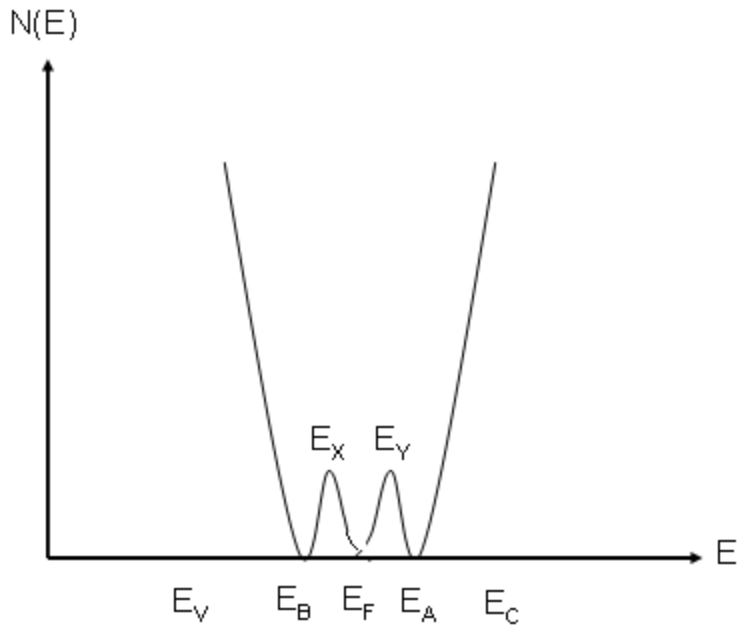

Figure 5.7. The Davis and Mott Model

5.5. Absorption Spectra of Amorphous Solids

The disorder encountered in amorphous materials leads to localised defect states at the edges of the valence and conduction bands. The transitions between these localised states are optically induced. Therefore, the spectra for optical absorption bands can be measured and analysed for such transitions. The absorption edges of amorphous materials can be divided into three distinct regions (Figure 5.8).

Region A arises from transitions involving the defect states directly. The absorption edge extending in regions A and B is complicated and contains defect-induced tail at the lowest energies, and exponential region at intermediate energies and a power law at the highest energies [208]. The high absorption coefficient in region C is caused by the transitions between the extended states. This is then followed by an exponential region B [208]. In region B, the disorder can introduce band tailing which leads to energy levels in the forbidden energy gap of a semiconductor and the electron states in these tails are

localised [214]. The analysis of the exponential portion (region B, $\alpha(\nu) < 10^4$ cm^{-1}) of the absorption spectrum is given by equation 5.8 [214]:

$$\alpha(\nu) = \exp\left(\frac{h\nu}{\Delta E}\right) \qquad \textit{(Eq. 5.5)}$$

$\alpha(\nu)$ is the absorption coefficient for the given photon angular frequency (ν) and h (Planck's Constant), ΔE is the width of the of localised states.

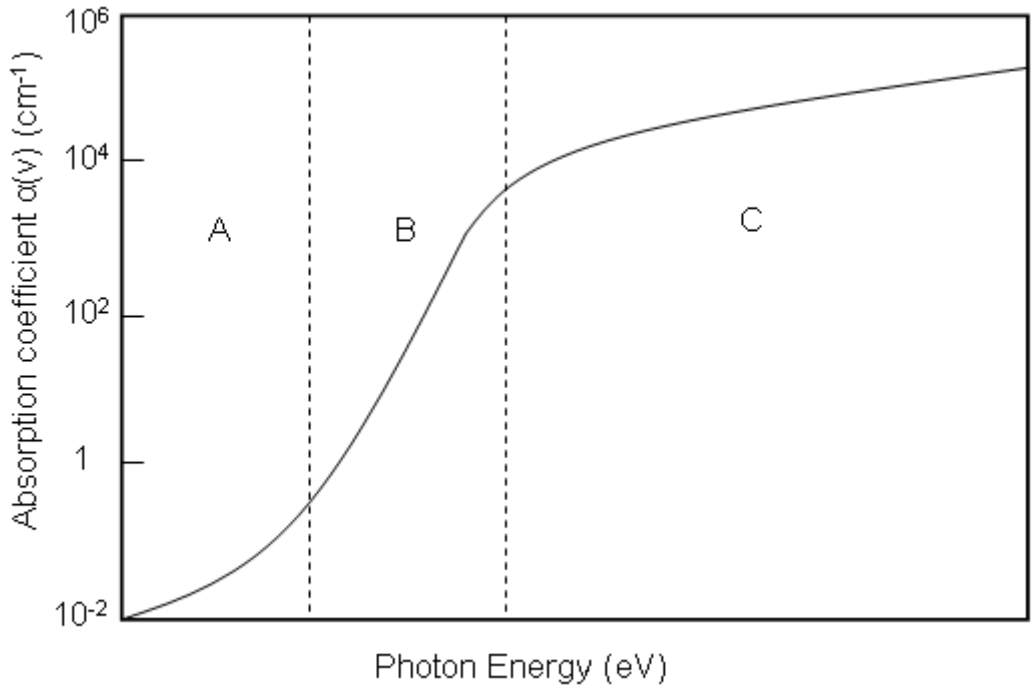

Figure 5.8. Absorption Spectrum of amorphous solids

At high absorption coefficient, the following equation is proposed [213]:

$$\alpha(\nu)h\nu = B(h\nu - E_{OPT})^n \qquad \textit{(Eq. 5.6)}$$

where α is the absorption coefficient, E_{OPT} is the optical energy band gap, $h\nu$ is the energy of the incident photons and B is a constant. The exponent n of the energy dependence of the optical band gap can distinguish four cases of electronic transitions, which are summarised as follows [213]:

- $n = 1/2$ for direct allowed transition
- $n = 3/2$ for direct forbidden transition
- $n = 2$ for indirect allowed transition
- $n = 3$ for indirect forbidden transition

The constant B is calculated by equation below:

$$B = \frac{4\pi\sigma_0}{nc\Delta E} \qquad \textit{(Eq. 5.7)}$$

where σ_0 is the electrical conductivity, n is the refractive index, c is the speed of light and ΔE is the width of the tail of the localised sites [208].

5.6. Conduction Mechanism in Amorphous Materials

The mechanism of ionic conduction involves the drift of ions or vacancies under the influence of an electric field by hopping over a potential barrier from one site to the next neighbouring site [208]. The high density of structural defects in amorphous dielectric films lead to a high activation energy, large transit time, transportation of materials from one electrode to another and the polarisation effects in a DC field to be dominant features of the ionic conduction [213].

Impurity conduction is a process in which electrons move between centres without activation into the conduction band. Electrons occupy an isolated donor level and have a wave function localised slightly below the conduction band minimum [215]. For the impurity conduction to be of significance in amorphous films, it must contain both donor and acceptor (trap) centres. In the absence of acceptors, impurity conduction is not possible until the interaction between centres is very large. For low concentrations, the electrons move by the hopping process from one centre to another [215].

5.6.1. The Hopping Process

The hopping process requires less energy than activation into the free band and this energy may, for a limited high density of localised centres, tend to zero as in the case of impurity band conduction in semiconductors [215]. This process is identified in the case of heavily disorderd solids such as amorphous and glassy dielectric films.
Hopping conduction is present in highly disordered and amorphous materials. Below is a summary of the hopping conduction features [215]:

- Linear dependence of current on voltage.
- Relatively low activation energy.
- Monolithic increase of AC conductivity with frequency.
- Slight decrease of polarizability with frequency.

5.6.2. Distinction between Electronic and Ionic Conduction

In crystalline materials, ionic conduction is characterised by low mobilities and high activation energies, while electronic conduction is associated with relatively higher mobilities and low activation energy [215]. For amorphous materials, mobility may be very low, therefore, for hopping conduction, activation energy will be small [215].

5.6.3. The Shottky Conduction Mechanism

If the potential barrier is too thick or not at sufficient temperature to allow tunnelling to occur, electrons can be thermally excited to cross over a barrier into the conduction band of the insulator material [208]. The Shottky current density J_S of the thermal emission is given by the equation below:

$$J_S = AT^2 \exp\left(-\frac{\phi}{kT}\right) \qquad \textit{(Eq. 5.8)}$$

Where A is a constant and T is absolute temperature in Kelvin. When an electric field is applied, the potential barrier is lowered by $\Delta\varphi$ and the above Shottky current density J_S of the thermal emission becomes:

$$J_S = AT^2 \exp\left(\frac{-\phi - \beta_S E^{1/2}}{kT}\right) \qquad \textit{(Eq. 5.9)}$$

where E is the applied electric field and β_S is the Shottky field-lowering coefficient, given by:

$$\beta_S = \left(\frac{e^3}{4\pi\varepsilon_r\varepsilon_0}\right)^{1/2} \qquad \textit{(Eq. 5.10)}$$

where ε_0 is the free space permittivity and ε_r is the relative permittivity [208].

5.6.4. The Poole-Frenkel Conduction Mechanism

In the Poole-Frenkel process, the thermally excited electrons are driven by the applied electric field to move from localised traps to the conduction band. This process is also known as the field-assisted thermal ionisation since the emission of electrons occurs from trapping centres in insulators by the joint effect of temperature and electric field [208]. The Poole-Frenkel field-lowering coefficient, β_{PF} is given by the following equation:

$$\beta_{PF} = \frac{\Delta\varphi}{E^{1/2}} = \left(\frac{e^3}{\pi\varepsilon_0\varepsilon_r} \right)^{1/2} \qquad \textit{(Eq. 5.11)}$$

The Poole-Frenkel coefficient in a uniform electric field is twice that due to the Shottky effect, as expressed in the equation:

$$\beta_{PF} = 2\beta_S \qquad \textit{(Eq. 5.12)}$$

By taking a number of factors into account, it is possible to discriminate between the two types of emission processes [208].

Chapter 6: Experimental Procedures, Set-Up and Related Instrumentation

6.1. Introduction

In this work mixed metal oxides of In_2O_3, ZnO, SnO_2 and sole NbO_2 were used in the fabrication of ozone sensing devices. These metal oxides were deposited via the VTE technique on both alumina and glass substrate materials. Copper interdigitated electrodes were formed and utilized to gain electrical measurements from the sensing device.

Characterisation and analysis of the material is a critical area in the development of sensing materials and devices. Analysis of the physical, chemical and electrical properties are important in the development and understanding of the devices and sensing mechanism.

As outlined in previous chapters, thin film evaporation and etching techniques were used to fabricate specific electrode patterns on alumina substrates.

X-ray diffraction (XRD) was used to determine the structural composition of the sensing material. Scanning electrode microscope (SEM) was utilized to compare the surface morphology and porosity of the sensing films. Optical measurements of the sensing layers deposited on glass substrates were carried out using a CARY 1E UV-Visible

Spectrometer. X-ray Photoelectron Spectroscopy (XPS) has been used to analyse the composition of the films.

This chapter discusses in detail the fabrication process of the sensors and the equipment involved. Also discussed are the analysis techniques mentioned above.

6.2. The Thin Film Device Structure

Interdigitated structures (IDS) are commonly used as a basis for gas sensitive layers [216]. The advantage of sensors based on this structure is the simple and cheap fabrication process and the ability to use the sensor in a wide range of applications without crucial changes to the sensor design [162]. The IDS is an arrangement of two comb electrodes interlocked into each other, as discussed in Chapter 3. The structure can be considered as many resistors in parallel sandwiched between the alumina substrate and the sensing layer (Figure 6.1). The oxide layer is deposited over the conductor in a rectangular pattern. The IDS measures an area of 3mm x 3mm. Each electrode has a total of five interdigits, with each interdigit having a thickness of 0.1mm and a length of 2.5mm. The space between each electrode is 0.2mm.

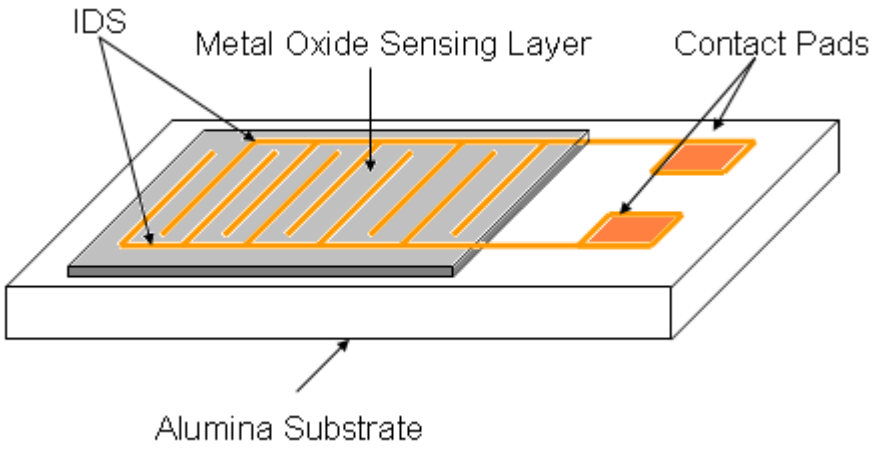

Figure 6.1. Structure overview

The electrode mask patterns were designed and created using common PCB CAD package software (EAGLE 2.61). The software package is often used for designing PC board layouts and other circuit schematics. On completion of the electrode design the pattern is printed onto high quality acetates using a laser printer. An overview of the device is illustrated in Figure 6.1.

6.3. Fabrication Materials, Equipment and Processes

6.3.1. Substrate Preparation

Alumina and glass substrates were used in this work. The surface of the substrate should be completely free of contaminants. Contaminations create a protective non – adhesive chemical layer on the surface of the substrate. This yields to significant bonding adhesion degradation between the substrate and the deposited oxide layer. Moreover, contaminants could chemically react with the deposited material and change the properties of the device being fabricated.

Some of the different types of contaminants found are classified as particulates, ionic residues, organic and inorganic residues. Particulates and organic residues can be removed from the substrate by washing in a light industrial alcohol (acetone or isopropanol) and rinsing with deionised water [159]. The major source of circuit failure is due to ionic residues, such as oils, grease or salt from human handling and substrate machining. To ensure proper substrate cleaning, and in order to eliminate contaminants, the following steps should be followed [208]:

- Firstly, the substrates are washed using de – ionized water or a light alcohol (acetone).
- The substrates are then placed into a 60 – 70 % nitric acid bath and heated to 60°C for 15 minutes. This removes ionic contaminants present on the surface of the substrate material by dissolving the contaminant into the acid solution.
- An ultrasonic degreaser was used to remove any contaminants left after the acid solution.

- Finally, the substrates are washed with acetone and de – ionized water to remove any residual nitric acid. The substrates are then dried using a lint free cloth.

6.3.2. The VTE System and the Deposition of Cu IDS Electrodes

Short strips of Cu wire were cleaned with alcohol and rinsed in deionised water prior to being placed in a molybdenum boat, which was then placed between the electrodes of an Edwards E306A coating system. A maximum of four boats may be used for one deposition depending on the desired thickness of the Cu layer to be deposited.

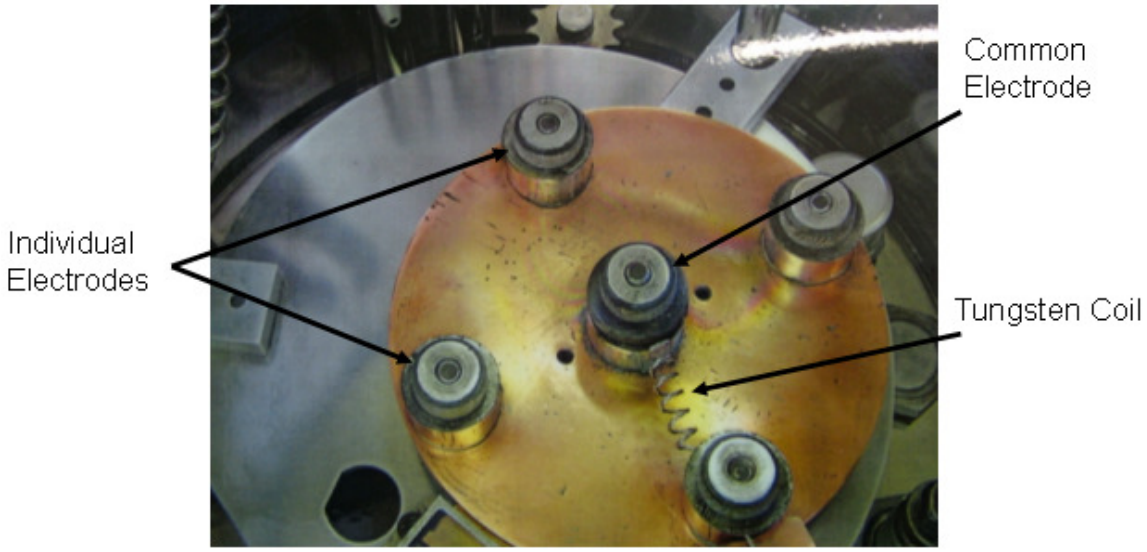

Figure 6.2. Overview of Edwards E306A Coating System containing four electrodes

The Alumina substrate placed in the substrate holder located approximately 12 inches directly above the boat.

Creating a usable vacuum anywhere in an atmospheric environment requires removing the molecules present in the atmosphere (nitrogen, oxygen, carbon dioxide, etc.). The vacuum process was started by producing a rough vacuum using a roughing (rotary)

pump, which removes most of the air from the system [208]. This process takes approximately 15mins or until a vacuum of $2x10^{-1}$ mbar is achieved. After an appropriate roughing vacuum was produced the Edwards E306A is then set to a high vacuum, which was achieved using an oil diffusion pump.

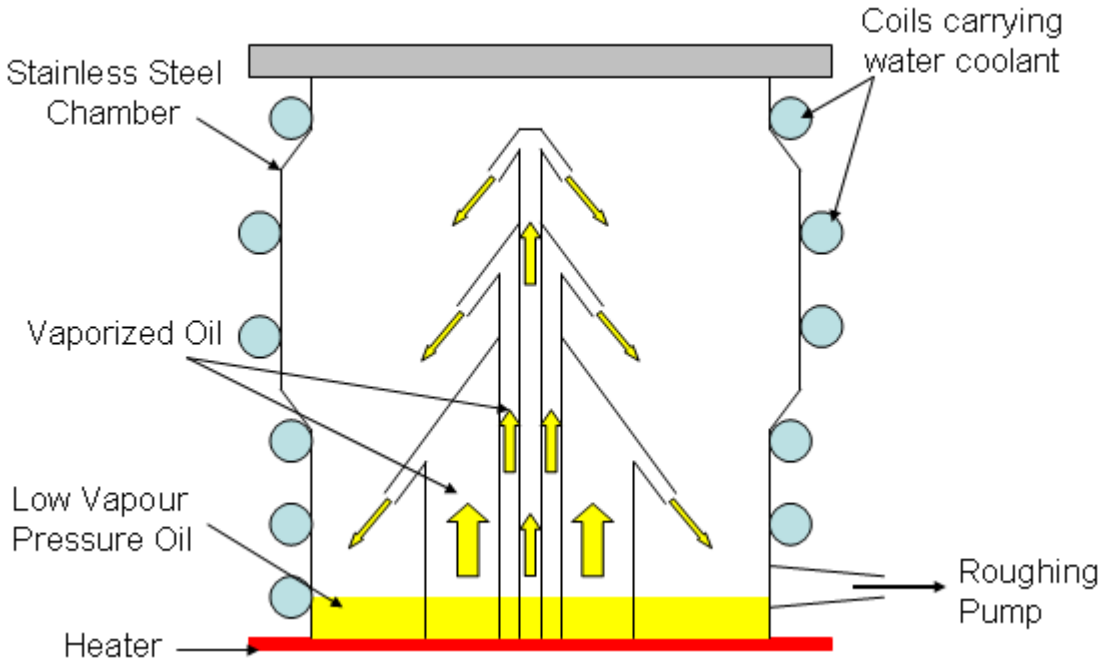

Figure 6.3. Diffusion Pump

A vacuum diffusion pump cannot begin with atmospheric pressure inside the chamber, hence the need for a roughing (rotary) pump mentioned above. The vacuum diffusion pump consists of a stainless steel chamber, containing vertically stacked cone-shaped jet-assemblies (Figure 6.3). Specialised oil with a low vapour pressure is used in the process and located at the base of the chamber. This oil is heated to boiling point via the heater at the base of the stainless steel chamber. The vaporized oil moves up and is expelled through the jet-assemblies. Exiting from the jets, the high energy oil droplets travel downwards in the space between the jet-assemblies and the side walls. This motion typically imparts a downward motion on the gas molecules present and transports them towards the pump outlet, thereby, creating a higher vacuum. At the base of the chamber,

the condensed molecules of atmospheric gases are removed by the roughing pump, while the condensed oil begins another cycle. The effect of removing molecules creates a high vacuum in the upper portion of the chamber. In order to prevent thermal runaway and overheating of the system, water (coolant) flows through cooling coils on the outside of the chamber.

When an appropriate vacuum was achieved, passing a current through the molybdenum boat started the deposition process. A quartz crystal was used to measure the thickness of the deposited layer. When the desired thickness was reached, the shutter was closed and the current switched off. Figure 6.4 illustrates the elements involved in a vacuum thermal evaporation system.

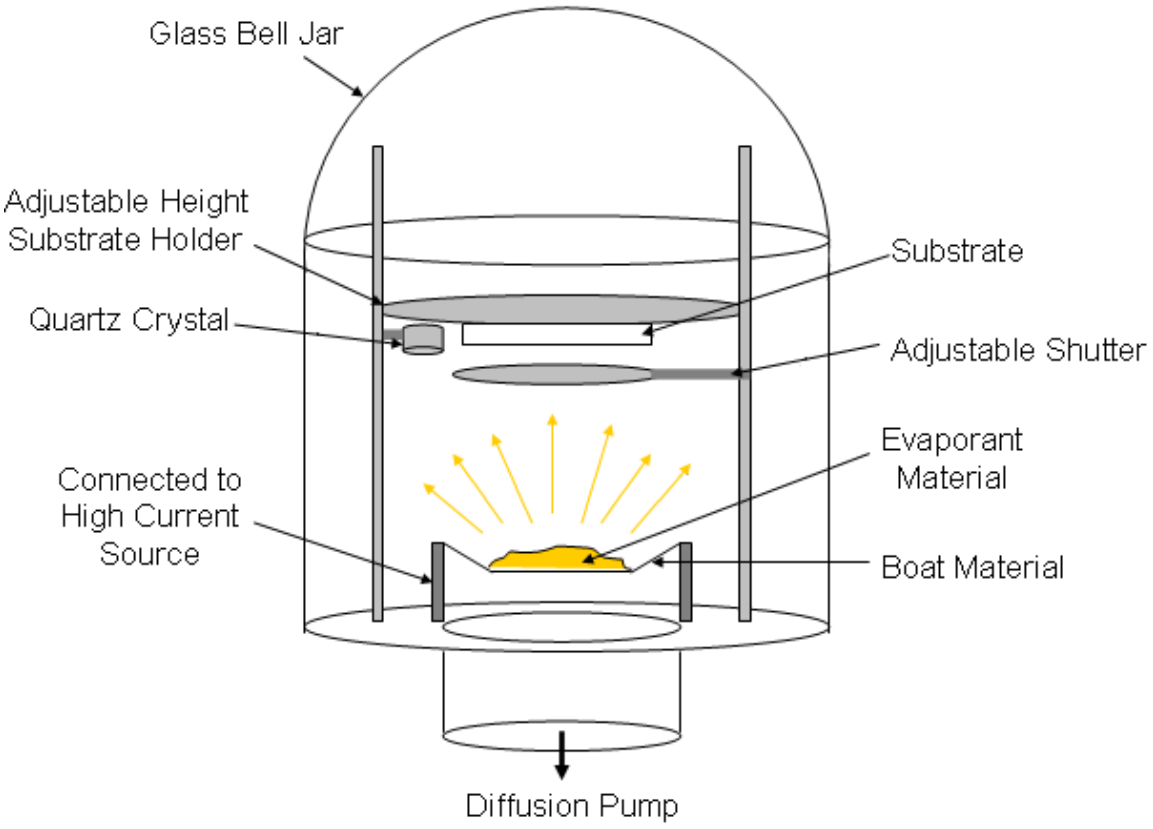

Figure 6.4. Vacuum Thermal Evaporation System

6.3.3. Application of the Photoresist

To transfer an image onto the substrate, which already has Cu deposited on it, the first step is to uniformly apply photoresist to the surface by a process called spin coating (Figure 6.5). For the resist to be reliable it must satisfy three criteria:

- Good bonding to the substrate.
- Thickness must be uniform over the entire substrate.
- The thickness must be reliably controlled (repeatable).

Spin coating has emerged as the most reliable technique for photoresist deposition. As shown in Figure 6.5 below a plastic dropper was used to deposit a small amount of photoresist (AZ5214) on to the substrate containing the deposited Cu. The spin coater was then gradually stepped up from 0 – 7000 rpm to eliminate excess photoresist. During the first couple of seconds of spinning the excess photoresist solution is thrown from the substrate and carefully drained away from contact with the substrate. The photoresist that remains on the substrate forms a very thin layer whose thickness is controlled via the speed and the length of time of the spinning process. After spinning the substrate is then soft baked at room temperature for 24 hours to improve adhesion to the surface.

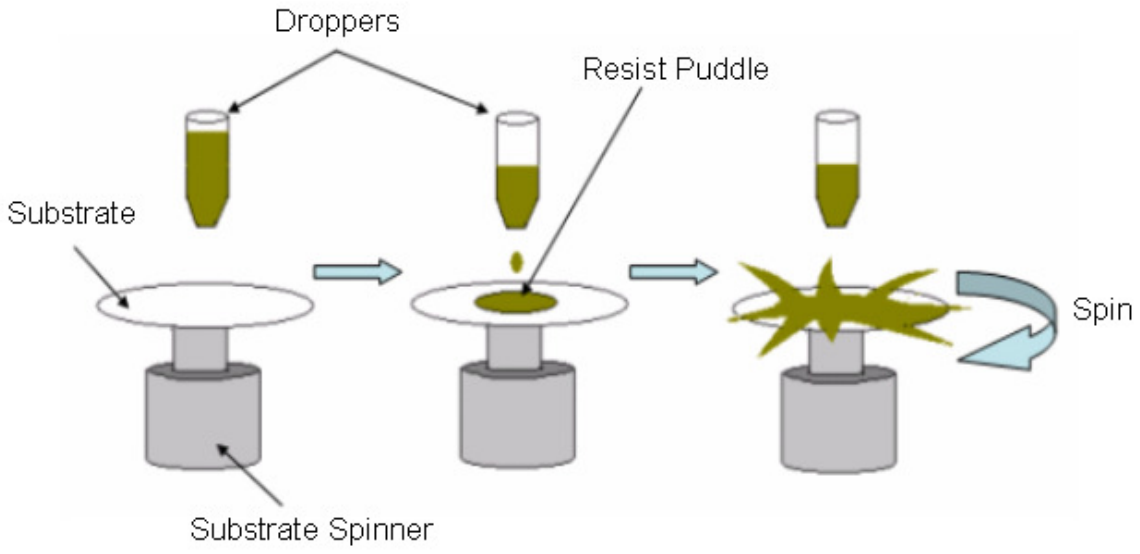

Figure 6.5. Application of Photoresist

6.3.4. UV Exposure and Etching Processes

The substrate is then cured at room temperature for 24 hours. As mentioned previously, the electrode designs were drawn up and printed on acetate in preparation for UV exposure. The acetate containing the design was placed over the substrate and exposed to UV light. After the exposure, the substrate was placed in a developer solution (Electrolube PDN250ML). The substrate was then rinsed in water and placed in the etching solution of SEMO 3207 fine etch crystals to reveal the electrode pattern. In order to remove the photoresist from the remaining pattern, the substrate was totally re-exposed to UV light and dipped in the developer solution, see Figure 6.6.

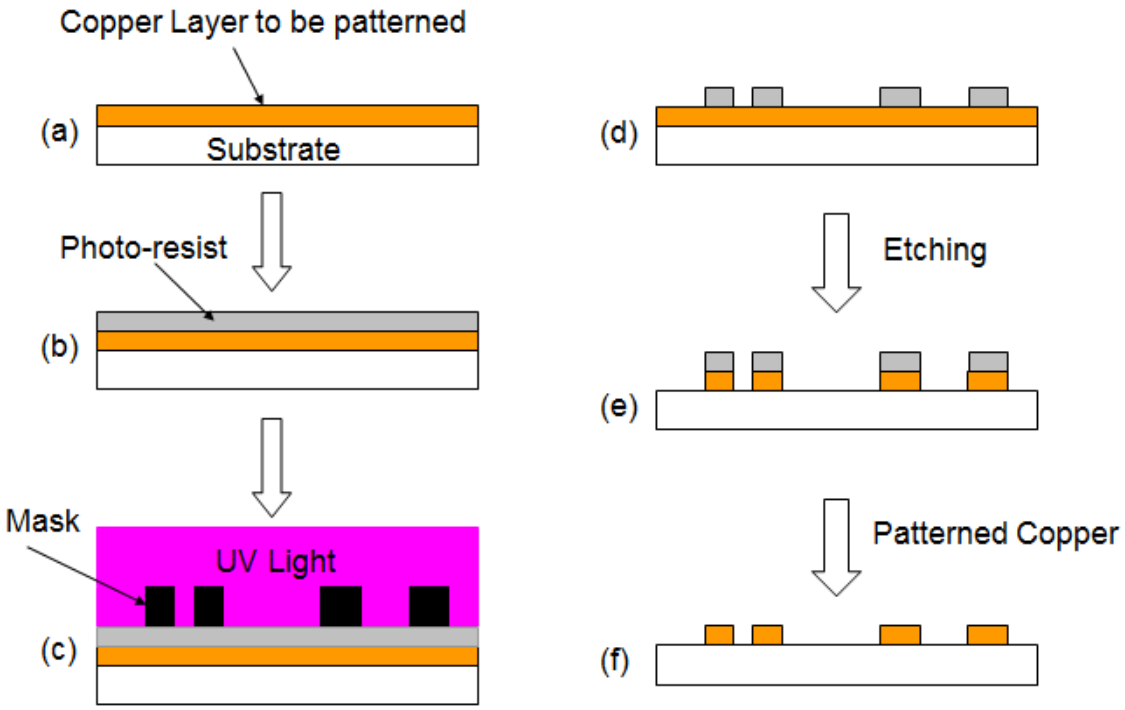

Figure 6.6. Electrode Patterning Process

6.3.5. VTE of Metal Oxide Sensing Layer

The VTE of metal oxide gas sensor thin films were prepared by heating the oxide mixture in a supporting structure such as a boat, coil, crucible or basket as shown in Figure 6.7 under high vacuum conditions at a deposition pressure of $5x10^{-5}$mbar. The vapour phase was condensed on the alumina substrate, containing the electrodes, at room temperature and covering an area of approximately 3.0 x 3.0mm. The film was deposited at various deposition rates varying from 0.1nm/s to 1.4nm/s. The film thickness was also varied from 20 – 100nm. Film thickness was monitored by a quartz crystal microbalance as shown in Figure 6.4.

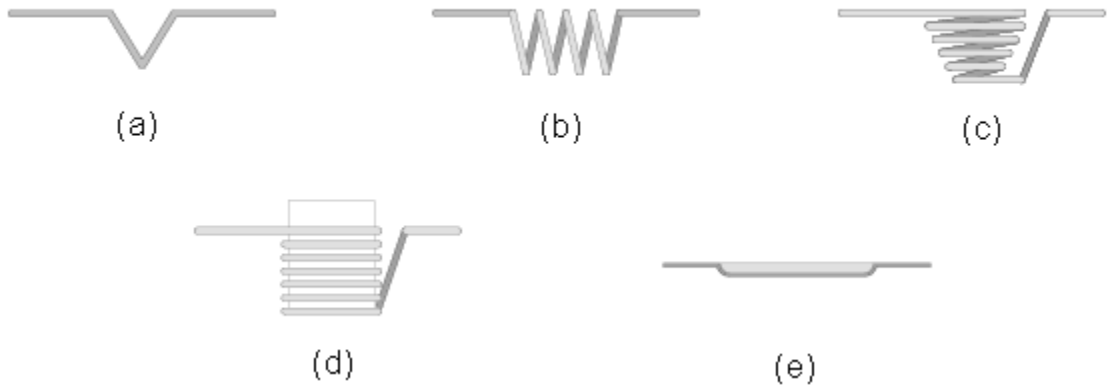

Figure 6.7. Supporting Structures: (a) wire hairpin, (b) coil, (c) wire basket, (d) alumina crucible with wire basket, (e) foil

6.3.6. Annealing Process

In general deposited layers contain a host of structural defects [162]. The application of a relatively mild heat treatment will anneal most of these defects out of the film. This should lead to a better adhesion of the film to the substrate surface and also to a corresponding decrease in film resistance.

Annealing was performed in a vacuum environment. Vacuum pressure was maintained at $6x10^{-4}$ mbar. Temperature inside the vacuum was gradually increased to 300°C and maintained for 45mins. The sensors were then left to cool to room temperature in the vacuum before being removed. Annealing has been shown to be very effective in increasing the carrier concentration [217]. In amorphous materials, the forbidden band has specific concentration of localized energy states, which originate from the statistical disordering of the atoms. During the annealing process the degree of disordering decreases or some voids are removed and this may cause a decrease in the number of unsatisfied bonds [217]. Point defects may be removed in which oxygen plays an important role. Thus the increase in electrical conductivity due to annealing may be due either to the rearrangement and elimination of point defects, which lead to the decrease in the carrier scattering or the formation of indium species of lower oxidation state (In^{2+}) [217].

6.4. Experimental Set-up for the Pen-Ray Generator

The equipment is set up as shown in Figure 6.8. The flow rate from the oxygen tank is kept constant at 0.25 l/min by the oxygen regulator. Oxygen tubing is used to carry oxygen from the regulator to the quartz tubing of the Pen–ray ozone generator.

Ozone is generated by pumping oxygen through the quartz tube under exposure from a pen ray ultraviolet (UV) lamp (Ultra-violet Products Ltd). The ozone generator utilizes the photochemical reaction of oxygen under short wave (185 nm) UV to produce a continuous and stable flow of ozone. Ozone concentration was controlled by means of an adjustable metal shutter enclosing the UV lamp (Figure 6.9). The UV spectrometer

(Figure 6.8) was used to calibrate and accurately measure ozone concentrations produced by the Pen-ray ozone generator for different setting of the metal shutter.

After the generator stage Teflon tubing is used to carry the generated ozone to the Teflon test chamber. The distance from the Pen-Ray ozone generator to the UV spectrometer/analyzer (Ecosensors) is kept constant and as short as possible to provide accurate measurements of the ozone concentration. The sensing devices were mounted in a teflon chamber with inlet and outlet valves.

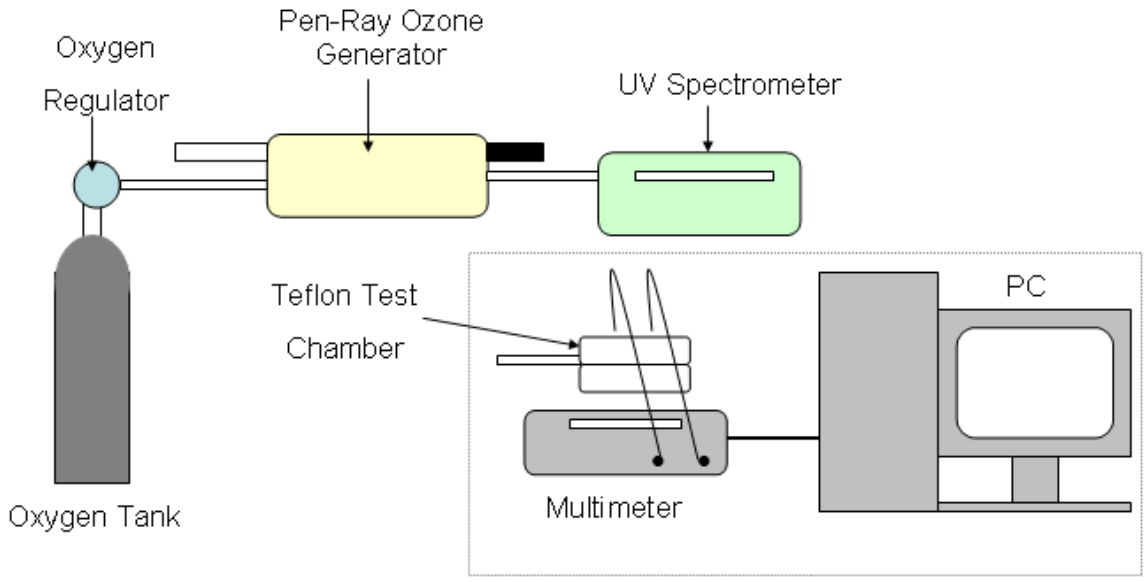

Figure 6.8. Experimental Set- Up

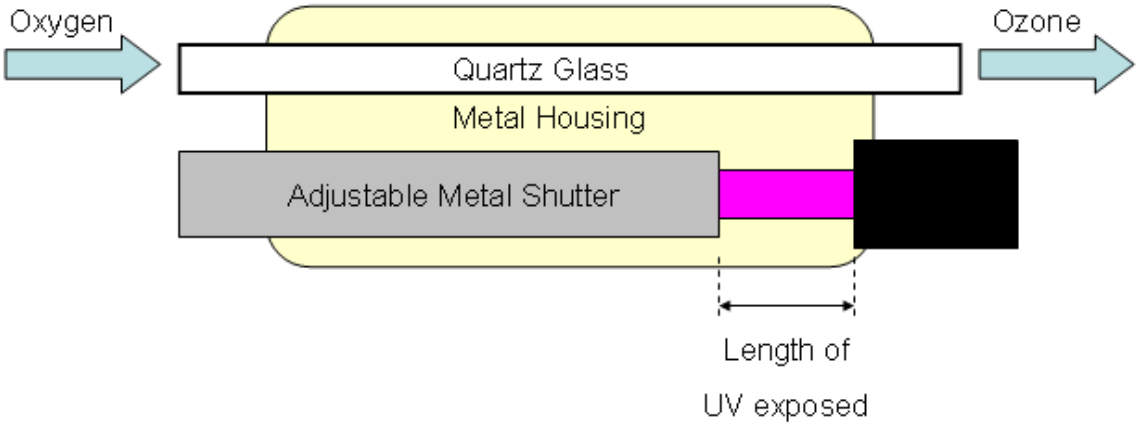

Figure 6.9. Top–View of Pen–Ray Ozone Generator Unit

6.5. Ozone Exposure Procedure

The flow rate of the ozone over the sensor is kept constant at 0.25l/min by an ozone regulator. This is to ensure accurate and consistent measurement values, as increasing the flow rate of the oxygen through the pen–ray ozone generator has the effect of decreasing the concentration of generated ozone. Another factor that must be held constant to ensure accurate readings is the length of the UV lamp exposed to the oxygen passing through the generator. As increasing the length of the exposed UV lamp results in an increase in the concentration of ozone generated (Figure 6.10).

Before measurements are taken, the teflon chamber which houses the fabricated sensor must be flushed for 30 minutes with oxygen, this is to ensure that the sensor reaches a baseline resistance for oxygen. When the sensor reaches equilibrium, the desired length of UV lamp is exposed to the passing oxygen and converted into ozone.

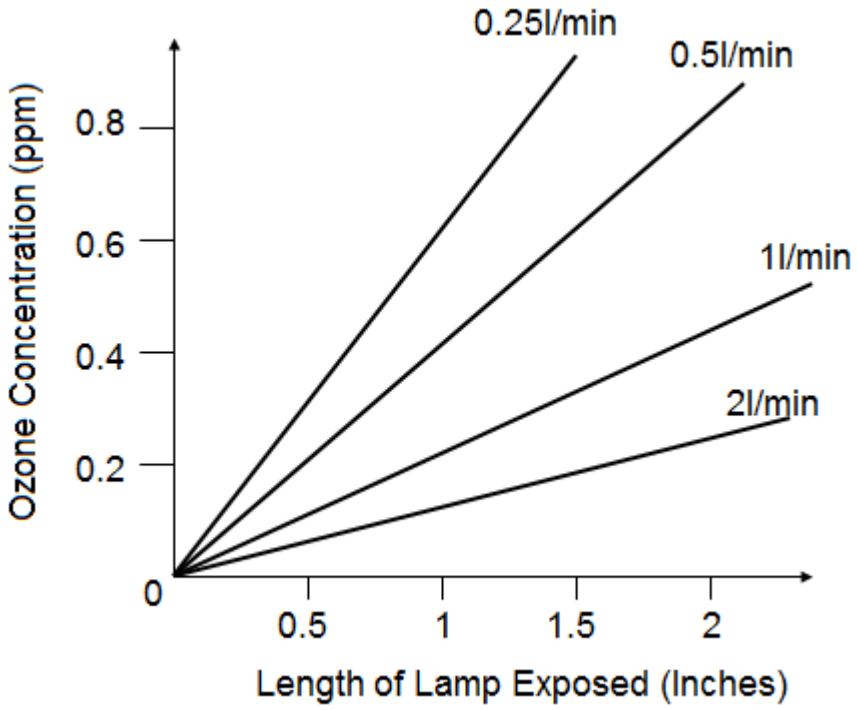

Figure 6.10. Concentration of Ozone Generated (adapted after UVP Pen – Ray Lamps Group)

The generated ozone is then introduced into the teflon chamber and interacts with the metal oxide sensor. The result of this interaction is recorded on a Thurlby multimeter before being sent to the PC for further analysis (Figure 6.8). In this work, measurements were recorded at 10, 20 and 30 second intervals, and the overall exposure time to ozone of the sensor was between 2-8mins.

6.6. UV absorption by Ozone

The principle of operation of UV measurement is based on the absorption of UV light by ozone molecules and subsequent use of photometry to measure reduction of the quanta of light reaching the detector at 254 nm [59]. The degree of reduction depends on the path-length of the UV sample cell, the ozone concentration introduced into the sample cell, and the wavelength of the UV light, as expressed by the Beer-Lambert law shown in Equation 6.1:

$$I = I_0 \exp(-\alpha LC) \qquad \textit{(Eq. 6.1)}$$

where I is the light intensity after absorption by ozone, I_0 is the light intensity at zero ozone concentration, α is the specific ozone molar absorption coefficient, L is the path length and C is the calculated ozone concentration

The air sample containing the target gas is drawn through an optical absorption cell where it is irradiated by a low pressure, cold cathode mercury lamp. A photo-detector, located at the opposite end of the sample cell, measures the reduction in the UV intensity at 254 nm caused by the presence of ozone in the sample cell. To compensate for possible irregularities in output, another photo-detector is used in some instruments to monitor the intensity of the mercury vapour lamp [218].

Although some ozone analyzers measure reference and sample air simultaneously using two absorption cells, most analyzers alternate these measurements, using only one cell. In the first part of the cycle, sample air is passed through a scrubber with manganese dioxide to remove ozone. The scrubbed sample air then enters the sample absorption cell to establish a reference light intensity at zero ozone concentration (I_0). In the second part of the cycle, sample air is redirected to bypass the scrubber and enter the sample cell directly for measurement of the attenuated light intensity (I). The difference is related to the ozone concentration according to the Beer-Lambert law shown above (Eq. 6.1). Thus, ozone in a sample stream can be measured continuously by alternatively measuring the light level at the sample detector, first with ozone removed and then with ozone present [38]. Any ozone analyzer used for routine ambient air monitoring must be calibrated against a suitable ozone primary standard or a secondary standard directly traceable to a primary standard.

6.7. Analysis Techniques

6.7.1. X-ray Diffraction (XRD)

Qualitative XRD was performed using a Philips X'pert PRO Multi-Purpose Diffractometer (MPD) X-ray diffractometer PW3050/60 θ-θ (Philips, Eindhoven, Netherlands) within a scan range of 5 to 70 (º2θ). A step size and scan speed of 0.01 (º2θ) and 0.02 (º2θ/s) respectively was implemented with 10s per step. The CuKα Diffractometer anode was run under a tension of 40kV and a current of 35mA [199]. An X'Celerator strip detector was used to collect the diffracted data. The samples were mounted on glass slides and placed on a Eularian cradle. All samples were aligned at zero (º2θ) in order to prevent sample misalignment [208]. A glancing angle of 3 (º2θ) was applied in order to prevent anomalous data being obtained from the glass slide backing material [208].

Note that in order to detect crystallinity with the XRD technique, a certain size of crystallite is required. The absence of diffraction peaks provides an upper limit of the volume fraction of the crystalline phase. For XRD, the lower limit of detection is approximately a volume fraction of the crystalline phase of 0.001 [219]. This is why XRD data must be considered only in terms of the sensitivity of this method [208].

6.7.2. Scanning Electron Microscopy (SEM)

Electrons rather than light waves as in optical microscopy are used in scanning electron microscopy (SEM) to create high-resolution images. It can be a very useful tool capable of high magnification and good depth of field and can also be utilized in many diverse applications. The wavelength of an electron is much lower than the wavelength of visible light, therefore allowing increased resolution and magnification [220]. The electrons are thermionically emitted from the source cathode (commonly tungsten or lanthanum) at a voltage of approximately 30keV, and accelerated towards an anode. Tungsten is

commonly used due to its low vapour pressure and high melting point allowing it to be heated for electron emission. Electromagnetic optics is used to focus the electron beam (with typical energy of 50 – 500eV). The beam is focused to a spot of approximately 1 – 5 nm using one or two condenser lenses. The beam is deflected in a raster fashion over the sample surface using an objective lens with scanning coils as illustrated in Figure 6.11.

Resolutions of less than 1 nm are possible using this technique. The contrast between areas with different chemical compositions, especially when the average atomic number for the different regions varies can be highlighted by detection of backscattered electrons. An electron backscatter diffraction (EBSD) image can also be formed using these electrons to determine crystallographic structure. There are fewer backscattered electrons emitted and a specific backscattered detector is often used above the sample in a "doughnut" shape with the electron beam travelling through it [220].

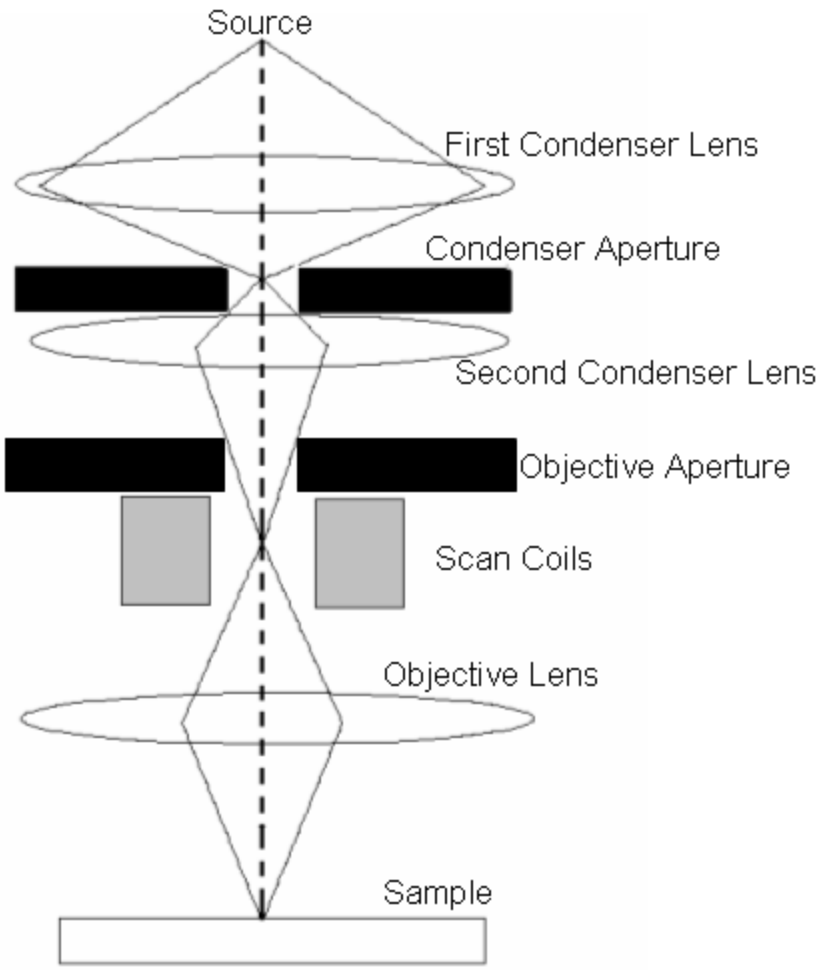

Figure 6.11. Optical Set-Up of an SEM System

The spatial resolution of the SEM depends on the beam spot which depends on the magnetic electron – optical system in use and the interaction volume. The SEM cannot image down to the atomic level and has a resolution of 1-20 nm. This is due to the fact that both the beam size and interaction volume are huge in comparison to the atomic distance of the samples. However, the advantage of SEM is its ability to image a large specimen area and also bulk materials. Surface morphology, topography, composition, and crystallographic information can also be obtained using SEM [220].

6.7.3. X-ray Photoelectron Spectroscopy (XPS)

6.7.3.1. XPS Spectra

XPS spectra are quantified in terms of peak intensities and peak positions. The peak intensities measure how much of a material is present at the surface, while the peak positions indicate the elemental and chemical compositions. Other values such as the Full Width Half Maximum (FWHM) are useful indicators of chemical state changes and physical influences. The broadening of a peak may indicate a change in the number of chemical bonds contributing to a peak shape, a change in the sample condition (x-ray damage) and/or differential charging of the surface (localised differences in the charge state of the surface).

The underlying assumption when quantifying the XPS spectra is that the number of electrons recorded is proportional to the number of atoms in a given state. The basic tool for measuring the number of electrons recorded for an atomic state is the quantification region. The Survey scans illustrate a survey spectrum where the surface is characterised using a quantification table based on values computed from different regions. The primary objectives of the quantification regions are to define the range of energies over which the signal can be attributed to the transition of interest and to specify the type of approximation appropriate for the removal of background signal not belonging to the peak.

6.7.3.2. Comparing XPS Samples

A direct comparison of peak area is not a recommended means of comparing samples for the following reasons. An XPS spectrum is a combination of the number of electrons leaving the sample surface and the ability of the instrumentation to record these electrons; the instrument records not all the electrons emitted from the sample. Further, the efficiency with which emitted electrons are recorded depends on the kinetic energy of the

electrons, which in turn depends on the operating mode of the instrument. As a result, the best way to compare XPS intensities is via the so called percentage atomic concentrations. The key feature of these percentage atomic concentrations is the representation of the intensities as a percentage, that is, the ratio of the intensity to the total intensity of electrons in the measurement. Should the experimental conditions change in anyway between measurements, e.g. the x-ray gunpowder output then peak intensities would change in an absolute sense, but all these being equal and would remain constant in relative terms.

6.7.3.3. The Peak Width Analysis

The peak width, defined as the Full Width Half Maximum (FWHM) ΔE , is a convolution of several contributions:

$$\Delta E = (\Delta E_n^2 + \Delta E_p^2 + \Delta E_a^2)^{1/2} \qquad \textit{(Eq. 6.2)}$$

where ΔE_n is the natural or inherent width of the core level, ΔE_p is the width of the photon source (X-ray line) and ΔE_a the analyser resolution, all expressed as FWHM. Equation 6.2 above assumes that all components have a Gaussian Line shape.

The analyser contribution is the same for all peaks in the spectrum when the analyser is operated in the Constant Analyser Energy (CAE) mode, but varies across the spectrum when the analyser is operated in the Constant Retard Ratio (CRR) mode (since in this case $\Delta E / E$ is a constant).

The inherent line width of a core level, i.e. the range of Kinetic Energy (KE) of the emitted photoelectron, is a direct reflection of uncertainty in the lifetime of the ion state

remaining after photoemission. Thus from the uncertainty principle we obtain the line width (in energy units, eV)

$$\Gamma = h/\tau \qquad \textit{(Eq. 6.3)}$$

with Plank's constant (h) expressed in electronvolt-seconds and the lifetime expressed in seconds. The narrowest core levels have lifetimes between 10^{-14} and 10^{-13} s, whilst the broader core levels have lifetimes close to or even slightly less than 10^{-15} s.

6.7.4. Optical Analysis

In this work a CARY 1E UV-Visible Spectrophotometer was used for the optical measurements of the samples. Figure 6.12 below demonstrates the optical system diagram. The UV-Vis spectrophotometer uses two light sources, a UV lamp (from a deuterium (D_2) source) and visible light (from a tungsten (W) lamp). After bouncing off a mirror (M1), the light beam passes through a slit and hits a diffraction grating which can be rotated allowing for a specific wavelength. At a specific position of the grating, only monochromatic (single wavelength) light successfully passes through a slit (Slit 2). After passing through Slit 2, any remaining unwanted higher orders of diffraction are removed via the filter. The light beam hits the second mirror (M2) before hitting a half mirror (H-M) which splits the beam (half is passed, half reflected). Half of the beam passes through the reference chamber containing only the supporting material on which the sample is deposited. The other half passes through the sample chamber containing the supporting substrate on which the thin sample layer is deposited. Both beams then pass through lenses (Lens 1 and Lens 2) to focus the beams on the detectors (D1 and D2). The intensity of each beam is measured separately; D1 measures the intensity of the reference beam (O_{REF}), while D2 measures the intensity of the Sample beam (O_{SAMP}). After

measurement, the intensities of both beams are compared in order to get an accurate reading for the sample layer and omit that of the supporting material.

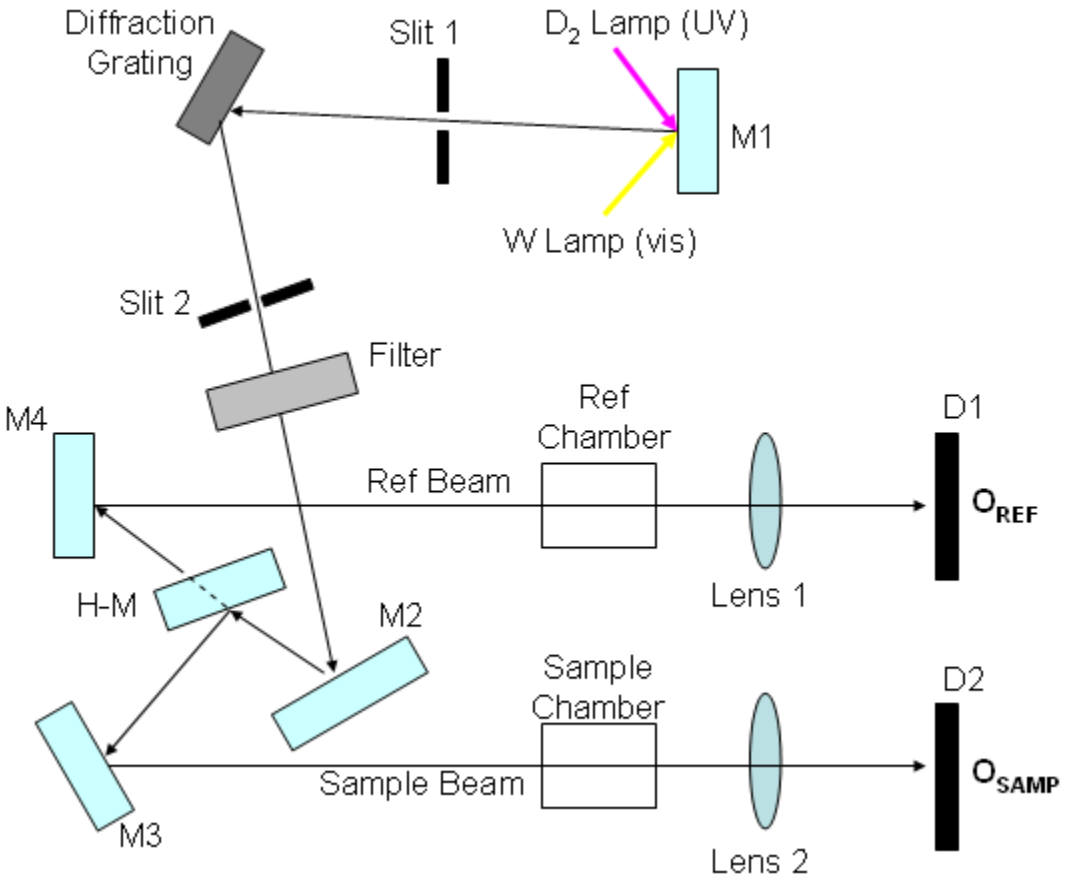

Figure 6.12. Optical System

Chapter 7: Results and Discussions

7.1. Introduction

This chapter details the results obtained from the experimental work undertaken throughout the course of this research. The initial data obtained from the sensors outlines the importance of the various parameters that influence the sensitivity and overall performance of the sensors. This preliminary data acts as a template for other sensors fabricated and optimized in the following work.

The main focus of this research was the design, fabrication and optimisation of room temperature ozone (ppb region) sensing elements. Conductometric gas sensors based on semiconducting metal oxides are one of the most investigated groups of gas sensors. This sensor type has attracted the attention of many users and scientists interested in gas sensing under atmospheric conditions due to the low cost and flexibility associated with their production, simplicity of their use and large number of detectable gases/possible application fields.

The metal oxide sensing layers were prepared using the Vacuum Thermal Evaporation (VTE) technique. The effects of deposition temperature, pressure and layer thickness on the ozone sensing properties were studied and optimised during the fabrication process. Metal oxides were mixed in different composites to improve the sensitivity. SEM

analysis was used to identify and quantify the effects of the deposition parameters on the sensing layer. XPS analysis was used to track the binding energies of the components and also to investigate the levels of contaminants present on the surface of the sensing layer.

Ozone is a strong clean oxidizing agent and is widely used as a disinfectant and deodorizing agent. However, ozone (O_3) has been classified as a dangerous pollutant by regulatory bodies around the world (Chapter 2). Ozone measurement for air quality monitoring and atmospheric research is largely carried out by spectroscopic or electrochemical methods [170]. These techniques are very accurate and sensitive to atmospheric ozone concentrations but require expensive equipment as well as a high level of expertise for correct operation and subsequent data interpretation [183]. As ozone has very low allowable limits of < 100ppb, very high sensitivities and selectivity are required to avoid cross–interference with other oxidizing gases.

Over the past 20 years, a great deal of research has been directed toward the development of small dimensional gas sensors for practical applications ranging from toxic gas detection to manufacturing process monitoring [221]. Such devices should allow continuous monitoring of the concentration of target gases in the environment in a quantitative and selective way [222]. However, many of these efforts have not reached commercial viability because of the problems associated with the sensor fabrication and the technologies applied to gas–sensing systems. With the increasing demand for better gas sensors of higher sensitivity and greater selectivity, intense efforts are being made to find more suitable materials with the required surface and bulk properties for use in gas sensor devices [221].

Gas sensors based on metal oxide semiconductors have been the subject of many extensive investigations, primarily focusing on SnO_2 [221]. Using metal oxides has many advantages, such as simplicity in device structure, low cost of fabrication, robustness in practical applications, and adaptability to a wide variety of reductive and/or oxidative gases [221]. There have been many attempts to utilize thin films for gas sensing applications. However, those attempts have barely been successful due to the physical shape of the thin films, mostly fabricated by dry processing methods, like RF sputtering, not being stable enough at the elevated temperatures required for sensor operation [221].

Most of the current metal oxide ozone gas sensors on the market operate at elevated temperatures (200ºC – 600ºC). The gas detection technique is primarily based on a change in the electrical resistance of the semiconducting metal oxide films.

The sensitivity and selectivity of metal oxide gas sensors is dependent on operating temperature. Qu et al found that when operating the sensor at 200ºC the sensitivity to 100 ppb of ozone was 1.4, while operating at 300ºC the sensitivity of the device increased to 2.5 [146]. There is also the possibility of operating the sensor at two different temperatures to take advantage of the greater sensitivity achiever at lower temperatures (~400ºC) and the faster response times which are achieved at the higher temperatures (~600ºC) [146].

In addition to SnO_2, various other semiconducting metal oxides have been extensively investigated to gain a comprehensive understanding about the gas sensing mechanisms [223]. In2O3 and WO_3 are among the most widely investigated materials for the detection of strongly oxidizing gases, such as O_3 [155, 161, 170, 176, 183].

Room temperature operation is a very desirable characteristic as it not only reduces fabrication and operating costs of the sensor, but also eases implementation into other portable/handheld devices [161], [224].

Niobium oxide has been studied extensively due to its broad range of applications [225]. It is widely used in catalysts, gas sensors, electrochromic devices and optical fibres [226-229]. The detection principle of this material is based on the reversible modulation of the electrical conductance in the presence of oxidizing or reducing gases. Niobium oxide has been especially tested as an oxygen sensor where its conductivity decreases when oxygen partial pressure is increased [227].

7.2. Preliminary Investigations

Thin films of various metal oxides were fabricated (mixed In_2O_3, ZnO and SnO_2, as well as single NbO_2). In the following sections these metal oxides and their mixtures in various concentrations in the form of evaporated thins films were studied in terms of their susceptibility to detect ozone in the low ppb region. Thin film devices consisting of interdigitated electrode structures were fabricated and explored to reveal the effect on electrical properties after exposure to various concentrations of ozone.

A systematic study of a large range of oxides showed that sensitivity of conductivity to the presence of traces of gases in air was a phenomenon common to oxides and not specific to few special cases. However, if the conductivity of the sensing film is too high, then an effect is not expected [230]. Similarly, if the conductivity is too low, then an effect will be difficult to measure [230].

Mixed oxides have emerged as a promising candidate for improving gas detection, such mixed oxide films may benefit from the combination of the best sensing properties of their pure components [231]. The formation of mixed oxides leads to the modification of the electronic structure of the overall film. This includes changes in the bulk as well as in the surface properties. The bulk electronic structure, band gap, Fermi level position and transport properties are altered. In particular, surface properties are expected to be influenced by new boundaries between grains of different chemical composition. It is anticipated that all of these phenomena will contribute advantageously to the gas detection mechanism [231]. The use of mixed oxides in gas detection has been successfully implemented in many cases (Table 3.4).

In this work, In_2O_3 was used as the main oxide in the fabrication of the sensing layer due to its extensive use and success for the detection of oxidizing gases (table 3.4). Indium oxide is a wide band gap (E_g ~ 3.7eV) semiconductor with many applications in both microelectronic and optoelectronic devices.

A lot of research has been undertaken on materials such as In_2O_3, ITO, WO_3, SnO_2 that are appropriate for ozone sensing. However, conventional gas sensors comprising of these materials have best sensing properties at working temperature of more than 200ºC.

Making use of the photoreduction effect provides the opportunity to produce ozone sensors which work without the additional heater element. The scope of this work is to present the ozone sensing properties of vacuum thermal evaporated thin films at room temperature. The following sections focus on the preparation of In_2O_3 based films with different properties, brought about by changing the fabrication parameters such as deposition rate, film thickness and studying their structural, optical and sensing properties.

Gas sensing effects on compositions based on In_2O_3 have been described [232], where large effects on the response of doping with substitutional impurities. The effect of ozone may be generic for oxides: SnO_2 shows large effects at sufficiently low temperatures (~200ºC) [230], though problems of baseline stability were noted at such temperatures. The effect decreases with increasing temperature, to virtually zero at 400ºC.

Other n-type oxides which give resistance increase in the presence of trace levels of ozone are MoO_3, ZnO, WO_3 and In_2O_3 [219].

Zinc oxide (ZnO) is a wide band gap semiconductor, ZnO thin films have been considered for gas sensing because of their sensitivity to a variety of reactive gases [233]. As discussed previously, a general drawback of gas sensors based on semiconducting metal oxides has been the need for an active heating element since they exhibit an optimum working temperature for sensing of ~ 300-500ºC. The gas sensing properties of ZnO have been investigated, it was found that ZnO based films exhibit high sensitivity to oxidizing gases such as O_3 [232].

7.3. Sensing Layer Properties

Thin films of metal oxides were vacuum thermally evaporated on suitably prepared glass slides and alumina substrates containing copper interdigitated electrodes from both tungsten and molybdenum boats at a deposition rate of between 0.1 – 1.5nm/s. The Edwards Coating System contains an Edwards FTM5 quartz crystal to monitor both the film thickness and the rate of deposition on the substrate. The crystal was positioned directly above the evaporation source. The deposited mass on the quartz crystal alters the

natural frequency of vibration of the crystal, thereby enabling it to measure the deposition rate and final thickness of the deposited film.

Thin films of 40–100nm in thickness were fabricated and exposed to ozone concentrations from 50 – 240ppb. Interdigitated electrodes were used to maximise the admittance between two conducting structures in order to exploit the ozone-induced changes in the electrical properties of the material deposited on top of them.

7.4. 100nm Sensing Layer of 90%In_2O_3:5%ZnO:5%SnO_2

7.4.1. Deposition Rate of 0.1 - 0.3nm/s

Thin films of approximately 100nm consisting of In_2O_3:ZnO:SnO_2, and deposited at a rate of 0.1 – 0.3 nm/s do not respond to ozone levels 120-240ppb. Slow deposition rates do not favour the formation of an oxide layer, which may be used as a working/reliable gas sensor. This may be due to the fact that slow deposition rates allow the evaporating material to interact with impurities, which may be present in the vacuum chamber and hence contaminate the sample. Another reason for the poor response of these sensors is that the resistance of slowly evaporated thin films is much larger than that of films evaporated at a higher deposition rate. As a result there may not be many free electrodes in the film with which the ozone gas can react with in order to produce sufficient changes in the electrical properties.

7.4.2. Deposition Rate of 0.6 - 0.8nm/s

The deposition rate was then increased to 0.6 – 0.8nm/s in an attempt to show sensitivity to ozone in the ppb region while operating the sensor at room temperature. The resulting response graph is shown in Figure 7.1. From this graph it can be seen that the sensors respond well to 120ppb and 240 ppb of ozone.

The ozone is introduced into the chamber at time $t = 330s$. The response time of the sensor cannot be accurately calculated from Figure 7.1 as the sensor is not very stable, however it is estimated that the response time is $T_{RES(90)} = 300s$. This is a relatively slow response time when compared to response time of approximately 60 seconds reported by City Technology, however this sensor was operated at elevated temperatures which has been known to increase the response time of the sensing materials. From Figure 7.1, below $T_{REC(90)}$ cannot be measured as the sensor does not return to a stable baseline which is required for this calculation.

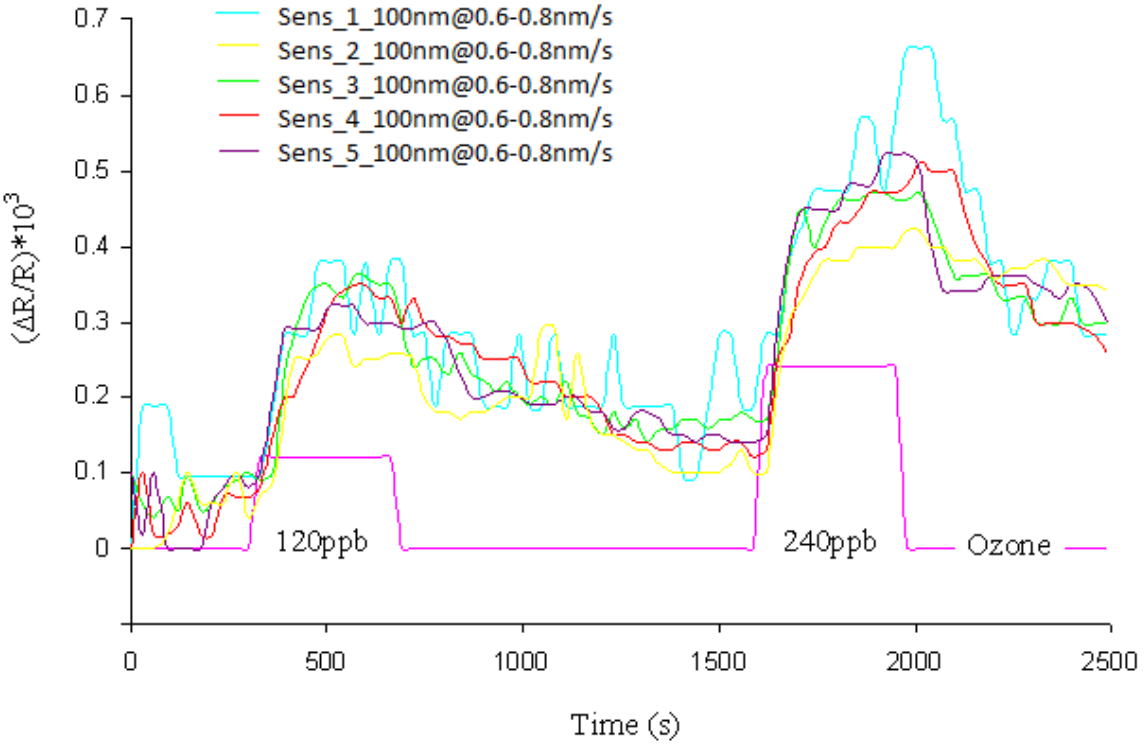

Figure 7.1. Response of 100nm of $90In_2O_3$:5ZnO:$5SnO_2$ deposited at a rate of 0.6nm/s to 120 and 240ppb

7.4.3. Deposition Rate of 1.1 - 1.4nm/s

Increasing the deposition rate further to 1.1 – 1.4 nm/s results in an increase in response as can be seen from Figure 7.2. There still exists the problem of the sensor failing to return to baseline resistance after the removal of ozone from the chamber. The response time was estimated to be $T_{RES(90)} = 330s$.

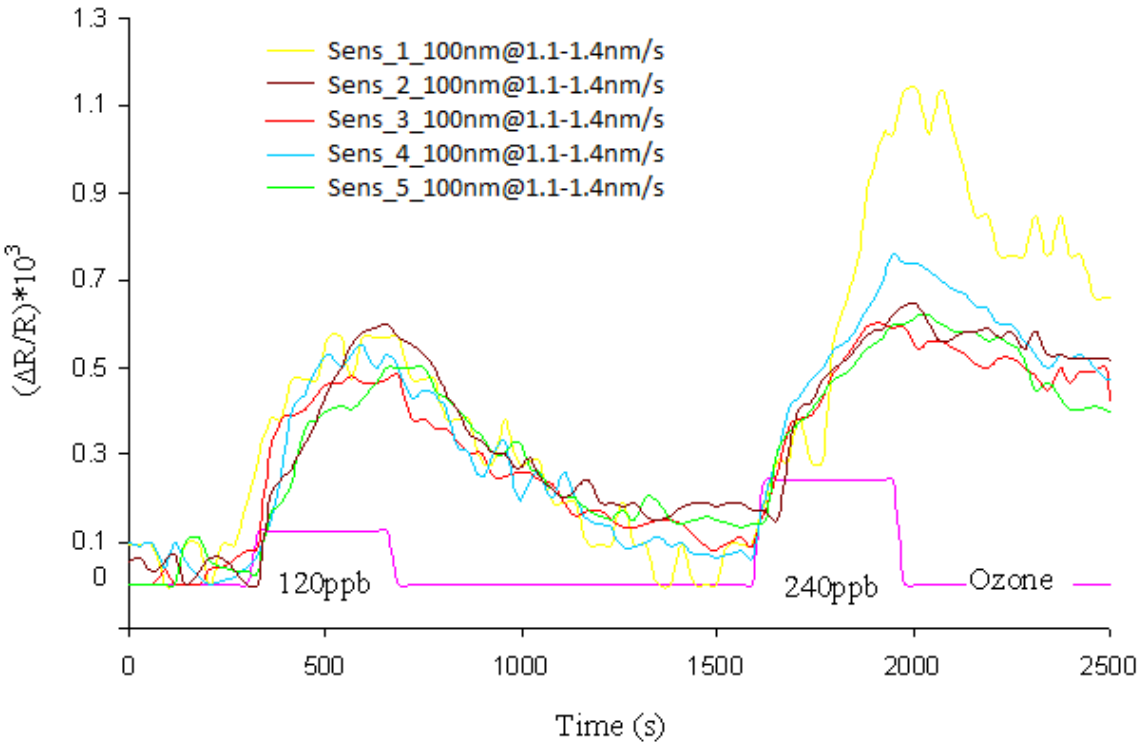

Figure 7.2. Response of 100nm of $90In_2O_3$:5ZnO:$5SnO_2$ deposited at a rate of 1.1-1.4nm/s to 120 and 240ppb

As can be seen from Figure 7.3, increasing the deposition rate for the 100nm sensing layer has the effect of increasing the response of the sensor on exposure to 120 and 240ppb of ozone. The influence of film thickness on the gas response has been shown to depend on the nature of the gas under investigation (oxidizing or reducing) [234]. The

effect of sensing layer thickness was most pronounced for oxidizing gases. Increasing the thickness of the sensing layer had the effect of greatly reducing the response of the sensor to the oxidizing gas [234]. Both greater grain size and decreased gas permeability of the film explain this drop in gas response. In general, the conductivity of semiconducting oxides are closely linked to their deviation from stoichiometry. Due to high activity, ozone decomposition occurs on the top layer of the In_2O_3 based film. Therefore, for more effective detection of ozone (and other oxidizing gases) thinner films should be used [234].

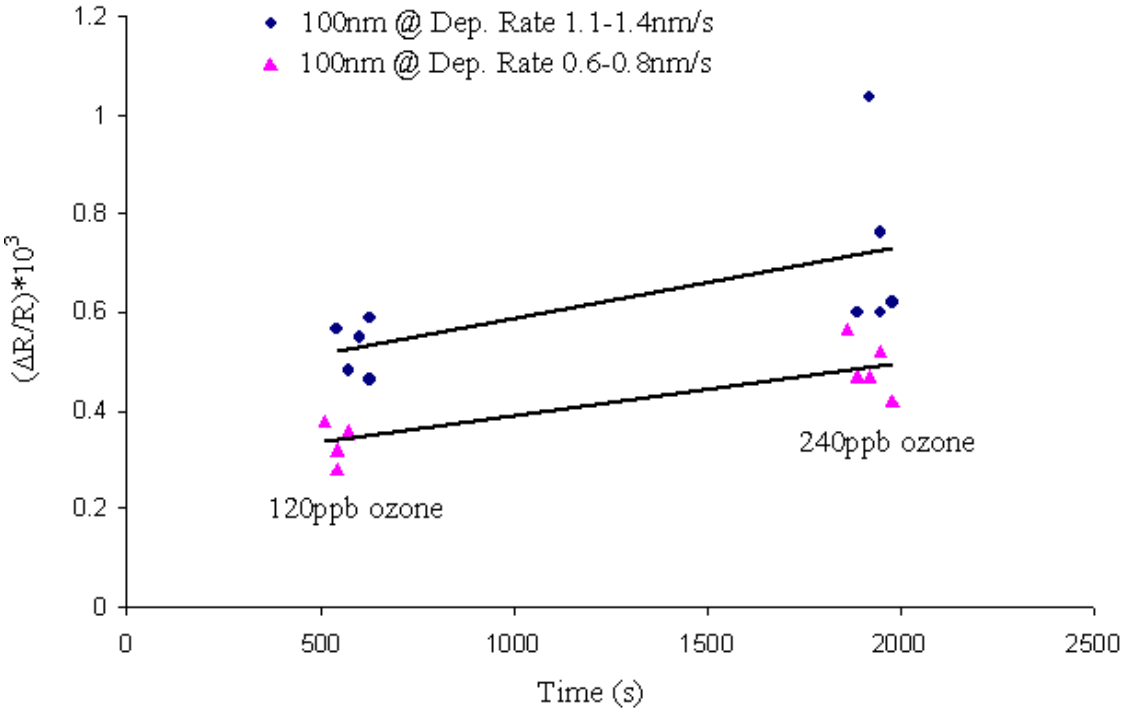

Figure 7.3. Comparison of maximum responses of 100nm sensing layer at deposition rates of 0.6nm-1.4nm/s

As discussed in previous chapters (see Chapter 4, section 4.5) thin films are best suited to the detection of oxidizing gases. Therefore in an attempt to increase the sensitivity of the device the thickness of the sensing layer was reduced.

The devices above, consisting of a sensing layer of 100nm do not show adequate sensitivity or response to ozone concentrations down to 50ppb.

From Figure 7.4 below, it can be seen that film thickness is inversely proportional to film resistance. Film thickness can be easily controlled by either evaporating a weighted amount of material or by simply terminating the evaporation process when the desired thickness is reached.

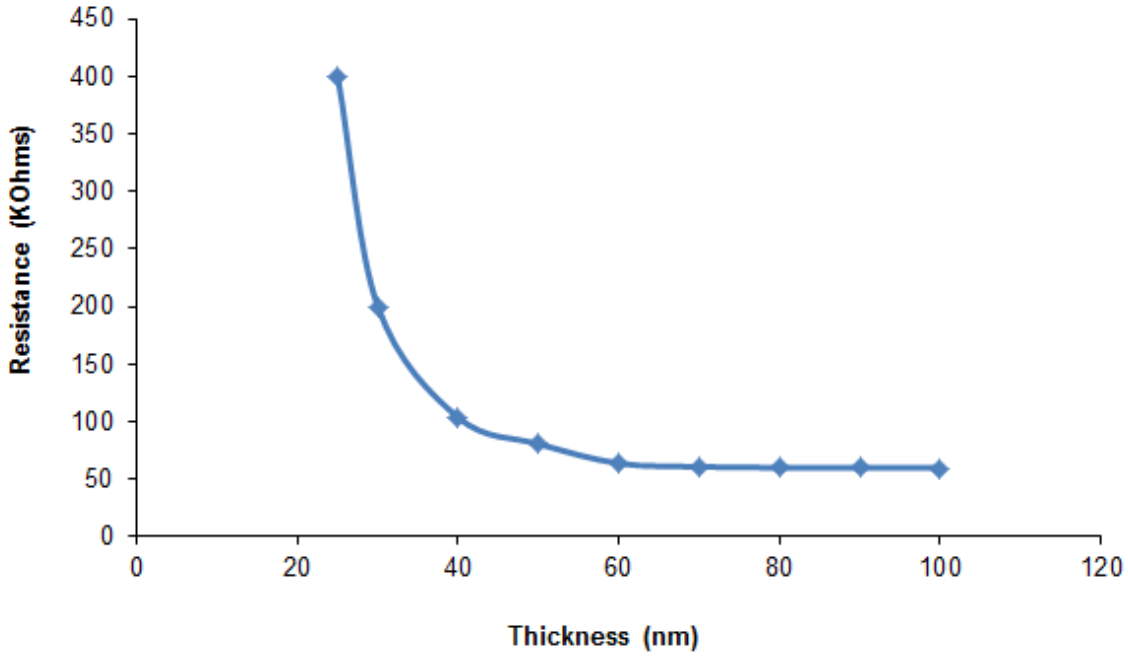

Figure 7.4. Resistance Vs Thickness

Increasing the deposition rate has the effect of decreasing the resistance of the thin oxide film (40nm). Controlling the evaporation rate is a much more complex task than thickness control as it requires the constant and real time adjustment of the source (boat) temperature. The emission of the source material does not remain constant throughout the

deposition process. This is due to variations in the effective source area and variation in the degree of heat transfer between the evaporant and its support material [162].

7.5. 40nm Sensing Layer of 90%In_2O_3:5%ZnO:5%SnO_2

7.5.1. Deposition Rate of 0.1-0.3nm/s

From Figure 7.5 below, it can be seen that the sensor response/resistance does not return to a stable resistance after ozone has been flushed from the chamber, therefore it is impossible for such a device to accurately or reliably measure ozone concentrations.

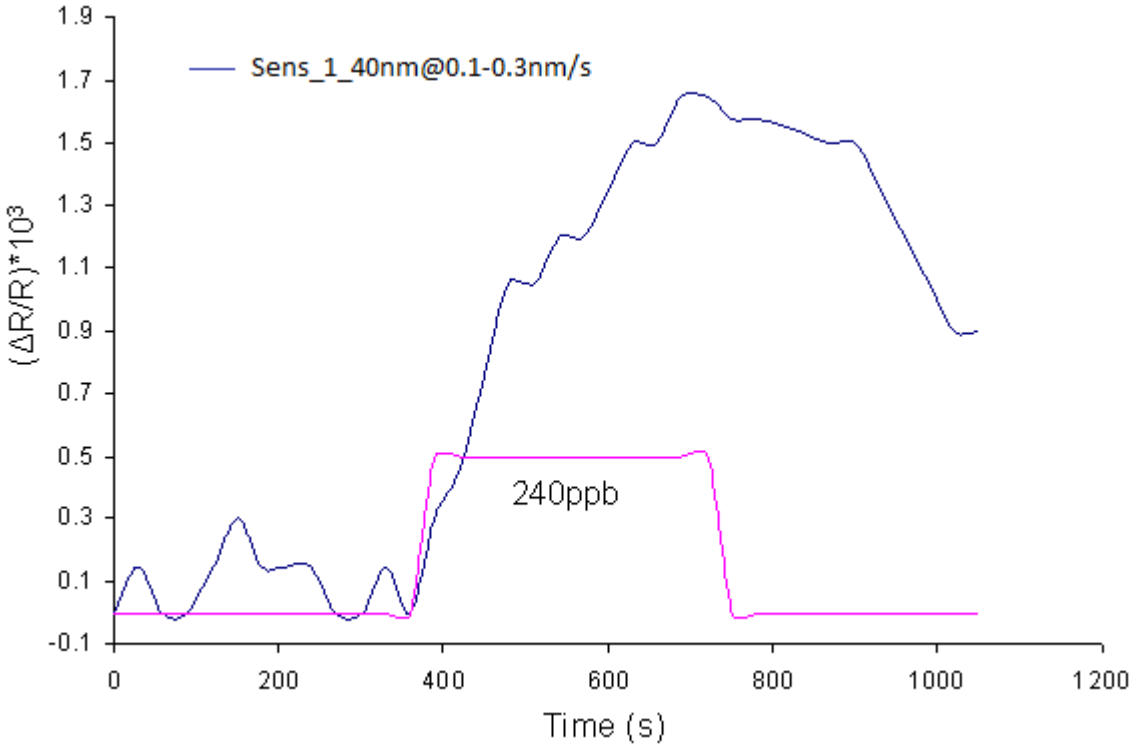

Figure 7.5 Response of 40nm of 90In_2O_3:5ZnO:5SnO_2 deposited at a rate of 0.1-0.3nm/s to 240ppb

In this case the recovery time cannot be estimated from the graph, however, it is possible to calculate the response time of the sensor as illustrated in Chapter 4. It can be deduced that $T_{RES(90)} = 240s$.

Despite the fact that this device cannot be used as an ozone sensor it shows considerable response to relatively low ozone concentrations. It should be noted that holding all fabrication parameters constant and varying the layer thickness has led to the increase in response.

From the SEM image below (Figure 7.6) it is important to note the non-uniformity of the sensing layer surface as well as the tightly compact nature of the structure. Compact sensing layers do not aid the sensing characteristics of metal oxide thin films. It has been shown that film thickness, grain size and porosity or gas-permeability are the major factors which effect the performance of the metal oxide sensing device [234].

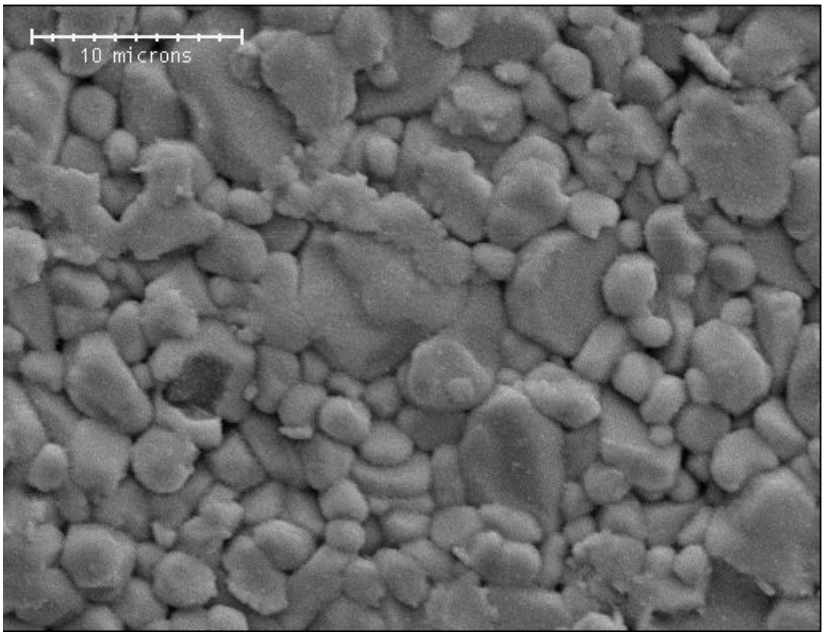

Figure 7.6. SEM image of the surface of sensing layer deposited at a rate of 0.1 – 0.3nm/s

Particles can be seen as being in the 500nm - 5μm range. Particles are tightly packed together with many particles ~ 5μm range. This SEM image will be compared to future results to show the effects of particle size and porosity has on the performance of the sensing layer.

7.5.2. Deposition Rate of 0.6-0.8nm/s

Increasing the deposition rate of the metal oxide sensing layer leads to a significant increase in the overall sensor performance. The response and recovery times of the this device to 240ppb of ozone are calculated from Figure 7.7, where $T_{RES(90)} = 60s$ and $T_{REC(90)} = 180s$. The difference in the response and recovery times observed ($T_{REC(90)}>T_{RES(90)}$) is typical of gas sensing mechanisms controlled by the adsorption/desorption processes [234].

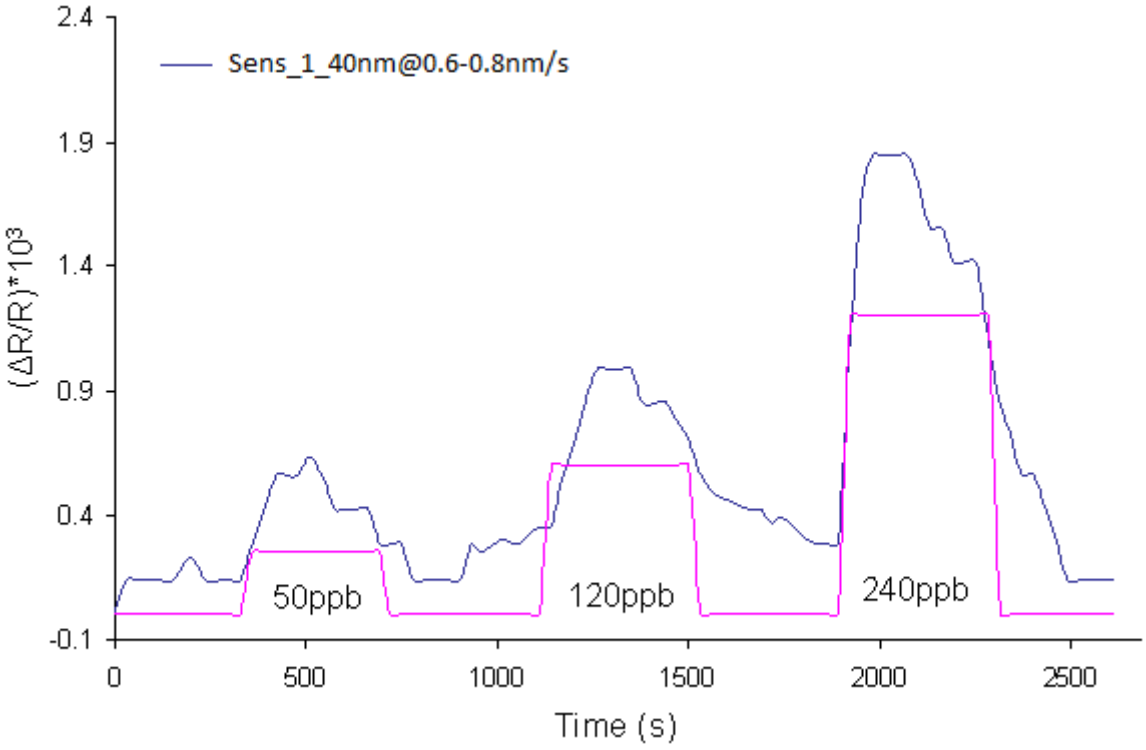

Figure 7.7. Response of 40nm of 90In_2O_3:5ZnO:5SnO_2 deposited at a rate of 0.6-0.8nm/s to 50, 120 and 240ppb

On comparison to previous results it can be deduced that these characteristics represent a large improvement on the 270second response time found for the previously fabricated devices. The recovery time $T_{REC(90)} = 180s$ is an extremely important factor as the

previous samples failed to return to a stable baseline resistance. This enables this sensor to be considered as a viable and reliable ozone sensor. The response times of these sensors are comparable to that found in the literature [235] for similar room temperature oxide based ozone sensors.

Sensing devices fabricated under these conditions also show a measurable and repeatable response to ozone concentrations as low as 50ppb (Figure 7.8) which is of particular significance for the protection of human health as discussed in Chapter 3.

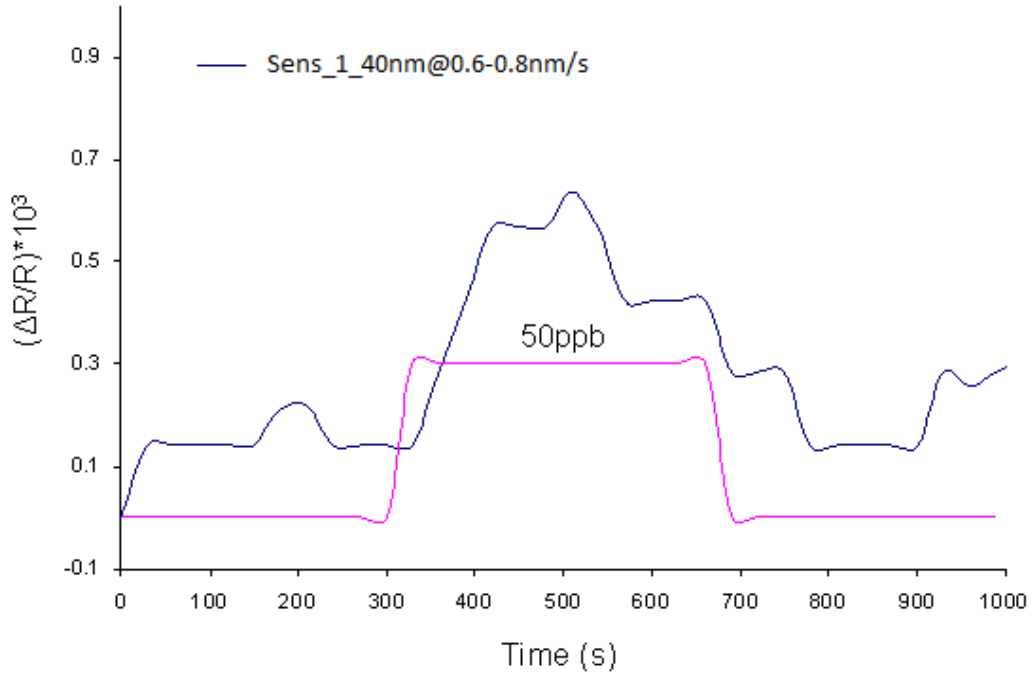

Figure 7.8 Response of 40nm of 90In_2O_3:5ZnO:5SnO_2 deposited at a rate of 0.6nm/s 50ppb

Shown in Figure 7.9 are the response curves of five sensors fabricated under similar conditions at different times, from the graph it can be seen that the sensing device is repeatable and has similar response and recovery times as well as similar response to the various ozone concentrations, it can be seen that there are a couple of outliers in the samples fabricated, this may be due to the time at which they were fabricated, which may

be explained by slight variations in the deposition parameters (such as layer thickness, deposition rate, humidity, etc.).

Figure 7.10 below gives a comparison of the different sensing devices and the response to various ozone concentrations. Also included in Figure 7.10 is an average response taken over all samples.

From the SEM image below (Figure 7.11) it is important to note the non-uniformity of the sensing layer surface as well as the porous nature of the structure. Particles are in range of 500nm - 5µm.

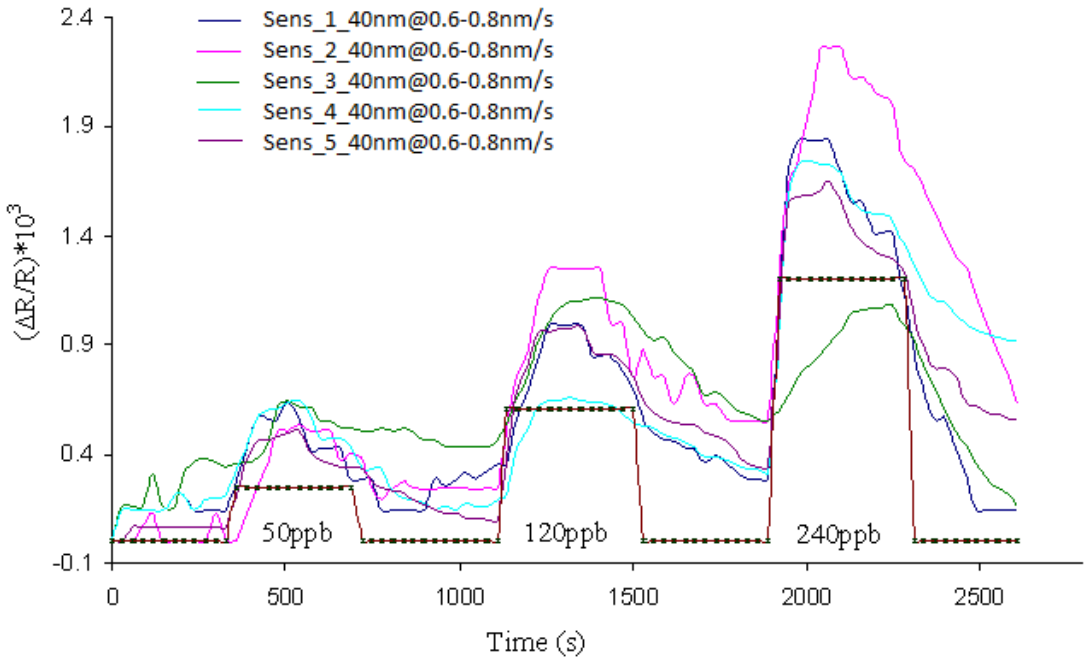

Figure 7.9 Repeatable response of 40nm of $90In_2O_3:5ZnO:5SnO_2$ deposited at a rate of 0.6-0.8nm/s to 50, 120 and 240ppb

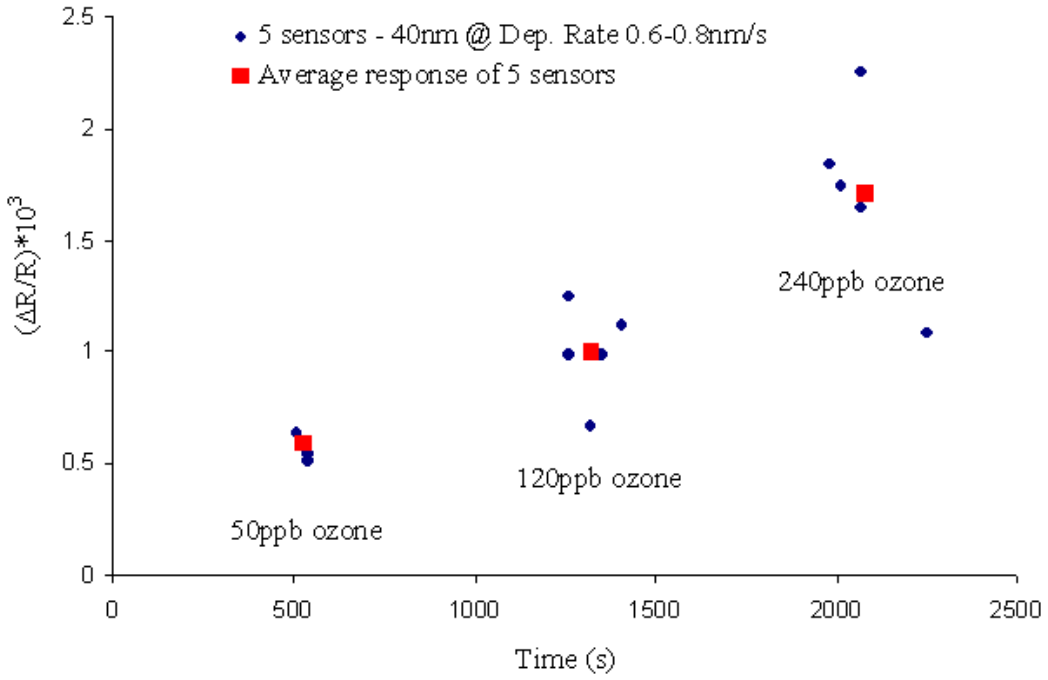

Figure 7.10. Comparison of repeatable response of 40nm of $90In_2O_3:5ZnO:5SnO_2$ deposited at a rate of 0.6-0.8nm/s to 50, 120 and 240ppb and average response

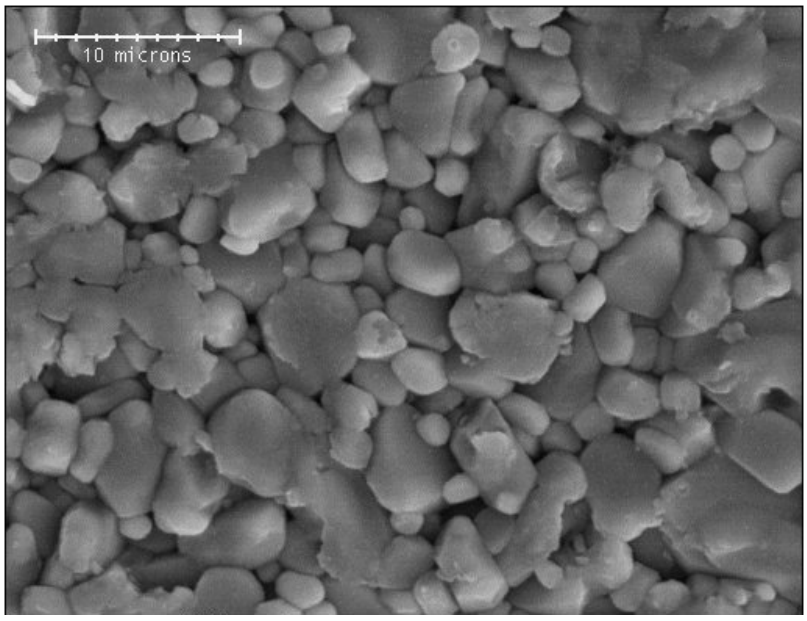

Figure 7.11. SEM image of the surface of sensing layer deposited at a rate of 0.6 – 0.8nm/s

7.5.3. Deposition Rate of 1.1-1.4 nm/s

As discussed earlier, holding all fabrication parameters constant while increasing the deposition rate of the source material yields a significant increase in the response of the sensor to 50, 120 and 240ppb of ozone [234]. Figure 7.12 illustrates this point showing a comparison of the average measured response for a 0.3 - 0.6nm/s and 1.1 - 1.4nm/s deposition rates.

Despite this significant increase in the sensor response the overall sensor performance suffers, in particular the recovery of the sensor to a stable baseline as shown in Figure 7.13. It is evident that increasing the deposition rate of the sensing layer leads to a significant increase in the response of the sensing device.

Figure 7.14 shows a comparison of the various sensors fabricated under constant fabrication parameters. This graph is adjusted to take into account the fact that these sensors fail to return to a stable or constant baseline.

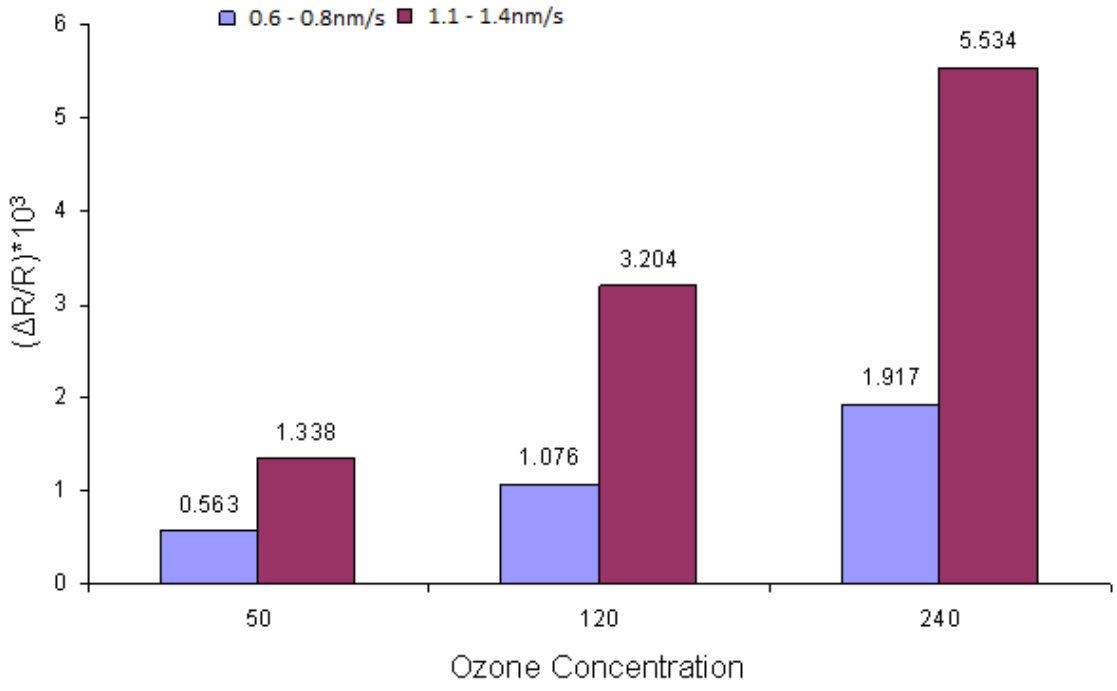

Figure 7.12. Response comparison of 0.6nm/s and 1.1-1.4nm/s

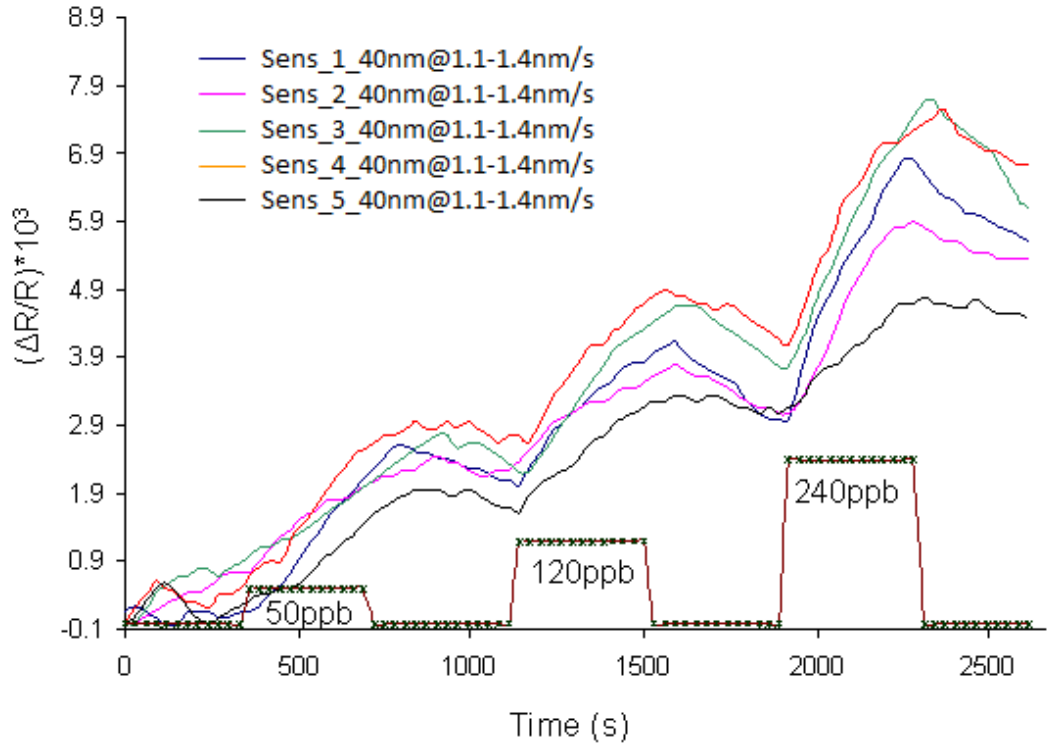

Figure 7.13. Repeatable response of 40nm of $90In_2O_3$:5ZnO:$5SnO_2$ deposited at a rate of 1.1-1.4nm/s to 50, 120 and 240ppb

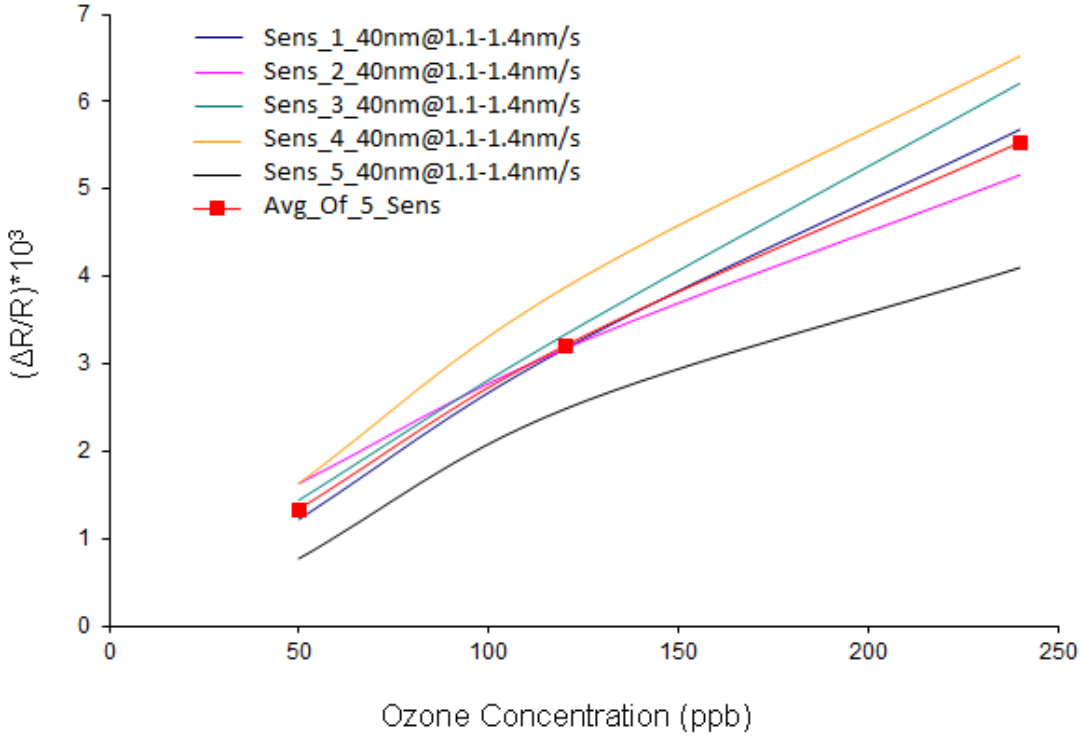

Figure 7.14. Comparison of repeatable response of 40nm of $90In_2O_3:5ZnO:5SnO_2$ deposited at a rate of 1.1-1.4nm/s to 50, 120 and 240ppb and average response

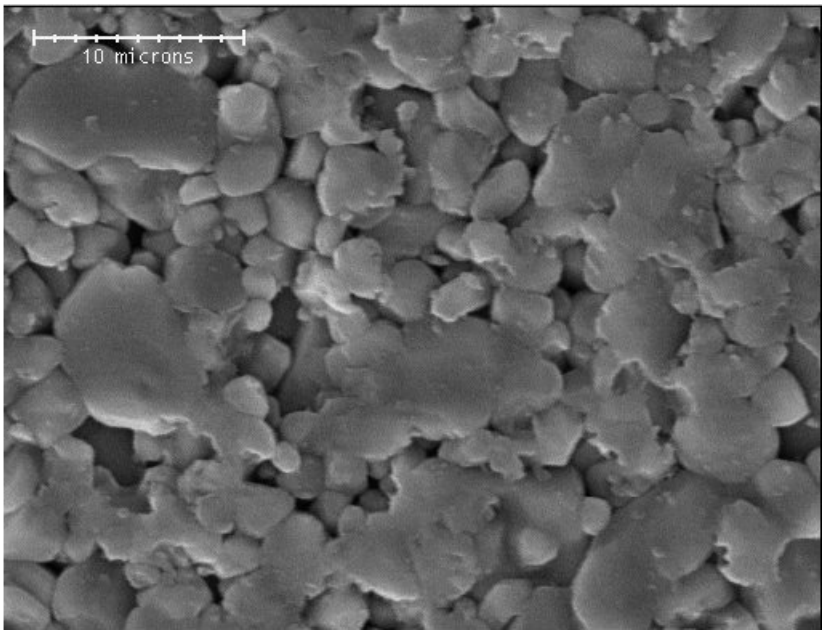

Figure 7.15. SEM image of the surface of sensing layer deposited at a rate of 1.1 – 1.4nm/s

From Figure 7.15 it is important to note the non-uniformity of the sensing layer surface as well as the porous nature of the structure. Particles are in range of 500nm - 10μm. This SEM image is compared to previous SEM images of thin oxide film layers deposited at different deposition rates to show the effect on particle size and porosity, which in turn affects the sensor response.

7.6. Effect of Fabrication Parameters on Sensor Response

Figure 7.16 shows the effect of thickness and deposition rate on the overall response of the ozone sensor to 240ppb ozone. By obtaining a surface plot of layer thickness Vs deposition rate Vs response, the interactions between deposition parameters are observed.

It can be seen that in order to obtain good sensitivity measurements both the deposition rate and the layer thickness must be controlled.

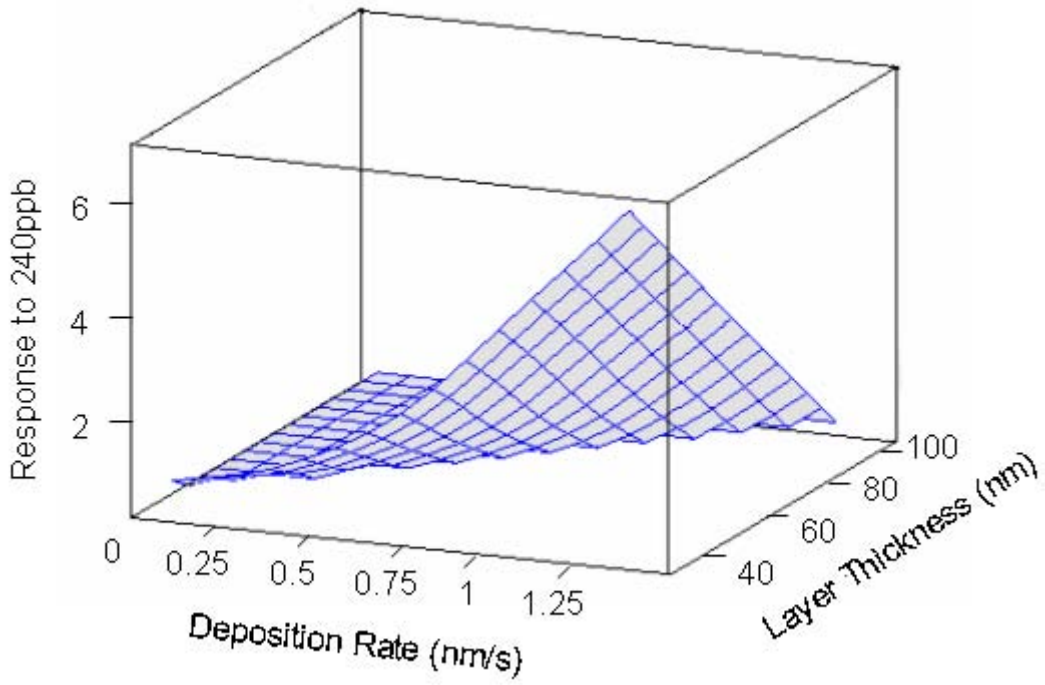

Figure 7.16 Surface Plot of Deposition Rate and Layer Thickness against the Response to 240ppb of Ozone

High deposition rate combined with relatively thin sensing layer yields the highest sensor response to 240ppb of ozone.

7.7. SEM Analysis

To understand the nature of sensing layer, the surfaces of the sensing layers were examined with Scanning Electron Microscope (SEM).

Figures 7.17 below shows the SEM images with 3000x magnification of (a) 0.1-0.3nm/s, (b) 0.6 – 0.8nm/s and (c) 1.1-1.4nm/s.

As can be seen from these images the surface of the sensing layers are non-uniform with particles of various sizes.

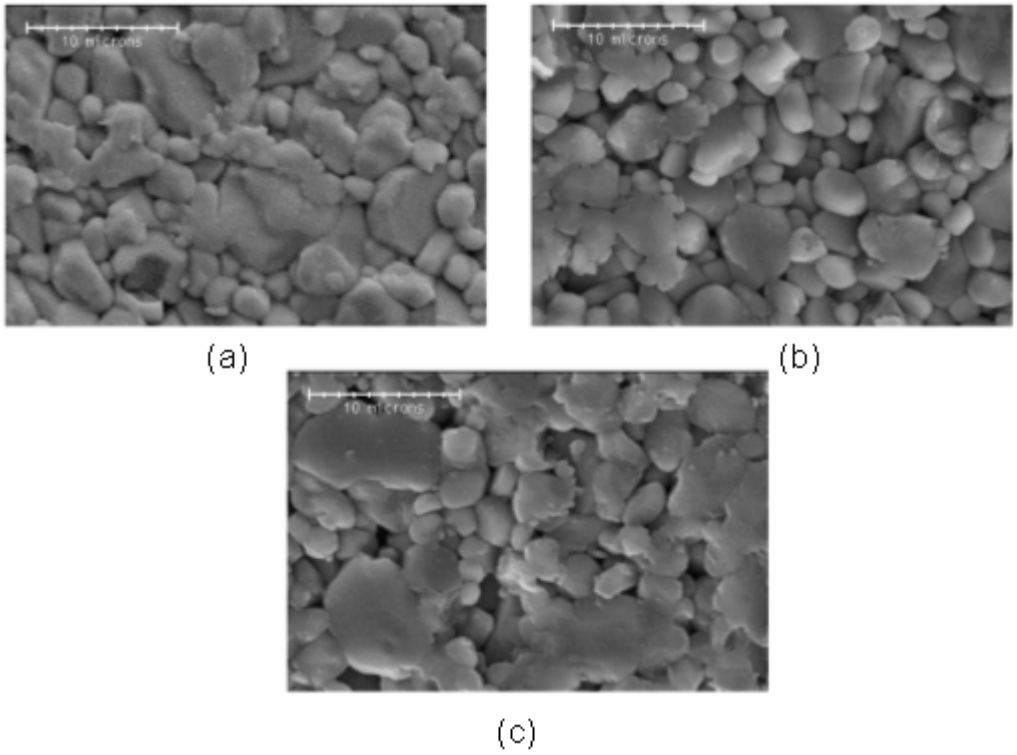

Figure 7.17 SEM image of sensing layers at various deposition rates (a) 0.1-0.3nm/s, (b) 0.6-0.8nm/s and (c) 1.1-1.4nm/s

This high level of structural defects is believed to enhance the sensing capabilities of the devices. Another important characteristic from the SEM images is the varying degrees of porosity observed from the three different sensing layers. Figure 7.17(a) is the least porous of the samples while Figure 7.17(b and c) show much greater levels of porosity. Figure 7.17(b) is also the most uniform of the structures and is seen to have the smallest particle size which is known to have a significant effect on the performance of the sensing element.

As cab be seen from Figure 7.12 there is a significant increase in sensitivity when comparing sensing layers in 7.17(b) and 7.17(c). This increase is due to the highly porous and non-uniform structure of the sensing layer.

7.8. Varying the composition of the sensing material

Using the fabrication processes and techniques outlined in previous section it was found that slight variations in the molar percentages of the source materials can have a significant effect on the performance of the device. The following sections outline the mol. % investigated in this work.

The mol. % in the source material differs from the % mass concentration found on the surface of the sensing layer after the fabrication process. XPS analysis is used to provide an insight into the concentrations of materials found on the surface of the layers.

7.8.1. Source Material 90%In_2O_3:3%ZnO:7%SnO_2

The effect of increasing the mol. % of SnO_2 in the source material from 5% to 7%, while simultaneously decreasing the mol. % of ZnO in the source material from 5% to 3% has the following effect on the overall performance of the sensor.

Figure 7.18 shows the response of the 40nm thick 90%In2O3:3%ZnO:7%SnO2 sensing layer deposited at a rate 0.6 – 0.8nm/s.

The device shows little response to 50ppb of ozone but shows a measurable response to 120ppb and 240ppb ozone. The sensor also shows relatively good response and recovery times. Comparing the performance of this sensor with that of 90%In2O3:5%ZnO:5%SnO2 previously investigated shows that there is a significant decrease in sensor response to the various ozone concentrations.

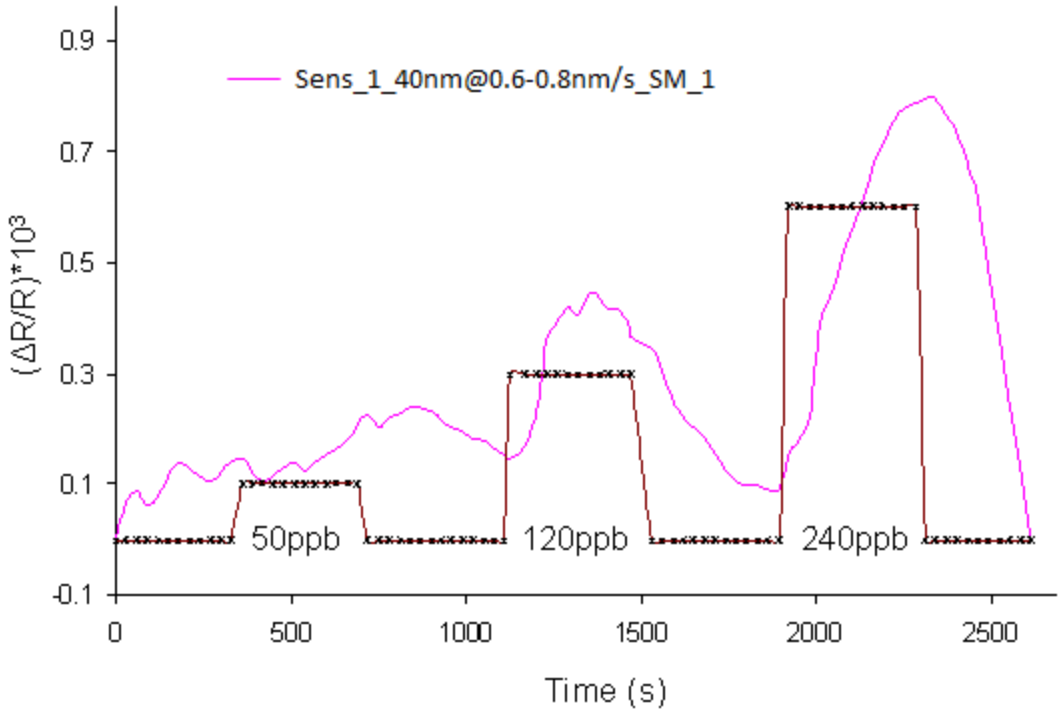

Figure 7.18 Response of 40nm of 90In_2O_3:3ZnO:7SnO_2 deposited at a rate of 0.6-0.8nm/s to 50, 120 and 240ppb

The response and recovery times of the this device to 240ppb of ozone are calculated from Figure 7.18 below, where $T_{RES(90)} = 250s$ and $T_{REC(90)} = 200s$. These times are significant increases when compared with the 90%In2O3:5%ZnO:5%SnO2 sample particularly for the response time which shows an increase from 60s to 250s (Figure 7.26).

Figure 7.19 below shows the response of five sensors fabricated under constant conditions. From this figure it can be seen that the sensing device is repeatable with similar response and recovery times as well as similar response to the various ozone concentrations over the five separate samples.

From Figure 7.19 and Figure 7.20 it can be seen that there are some outliers in the samples, this may be attributed to a number of factors such as slight differences in layer thickness, deposition rates and vacuum pressure during the deposition process.

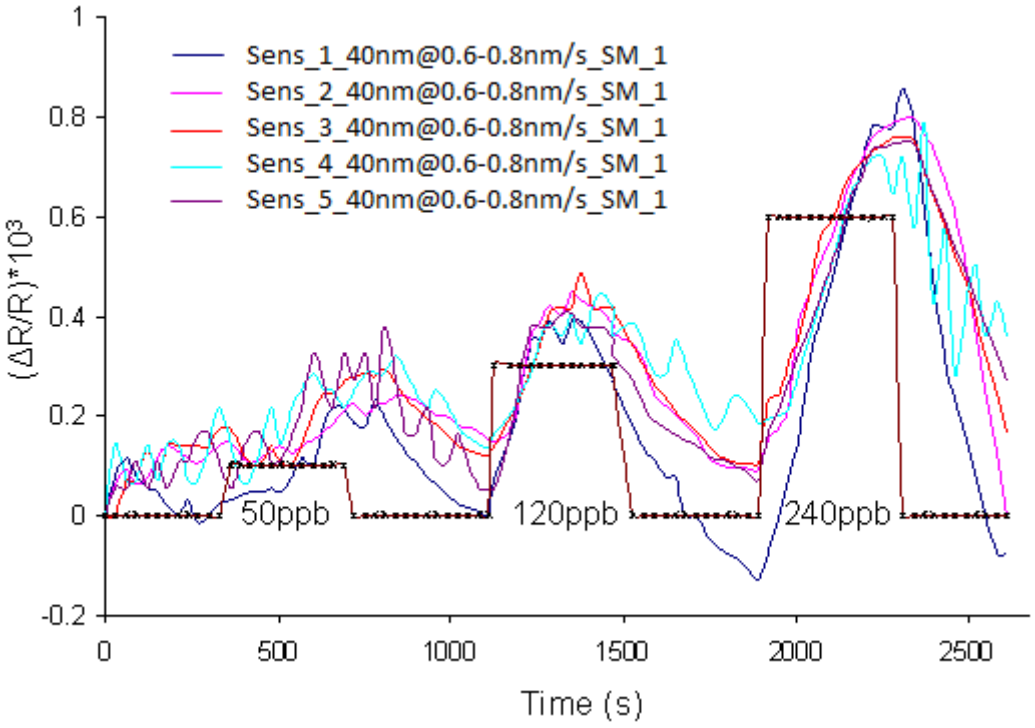

Figure 7.19 Repeatable response of 40nm of $90In_2O_3:3ZnO:7SnO_2$ deposited at a rate of 0.6-0.8nm/s to 50, 120 and 240ppb

Figure 7.20 gives a comparison of the different sensing devices fabricated and the response to various ozone concentrations. Also included is an average response taken over all samples.

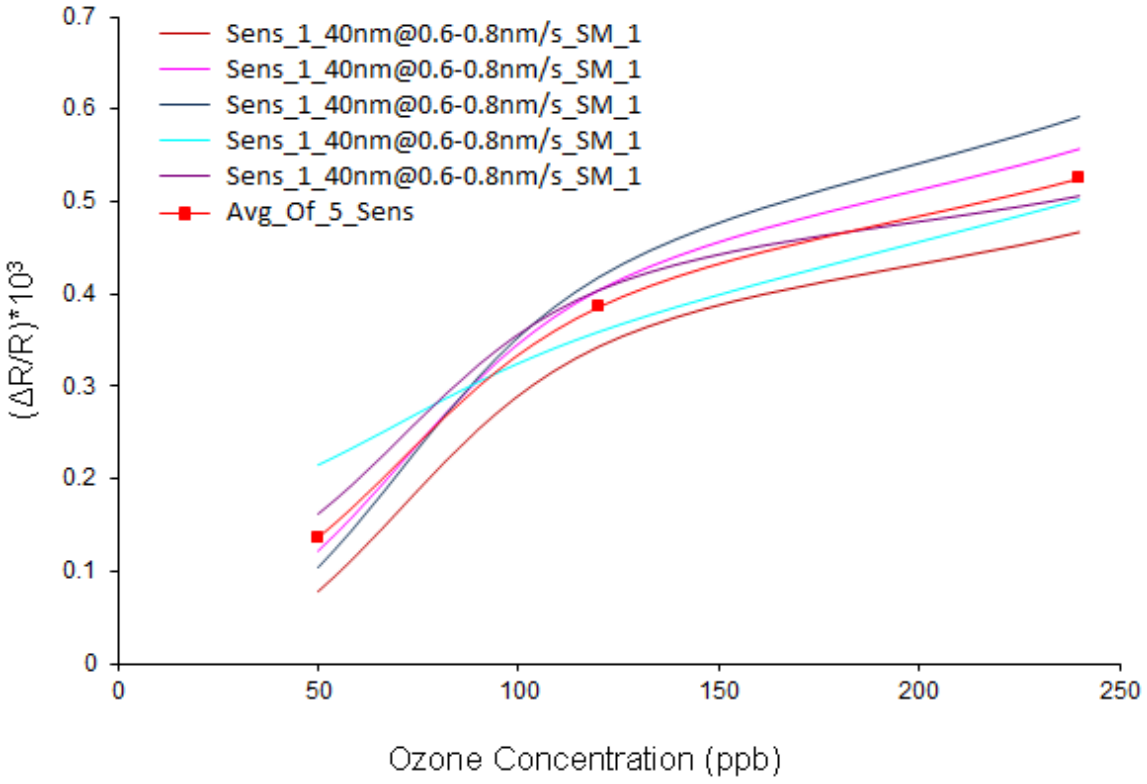

Figure 7.20 Comparison of repeatable response of 40nm of $90In_2O_3$:3ZnO:$7SnO_2$ deposited at a rate of 0.6-0.8nm/s to 50, 120 and 240ppb and average response

7.8.2. Source Material 90%In_2O_3:7%ZnO:3%SnO_2

Figure 7.21 shows the response of the 40nm thick 90%In2O3:7%ZnO:3%SnO2 sensing layer deposited at a rate 0.6 – 0.8nm/s.

The device shows a measurable response to 50ppb, 120ppb and 240ppb of ozone. The sensor also shows relatively good response and recovery times when compared to previous samples (Figure 7.26). The response and recovery times of the this device to 240ppb of ozone are calculated from Figure 7.21 below, where $T_{RES(90)} = 120s$ and $T_{REC(90)} = 140s$. The performance of this sensing device compared to that of the 90%In2O3:5%ZnO:5%SnO2 previously investigated reveal comparable results.

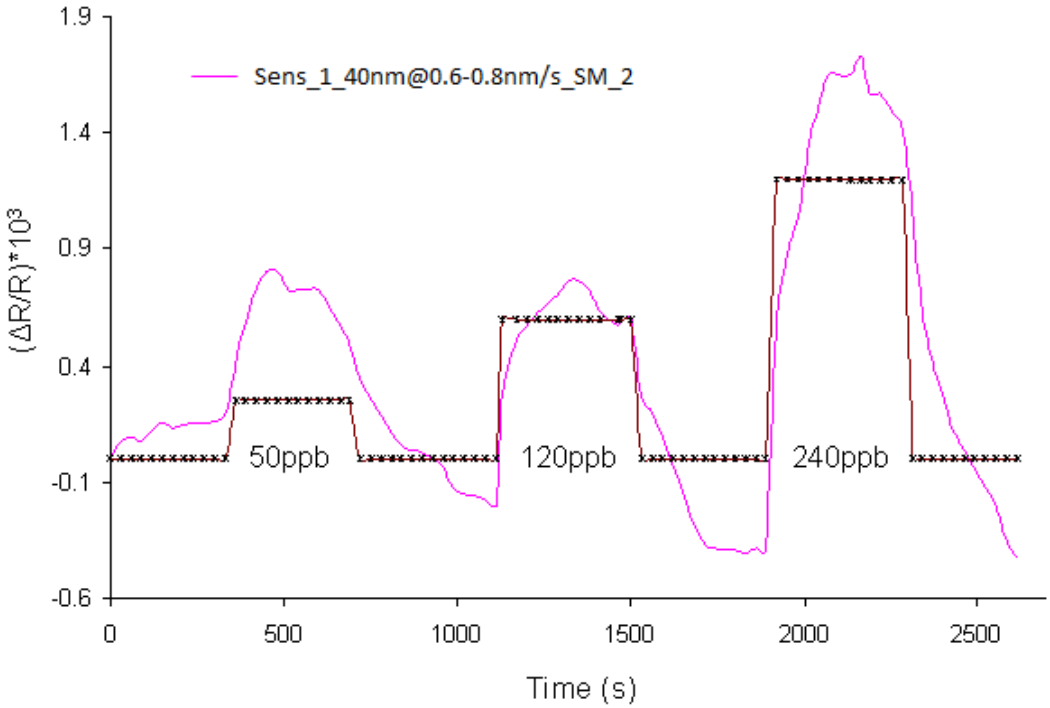

Figure 7.21 Response of 40nm of 90In_2O_3:7ZnO:3SnO_2 deposited at a rate of 0.6 - 0.8nm/s to 50, 120 and 240ppb

However on comparing to 90%In2O3:3%ZnO:7%SnO2 results show that there is a significant increase in sensor response for increasing the mol. % of ZnO while decreasing the mol. % of SnO_2 present in the source material.

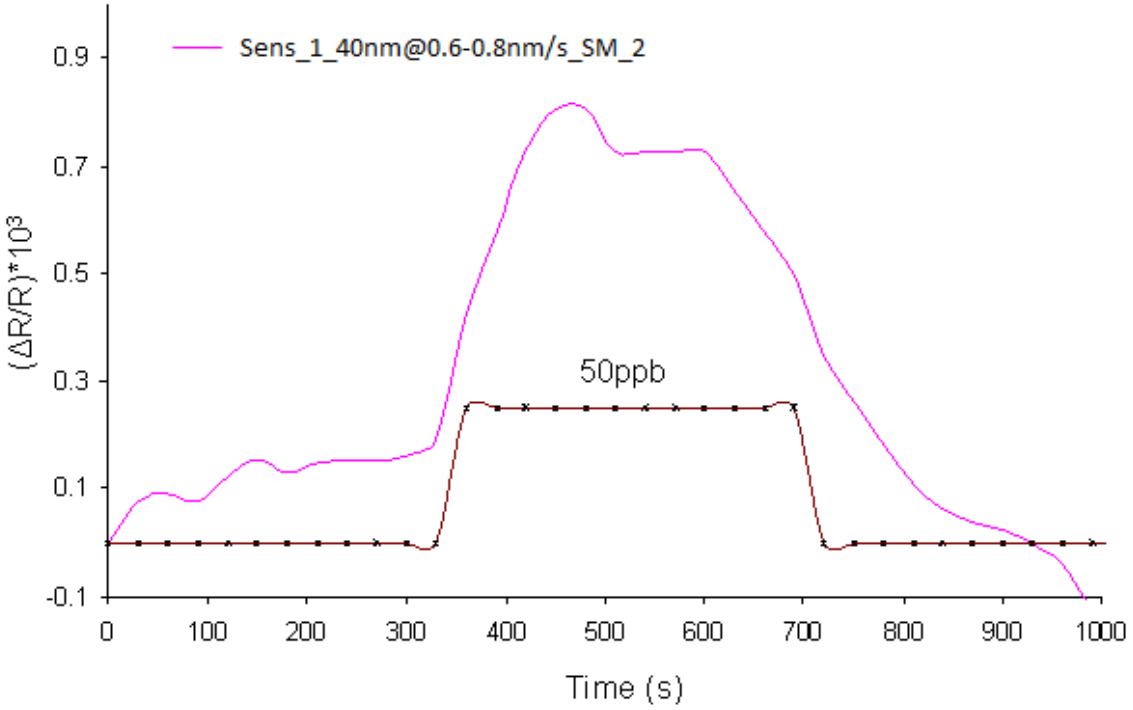

Figure 7.22 Response of 40nm of 90In_2O_3:7ZnO:3SnO_2 deposited at a rate of 0.6nm/s 50ppb

Similar to the device fabricated from the source material 90%In2O3:5%ZnO:5%SnO2 sensing devices fabricated under these conditions also show a measurable and repeatable response to ozone concentrations as low as 50ppb (Figure 7.22) which is of significance for the protection of human health as discussed in Chapter 3.

Shown below are five sensors fabricated under similar conditions at different times, from the graph (Figure 7.23) it can be seen that the sensing device is repeatable and has similar response and recovery times as well as similar response to the various ozone concentrations. From Figure 7.23 it can be seen that there are a couple of outliers in the samples fabricated, which may be explained by slight variations in the deposition parameters (such as layer thickness, deposition rate, humidity, etc.).

Figure 7.24 gives a comparison of the different sensing devices and the response to various ozone concentrations. Also included in Figure 7.24 is an average response taken over all samples.

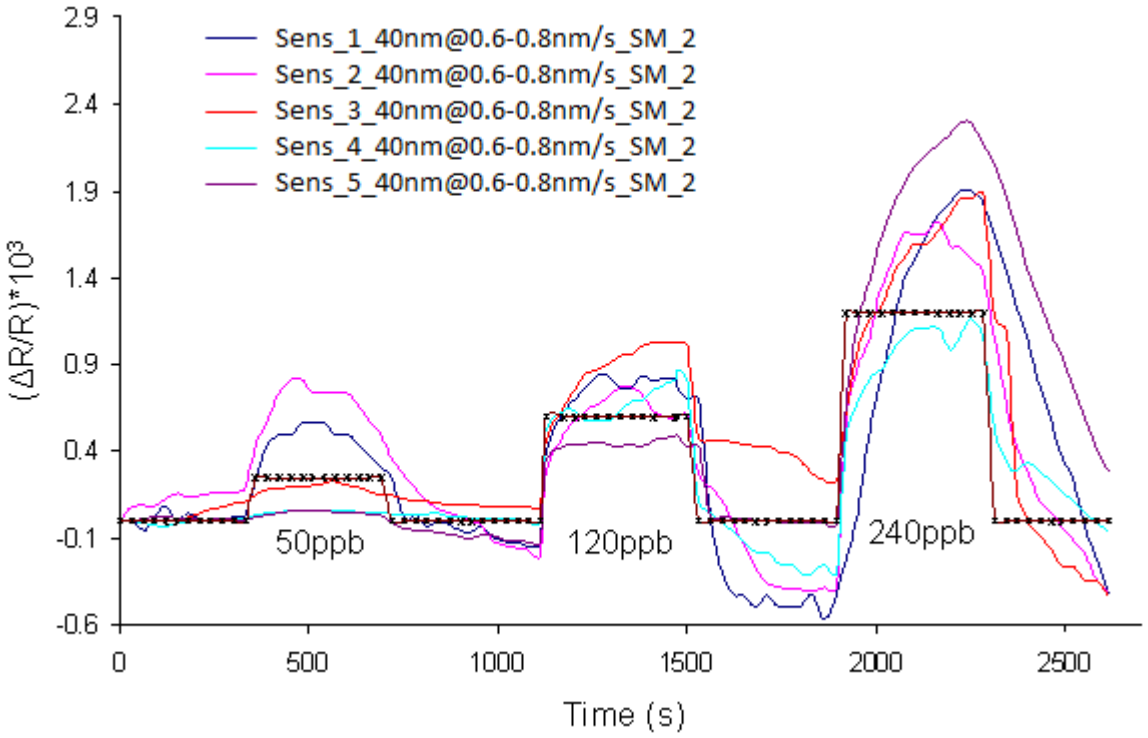

Figure 7.23 Repeatable response of 40nm of 90In_2O_3:7ZnO:3SnO_2 deposited at a rate of 0.6-0.8nm/s to 50, 120 and 240ppb

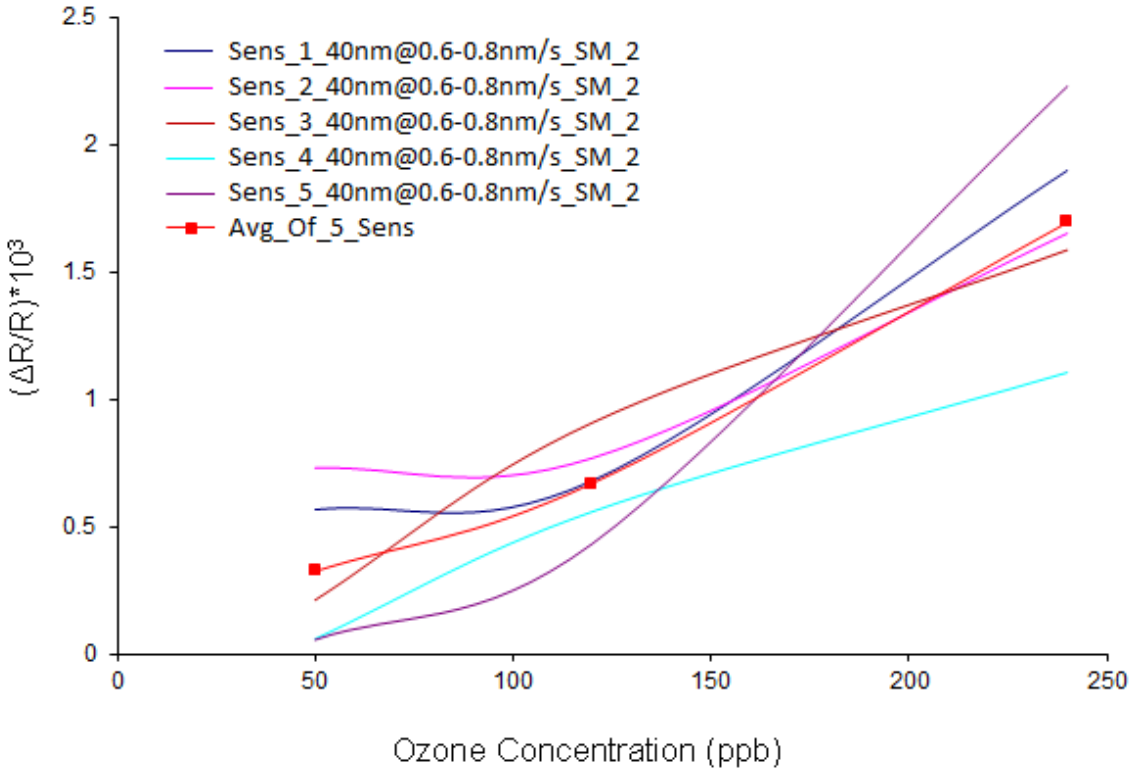

Figure 7.24 Comparison of repeatable response of 40nm of 90In_2O_3:7ZnO:3SnO_2 deposited at a rate of 0.6-0.8nm/s to 50, 120 and 240ppb and average response

7.9. Comparison of Response, $T_{RES(90)}$ and $T_{REC(90)}$ of sensors with varying mol. % concentrations in the source material.

Figure 7.25 shows the average response for each of the various source materials. It is important to note for this figure that the sensor responses have been suitably adjusted to take into account the fact that the baseline for each sample may not return to stable levels. It is clear that the sensor containing the 90%In_2O_3:5%ZnO:5%SnO_2 mol. % in the source material has the greatest response to ozone concentrations from 50ppb – 240ppb of ozone.

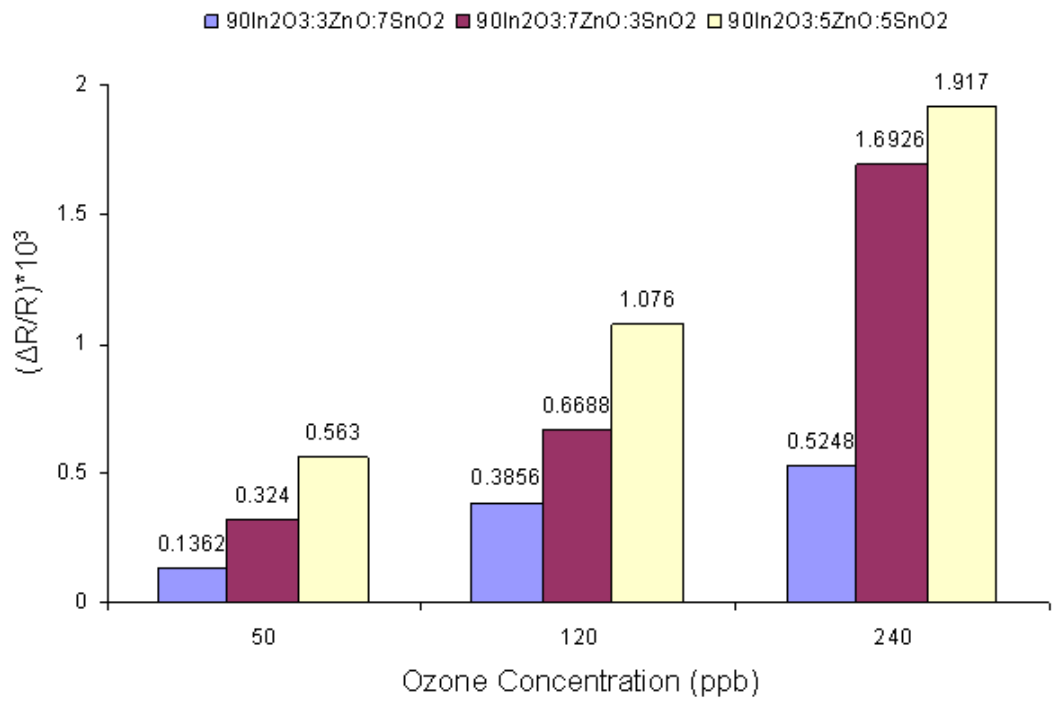

Figure 7.25 Comparing average responses of various concentrations of In_2O_3, ZnO and SnO_2

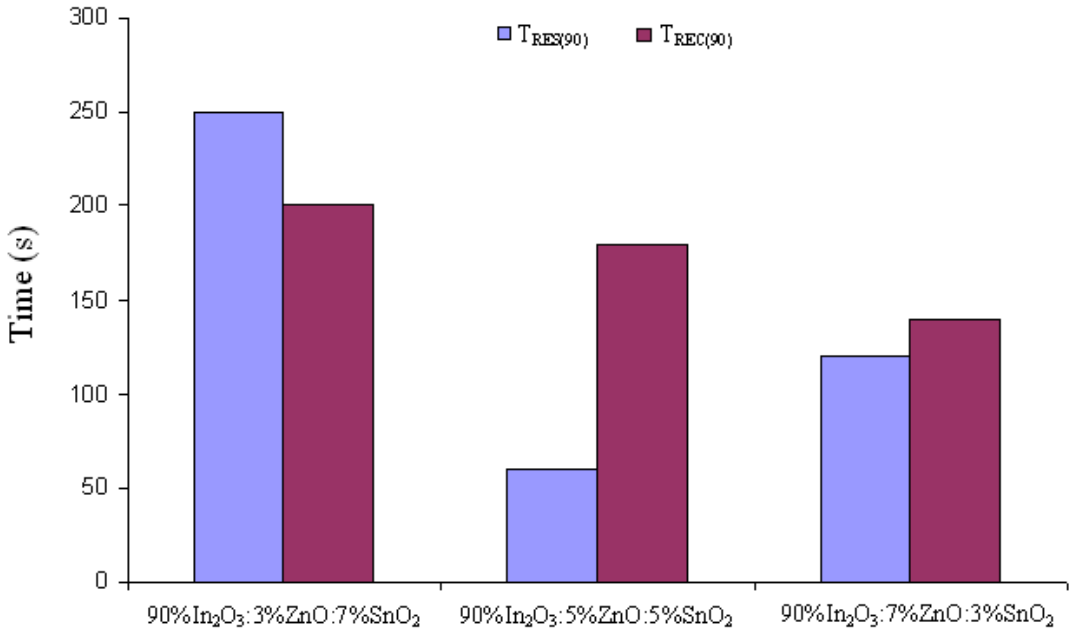

Figure 7.26 Comparison of response and recovery times for the samples fabricated with different mol. % source materials

From Figure 7.26 it can be seen that 90%In_2O_3:5%ZnO:5%SnO_2 sensor shows by far the best response time while the recovery time is comparable to that of the 90%In_2O_3:7%ZnO:3%SnO_2. This high response for 90%In_2O_3:5%ZnO:5%SnO_2 is further investigated in the following sections via XPS analysis.

7.10. XPS Results

7.10.1. XPS Spectra

XPS spectra are quantified in terms of peak intensities and peak positions. The peak intensities measure how much of a material is present at the surface, while the peak positions indicate the elemental and chemical compositions. Other values such as the Full Width Half Maximum (FWHM) are useful indicators of chemical state changes and physical influences. The broadening of a peak may indicate a change in the number of chemical bonds contributing to a peak shape, a change in the sample condition (x-ray damage) and/or differential charging of the surface (localised differences in the charge state of the surface).

The underlying assumption when quantifying the XPS spectra is that the number of electrons recorded is proportional to the number of atoms in a given state. The basic tool for measuring the number of electrons recorded for an atomic state is the quantification region. The CASA Survey scans illustrate a survey spectrum where the surface is characterised using a quantification table based on values computed from the specified regions. The primary objectives of the quantification regions are to define the range of energies over which the signal can be attributed to the transition of interest and to specify the type of approximation appropriate for the removal of background signal not belonging to the peak.

7.10.2. Comparing Samples Using XPS

An XPS spectrum is a combination of the number of electrons leaving the sample surface and the ability of the instrumentation to record these electrons. The efficiency with which emitted electrons are recorded depends on the kinetic energy of the electrons, which in turn depends on the operating mode of the instrument. As a result, the recommended procedure to compare XPS intensities is via 'percentage atomic concentrations'. The key feature of these percentage atomic concentrations is the representation of the intensities as a percentage, i.e., the ratio of the intensity to the total intensity of electrons in the measurement.

7.10.3. XPS Analysis of 90%In_2O_3:5%ZnO:5%SnO_2 (100nm) deposited at a rate of 0.6 - 0.8nm/s

Wide scan XPS spectra (from 0 – 1400 eV) of the 100nm sample deposited at a rate of 0.6 - 0.8nm/s is shown in Figure 7.27. The peak positions were referenced to carbon at 284.6 eV which is recognised as standard practice. Peaks of Zn $2p_{3/2}$, Zn $2p_{5/2}$, O 1s, Sn $3d_{3/2}$, In $3d_{3/2}$, In $3d_{5/2}$, C 1s and Mo 3d were detected at binding energies of 1021.28, 1044.53, 530.6, 486.21, 444.34, 451.88, 284.6 and 231.6 eV respectively.

The presence of carbon C 1s at 284.6 can be attributed to surface contamination as a result of the sample being exposed to air before the XPS measurements as well as the contamination due to the decomposition of the precursor itself [236]. Also of note is the presence of Molybdenum (Mo 3d) as a result of the platform used to deposit the metal oxide sensing layer. Table 7.1 outlines the peaks present in the wide scan XPS spectra for 100nm thick sensing layer consisting of 90%$In_2O_3$5%ZnO:5%SnO_2 deposited at a rate of 0.6 – 0.8nm/s.

Table 7.1. XPS Survey Results for 100nm of $90In_2O_3:5ZnO:5SnO_2$ deposited at a rate of 0.6 - 0.8nm/s

Name	FWHM	Area	At %
Zn 2p	2.86297	4790.6	1.00
O 1s	3.52231	20232.9	27.29
Sn 3d	2.60628	3440.8	0.92
In 3d	2.7979	22211.1	6.60
C 1s	2.63069	15264.1	60.33
Mo 3d	6.28455	9265.5	3.85

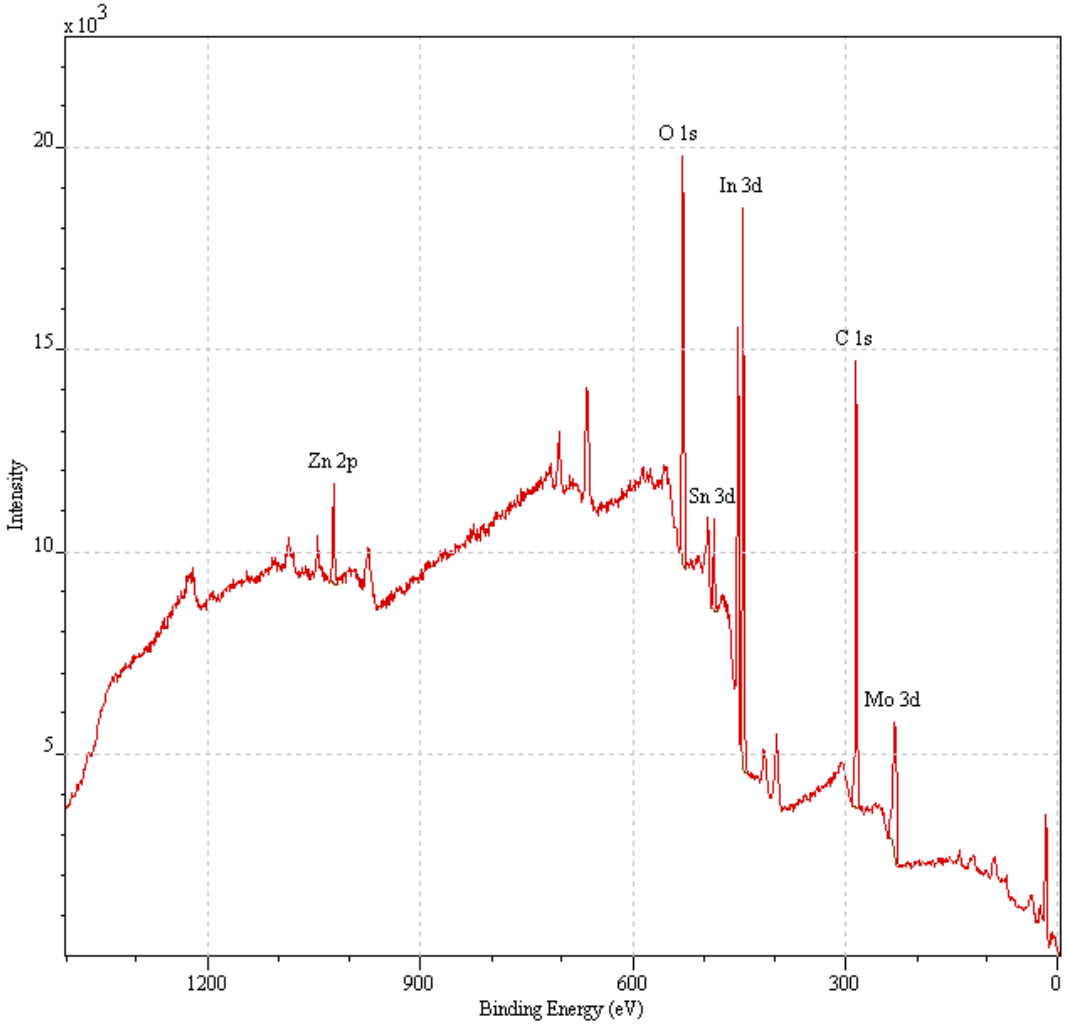

Figure 7.27 Wide range spectrum obtained from sample

A narrow scan XPS spectra (440 – 456 eV) of the In 3d region is shown in Figure 7.28 below, which shows the doublet corresponding to In $3d_{3/2}$ and In $3d_{5/2}$. The 3d doublets were curve fitted using Shirley type base line with mixed Gaussian (50%) and Lorentzian (50%) (GL(50)).

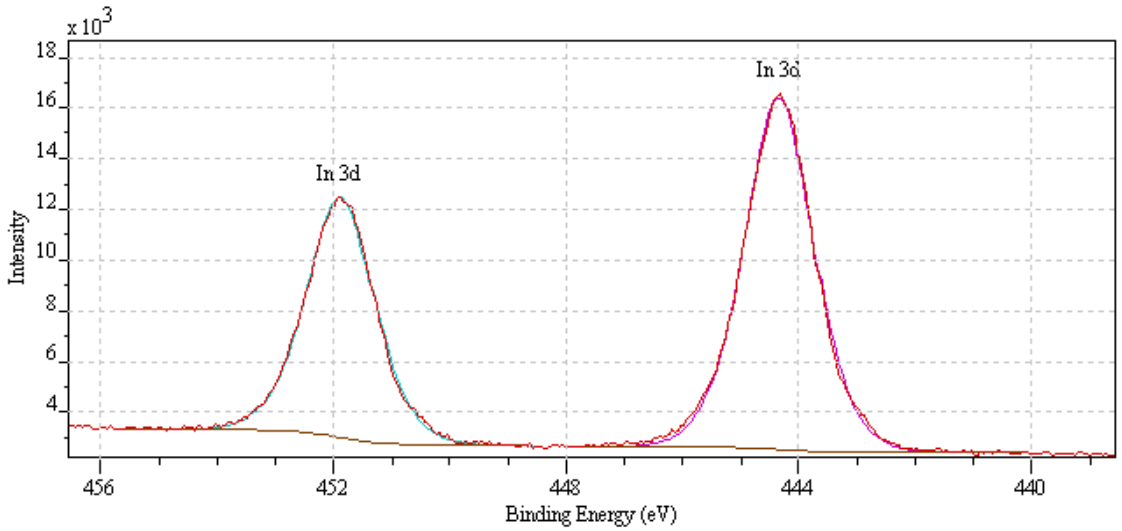

Figure 7.28 In3d doublet spectrum region

The important specifics of this In3d region are summarized in Table 7.2 below. Of particular interest when comparing this sample to others will be the position and intensities of the In $3d_{3/2}$ and the $In3d_{5/2}$ peaks.

A narrow scan XPS spectra (from 1015 eV to 1055 eV) of the Zn 2p region is shown in Figure 7.29 The two peaks at 1044.53 eV and 1021.28 eV which correspond to the binding energies of Zn $2p_{1/2}$ and Zn $2p_{3/2}$ respectively, which are very close to the standard bulk ZnO binding energy values [237]. Table 7.3 details the specifics of the Zn 2p doublet region.

Table 7.2 In3d region components

Component	**In $3d_{3/2}$**	**In $3d_{5/2}$**
Line Shape	GL(50)	GL(50)
Area	2694.6	18029.1
FWHM	1.39687	1.37037
Position (eV)	444.34	451.88
Concentration (%)	60.01	39.99

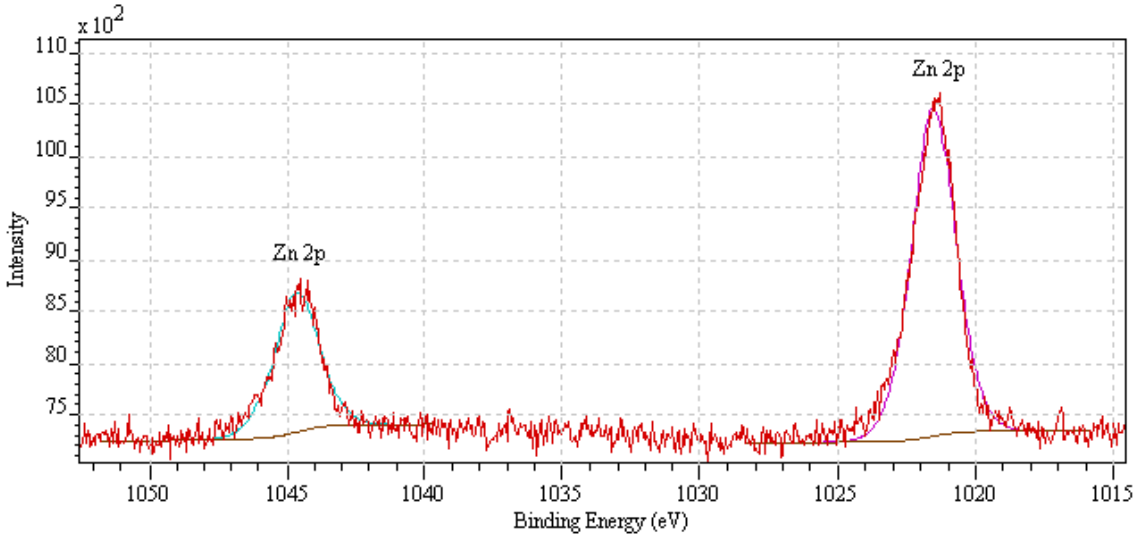

Figure 7.29 Zn2p doublet region spectrum

Table 7.3 Zn 2p region components

Component	**Zn $2p_{3/2}$**	**Zn $2p_{1/2}$**
Line Shape	GL(50)	GL(50)
Area	5378.7	2371.3
FWHM	1.74116	1.75378
Position (eV)	1021.28	1044.53
Concentration (%)	69.09	30.91

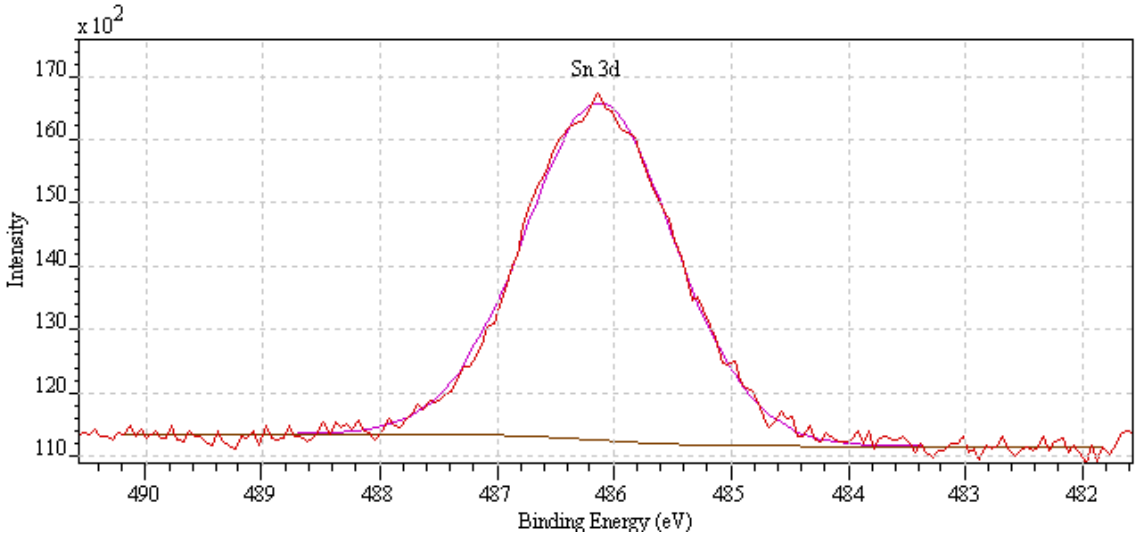

Figure 7.30 Sn3d 5/2 narrow region spectrum

Figure 7.30 shows XPS spectra from 482 eV to 490 eV of the Sn 3d region, the peak at 486.121 eV corresponds to the Sn 3d $_{5/2}$ which is close to the standard Sn $3d_{5/2}$ value [238].

Table 7.4. Sn3d region component

Component	**Sn $3d_{3/2}$**
Line Shape	GL(30)
Area	4340
FWHM	1.50482
Position (eV)	486.121
Concentration (%)	100

Shown in Figure 7.31 is the photoelectron spectrum of O 1s. The sub peaks are a Gaussian Lorentzian (GL (30)) distribution fitting for the O 1s peak. They are centred at 531.092 eV and 529.722 eV. The low binding energy component (529.722 eV) can be attributed to oxygen species in the metal oxides (indium, tin and zinc). The intensity of this component measures the amount of oxygen atoms in a fully oxidised stoichiometric surrounding. The higher binding energy (531.092 eV) component is associated with

lattice oxygen in the oxygen deficient regions. Therefore the intensity of this component measures the concentration of oxygen vacancies. It can be seen that the intensity of this component is higher than that of the lower binding energy component thereby indicating a large oxygen deficient state at the surface [27]. Table 7.5 details the specifics of the two O 1s component peaks, the position as well as the intensity of these peaks are important when compared to future results.

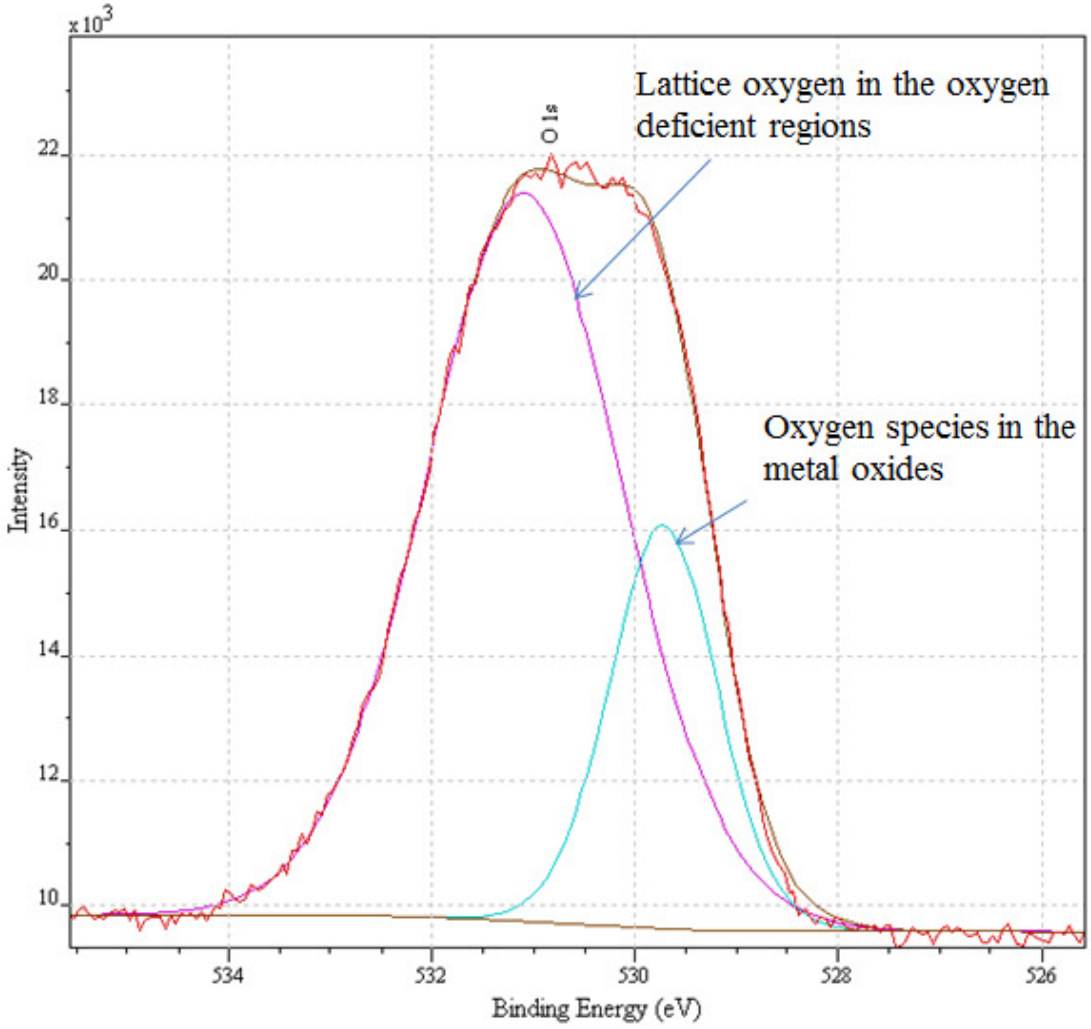

Figure 7.31 O1s narrow region spectrum

Table 7.5 O 1s region components

Component	**O 1s**	**O 1s**
Line Shape	GL(30)	GL(30)
Area	19207.5	5821.3
FWHM	2.28527	1.24528
Position (eV)	531.1	529.7
Concentration (%)	76.74	23.26

7.10.4. XPS Analysis of 40nm layer of $90In_2O_3:5ZnO:5SnO_2$ deposited at a rate of 0.1-0.3nm/s

Wide scan XPS spectra (from 0 – 1400 eV) of the 40nm thick sensing layer with a deposition rate of 0.1 - 0.3nm/s is shown in Figure 7.32. The peak positions were referenced to carbon at 284.6 eV. Peaks of Zn $2p_{3/2}$, Zn $2p_{5/2}$, O 1s, Sn $3d_{3/2}$, In $3d_{3/2}$, In $3d_{5/2}$, C 1s and Mo 3d were detected at binding energies of 1021.54, 1044.66, 530.5, 485.96, 444.26, 451.79, 284.6 and 231.5 eV respectively.

The presence of carbon C 1s at 284.6 as mentioned before can be attributed to surface contamination as a result of the sample being exposed to air before the XPS measurements as well as the contamination due to the decomposition of the precursor itself [236].

Table 7.6 XPS Survey Results for $90In_2O_3:5ZnO:5SnO_2$ deposited at 0.1-0.3nm/s

Name	**FWHM**	**Area**	**At %**
Zn 2p	2.82938	7743.7	1.64
O 1s	3.44278	19860.1	27.11
Sn 3d	2.95545	1558.8	0.42
In 3d	2.74661	23879.3	7.18
C 1s	2.49478	14796.1	59.18
Mo 3d	6.22871	10626.3	4.47

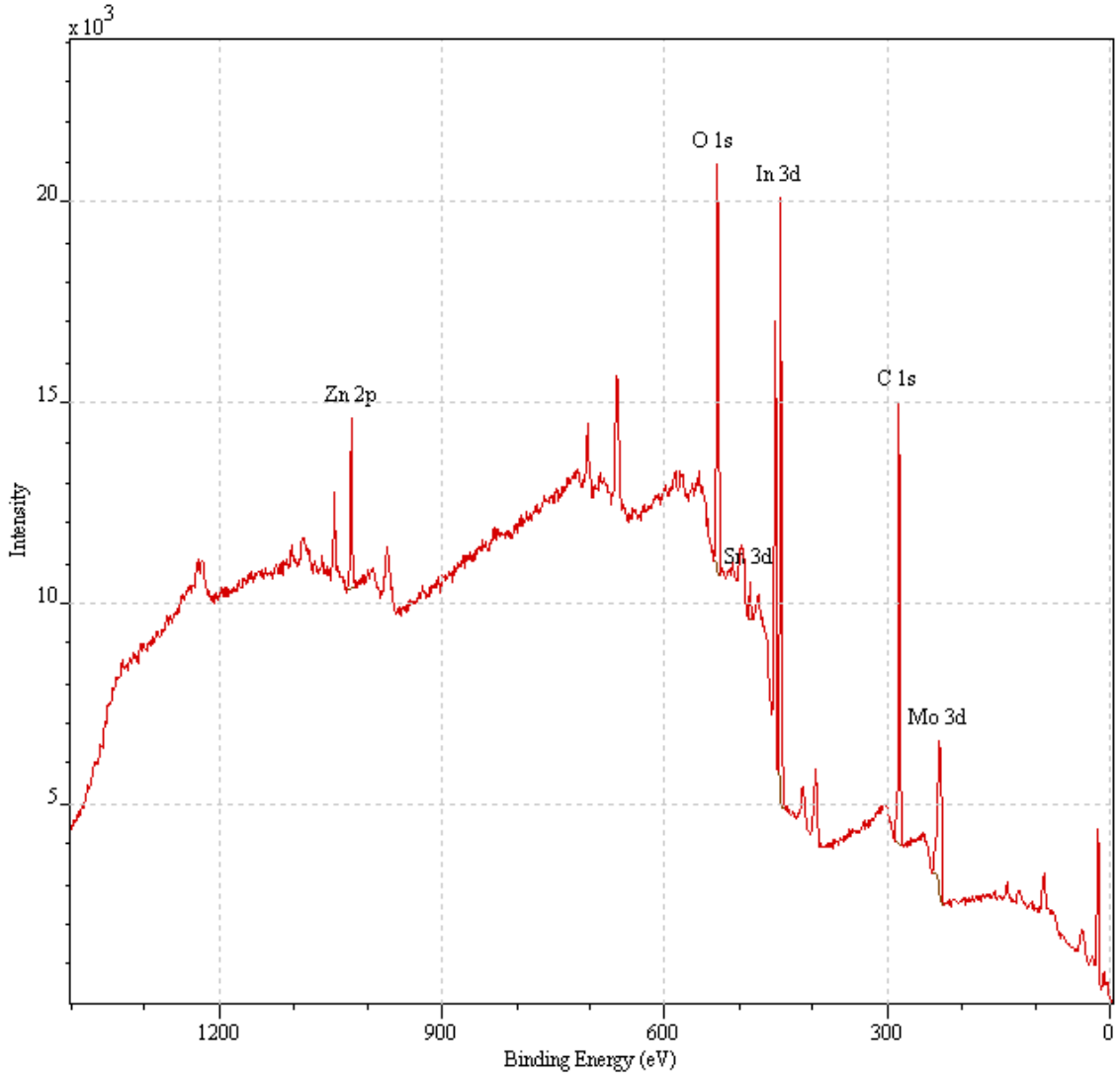

Figure 7.32 Wide range spectrum obtained from sample

A narrow scan XPS spectra (440 – 456 eV) of the In 3d region is shown in Figure 7.33 below, which shows the doublet corresponding to In $3d_{3/2}$ and In $3d_{5/2}$. The 3d doublets were curve fitted using Shirley type base line with mixed Gaussian (50%) and Lorentzian (50%) (GL(50)). This In3d narrow scan spectra will be compared to other samples in the following sections in order to gain an insight and explain the difference in sensor performance for varying the fabrication parameters.

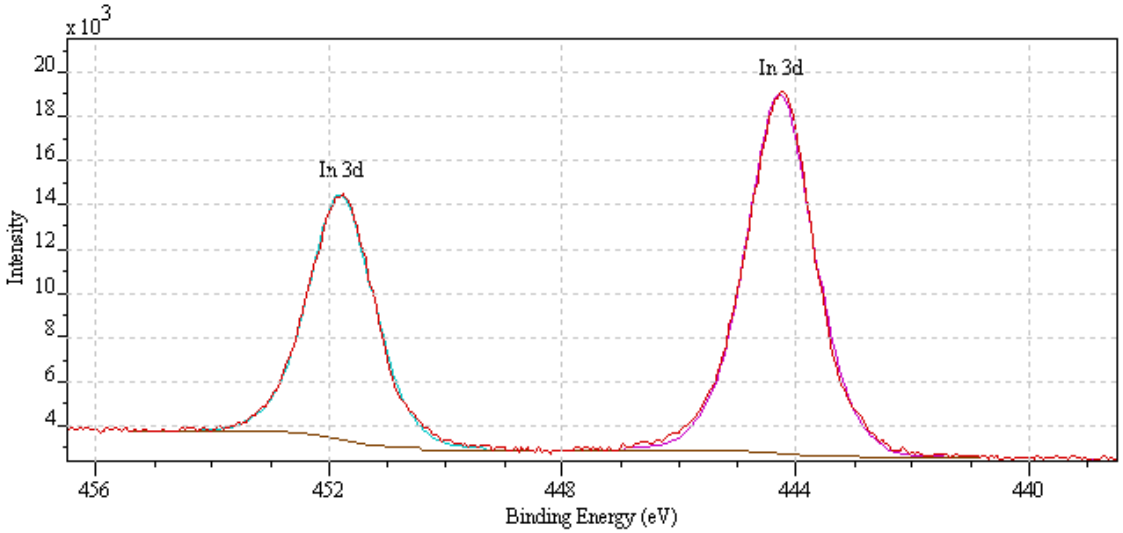

Figure 7.33 In3d doublet spectrum region

Table 7.7 lists the important specifics of the In 3d spectrum region components. Of particular interest is the position of the binding energies (eV) of each of the peak components. It has been mentioned previously that slight shifts in the binding energies of the component regions can lead to significant changes in the overall sensing layer performance.

Table 7.7 In3d region components

Component	**In $3d_{3/2}$**	**In $3d_{5/2}$**
Line Shape	GL(50)	GL(50)
Area	30345.4	20250.4
FWHM	1.34828	1.31255
Position (eV)	444.264	451.786
Concentration (%)	60.07	39.93

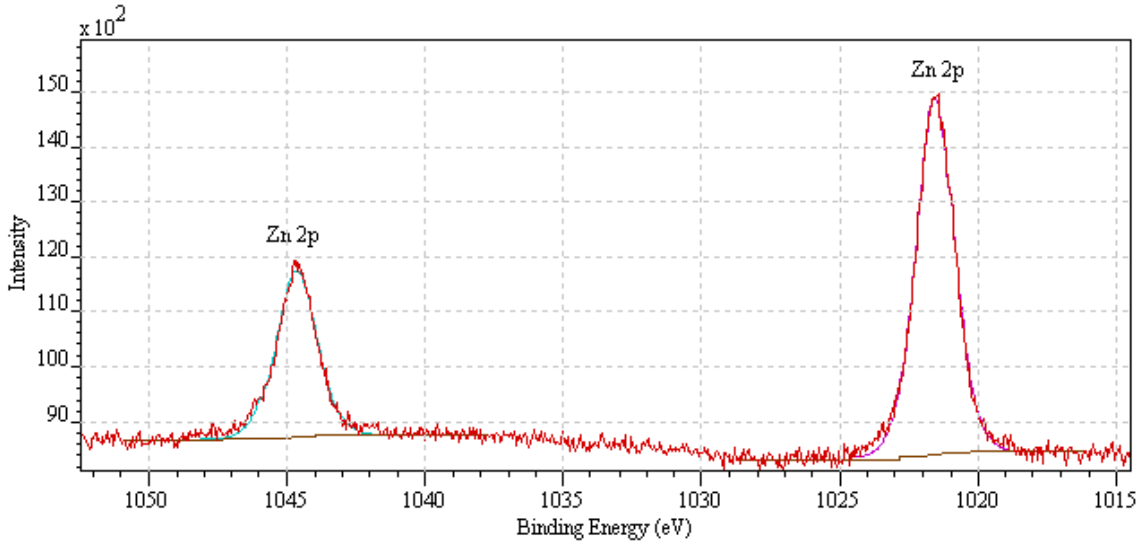

Figure 7.34 Zn2p doublet region spectrum

A narrow scan XPS spectrum (from 1015 eV to 1055 eV) of the Zn 2p region is shown in Figure 7.34. The two peaks at 1044.66 eV and 1021.54 eV correspond to the binding energies of Zn $2p_{1/2}$ and Zn $2p_{3/2}$ respectively, which are very close to the standard bulk ZnO binding energy values [237]. Table 7.8 details the specifics of the Zn 2p doublet region.

Table 7.8 Zn 2p region components

Component	**Zn $2p_{3/2}$**	**Zn $2p_{1/2}$**
Line Shape	GL(50)	GL(50)
Area	9558.2	4816.9
FWHM	1.58753	1.70795
Position (eV)	1021.54	1044.66
Concentration (%)	66.36	33.64

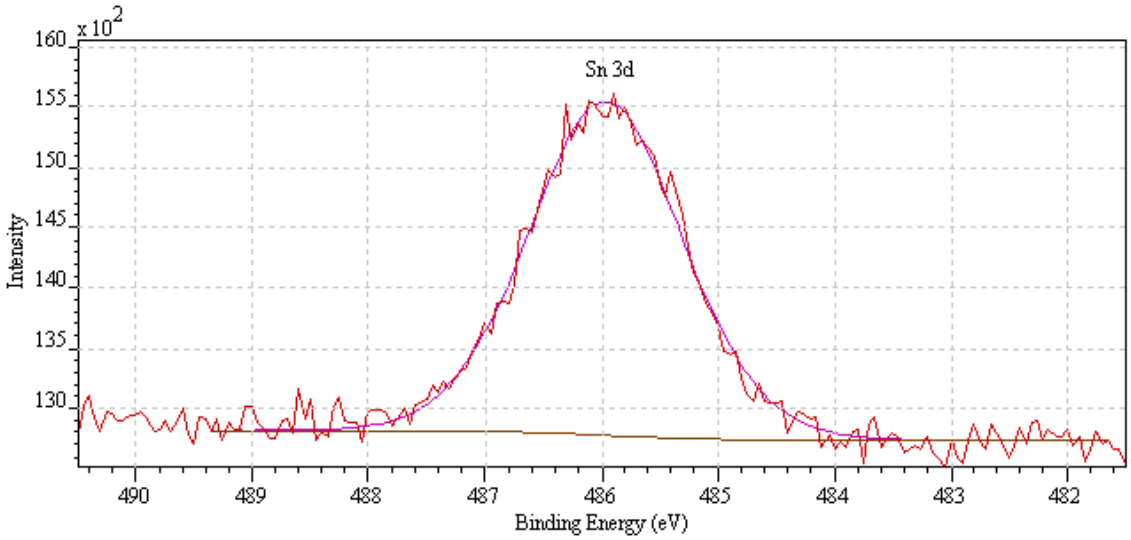

Figure 7.35 Sn3d 5/2 narrow region spectrum

Figure 7.35 shows XPS spectra from 482 eV to 490 eV of the Sn 3d region, the peak at 485.96 eV corresponds to the Sn 3d $_{5/2}$ which is close to the standard Sn $3d_{5/2}$ value [226]. Table 7.9 shows details of the Sn 3d region components. As with the previous narrow region spectra, this spectrum will be compared to similar sample spectra in order to explain the effects of varying fabrication procedure on the oxide sensing layer.

Table 7.9 Sn 3d region components

Component	**Sn $3d_{3/2}$**
Line Shape	GL(30)
Area	2333.7
FWHM	1.55262
Position (eV)	485.96
Concentration (%)	100

Shown in Figure 7.36 is the photoelectron spectrum of O 1s, with a binding energy of 530.58 eV. The sub (component) peaks are a Gaussian Lorentzian (GL (30)) distribution fitting for the O 1s peak. They are centred at 531.170 eV aand 529.63 eV. The low binding energy component (529.63 eV) is attributed to the O^{2-} ions.

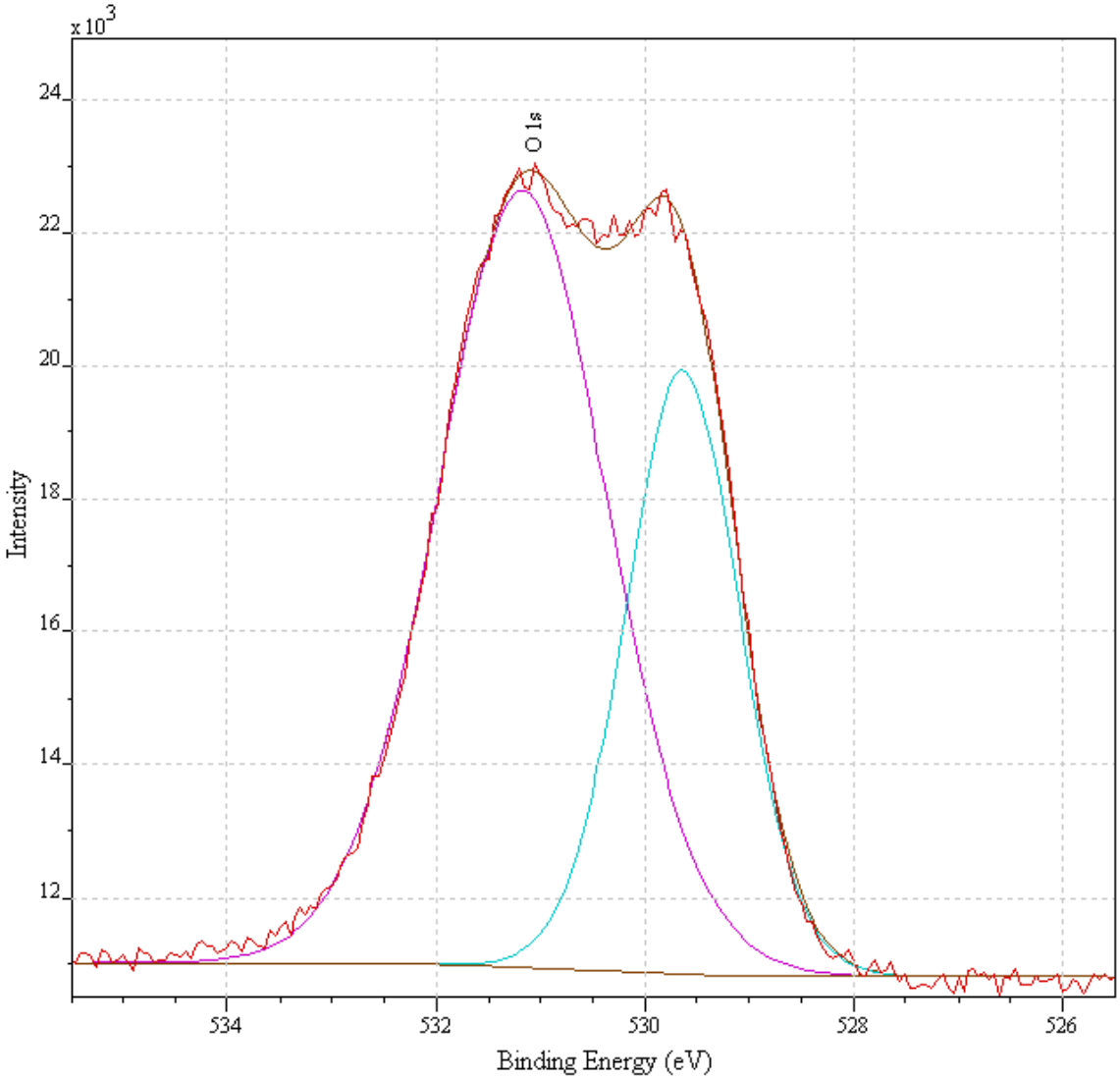

Figure 7.36 O1s narrow region spectrum

The intensity of this component measures the amount of oxygen atoms in a fully oxidised stoichiometric surrounding. The higher binding energy (531.170 eV) component is associated with O^{2-} ions in the oxygen deficient regions [27, 239].

Table 7.10 O 1s region components

Component	**O 1s**	**O 1s**
Line Shape	GL(30)	GL(30)
Area	16292.2	8412.5
FWHM	1.92491	1.27885
Position (eV)	531.17	529.63
Concentration (%)	65.95	34.05

Table 7.10 details the specifics of the two O 1s component peaks, the position as well as the intensity of these peaks are important when compared to future results.

7.10.5. XPS Analysis of 40nm layer of $90In_2O_3:5ZnO:5SnO_2$ deposited at a rate of 0.6 - 0.8nm/s

Wide scan XPS spectra (from 0 – 1400 eV) of the 40nm thick sensing layer deposited at a rate of 0.6-0.8nm/s is shown in Figure 7.37. The peak positions were referenced to carbon at 284.6 eV (standard practice). Peaks of Zn $2p_{3/2}$, Zn $2p_{5/2}$, O 1s, Sn $3d_{3/2}$, In $3d_{3/2}$, In $3d_{5/2}$, C 1s and Mo 3d were detected at binding energies of 1021.69, 1044.79, 530.45, 486.15, 444.36, 451.89, 284.6 and 231.45 eV respectively.

Table 7.11 XPS Survey Results for $90In_2O_3:5ZnO:5SnO_2$ deposited at a rate of 0.6-0.8nm/s

Name	**FWHM**	**Area**	**At %**
Zn 2p	2.81301	5929.3	1.25
O 1s	3.41576	18793.1	25.55
Sn 3d	2.80922	2215.9	0.60
In 3d	2.81415	20898.5	6.26
C 1s	2.58419	15850.0	63.14
Mo 3d	6.16594	7624.6	3.20

Table 7.11 outlines the peaks present in the wide scan XPS spectra for 40nm thick sensing layer consisting of 90%$In_2O_3$5%ZnO:5%SnO_2 deposited at a rate of 0.6 – 0.8nm/s.

A narrow scan XPS spectra (440 – 456 eV) of the In 3d region is shown in Figure 7.38, which shows doublet corresponding to In $3d_{3/2}$ and In $3d_{5/2}$. As with the previous samples the 3d doublets were curve fitted using Shirley type base line with mixed Gaussian (30%) and Lorentzian (70%) (GL(30)).

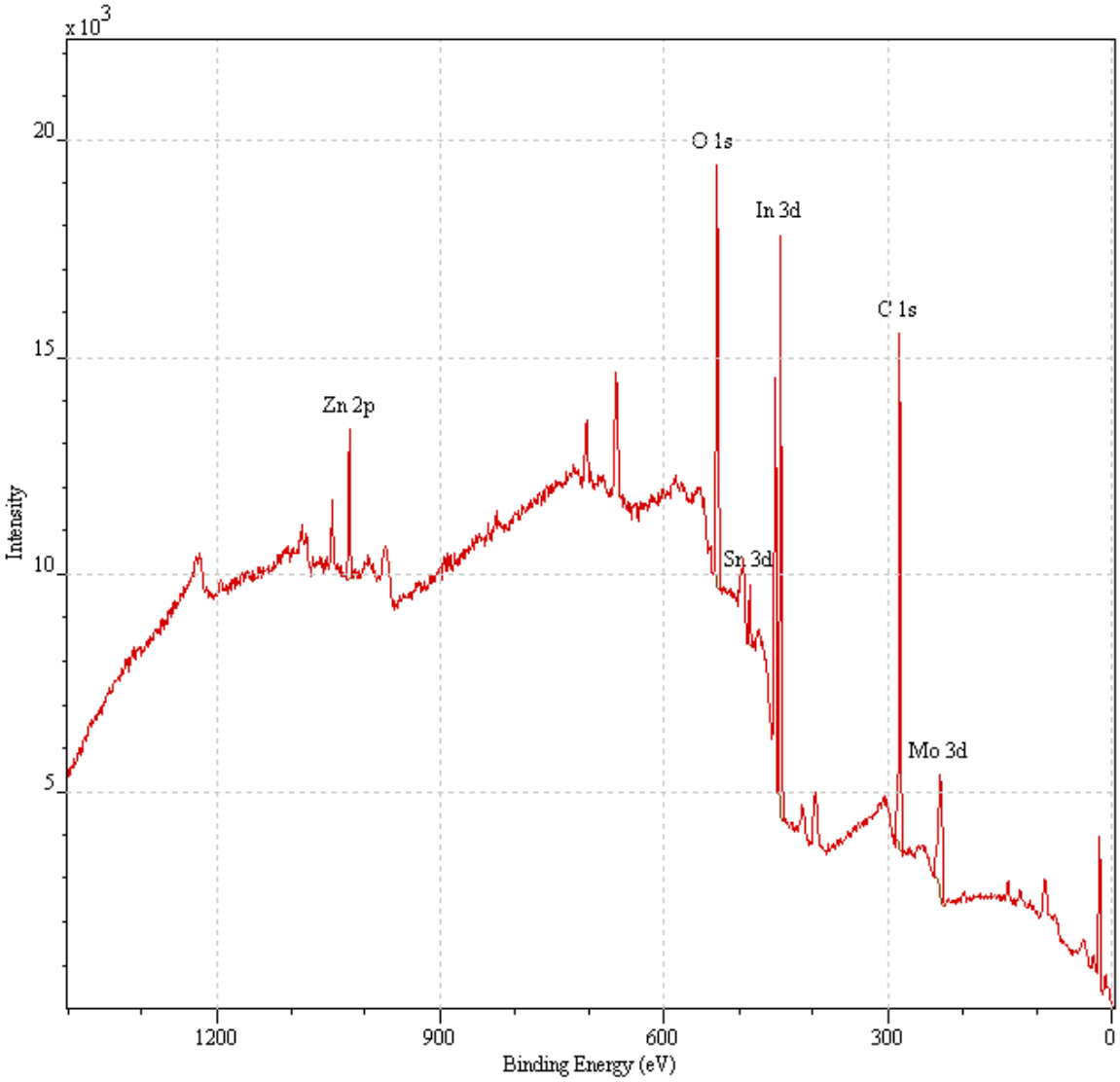

Figure 7.37 Wide range spectrum obtained from sample

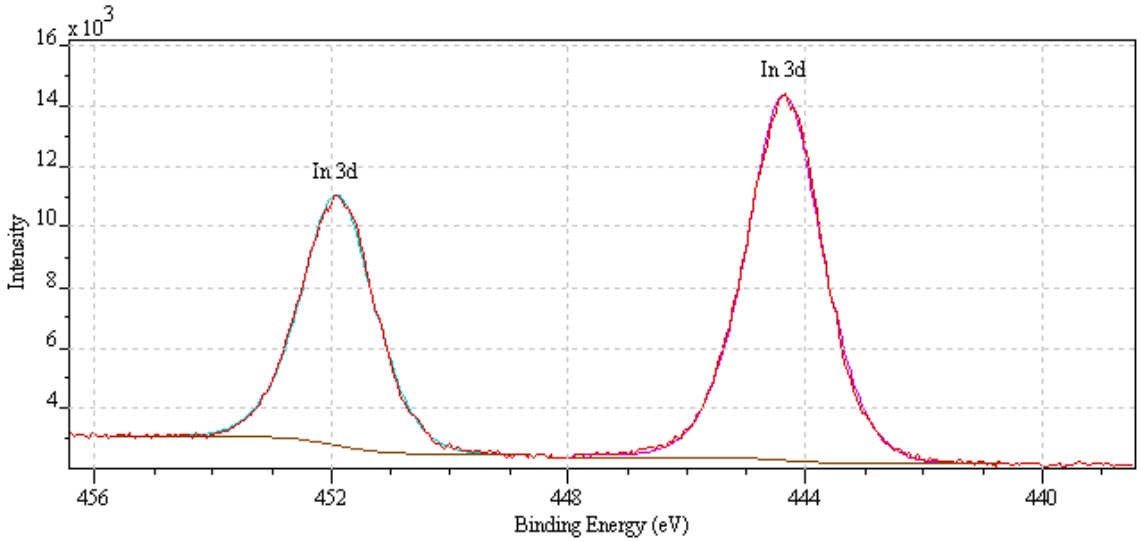

Figure 7.38 In3d doublet spectrum region

Table 7.12 In3d region components

Component	**In $3d_{3/2}$**	**In $3d_{5/2}$**
Line Shape	GL(50)	GL(50)
Area	25008.2	16742.8
FWHM	1.49198	1.44885
Position (eV)	444.36	451.89
Concentration (%)	59.99	40.01

Table 7.13 Zn 2p region components

Component	**Zn $2p_{3/2}$**	**Zn $2p_{1/2}$**
Line Shape	GL(50)	GL(50)
Area	7545.2	3708.2
FWHM	1.65239	1.7415
Position (eV)	1021.69	1044.79
Concentration (%)	66.92	33.08

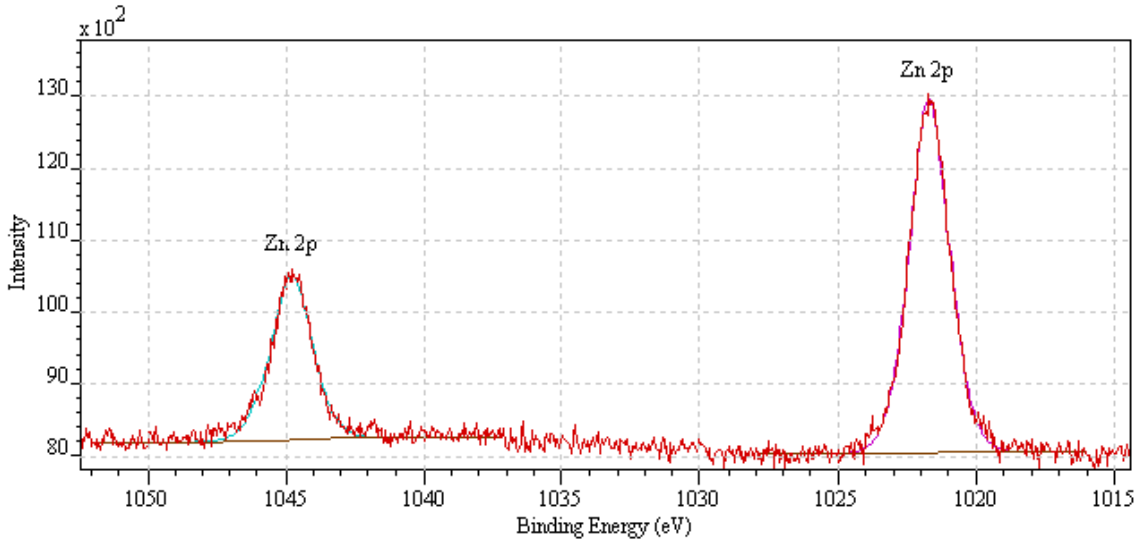

Figure 7.39 Zn2p dublet region spectrum

A narrow scan XPS spectra (from 1015 eV to 1055 eV) of the Zn 2p region is shown in Figure 7.39. The two peaks at 1044.79 eV and 1021.69 eV which correspond to the binding energies of Zn $2p_{1/2}$ and Zn $2p_{3/2}$ respectively as shown in Table 7.13.

Figure 7.40 shows XPS spectra from 482 eV to 490 eV of the Sn 3d region, the peak at 486.151 eV corresponds to the Sn 3d $_{5/2}$ which is close to the standard Sn $3d_{5/2}$ value [238].

Table 7.14 Sn 3d region components

Component	**Sn $3d_{3/2}$**
Line Shape	GL(30)
Area	2751.3
FWHM	1.47549
Position (eV)	486.151
Concentration (%)	100

Shown in Figure 7.41 is the photoelectron spectrum of O 1s, with a binding energy of 530.58 eV. The binding energies of the various core levels match well with XPS spectrum of bulk ZnO. The sub peaks are a Gaussian Lorentzian (GL (30)) distribution

fitting for the O 1s peak. They are centred at 531.37 eV aand 529.760 eV. The low binding energy component (529.760 eV) can be attributed to the to O^{2-} ions. The intensity of this component measures the amount of oxygen atoms in a fully oxidised stoichiometric surrounding. The higher binding energy (531.37 eV) component is associated with O^{2-} ions in the oxygen deficient regions [27, 30]. Therefore the intensity of this component measures the concentration of oxygen vacancies. It can be seen that the intensity of this component is higher than that of the lower binding energy component thereby indicating a large oxygen deficient state at the surface [239].

Table 7.15 O 1s region components

Component	**O 1s**	**O 1s**
Line Shape	GL(30)	GL(30)
Area	15123.0	6782.3
FWHM	1.84452	1.39059
Position (eV)	531.37	529.76
Concentration (%)	69.04	30.96

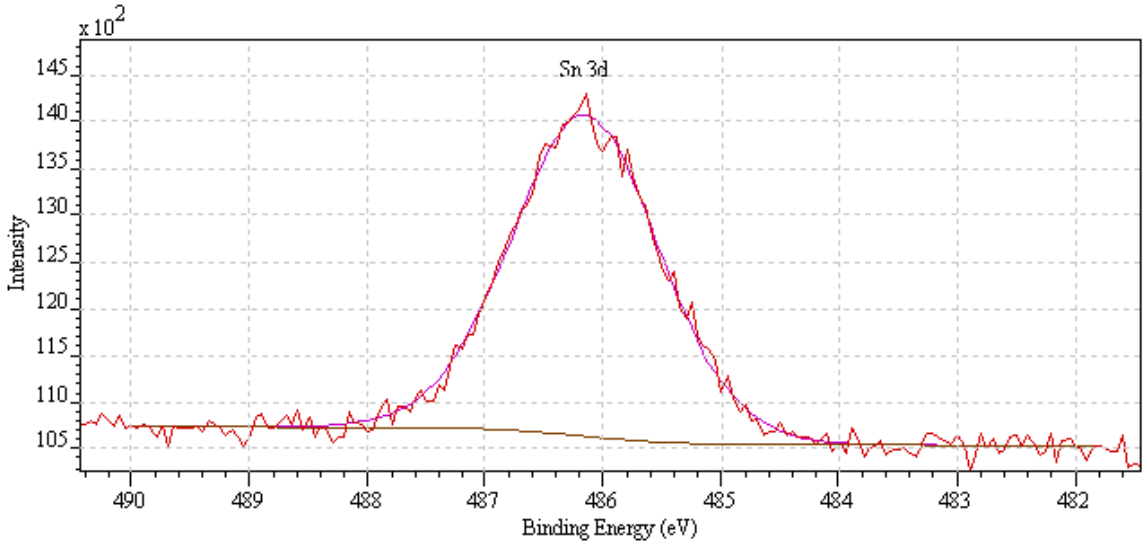

Figure 7.40 Sn3d 5/2 narrow region spectrum

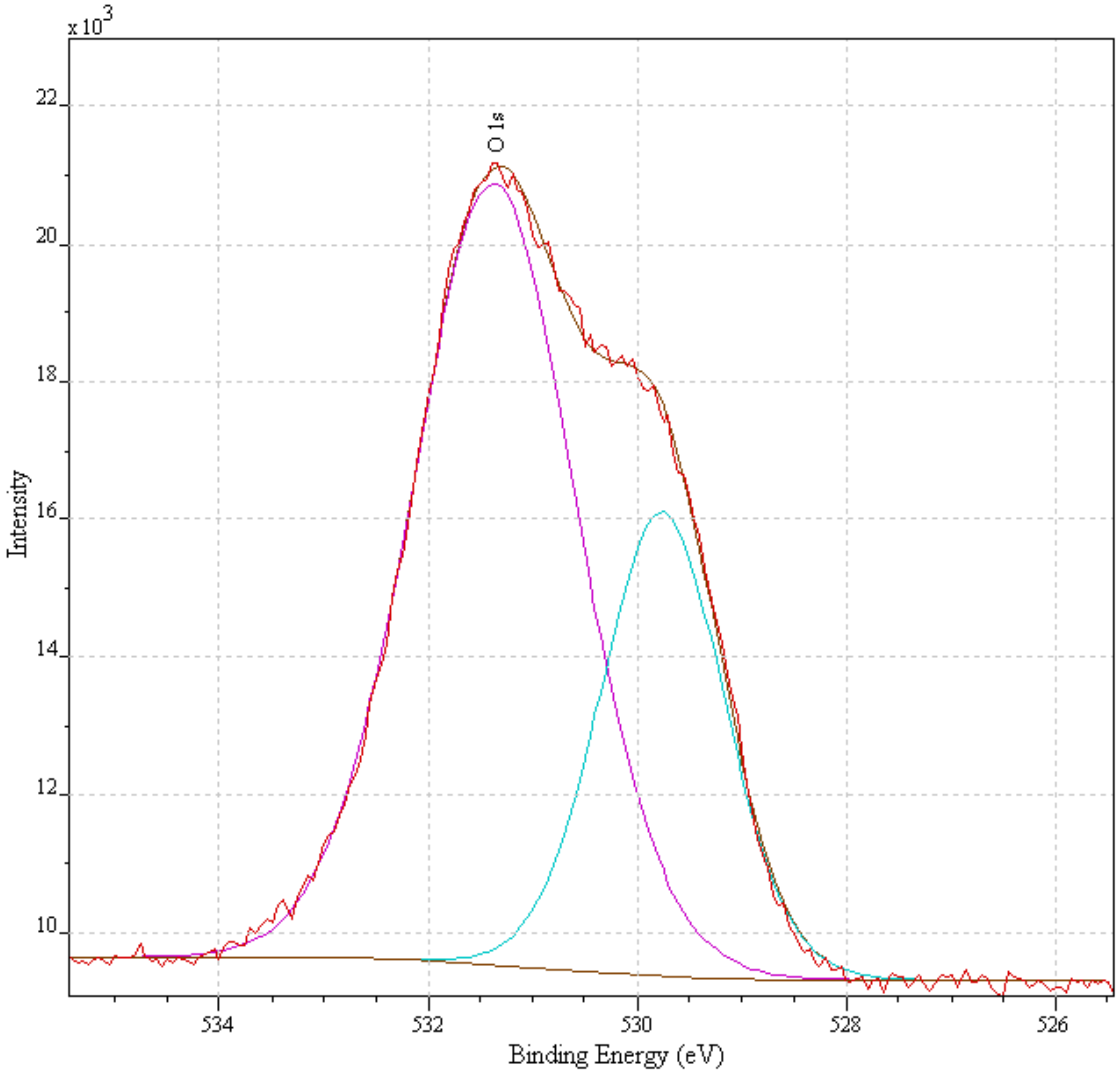

Figure 7.41 O1s narrow region spectrum

7.10.6. XPS Analysis of 40nm layer of $90In_2O_3:5ZnO:5SnO_2$ deposited at a rate of 1.1-1.4nm/s

Table 7.16 XPS Survey Results for $90In_2O_3:5ZnO:5SnO_2$ deposited at a rate of 1.1-1.4nm/s

Name	FWHM	Area	At %
Zn 2p	2.77879	8323.7	1.63
O 1s	3.18235	11866.2	15.02
Sn 3d	2.73325	1210.8	0.30
In 3d	2.70826	7269.3	2.03
C 1s	2.56958	21409.7	79.43
Mo 3d	6.44175	4053.7	1.58

Wide scan XPS spectra (from 0 – 1400 eV) of this sample is shown in Figure 7.42. The peak positions were again referenced to carbon at 284.6 eV. Peaks of Zn $2p_{3/2}$, Zn $2p_{5/2}$, O 1s, Sn $3d_{3/2}$, In $3d_{3/2}$, In $3d_{5/2}$, C 1s and Mo 3d were detected at binding energies of 1021.88, 1044.97, 531.4, 486.1, 444.42, 451.94, 284.6 and 230.4 eV respectively.

The presence of carbon C 1s at 284.6 can be attributed to surface contamination as a result of the sample being exposed to air before the XPS measurements as well as the contamination due to the decomposition of the precursor itself [236].

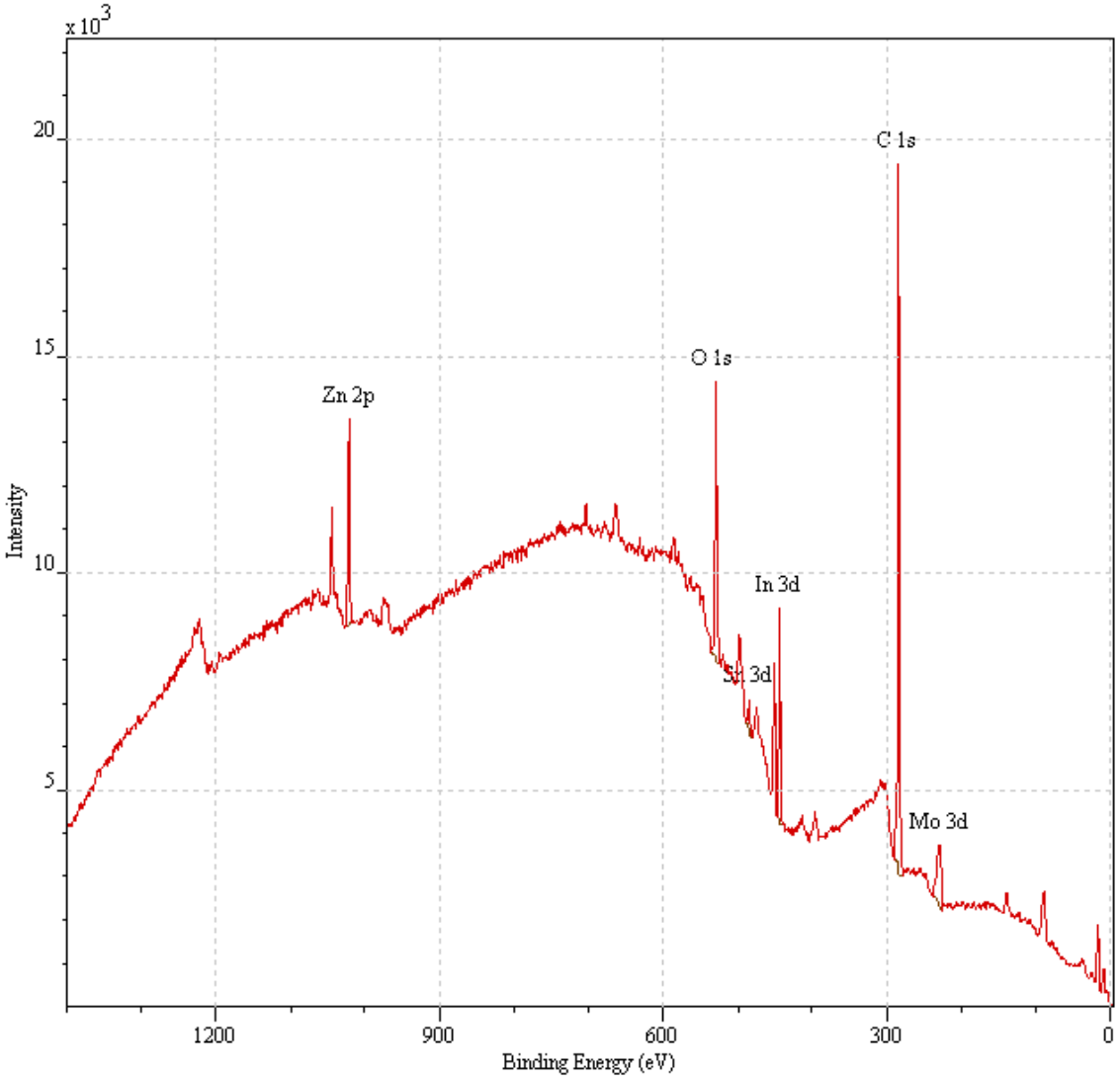

Figure 7.42 Wide range spectrum obtained from sample

A narrow scan XPS spectra (440 – 456 eV) of the In 3d region is shown in Figure 7.43, which shows doublet corresponding to In $3d_{3/2}$ and In $3d_{5/2}$. The 3d doublets were curve fitted using Shirley type base line with mixed Gaussian (30%) and Lorentzian (70%) (GL(30)).

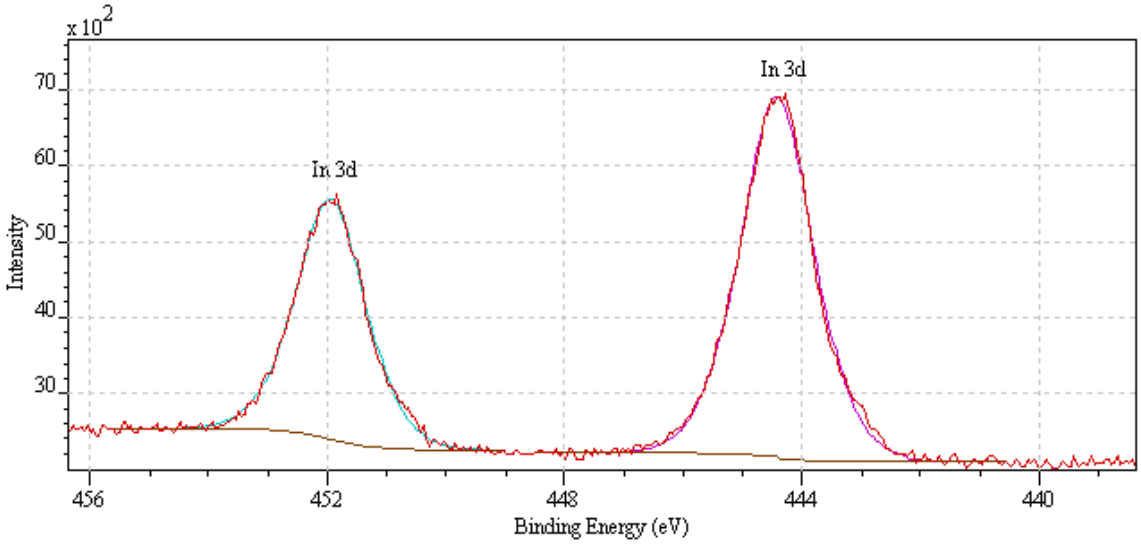

Figure 7.43 In3d doublet spectrum region

Table 7.17 In3d region components

Component	**In $3d_{3/2}$**	**In $3d_{5/2}$**
Line Shape	GL(50)	GL(50)
Area	9565.4	6080.9
FWHM	1.45655	1.3848
Position (eV)	444.42	451.94
Concentration (%)	61.23	38.77

Table 7.18 Zn 2p region components

Component	**Zn $2p_{3/2}$**	**Zn $2p_{1/2}$**
Line Shape	GL(50)	GL(50)
Area	11230.9	5578.3
FWHM	1.62191	1.73435
Position (eV)	1021.88	1044.97
Concentration (%)	66.69	33.31

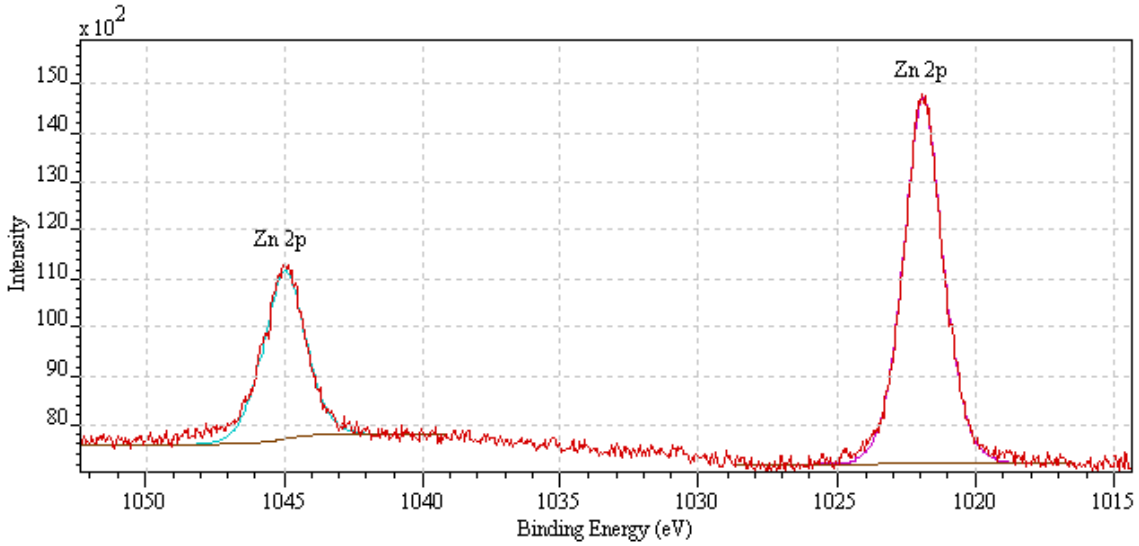

Figure 7.44 Zn2p dublet region spectrum

A narrow scan XPS spectra (from 1015 eV to 1055 eV) of the Zn 2p region is shown in Figure 7.44. The two peaks at 1044.97 eV and 1021.88 eV which correspond to the binding energies of Zn $2p_{1/2}$ and Zn $2p_{3/2}$ respectively, which are very close to the standard bulk ZnO binding energy values [237].

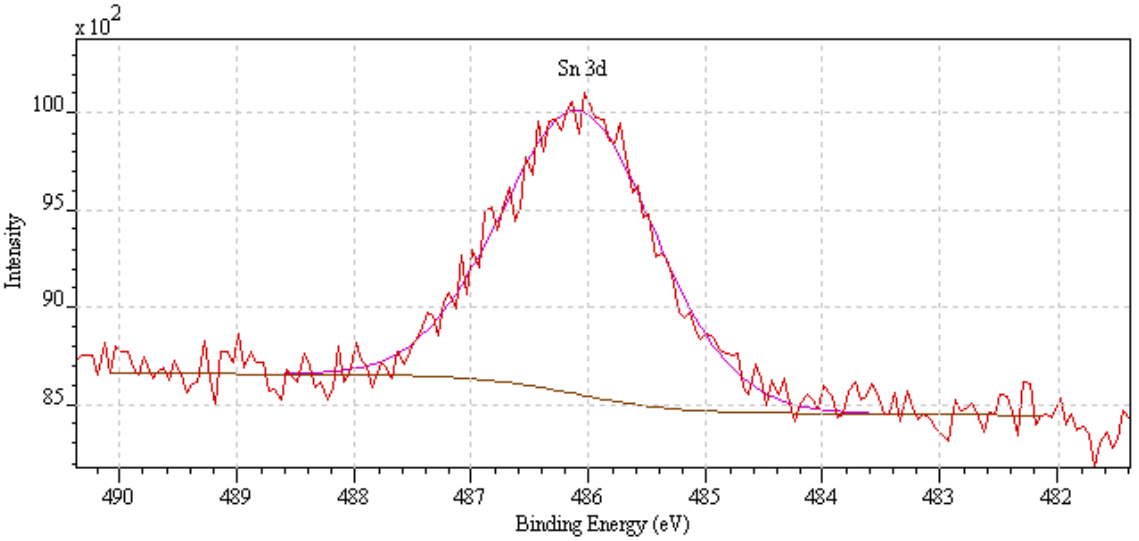

Figure 7.45 Sn3d 5/2 narrow region spectrum

Table 7.19 Sn 3d region components

Component	**Sn $3d_{3/2}$**
Line Shape	GL(30)
Area	1225.5
FWHM	1.55117
Position (eV)	486.08
Concentration (%)	100

Figure 7.45 shows XPS spectra from 482 eV to 490 eV of the Sn 3d region, the peak at 486.1 eV corresponds to the Sn 3d $_{5/2}$ which is close to the standard Sn $3d_{5/2}$ value [226]. Shown in Figure 7.46 is the photoelectron spectrum of O 1s, with a binding energy of 530.58 eV. The binding energies of the various core levels match well with XPS spectrum of bulk ZnO. The sub peaks are a Gaussian Lorentzian (GL (30)) distribution fitting for the O 1s peak. They are centred at 531.71 eV and 529.94 eV. The low binding energy component (529.94 eV) can be attributed to the O^{2-} ions. The intensity of this component measures the amount of oxygen atoms in a fully oxidised stoichiometric surrounding. The higher binding energy (531.71 eV) component is associated with O^{2-} ions in the oxygen deficient regions [27, 30].

Table 7.20 O 1s region components

Component	**O 1s**	**O 1s**
Line Shape	GL(30)	GL(30)
Area	10218.2	3717.7
FWHM	1.60704	1.45619
Position (eV)	531.71	529.94
Concentration (%)	73.32	26.68

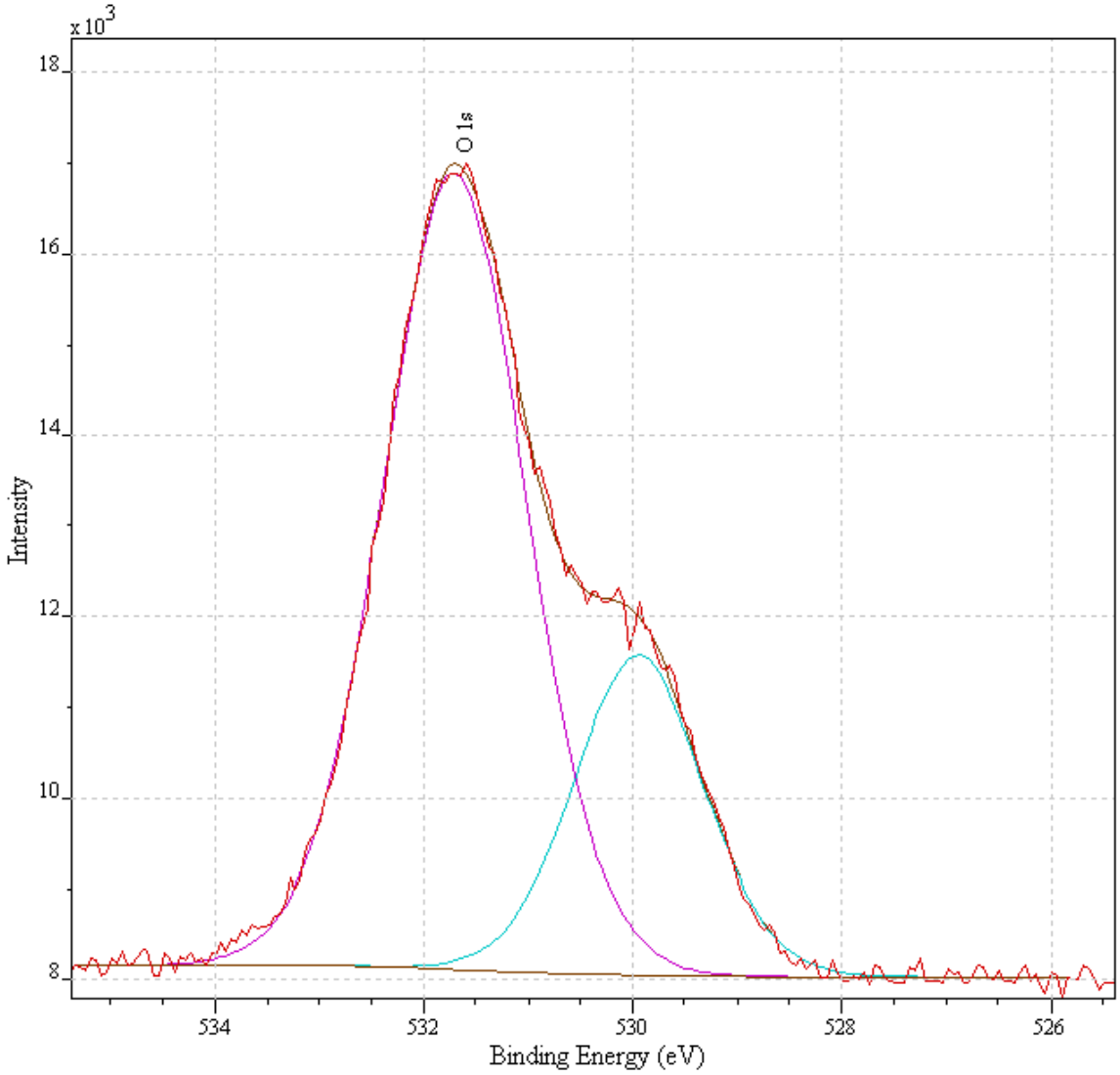

Figure 7.46 O1s narrow region spectrum

The following section presents a comparison of the important factors from the XPS analysis of the 40nm thick 90%:$In_2O_3$5%ZnO:5%SnO_2 deposited at deposition rates ranging from 0.1 -1.4nm/s. Of particular interest and importance are the binding energies and the shifting in these binding energies for varying the deposition rate while holding all other fabrication parameters constant.

7.10.7. Comparison of 40nm layer of $90\%In_2O_3:5\%ZnO:5\%SnO_2$ for various deposition rates

As can be seen from the previous sections, the presence of carbon C 1s at 284.6 can be attributed to surface contamination as a result of the sample being exposed to air before the XPS measurements as well as the contamination due to the decomposition of the precursor itself [236]. The presence of C1s peak is consistent throughout the XPS scans of these samples.

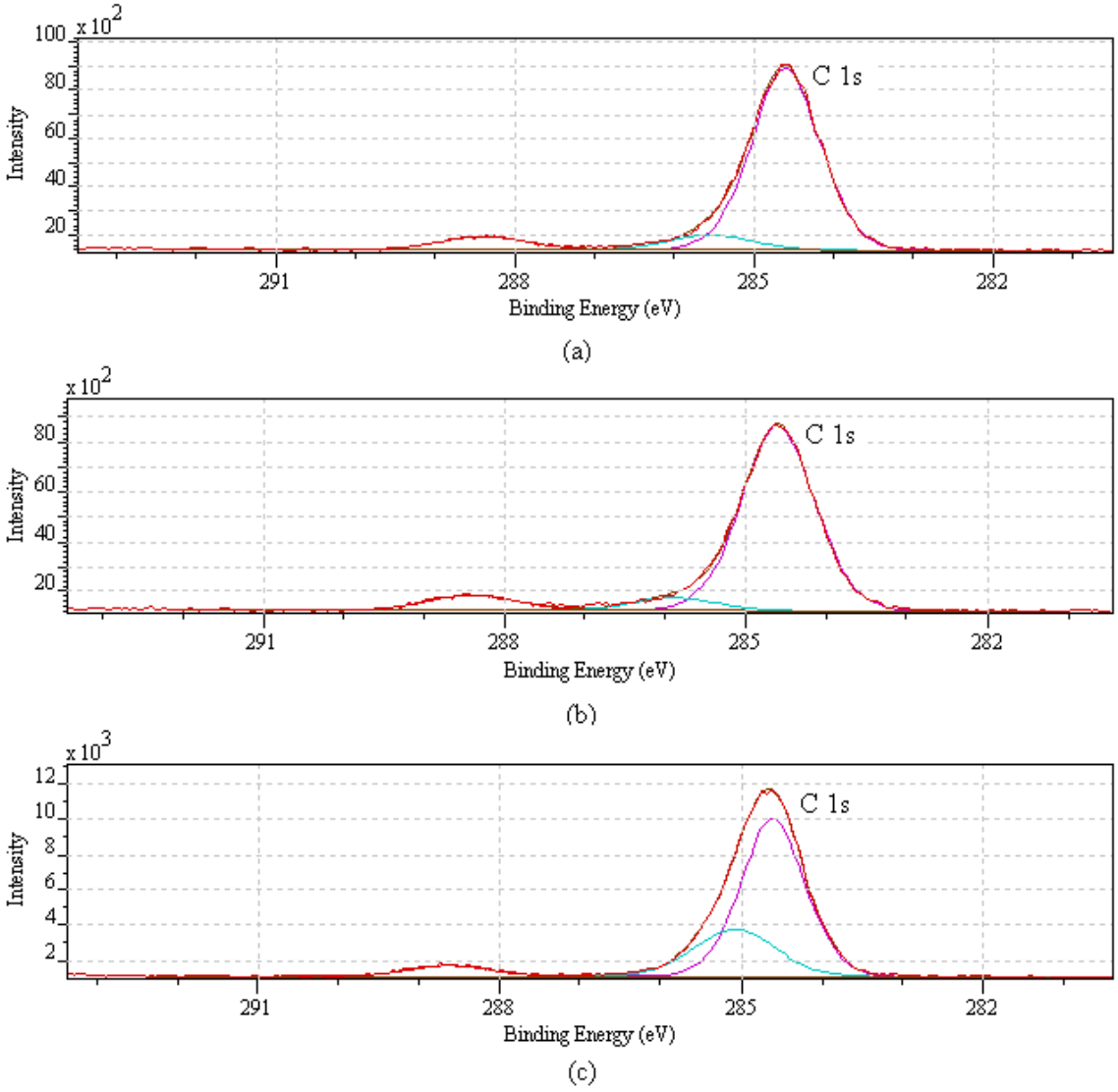

Figure 7.47 Plots of the C 1s narrow region spectra for deposition rates of (a) 0.1-0.3nm/s (b) 0.6-0.8nm/s (c) 1.1-1.4nm/s

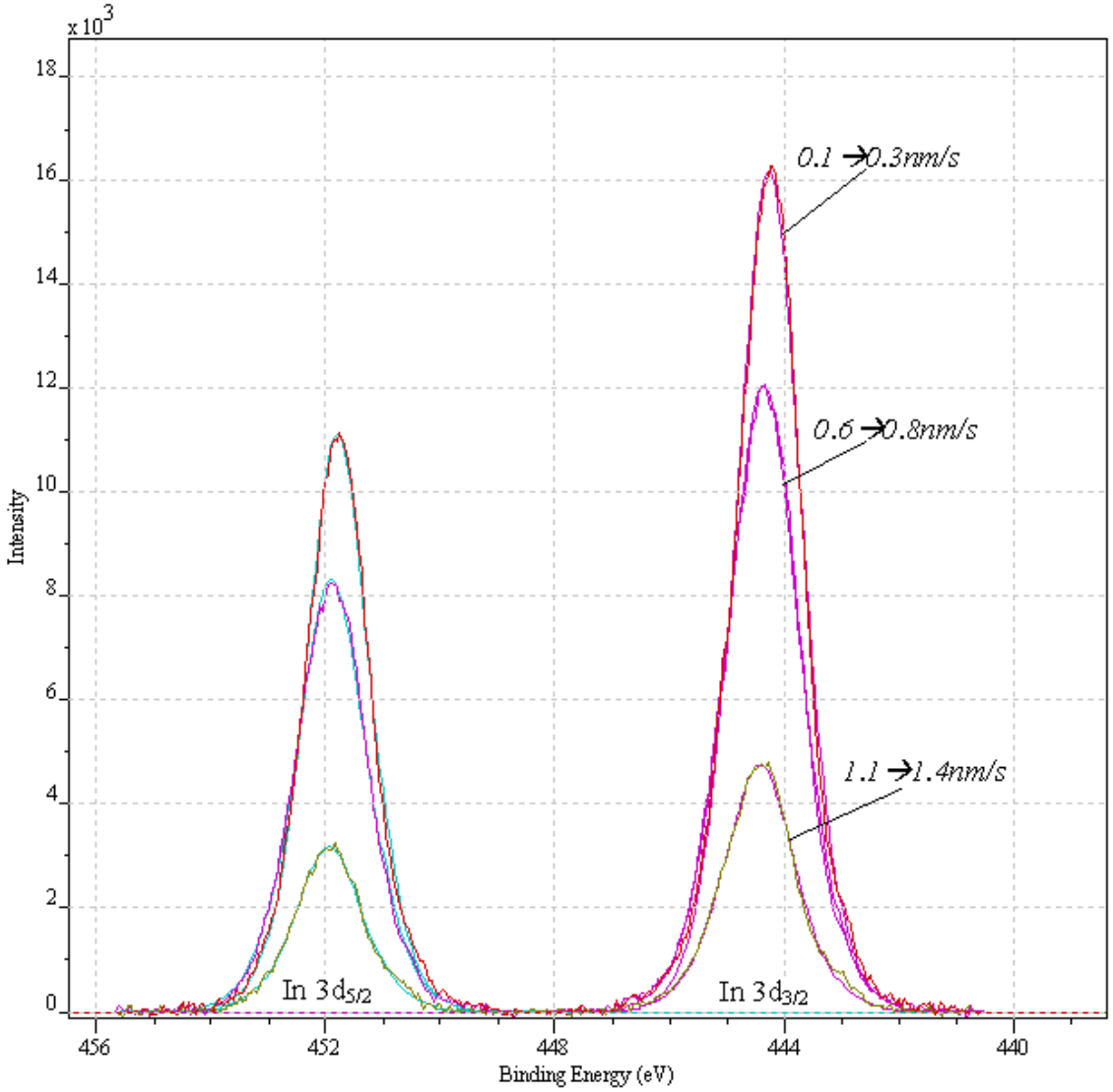

Figure 7.48 Illustration of slight shifts in binding energies of $In3d_{3/2}$ and $In3d_{5/2}$ peaks for samples prepared at different deposition rates

Table 7.21 Comparing shifts in binding energies of In3d peaks for varying deposition rates

Source Material → 90%In_2O_3:5%ZnO:5%SnO_2			
Deposition Rate (nm/s)	0.1→ 0.3	0.6 → 0.8	1.1 → 1.4
$In3d_{5/2}$ Position	451.786	451.894	451.937
$In3d_{3/2}$ Position	444.264	444.358	444.424

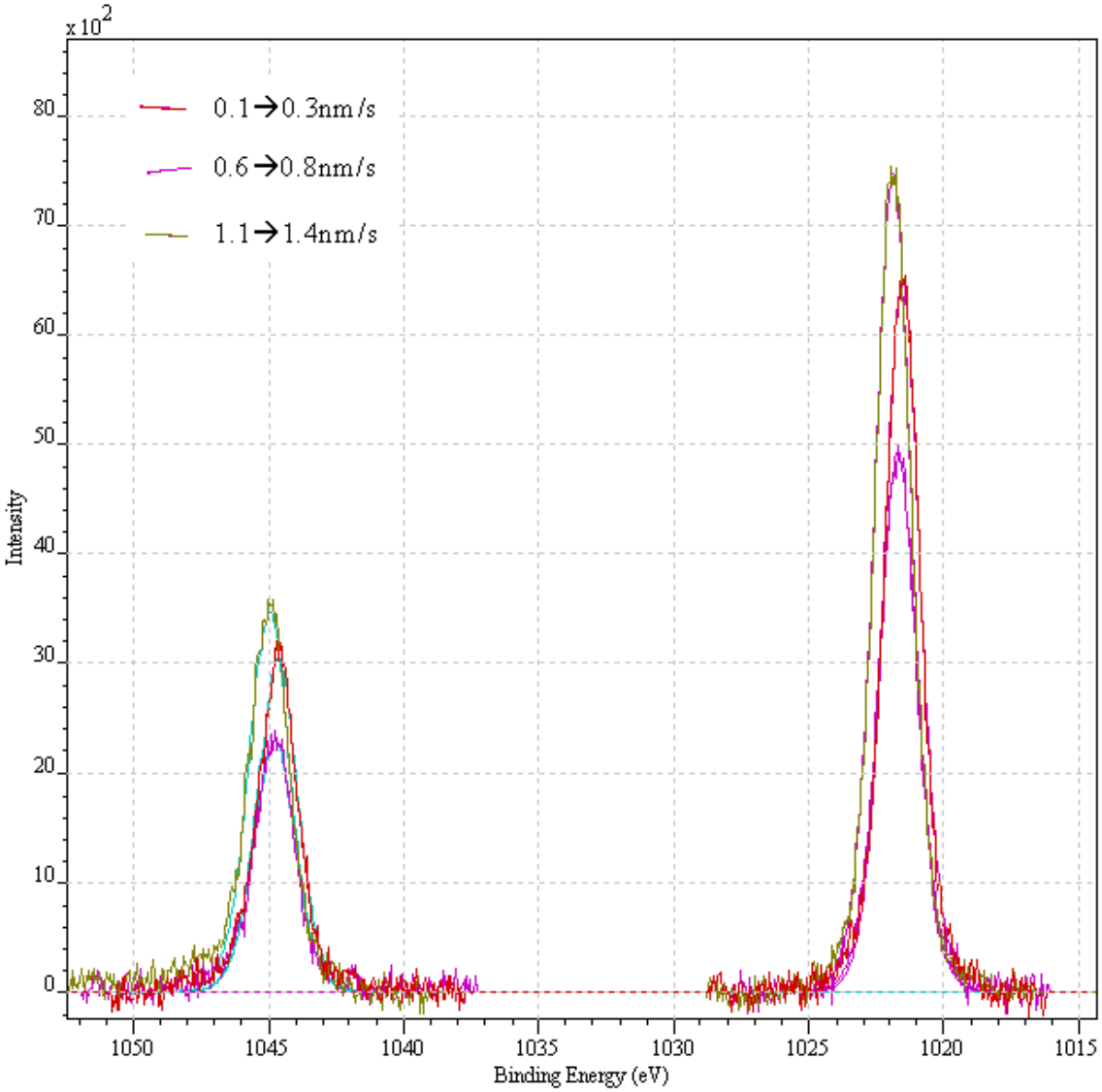

Figure 7.49 Illustration of slight shifts in binding energies of Zn2p peaks for samples prepared at different deposition rates

Table 7.22 Comparing shifts in binding energies of Zn2p peaks for varying deposition rates

Source Material → 90%In_2O_3:5%ZnO:5%SnO_2			
Deposition Rate (nm/s)	**0.1→ 0.3**	**0.6 → 0.8**	**1.1 → 1.4**
$Zn2p_{5/2}$ Position	1044.66	1044.79	1044.97
$Zn2p_{3/2}$ Position	1021.54	1021.69	1021.88

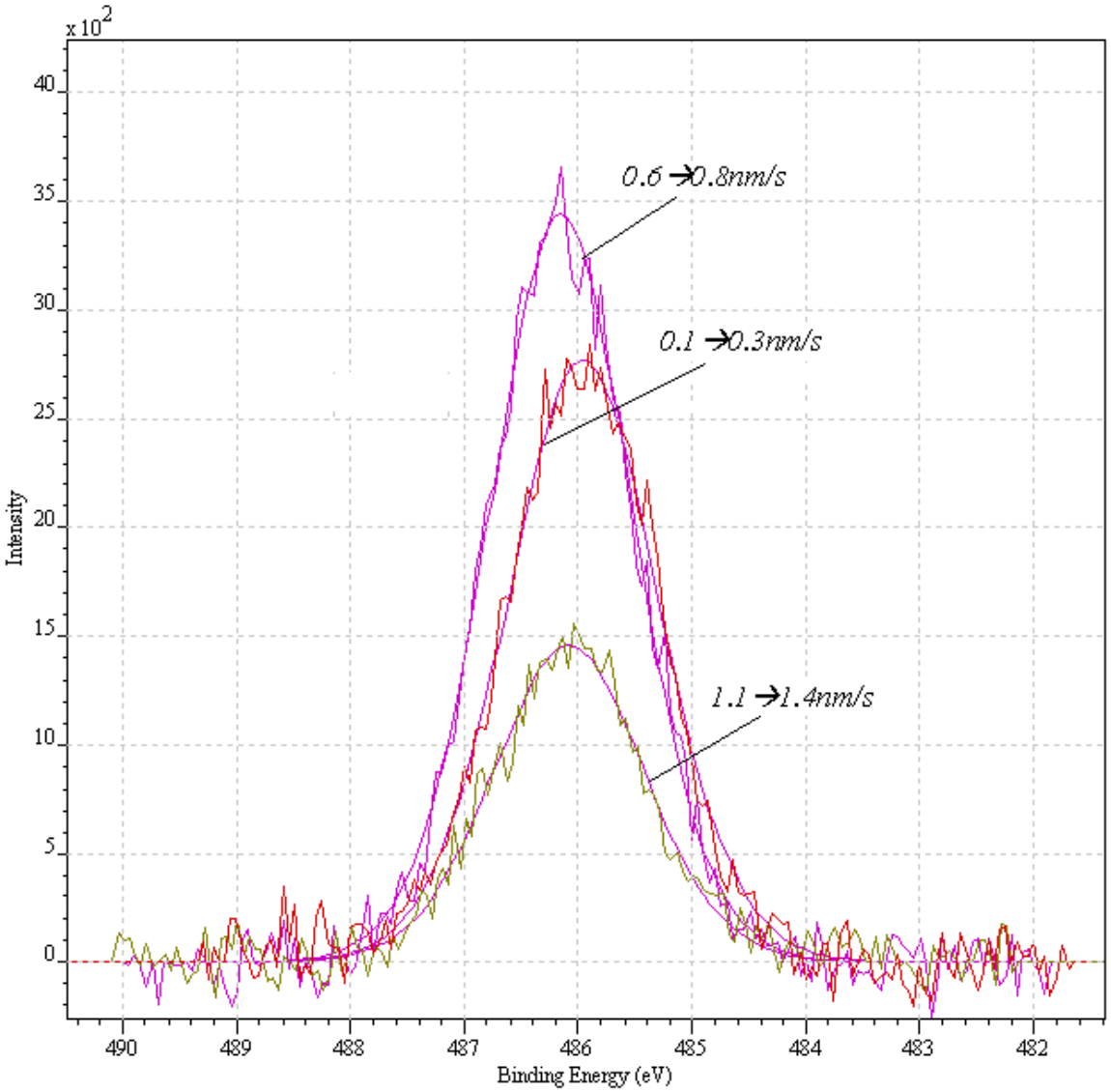

Figure 7.50 Illustration of slight shifts in binding energies of Sn3d peaks for samples prepared at different deposition rates

Table 7.23 Comparing shifts in binding energies of Sn3d peaks for varying deposition rates

Source Material→ 90%In_2O_3:5%ZnO:5%SnO_2			
Deposition Rate (nm/s)	**0.1→ 0.3**	**0.6 → 0.8**	**1.1 → 1.4**
$Sn3d_{5/2}$ Position	485.96	486.151	486.083

In_2O_3 is the most widely used oxide material for the detection of ozone concentrations in the pbb region [161] [167], [169], [171], [174], [240]. With the introduction of SnO_2 and ZnO, the intention is to increase the conductivity of the thin film and to create more free carriers. Degenerately doped semiconductors have conductivity levels comparable to that of some metals. Donor impurities create states near the conduction band. The gap between these energy states and the nearest energy band is usually referred to as dopant site bonding energy. It is so small that very little energy is required to ionise the dopant atoms and create free carriers in the conduction band. Usually thermal energy available at room temperature is sufficient to ionise most of the dopant.

Figure 7.47 – Figure 7.50 and Table 7.21 – Table 7.23 above illustrate the slight shift in binding energies for each of the In 3d, Zn2p and Sn 3d regions. These shifts in the binding energy (which is attributed to varying the deposition rate of the sensing layer) yield an increase in the response of the final sensing film.

From Figure 7.51 (a), (b) and (c) is the photoelectron spectrum of O 1s, for 40nm sensing layer of 90%In_2O_3:5%ZnO:5%SnO_2 deposited at rates of 0.1 – 0.3nm/s, 0.6 – 0.8nm/s and 1.1 – 1.4nm/s. As mentioned previously the sub peaks are a Gaussian Lorentzian (GL (30)) distribution fitting for the O 1s peak.

Table 7.24 gives a closer look at the binding energies for each of the separate peak components. Also included in Table 7.24 is the difference between the binding energies for each deposition rate. It can be seen that increasing the deposition rate of the source material yields an increase in the difference between the O 1s peaks. It is observed that the greater the difference in intensity of these two peaks, the greater the response of the sensor to 50, 120 and 240ppb of ozone (Figure 7.12).

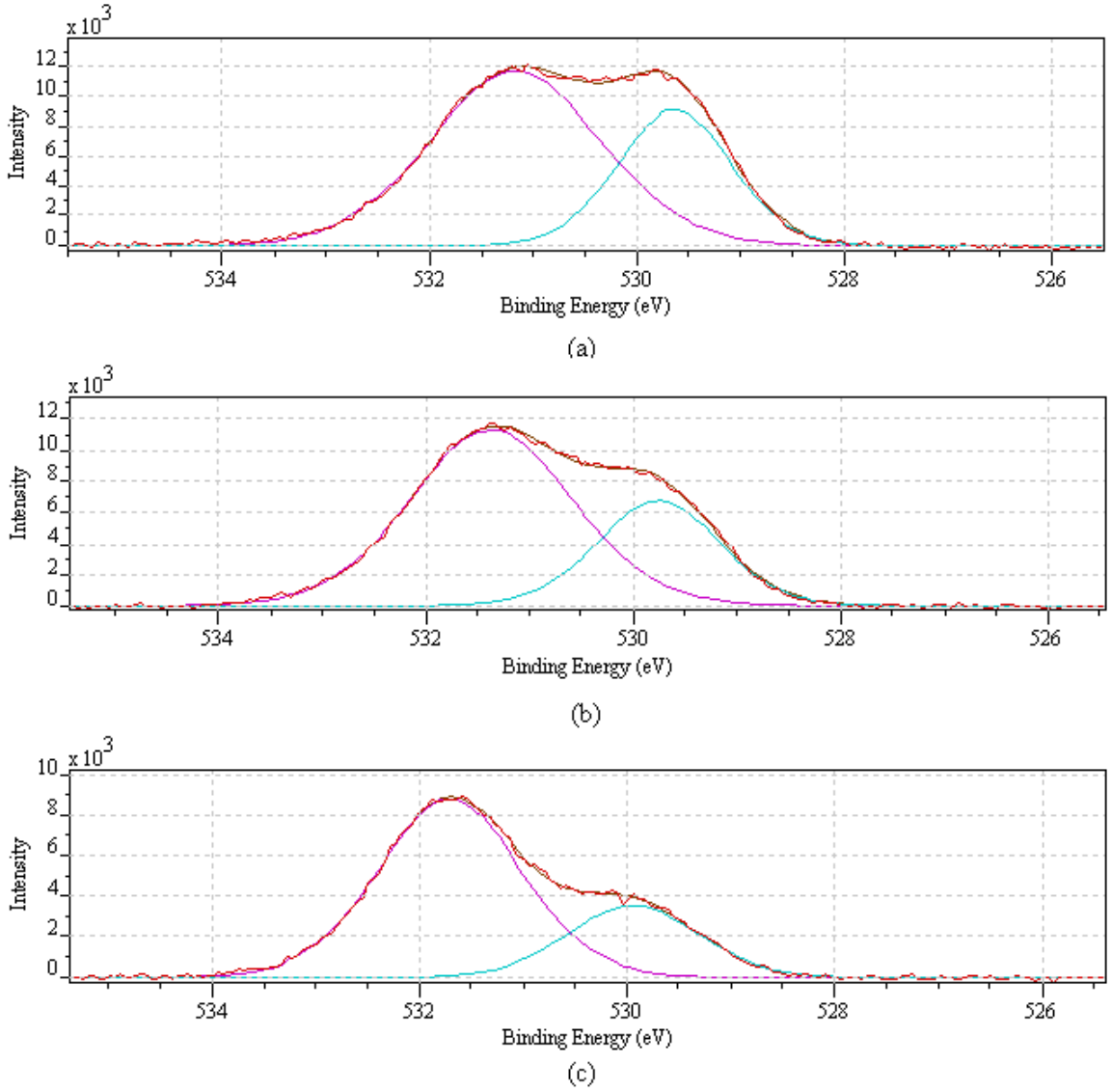

Figure 7.51 Binding Energy vs Intensity for O1s regions and components for (a) 0.1 – 0.3nm/s (b) 0.6 – 0.8nm/s (c) 1.1 – 1.4nm/s

Table 7.24 Comparing shifts in binding energies and intensities of O1s peaks for varying deposition rates

Source Material→ 90%In_2O_3:5%ZnO:5%SnO_2			
Deposition Rate (nm/s)	**0.1→ 0.3**	**0.6 → 0.8**	**1.1 → 1.4**
O1s_Pk1	*531.174*	*531.368*	*531.708*
O1s_Pk2	*529.638*	*529.759*	*529.941*
Difference between O1s Peak Positions	*1.536*	*1.609*	*1.757*

7.10.8. XPS Analysis of 40nm layer of $90In_2O_3:7ZnO:3SnO_2$ deposited at a rate of 0.6-0.8nm/s

Wide scan XPS spectra (from 0 – 1400 eV) of this sample is shown in Figure 7.52. The peak positions were referenced to carbon at 284.6 eV. Peaks of Zn $2p_{3/2}$, Zn $2p_{5/2}$, O 1s, Sn $3d_{3/2}$, In $3d_{3/2}$, In $3d_{5/2}$, C 1s and Mo 3d were detected at binding energies of 1021.72, 1044.85, 530.6, 486.1, 444.36, 451.89, 284.6 and 231.6 eV respectively.

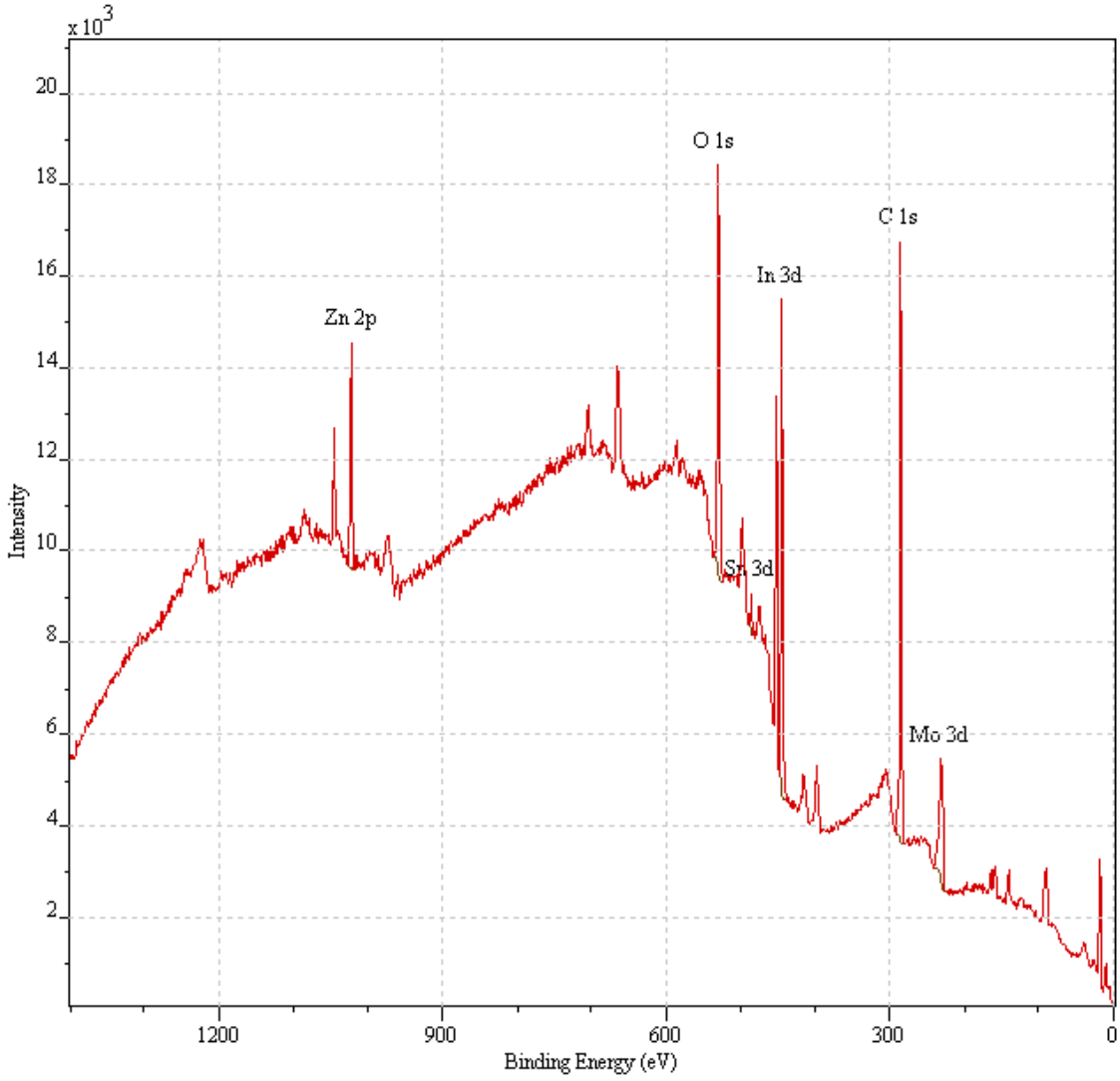

Figure 7.52 Wide range spectrum obtained from sample

Table 7.25 XPS Survey Results for $90In_2O_3:7ZnO:3SnO_2$ deposited at a rate of 0.6-0.8nm/s

Name	FWHM	Area	At %
Zn 2p	3.03827	9415.8	1.9
O 1s	3.38445	17842.1	23.25
Sn 3d	2.02128	1123.2	0.29
In 3d	2.82431	17761.4	5.10
C 1s	2.5533	17427.5	66.53
Mo 3d	6.02519	7314.1	2.94

A narrow scan XPS spectra (440 – 456 eV) of the In 3d region is shown in Figure 7.53, which shows doublet corresponding to In $3d_{3/2}$ and In $3d_{5/2}$. The 3d doublets were curve fitted using Shirley type base line with mixed Gaussian (30%) and Lorentzian (70%) (GL(30)).

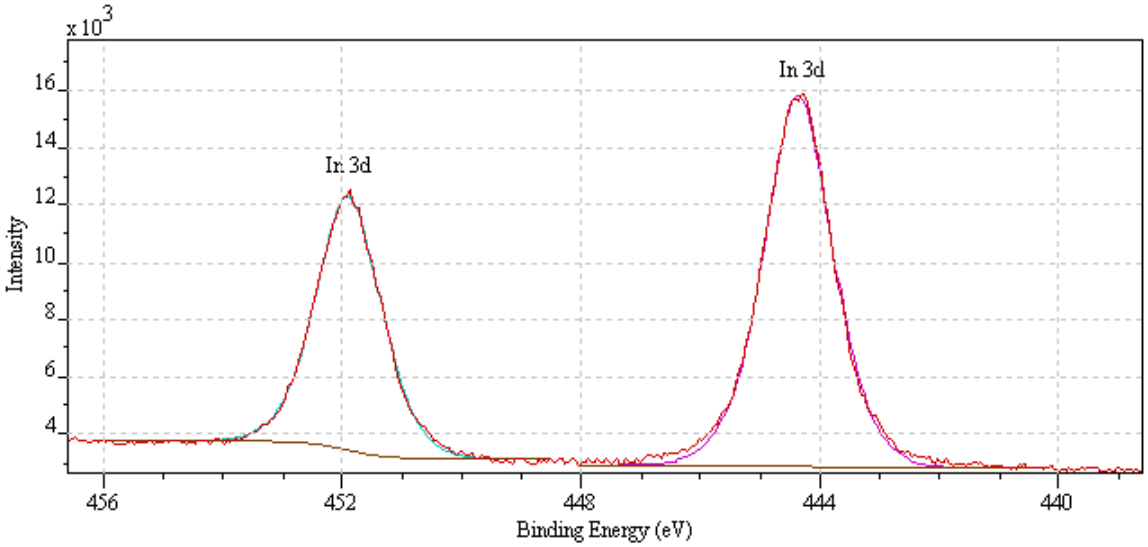

Figure 7.53 In3d doublet spectrum region

Table 7.26 In 3d region components

Component	**In $3d_{3/2}$**	**In $3d_{5/2}$**
Line Shape	GL(50)	GL(50)
Area	21325.5	14042.7
FWHM	1.33674	1.27714
Position (eV)	444.36	451.89
Concentration (%)	60.39	39.61

A narrow scan XPS spectra (from 1015 eV to 1055 eV) of the Zn 2p region is shown in Figure 7.54. The two peaks at 1044.85 eV and 1021.72 eV which correspond to the binding energies of Zn $2p_{1/2}$ and Zn $2p_{3/2}$ respectively, which are very close to the standard bulk ZnO binding energy values [237].

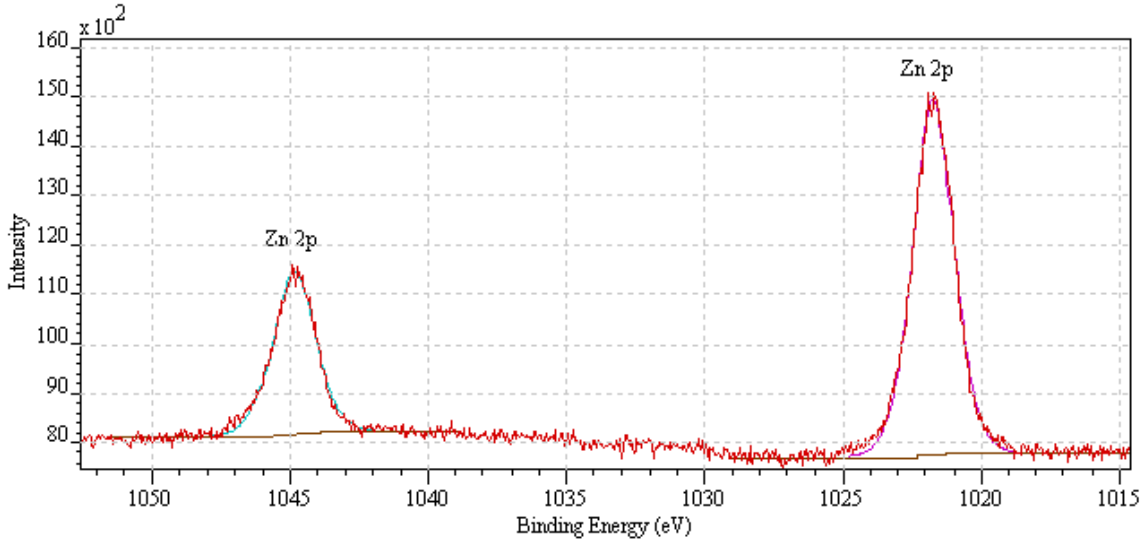

Figure 7.54 Zn2p doublet region spectrum

Table 7.27 Zn 2p region components

Component	**Zn $2p_{3/2}$**	**Zn $2p_{1/2}$**
Line Shape	GL(50)	GL(50)
Area	11318.2	5505.6
FWHM	1.69762	1.80095
Position (eV)	1021.72	1044.85
Concentration (%)	100	0

Figure 7.55 shows XPS spectra from 482 eV to 490 eV of the Sn 3d region, the peak at 486.09 eV corresponds to the Sn 3d $_{5/2}$ which is close to the standard Sn $3d_{5/2}$ value [226].

Table 7.28 Sn 3d region components

Component	**Sn $3d_{3/2}$**
Line Shape	GL(30)
Area	1422.9
FWHM	1.48607
Position (eV)	486.09
Concentration (%)	100

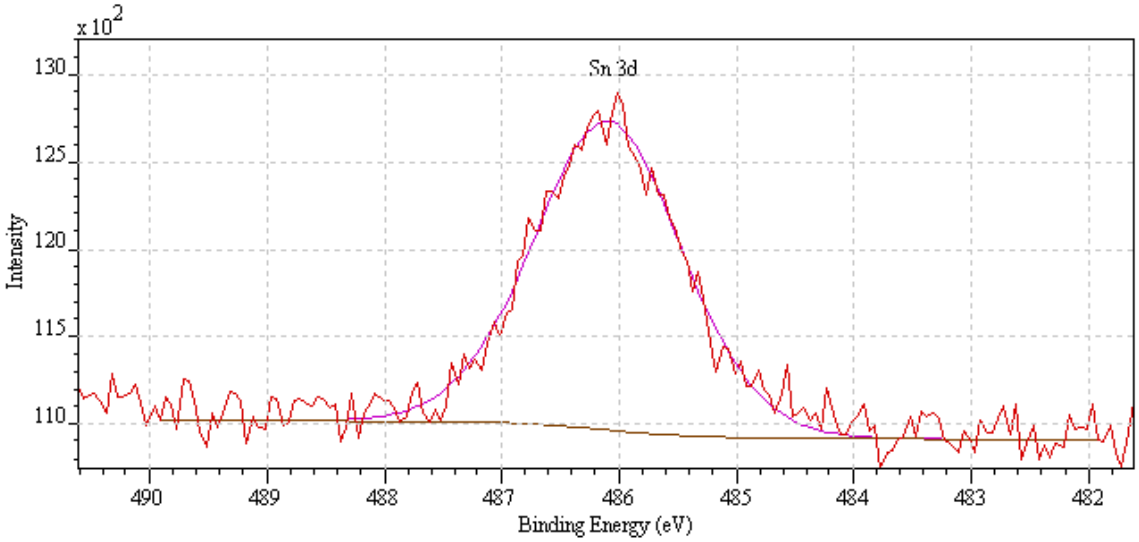

Figure 7.55 Sn3d 5/2 narrow region spectrum

Shown in Figure 7.56 is the photoelectron spectrum of O 1s, with a binding energy of 530.58 eV. The sub peaks are a Gaussian Lorentzian (GL (30)) distribution fitting for the O 1s peak.

Table 7.29 details the specifics of the O 1s component peaks, the position as well as the intensity of these peaks are important when compared to other samples which have slightly different concentrations of the source material.

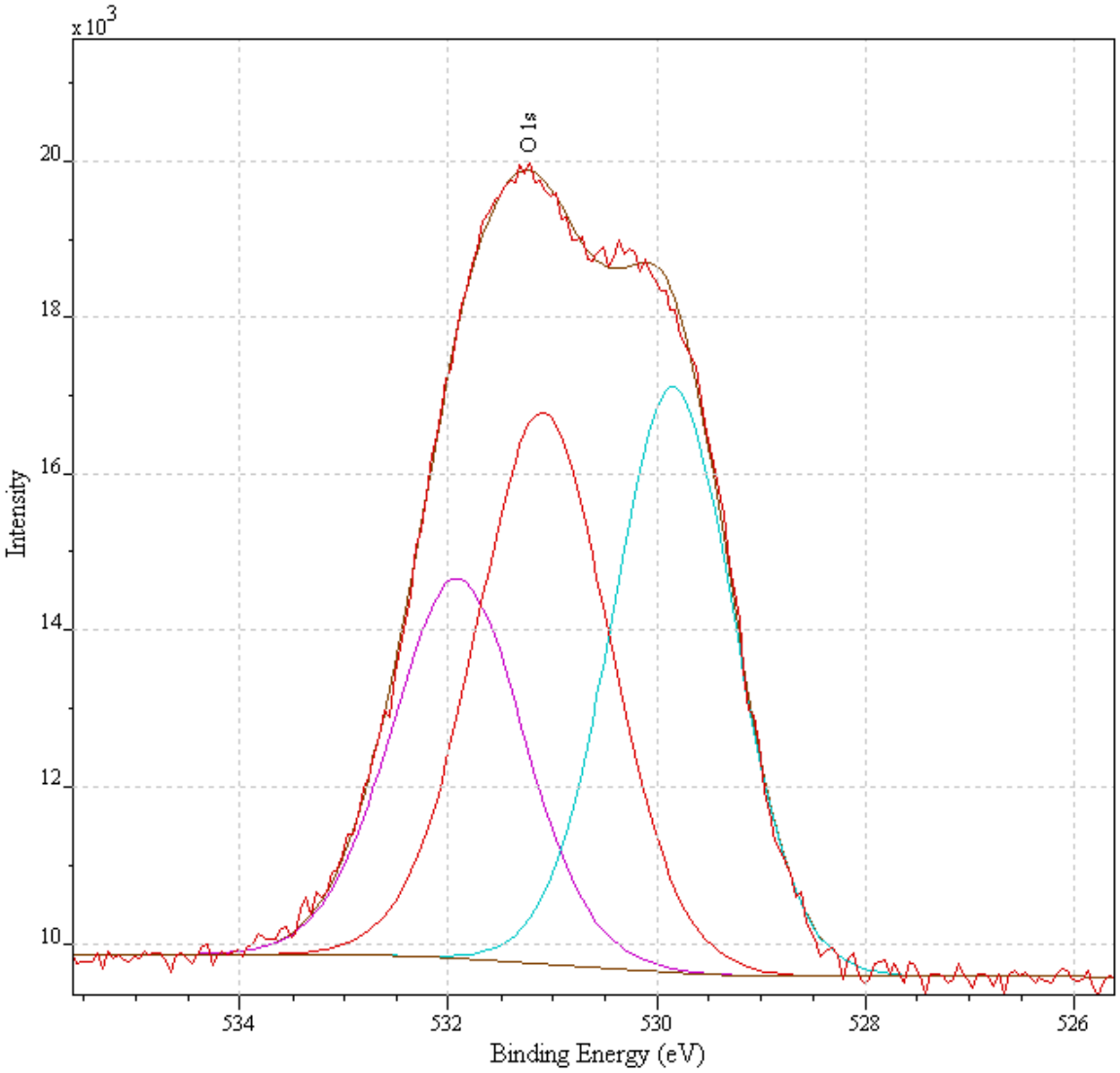

Figure 7.56 O1s narrow region spectrum

Table 7.29 O 1s region components

Component	**O 1s**	**O 1s**	**O 1s**
Line Shape	GL(30)	GL(30)	GL(30)
Area	5200.3	7443.9	7635.7
FWHM	1.47822	1.37418	1.5
Position (eV)	531.91	529.84	531.094
Concentration (%)	25.64	36.7	37.65

7.10.9. XPS Analysis of 40nm layer of $90In_2O_3:3ZnO:7SnO_2$ deposited at a rate of 0.6-0.8nm/s

Table 7.30 XPS Survey Results for $90In_2O_3:3ZnO:7SnO_2$ deposited at a rate of 0.6-0.8nm/s

Name	**FWHM**	**Area**	**At %**
Zn 2p	2.65079	4906.3	1.03
O 1s	3.21539	23342.2	31.65
Sn 3d	2.86848	5079.1	1.36
In 3d	2.67747	30703.7	9.17
C 1s	2.59124	13132.5	52.17
Mo 3d	5.69116	11040.8	4.62

Wide scan XPS spectra (from 0 – 1400 eV) of this sample is shown in Figure 7.57. The peak positions were referenced to carbon at 284.6 eV (standard practice). Peaks of Zn $2p_{3/2}$, Zn $2p_{5/2}$, O 1s, Sn $3d_{3/2}$, In $3d_{3/2}$, In $3d_{5/2}$, C 1s and Mo 3d were detected at binding energies of 1021.59, 1044.70, 530.6, 486.33, 444.45, 452.03, 284.6 and 231.6 eV respectively.

The presence of carbon C 1s at 284.6 can be attributed to surface contamination as a result of the sample being exposed to air before the XPS measurements as well as the contamination due to the decomposition of the precursor itself [236].

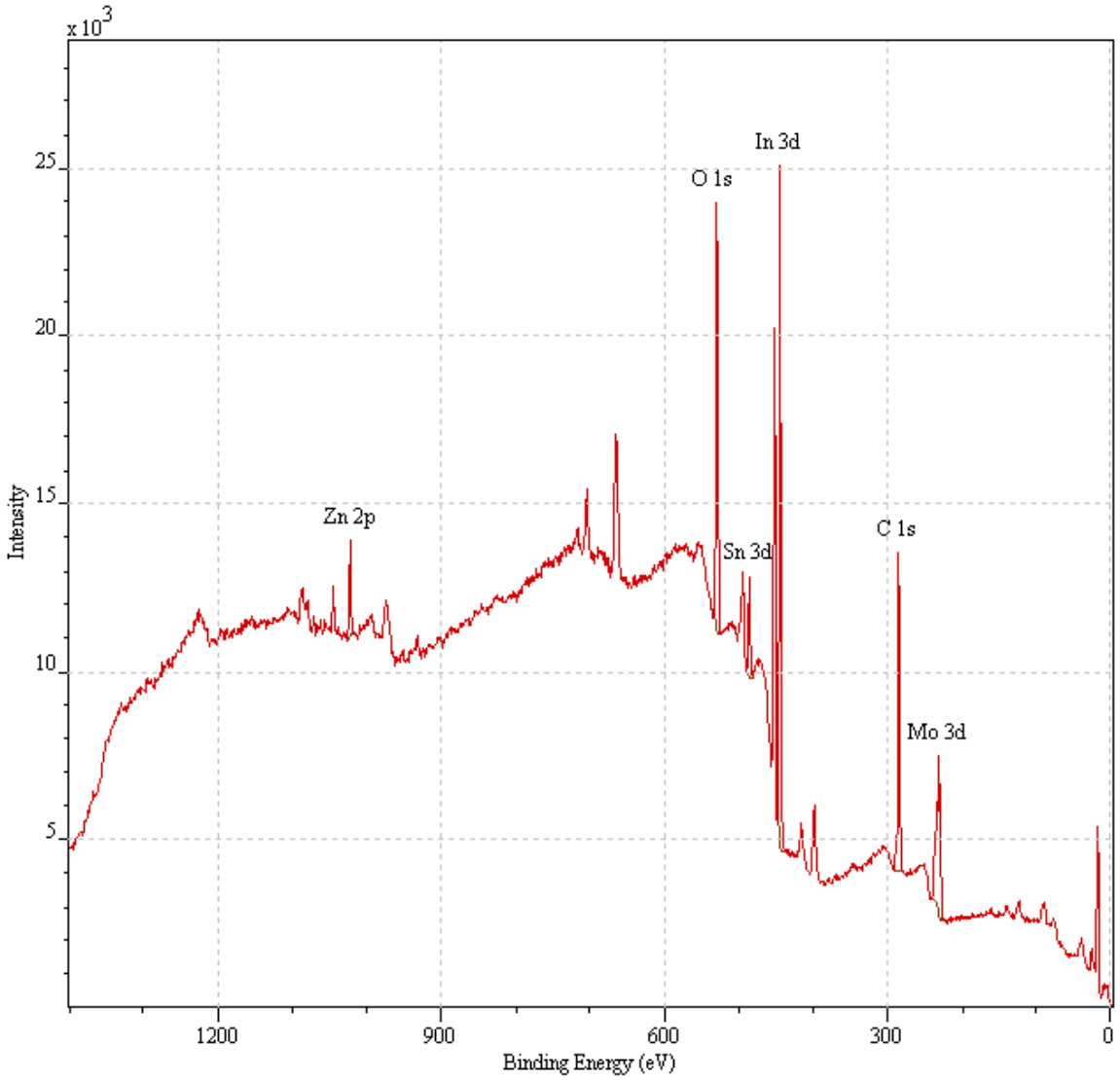

Figure 7.57. Wide range spectrum obtained from sample

Table 7.31 In 3d region components

Component	**In $3d_{3/2}$**	**In $3d_{5/2}$**
Line Shape	GL(50)	GL(50)
Area	38261.2	25600.7
FWHM	1.30636	1.28013
Position (eV)	444.49	452.03
Concentration (%)	60.01	39.99

A narrow scan XPS spectra (440 – 456 eV) of the In 3d region is shown in Figure 7.58, which shows doublet corresponding to In $3d_{3/2}$ and In $3d_{5/2}$. The 3d doublets were curve fitted using Shirley type base line with mixed Gaussian (30%) and Lorentzian (70%) (GL(30)).

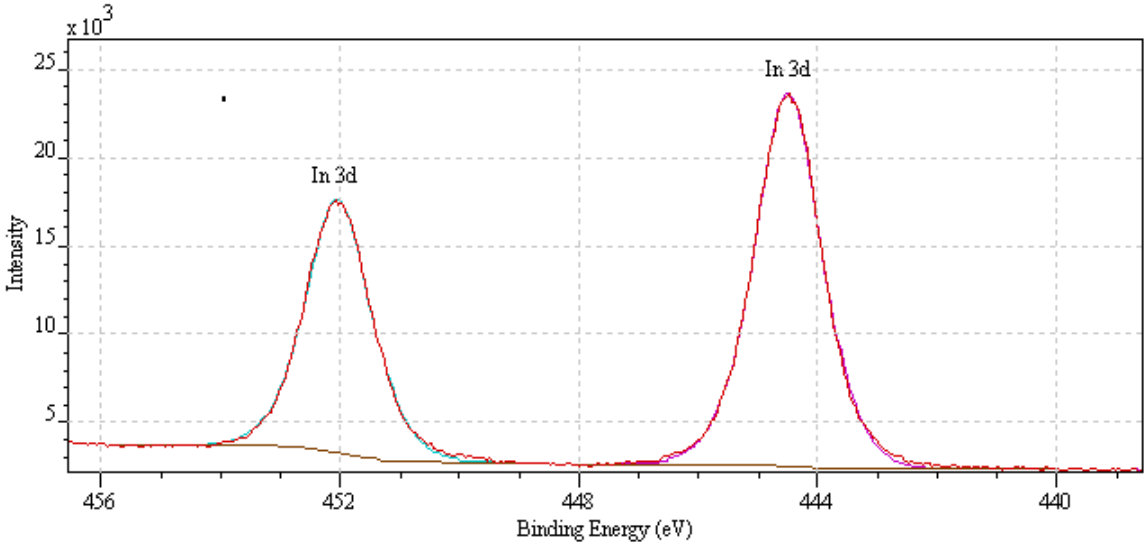

Figure 7.58 In3d doublet spectrum region

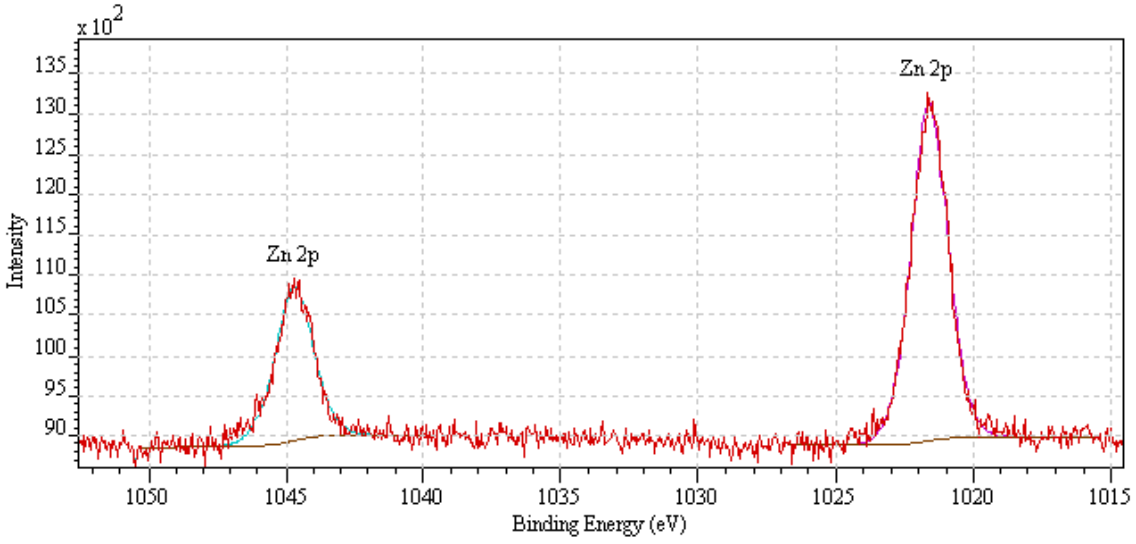

Figure 7.59 Zn2p doublet region spectrum

A narrow scan XPS spectra (from 1015 eV to 1055 eV) of the Zn 2p region is shown in Figure 7.59. The two peaks at 1044.7 eV and 1021.59 eV which correspond to the binding energies of Zn $2p_{1/2}$ and Zn $2p_{3/2}$ respectively, which are very close to the standard bulk ZnO binding energy values [237].

Figure 7.60 shows XPS spectra from 482 eV to 490 eV of the Sn 3d region, the peak at 486.33 eV corresponds to the Sn 3d $_{5/2}$ which is close to the standard Sn $3d_{5/2}$ value [238].

Table 7.32 Zn 2p region components

Component	**Zn $2p_{3/2}$**	**Zn $2p_{1/2}$**
Line Shape	GL(50)	GL(50)
Area	5868.0	2867.9
FWHM	1.50639	1.61002
Position (eV)	1021.59	1044.7
Concentration (%)	67.04	32.96

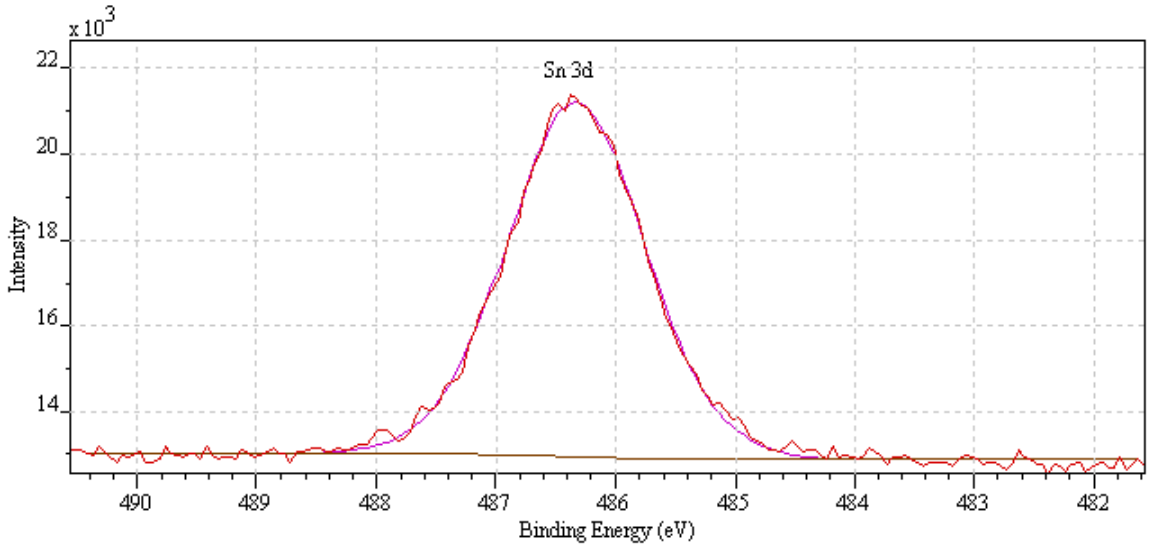

Figure 7.60 Sn3d 5/2 narrow region spectrum

Table 7.33 Sn 3d region components

Component	**Sn $3d_{3/2}$**
Line Shape	GL(30)
Area	6066.0
FWHM	1.35543
Position (eV)	486.33
Concentration (%)	100

Shown in Figure 7.61 is the photoelectron spectrum of O 1s, with a binding energy of 530.58 eV. The binding energies of the various core levels match well with XPS spectrum of bulk ZnO. The sub peaks are a Gaussian Lorentzian (GL (30)) distribution fitting for the O 1s peak. They are centred at 531.092 eV aand 529.722 eV.

Table 7.34 O 1s region components

Component	**O 1s**	**O 1s**
Line Shape	GL(30)	GL(30)
Area	17077.7	11562.0
FWHM	1.80049	1.40794
Position (eV)	531.18	529.96
Concentration (%)	59.63	40.37

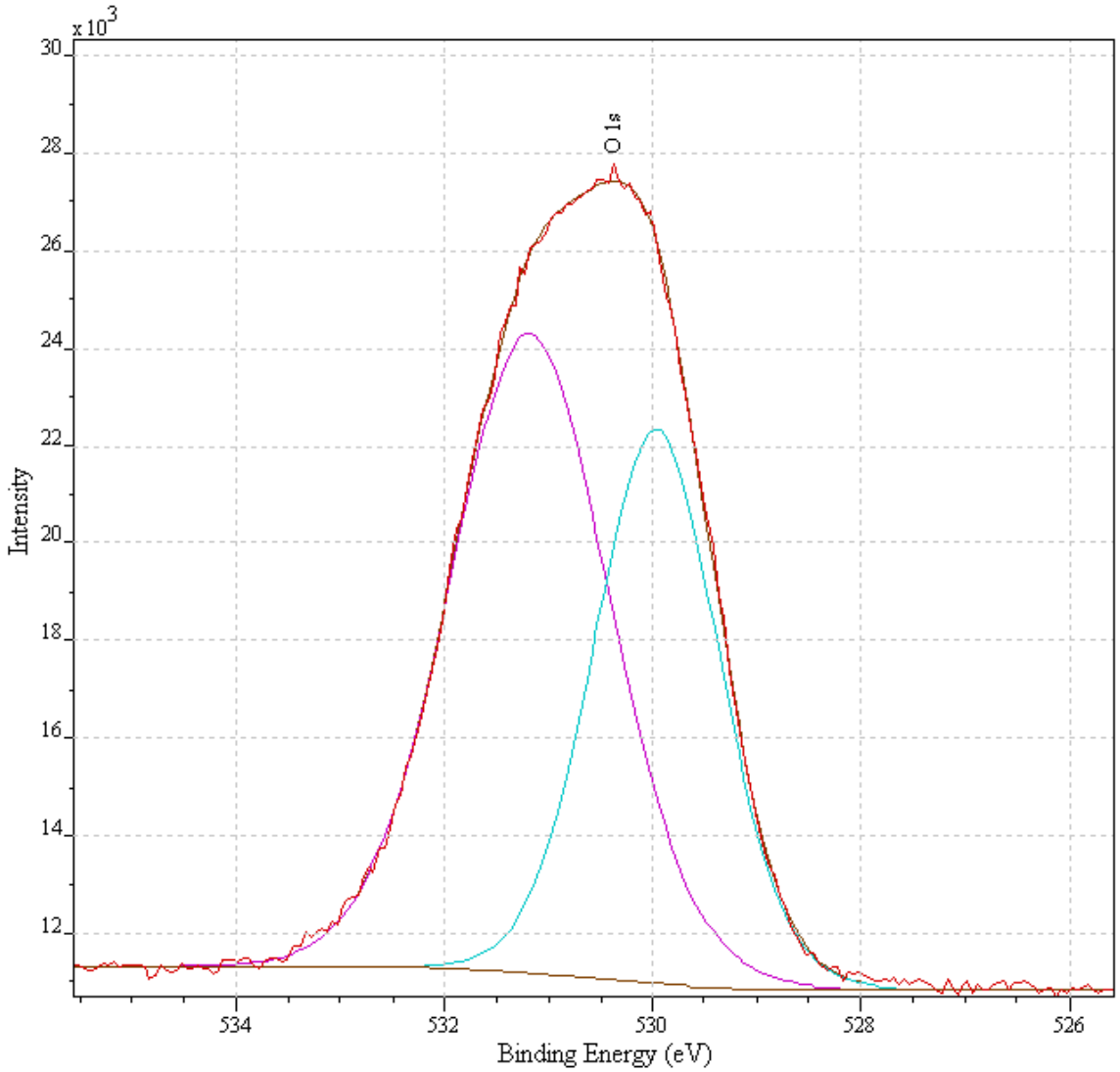

Figure 7.61 O1s narrow region spectrum

7.10.10. Comparison of 40nm layer of different source material concentrations deposited at a rate of 0.6 – 0.8nm/s

As can be seen from previous Tables, the presence of carbon C 1s at 284.6 can be attributed to surface contamination as a result of the sample being exposed to air before the XPS measurements as well as the contamination due to the decomposition of the precursor itself [236]. The presence of C1s peak is consistent throughout the XPS scans of these samples.

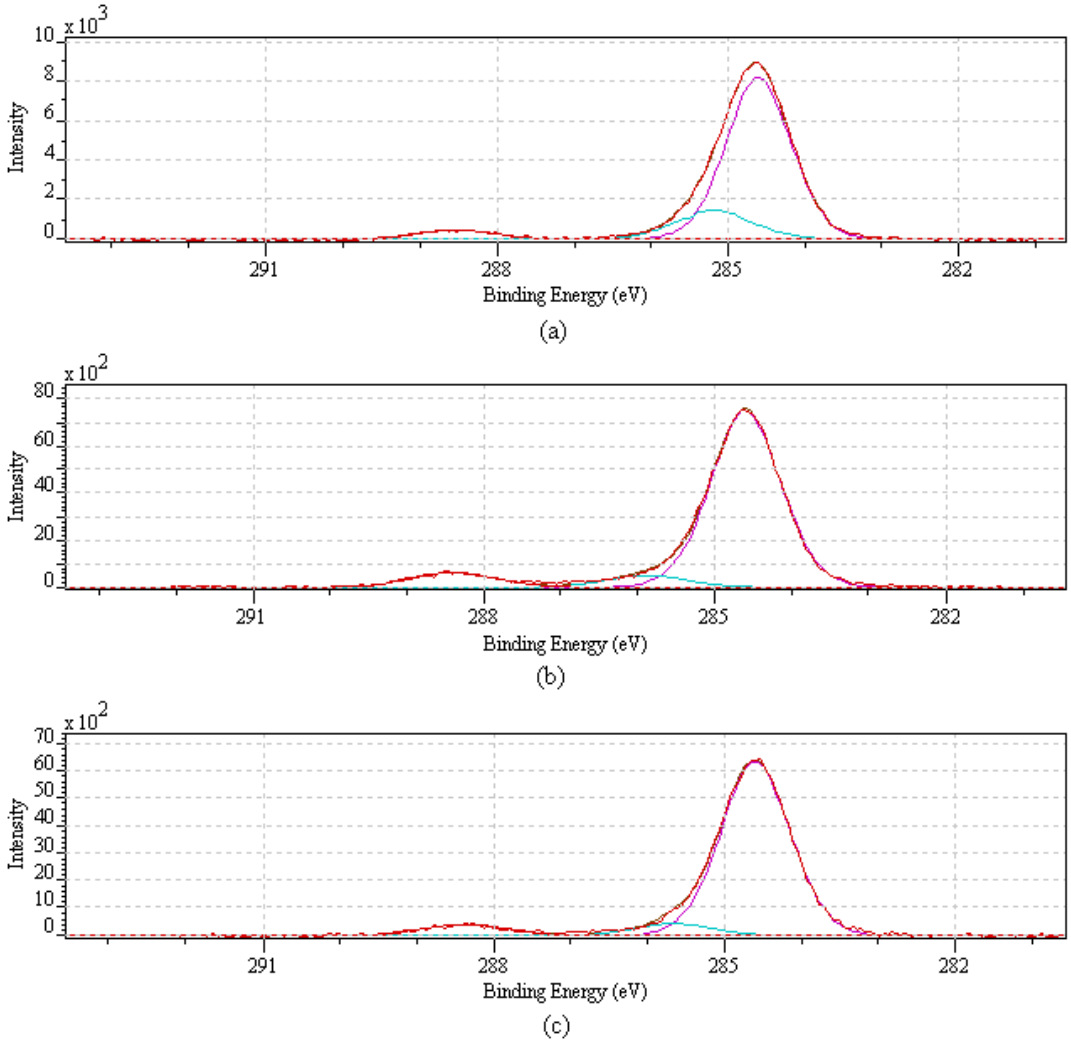

Figure 7.62 Plots of the C 1s narrow region spectra for deposition rates for (a) 90%In_2O_3:7%ZnO:3%SnO_2 (b) 90%In_2O_3:5%ZnO:5%SnO_2 (c) 90%In_2O_3:3%ZnO:7%SnO_2

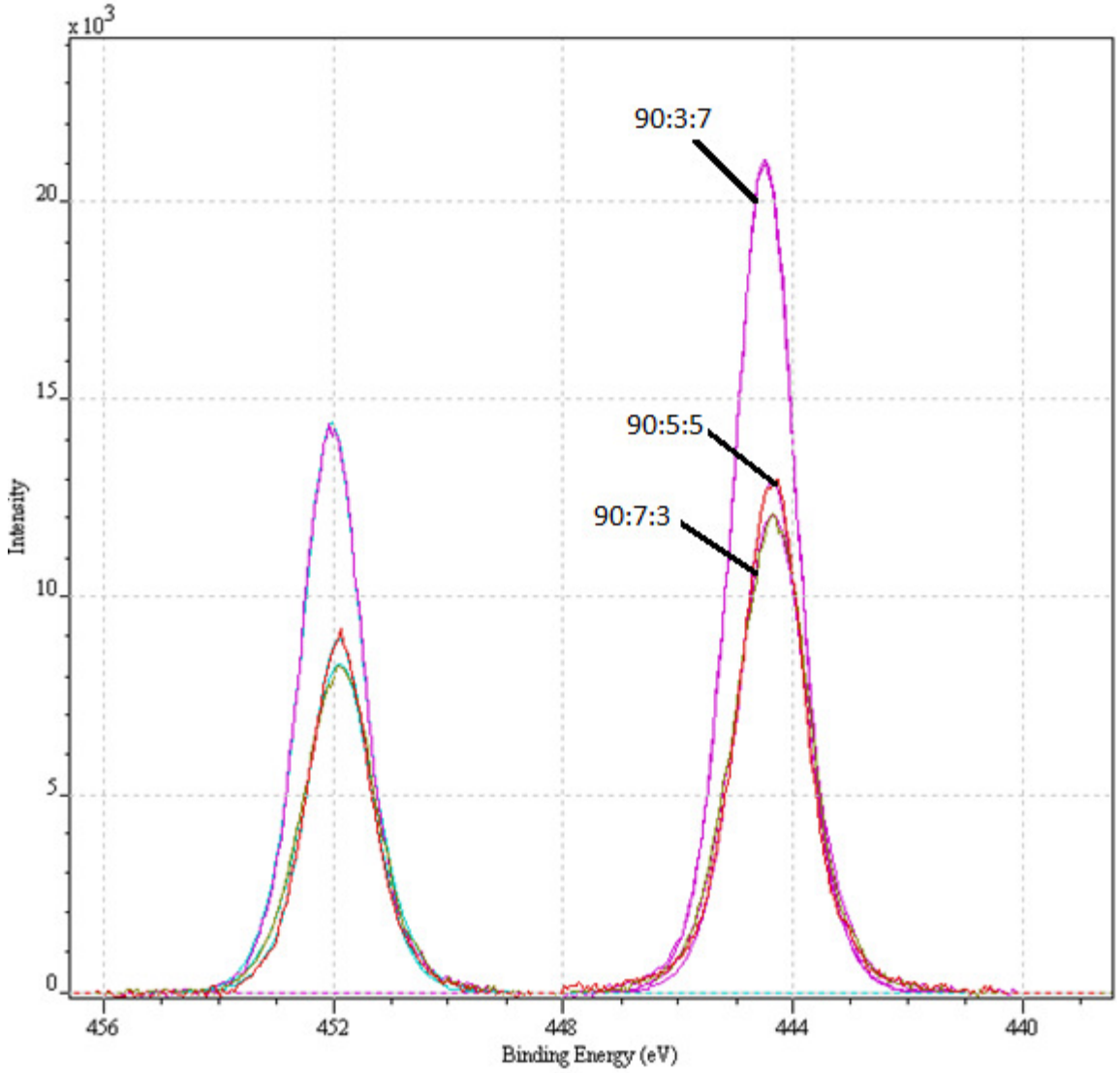

Figure 7.63 Illustration of shifts in binding energies of In3d peaks for samples prepared with various concentrations

Table 7.35 Comparing shifts in binding energies of In3d peaks for varying source material

40nm Sensing Layer @ 0.6 → 0.8nm/s			
%In_2O_3:%ZnO:%SnO_2	**90:7:3**	**90:5:5**	**90:3:7**
In3d Peaks	451.893	451.894	452.03
In3d Peaks	444.363	444.358	444.498

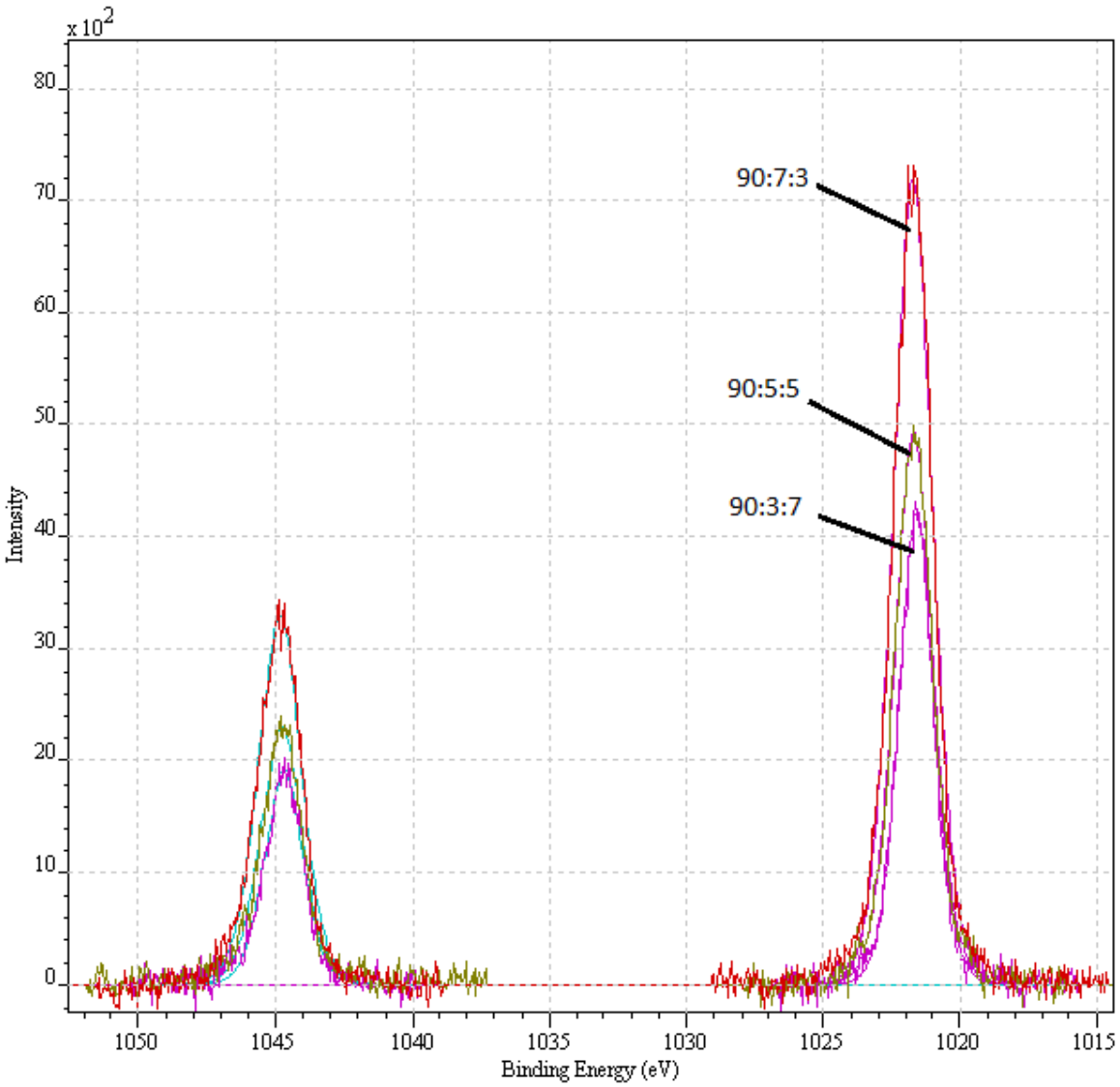

Figure 7.64 Illustration of shifts in binding energies of Zn2p peaks for samples prepared with various concentrations

Table 7.36 Comparing shifts in binding energies of Zn2p peaks for varying source material

40nm Sensing Layer @ 0.6 → 0.8nm/s			
%In_2O_3:%ZnO:%SnO_2	**90:7:3**	**90:5:5**	**90:3:7**
Zn2p Peaks	1044.85	1044.79	1044.70
Zn2p Peaks	1021.72	1021.69	1021.59

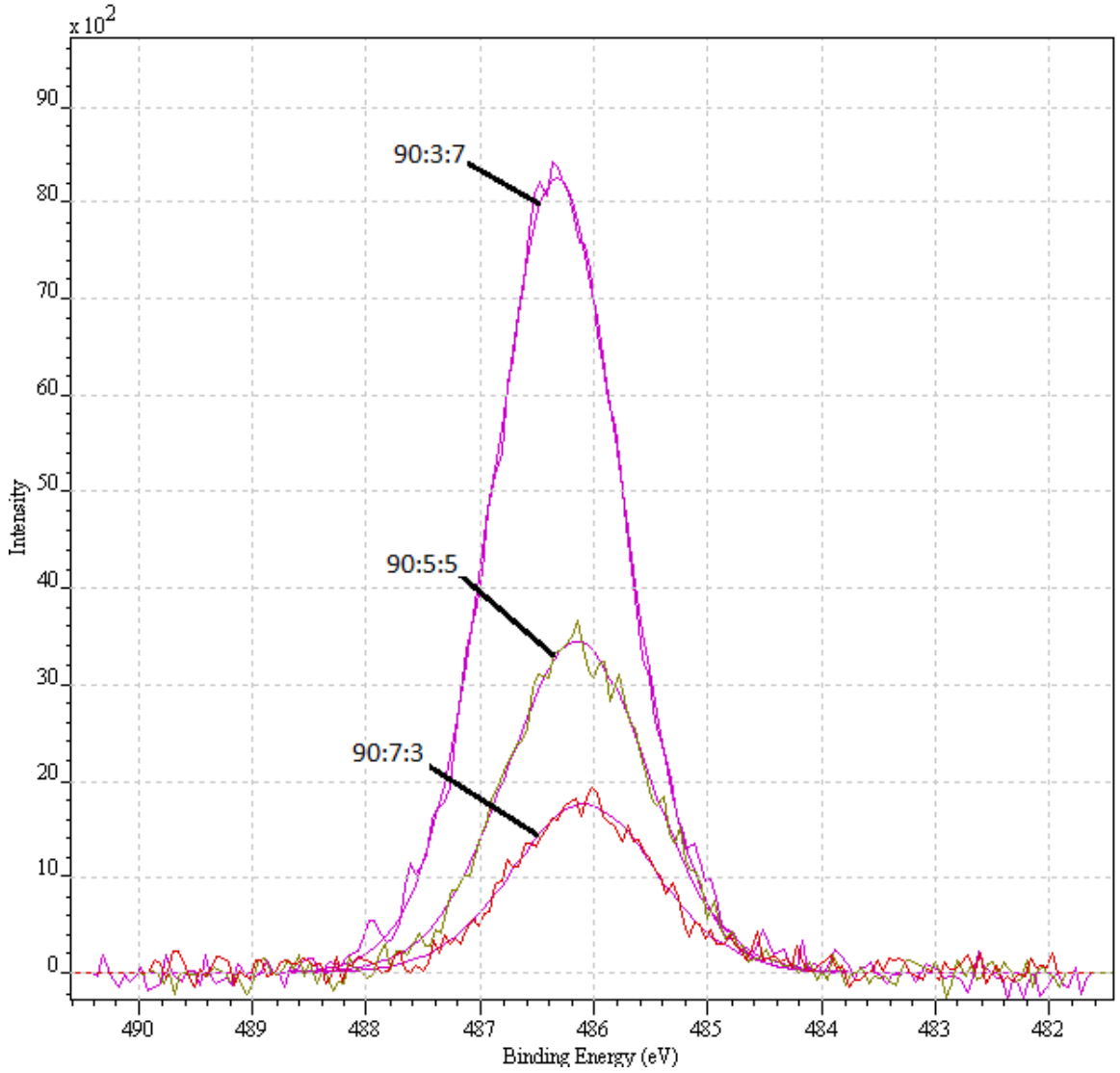

Figure 7.65 Illustration of shifts in binding energies of Sn3d peaks for samples prepared with various concentrations

Table 7.37 Comparing shifts in binding energies of Sn3d peaks for varying source material

40nm Sensing Layer @ 0.6 → 0.8nm/s			
%In_2O_3:%ZnO:%SnO_2	**90:7:3**	**90:5:5**	**90:3:7**
Sn3d Peaks	486.091	486.151	486.329

Slight variations in the molar percentages of the source material have been shown to have significant effects on the performance of the sensing device. From the previous three Figures and Tables it can be seen that there is a slight shift in the binding energies of these metal oxide peaks caused by varying the composition of the source material. The mixing of oxides may lead to more oxygen vacancies being present at the surface of the sensing layer. Oxygen vacancies play an important role as adsorption sites for gaseous species.

Table 7.38 Comparing shifts in binding energies of O1s peaks for varying source material

40nm Sensing Layer @ 0.6 → 0.8nm/s			
%In_2O_3:%ZnO:%SnO_2	**90:7:3**	**90:5:5**	**90:3:7**
O1s Component Pk_1	531.094	531.368	531.182
O1s Component Pk_2	529.843	529.759	529.963
O1s Component Pk_3	531.911	_____	_____

The O1s peaks observed in the wide spectrum scans can be deconvoluted into three separated features, located at binding energy values of 529.843 eV, 531.094 eV and 531.911 eV. The 529.843 eV peak (Pk_1) is assigned to lattice oxygen and the 531.094eV (Pk_2) peak to lattice oxygen in oxygen deficient regions. The metal hydroxide and/or oxy-hydroxide oxygen feature is observed at a binding energy of 531.911 eV (Pk_3).

This higher binding energy peak is possibly due to the indium hydroxide on the outer most surface of the sensing layer. This compound possibly deteriorates the ozone sensitivity of the device due to the fact that hydroxide groups have occupied the oxygen vacancies and as a result there is less chance for the ozone molecules to interact with the sensing film.

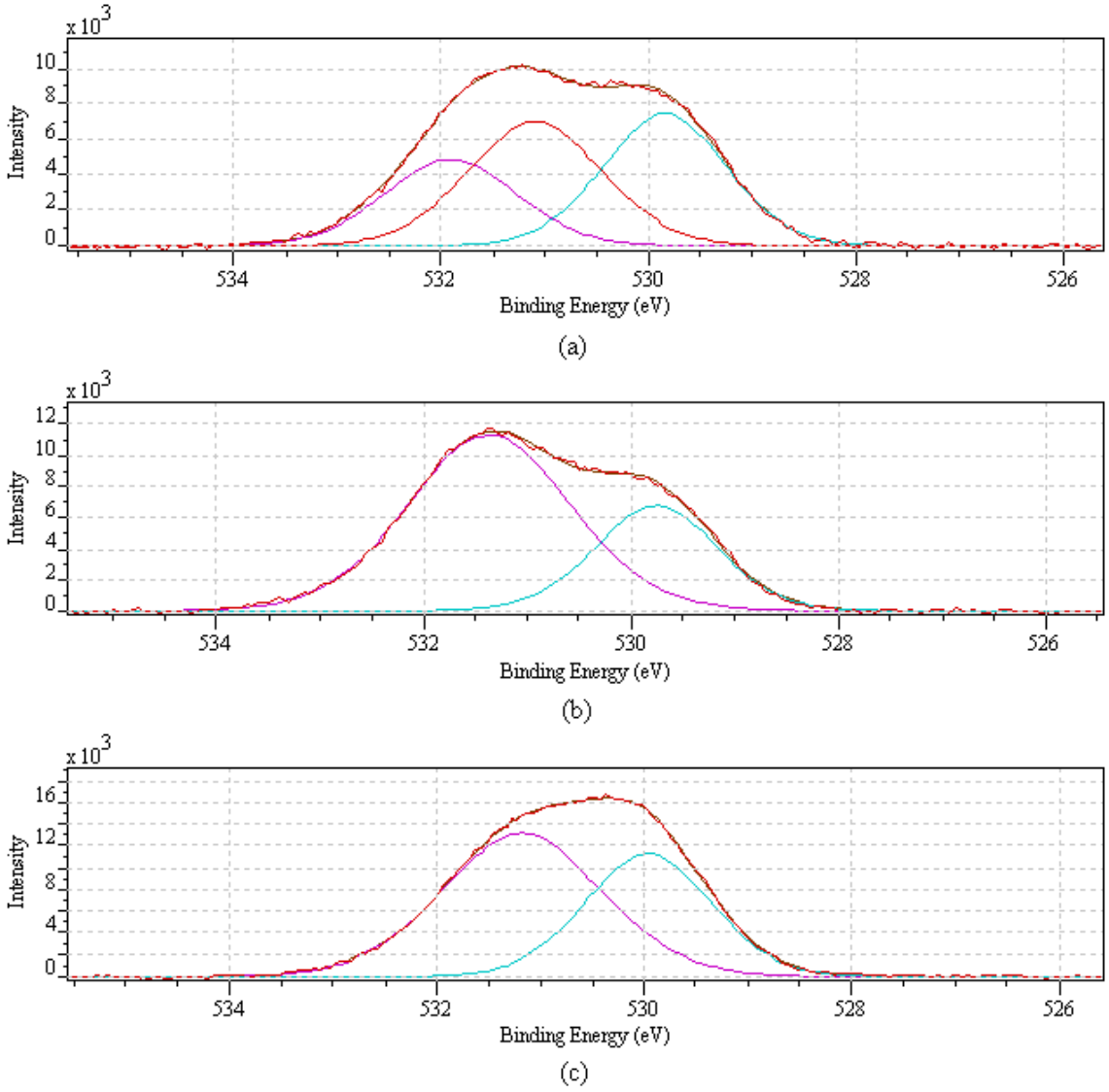

Figure 7.66 Binding Energy vs Intensity for O1s regions and components for (a) 90%In_2O_3:7%ZnO:3%SnO_2 (b) 90%In_2O_3:5%ZnO:5%SnO_2 (c) 90%In_2O_3:3%ZnO:7%SnO_2

7.11. XRD Analysis

X-ray diffractometer PW3050/60 θ-θ within a scan range of 5 to 90 (°2θ) was used to reveal the structure of the deposited thin films. The samples were mounted on glass slides and placed on a Eularian cradle. A glancing angle of 3 (°2θ) was applied in order to prevent anomalous data being obtained from the glass slide backing material. The XRD data disclosed an amorphous structure of In_2O_3:ZnO:SnO_2 (90:5:5) thin film, as shown in Figure 7.67 below.

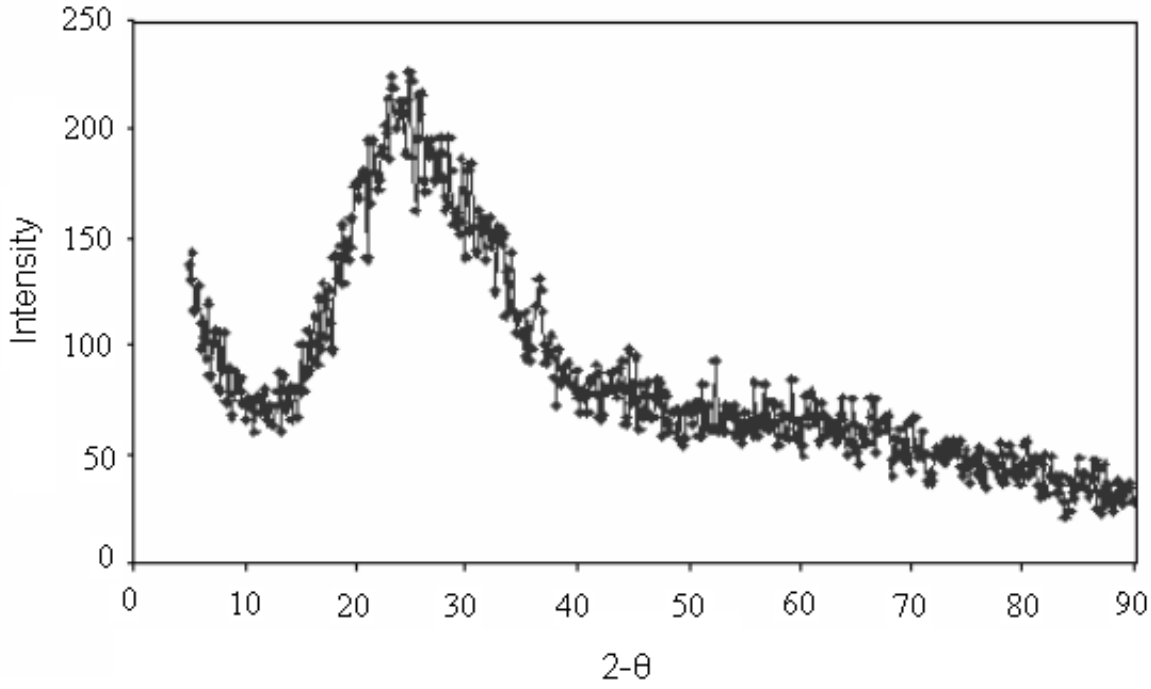

Figure 7.67 XRD pattern of 90In_2O_3:5ZnO:5SnO_2 thin film reveals the amorphous strucuture

7.12. Optical Absorbance

Figure 7.68 illustrates the plots of the optical absorbance spectra of 90 nm thin film for as-deposited and exposed to 2.5 ppm of ozone. The increase in optical density is associated with the changes in the optical band gap (Figure 7.69). Using the Mott and Davis theory [213], the estimated band gap for the as-deposited thin film was 4.1 eV and decreased to 4 eV after being treated with ozone.

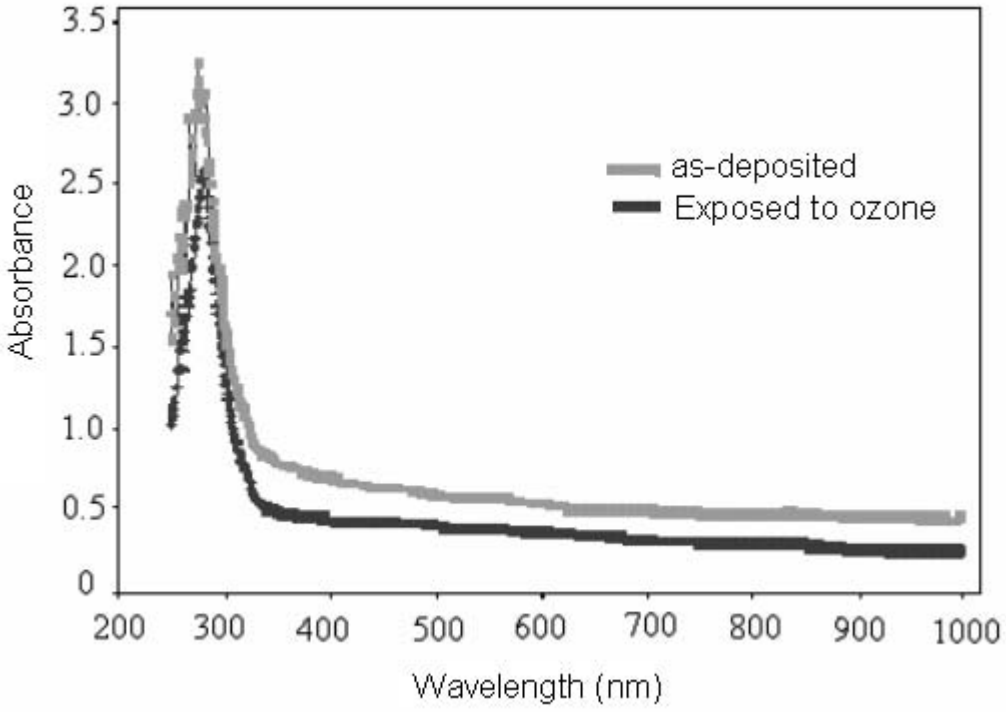

Figure 7.68 The optical absorbance spectra at UV-Vis wavelength range for 90 nm In_2O_3:ZnO:SnO_2 thin film: as-deposited and exposed to ozone for 1 hour

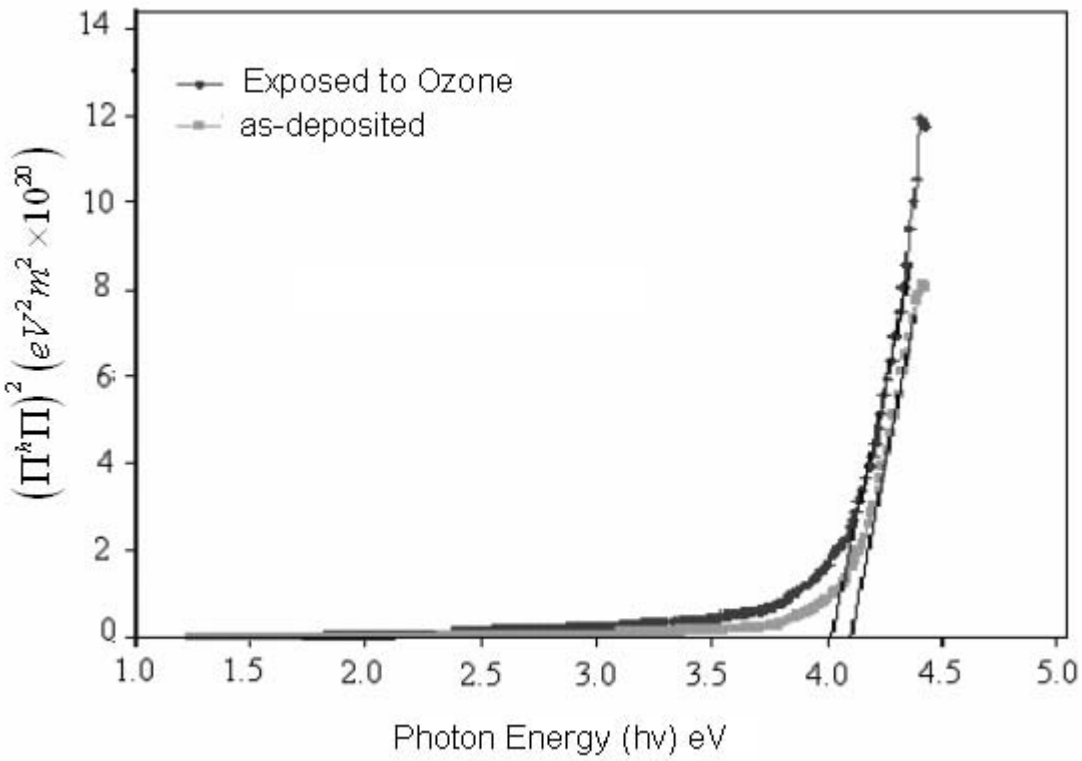

Figure 7.69 The plots of $(\alpha h\nu)^2$ versus photon energy $h\nu$ for as-deposited and exposed to ozone 90 nm In_2O_3:ZnO:SnO_2 thin film

7.13. Niobium Oxide

Niobium oxide has been studied extensively due to its broad range of applications [226]. It is widely used in catalysts, gas sensors, electro chromic devices and optical fibres [225 - 228]. The detection principle of this material is based in the reversible modulation of the electrical conductance in the presence of the target gas (oxidizing/reducing). Niobium oxide has been especially tested as an oxygen sensor where the conductivity decreases when the oxygen partial pressure is increased [227].

Among the niobium oxides, Nb_2O_5 is gaining popularity for gas detection applications and is a very promising material for the development of integrated gas sensors. Table 7.39 below shows a range of niobium oxide based gas sensors being utilized for various

target gas detection. Also illustrated are the sensors operating temperatures, which range from 20 - 750ºC as well as the response time for each of the individual sensors.

Table 7.39 Niobium Oxide based gas sensors

Material	**Target Gas**	**Operating Temp.**	**Detection Limits**	**Physical Parameter**	**Response Time**	**Ref.**
Nb_2O_5	CO, NH_3	400-500	100-1000 ppm	Electrical Conductivity	~3min	[241]
Nb_2O_5	NH_3	500	100-1000 ppm	Electrical Conductivity	~4min	[242]
Nb_2O_5	C_2H_5OH	500	2.1%	Electrical Conductivity	<1min	[243]
Nb_2O_5	NH_3, CO	400-500	100-1000ppm	Electrical Conductivity	~4min	[244]
Nb_2O_3	DMA, TMA, NH_3	300-640		Electrical Conductivity		[245]
Nb_2O_5 doped with TiO_2	Air/Fuel	550-750	0.01-100kPa	Electrical Conductivity	~5min	[246]

7.13.1. Optical Properties of Niobium Oxide

The analysis of the optical absorption spectra has been one of the most important productive tools for understanding and developing the theory of the electronic structure of amorphous materials. In general, thin films prepared via the thermal evaporation technique are amorphous and at most they are polycrystalline in nature.

The optical energy gaps E_{OPT} for as-deposited and exposed to ozone films were determined from the high absorption regions of the fundamental edges using the Mott and Davis Model.

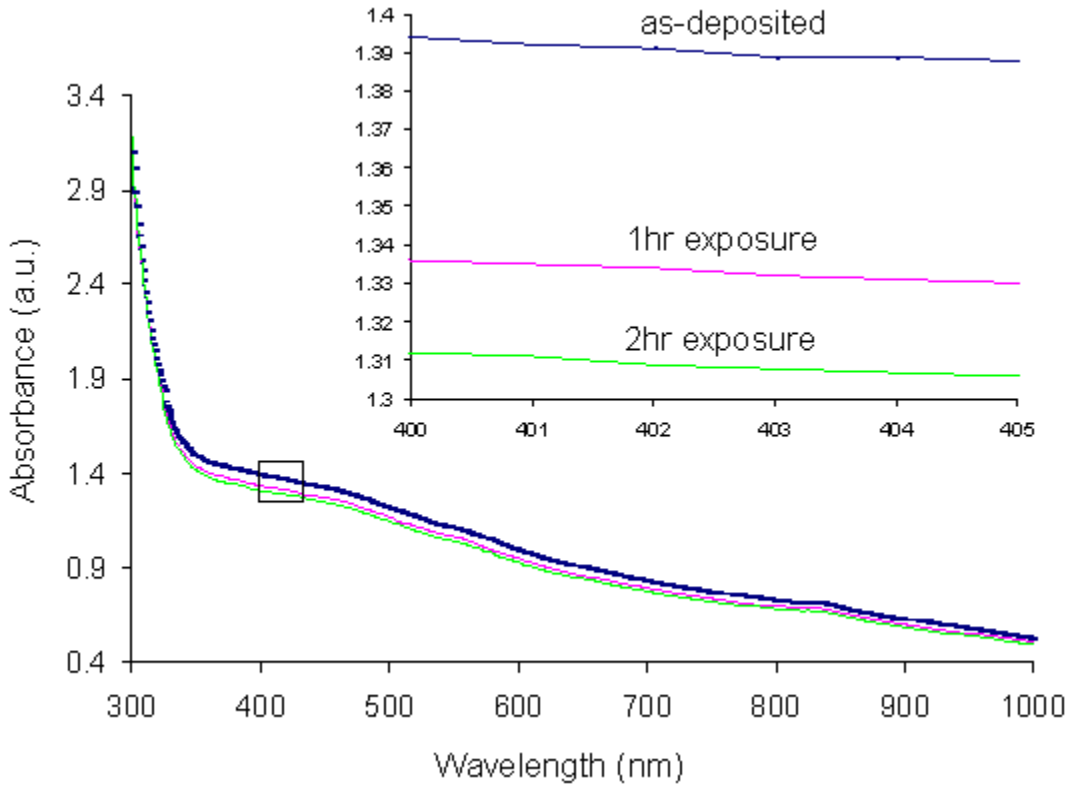

Figure 7.70 Plots of the optical absorbance spectra at UV-Vis wavelength range for NbO_2 for as-deposited, 1 hr and 2 hr exposure

Figure 7.70 above shows the plots of the optical absorbance spectra at UV-Vis wavelength range for the thermally evaporated NbO_2 film as-deposited and exposed to 3ppm of ozone for 1 and 2 hours. It can be seen from the above figure that there is no appreciable variation in the optical properties in the wavelength range 300nm to approximately 340nm. However, from 340nm to 1000nm the effect of ozone exposure manifested itself as a change in the optical density of the deposited thin film. The greatest effect was seen after exposure for 1 hour, with the rate of effect decreasing after

continuing the exposure procedure. This is highlighted further by the inset plot in Figure 7.70.

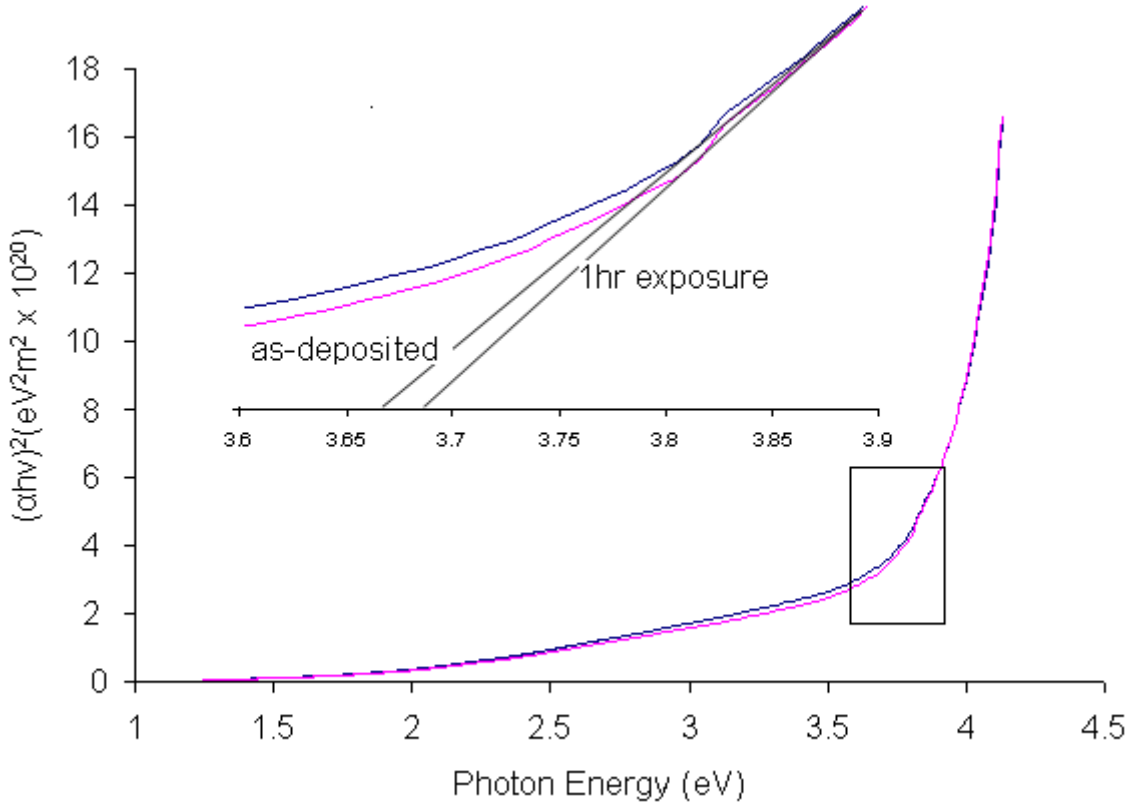

Figure 7.71 Plots of $(\alpha h\nu)^2$ versus photon energy for as-deposited and exposed to ozone for 1 hour

The change in the optical density is associated with the changes in the optical band gap, as can be seen from Figure 7.71. Using the Mott and Davis Theory [213], the estimated optical band gap for the as-deposited film is 3.66 and increases to approximately 3.68 after the film was exposed to 3ppm of ozone for 1 hour.

7.13.2. Niobium Oxide Response to Ozone

The principal detection process is the change of the oxygen concentration at the surface of these metal oxides, which is caused by the adsorption and heterogeneous catalytic reaction of oxidizing and reducing gaseous species [3]. There is a finite density of electron donors and/or acceptors bound to the surface of the semiconducting oxide. The electron donors/acceptors cause the formation of surface states followed by an exchange of electrons within the interior of the semiconductor thus forming a space charge layer close to the surface. By changing the surface concentration of the donors/acceptors, the conductance/resistance of the space charge region is modulated.

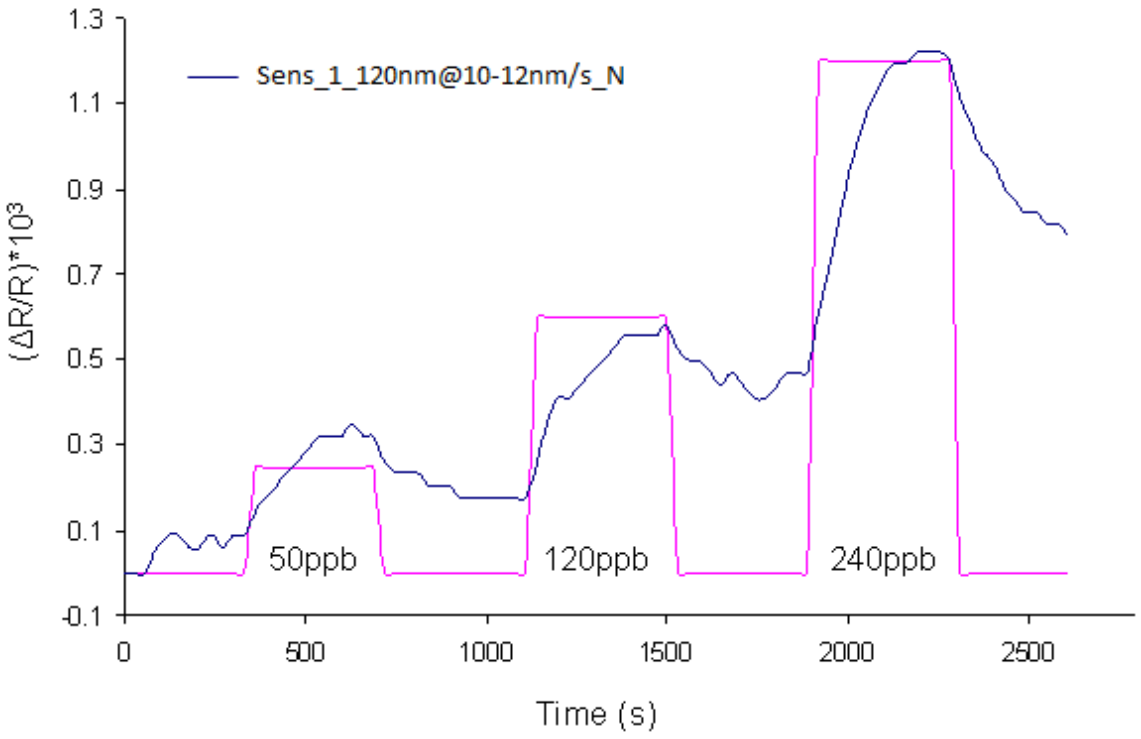

Figure 7.72 Response of 120nm of NbO_2 deposited at a rate of 10-12nm/s to 50, 120 and 240ppb ozone

As discussed in earlier chapters, when the oxide is an n-type there is a donation of electrons when reducing gases are introduced and a subtraction of electrons when

oxidizing gases are introduced. The result is that n–type oxides increase their resistance when oxidizing gases are present and decrease resistance when reducing gases are present. In contrast to n–type, p–type oxides decrease resistance when oxidizing gases are present and increase resistance when reducing gases are present.

As can be seen from Figure 7.72 the sensor responds well to 240 ppb of ozone, however, the recovery of the sensor is poor, as it fails to return to a baseline resistance when exposed to 50ppb, 120ppb and 240ppb of ozone.

Figure 7.73 shows the sensors response to 50ppb of ozone which is of particular significance for the health and safety of the respiratory system as discussed in Chapter 3.

Shown in Figure 7.74 below are five sensors fabricated under similar conditions at different times, from the graph it can be seen that the sensing device is relatively repeatable and has similar response and recovery times as well as similar response to the various ozone concentrations.

Figure 7.75 below gives a comparison of the different sensing devices and the response to various ozone concentrations. Also included in Figure 7.75 is an average response taken over all samples.

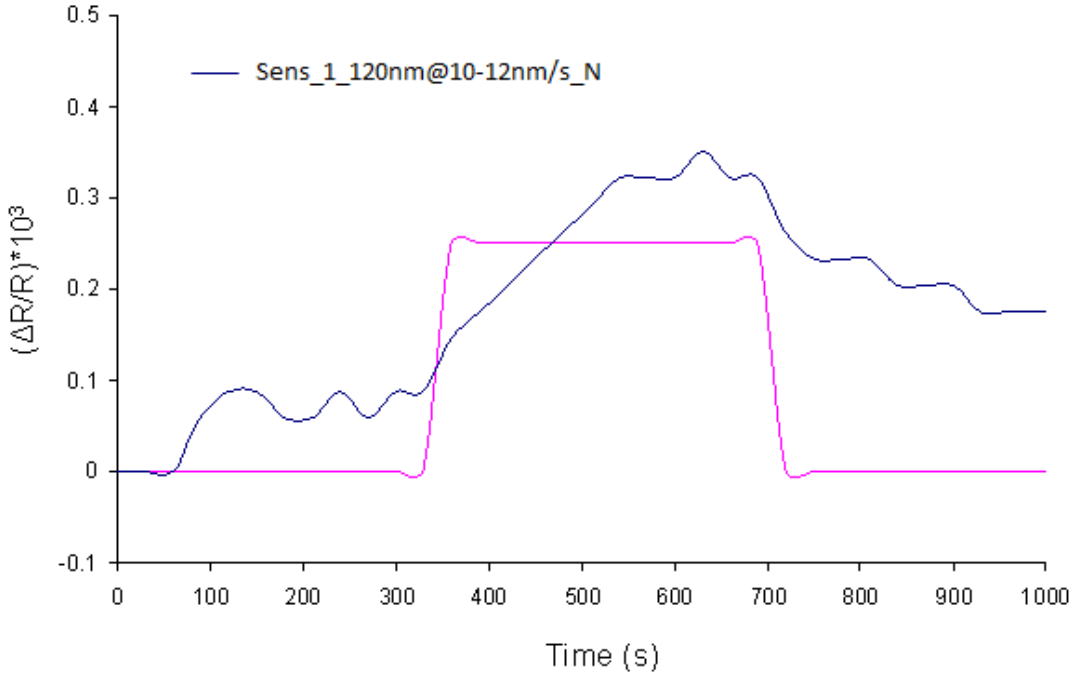

Figure 7.73 Response of 120nm ofNbO_2 deposited at a rate of 10 – 12nm/s to 50ppb of ozone

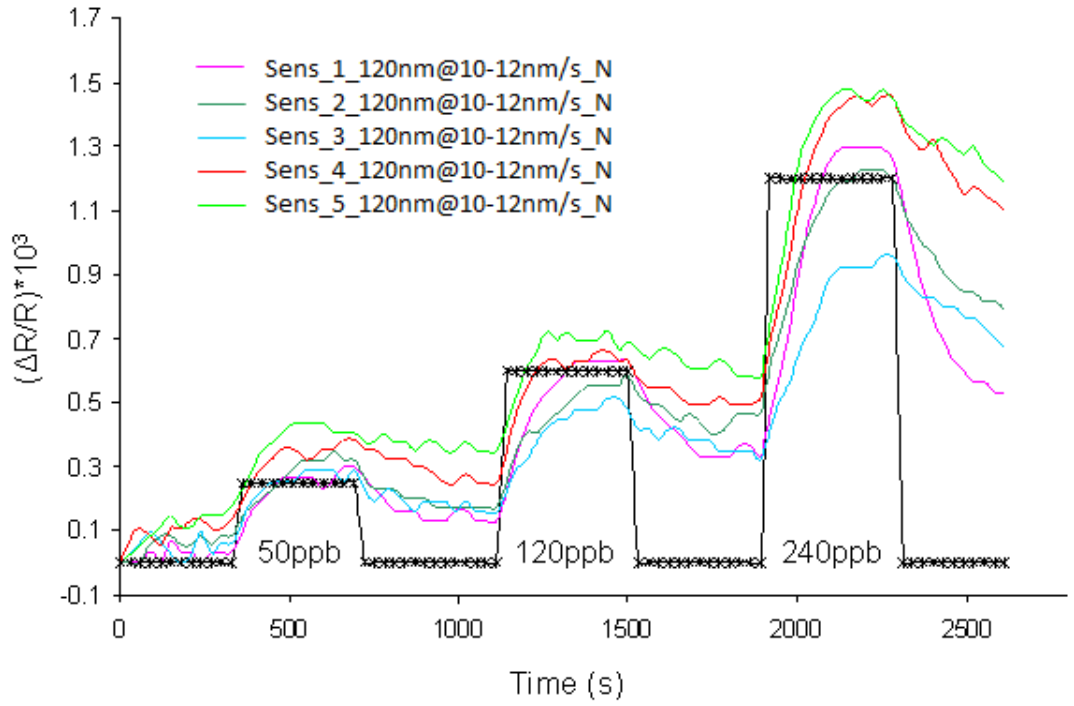

Figure 7.74 Repeatable response of 120nm of NbO_2 deposited at a rate of 10-12nm/s to 50, 120 and 240ppb ozone

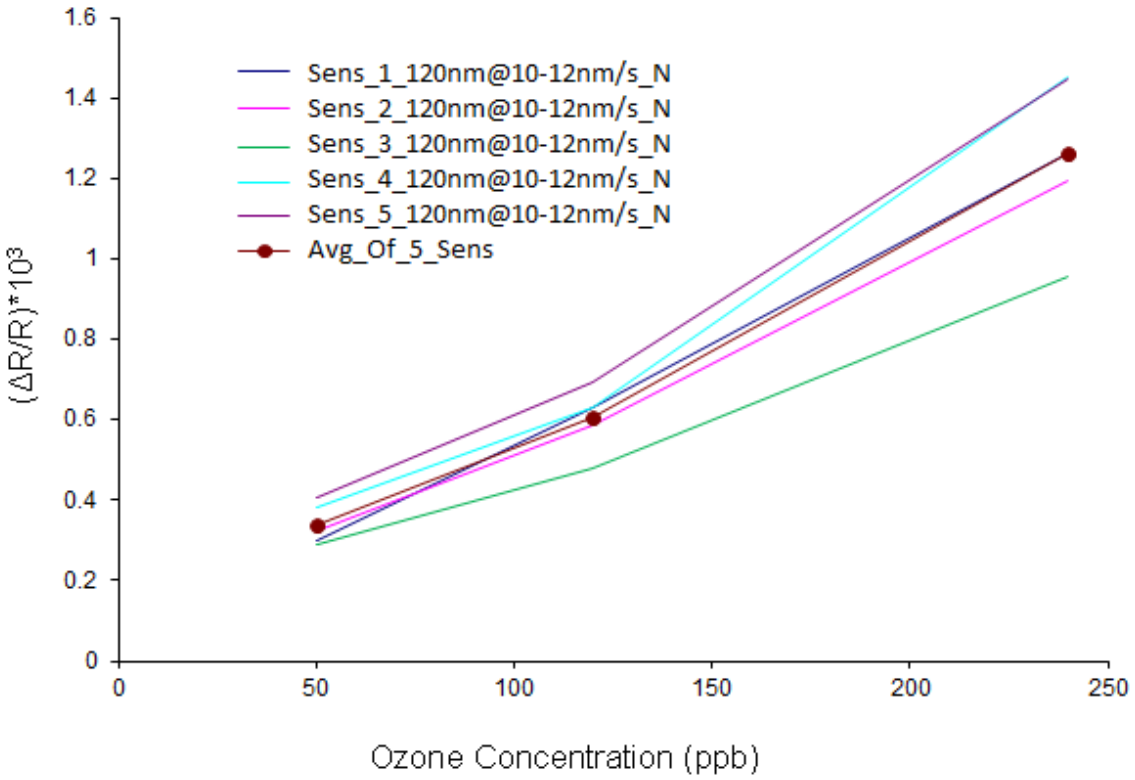

Figure 7.75 Comparison of repeatable response of 120nm of NbO_2 deposited at a rate of 10-12nm/s to 50, 120 and 240ppb and average response

Figure 7.76 shows the response of a 70nm thick NbO_2 sensing layer deposited at a rate 10 - 12nm/s at a pressure of $5x10^{-6}$mbar.

The device shows a measurable response to 50ppb, 120ppb and 240ppb of ozone. The sensor also shows relatively good response.

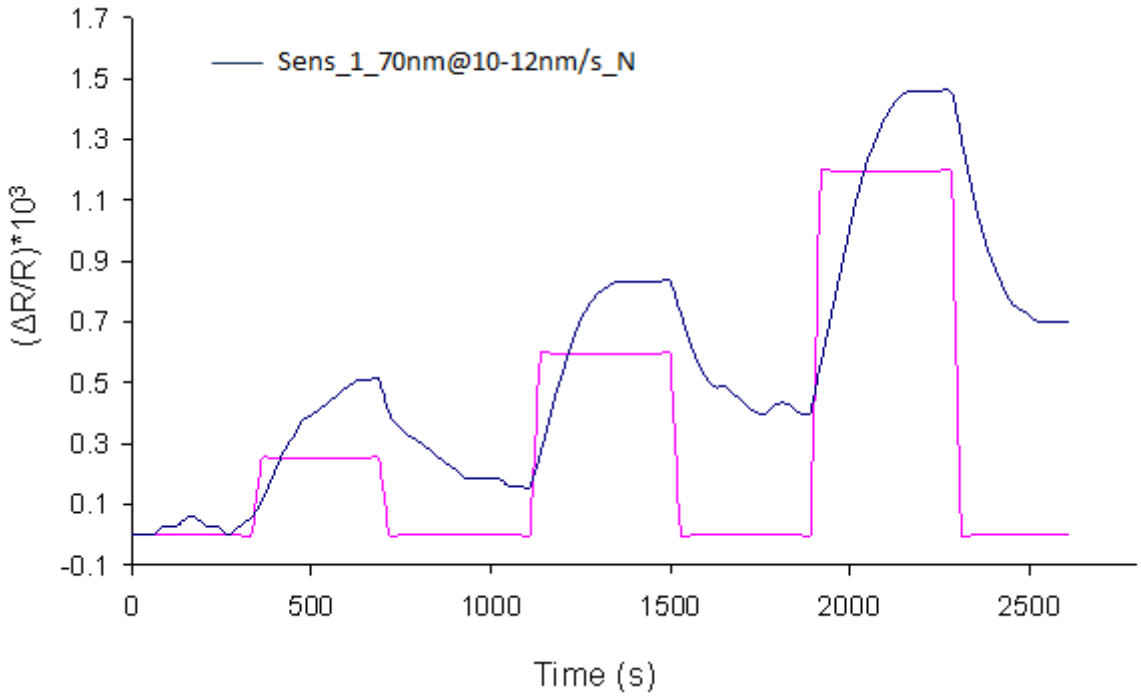

Figure 7.76 Response of 70nm of NbO_2 deposited at a rate of 10 - 12nm/s to 50, 120 and 240ppb

Figure 7.77 shows the sensor response to 50ppb of ozone. Closer comparison of these samples is discussed in the following sections.

Figure 7.78 shows the response of five sensors fabricated under constant conditions. It can be seen that this sensing device is repeatable with similar response and recovery times as well as similar response to the various ozone concentrations over the five separate samples.

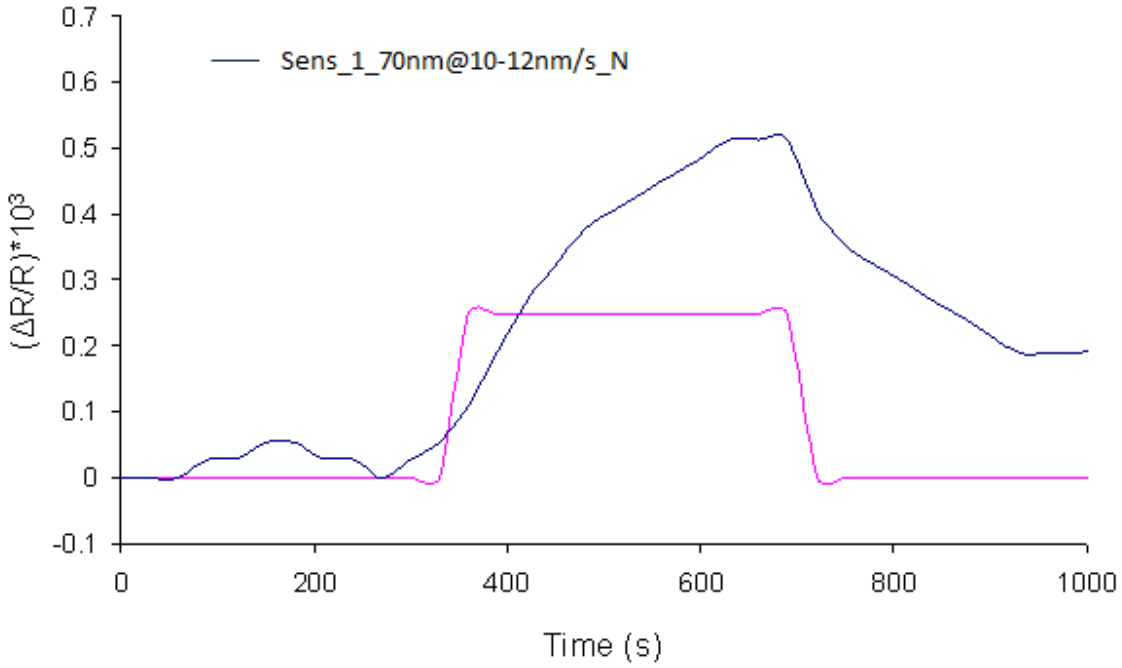

Figure 7.77 Response of 70nm ofNbO_2 deposited at a rate of 10 – 12nm/s to 50ppb of ozone

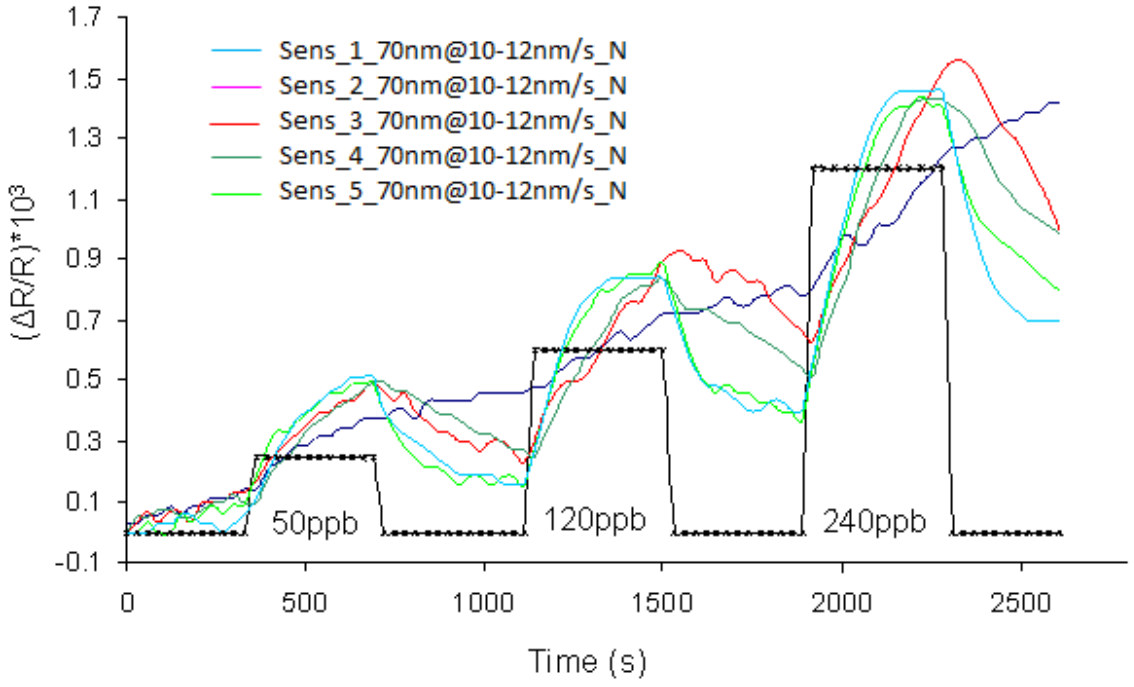

Figure 7.78 Repeatable response of 70nm of NbO_2 deposited at a rate of 10nm/s to 50, 120 and 240ppb ozone

Figure 7.79 gives a comparison of the different sensing devices fabricated and the response to various ozone concentrations. Also included is an average response taken over all samples.

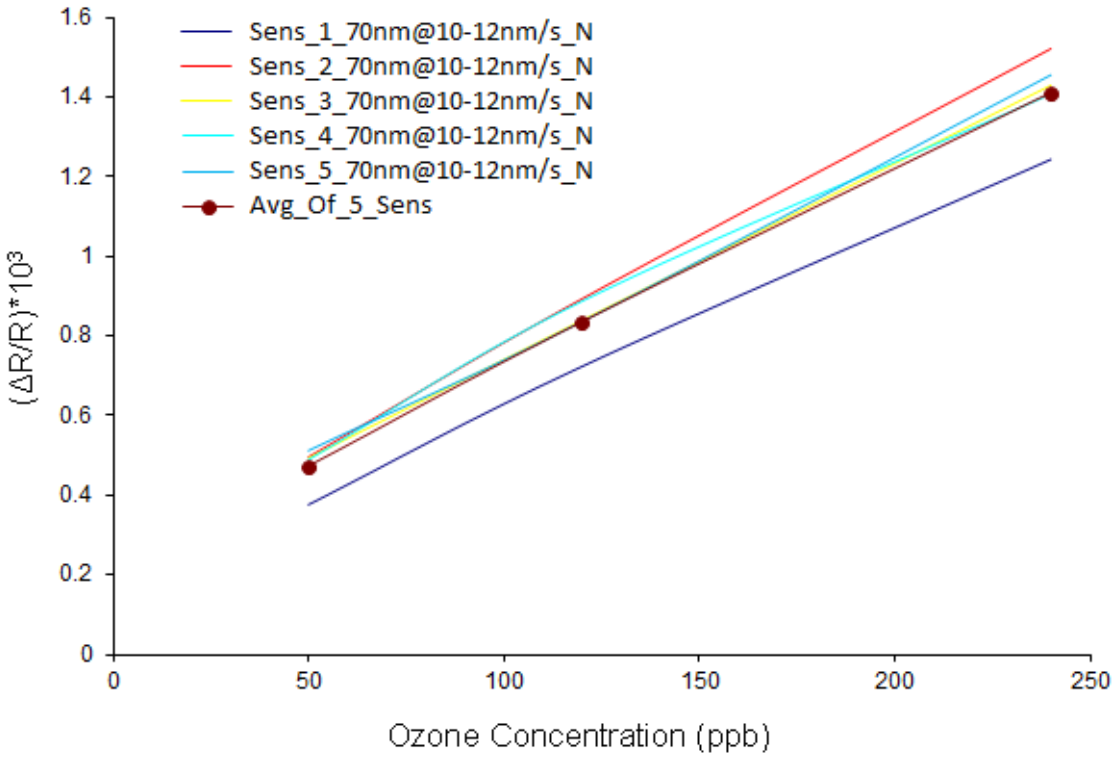

Figure 7.79 Comparison of repeatable response of 70nm of NbO_2 deposited at a rate of 10-12nm/s to 50, 120 and 240ppb and average response

A more in depth comparison of these NbO_2 sensing devices is described by the following graphs. As can be seen from Figure 7.80 below (and as seen for previously discussed samples) reducing the thickness of the sensing layer has the effect of increasing the response of the sensor. The reasons for this increase in response have been discussed in Chapter 3.

Figure 7.81 shows a bar graph comparing the average response times of the sensors fabricated with sensing layer of thickness 120nm and 70nm. It is clear from this bar chart

that decreasing the sensing layer thickness causes a significant improvement in the response time of the sensor.

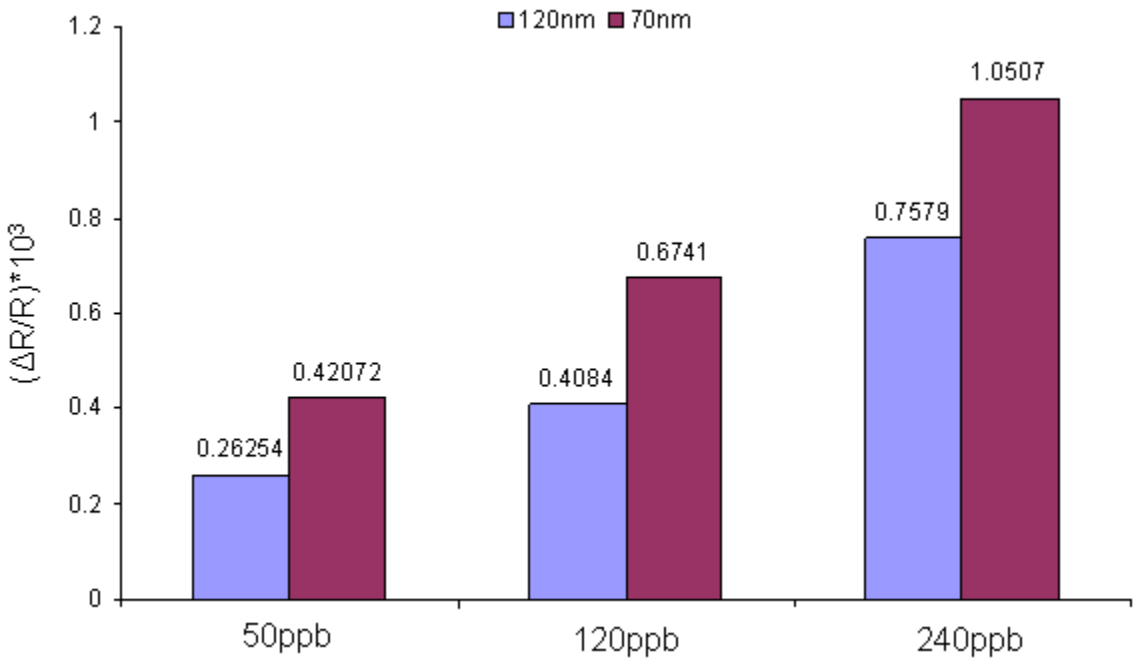

Figure 7.80 Comparing average responses of 70nm and 120nm of NbO_2

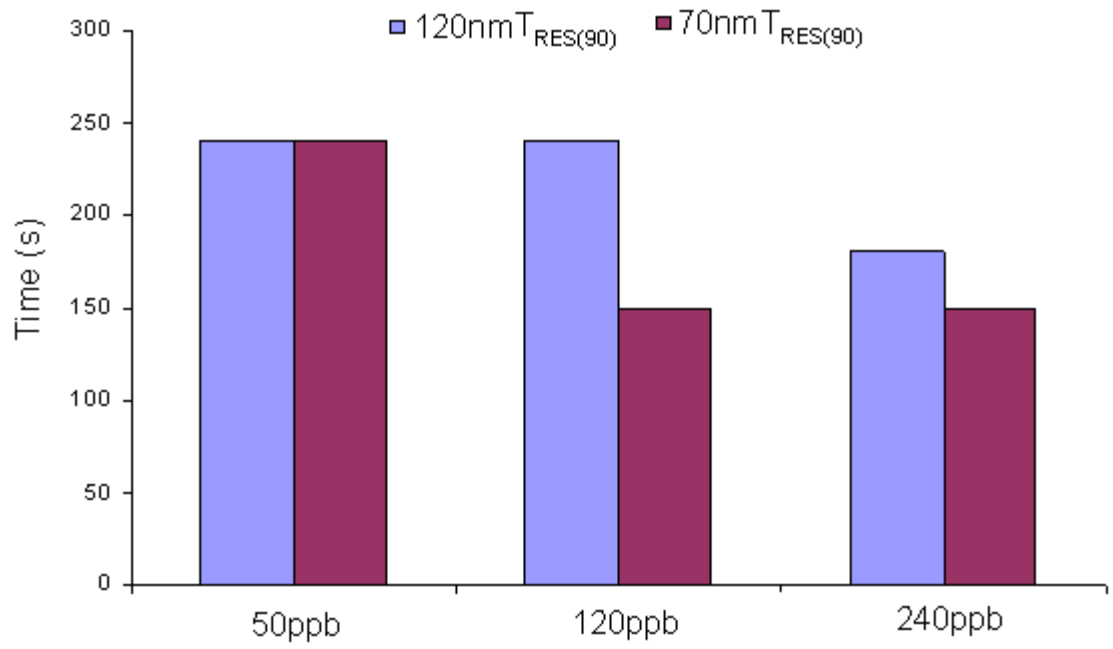

Figure 7.81 Comparison of response times for 70nm and 120nm of NbO_2

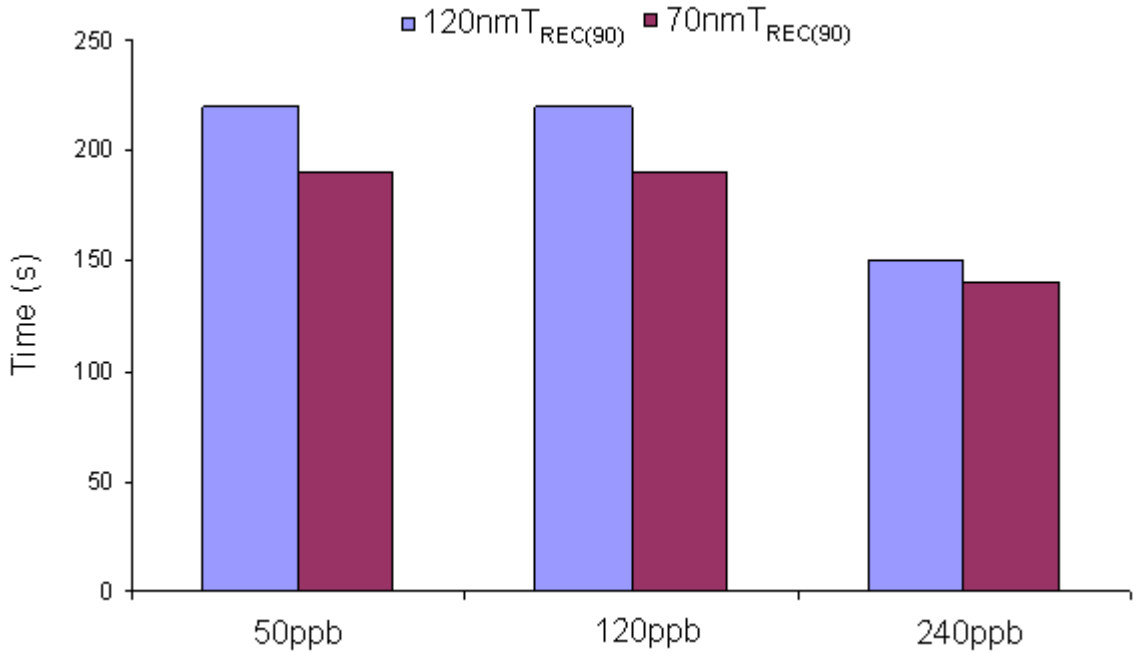

Figure 7.82 Comparison of recovery times for 70nm and 120nm of NbO_2

These results have shown that VTE of niobium oxide can be used for the detection ozone (50-240ppb) at room temperature. These sensors provide a cost effective means of fabrication and operation. The above results are consistent with previously discussed results for other sensor types. For these sensors NbO_2 was deposited at a rate of 10-12nm/s at a pressure of $5x10^{-6}$ mbar for sensing layers of 70nm and 120nm. The devices show a measurable and repeatable response to 50ppb, 120ppb and 240ppb of ozone. It can be seen from above results that decreasing the sensing layer thickness causes a significant improvement in the response (~ +60%) of the devices to ppb levels of ozone, Figure 7.81 and Figure 7.82 also show a decrease response time (~ -30%) and recovery time (~ - 15%) which is consistent with much of the literature in the area as well as previous findings in this work.

Chapter 8: Conclusions and Future Work

8.1. Summary and Conclusions

Due to the ever increasing industrialisation today, constant monitoring of air pollution is required in many areas (hospitals, factories etc.) to enhance and protect the health and safety of people in the surrounding atmosphere.

As discussed in Chapter 1 and Chapter 2 Ozone is a highly toxic gas which can have devastating effects on human health at very low concentrations. The greatest obstacle to achieving improved monitoring lies at the interface between the measuring device and the environment (target gas) to be monitored.

The endeavour of the research community is to increase the sensitivity, selectivity and stability of such devices, while providing a simple cost effective method of fabrication. Volatile organic components (acetone, benzene, and propanol) and harmful gases (nitrogen dioxide, ozone) are known to have adverse effect on the quality of the environment and its inhabitants. Hence it is critical to develop methods of early and inexpensive detection of their presence in the environment.

The work reported in this thesis is on the development of sensors/sensing elements for the detection of low concentrations of ozone (ppb region). As can be seen from the above sections there are numerous methods of gas and ozone detection. However, ozone sensing requires a typical set of parameters which need to be met in order to produce a practical

ozone sensor. UV absorption method may be the most widely used technique for the detection of ozone. This method is very reliable and stable as the ozone gas is contained within an optical cell. However, a major disadvantage of this method is the cost due to the complexity of the equipment and operation.

Metal oxide based semiconductor gas sensors have extremely high sensitivities with the added advantages of low fabrication costs, low operating costs, lower power consumption and portable.

In this work, the possibility of utilizing thin films of oxide materials fabricated via thermal evaporation for the detection of ozone concentrations in the ppb region was explored. There are several publications on the use of metal oxides for the detection of ozone, however most of which rely on elevated operating temperature which increases fabrication and operating costs of the sensing device. Another drawback of operating the sensor at high temperatures is that it limits the applications of such a sensor, making it difficult to be integrated into portable/handheld devices.

An important part in the process of sensing device development consisted of identifying suitable materials for use in thin film sensors. Each technology detailed in Chapter 3 has a particular set of limitations associated with it. In this case, materials which possess very high melting point may not be deposited via the thermal vacuum evaporation technique.

This work explored various ozone sensing layers and devices which were fabricated from numerous metal oxide materials, such as In_2O_3, SnO_2, ZnO, NbO_2 etc and their mixtures in different proportions. The fabrication method was based on the thermal evaporation of both the sensing electrodes and the metal oxide layer via an Edwards E306A vacuum thermal coating system. Slightly altering the fabrication parameters was found to have a significant effect on the overall performance of the sensing device. Also mixing the oxide materials in different proportions was found to change the sensitivity of these devices to ozone in the ppb region.

The detection principle of this sensor type is based on changes in the resistance of a metal oxide layer upon exposure to the target gas molecules (oxidising or reducing). The gas-solid interactions influence the density of the electronic species in the film and thereby the overall resistance of the film.

For room temperature operation [174] it is stated that the formation of O_3^- at the surface due to the interaction with the metal oxide layer is possible at relatively low temperatures (< 150ºC). This effect can be ruled out for elevated temperature operation (>150ºC) as this form of adsorbed oxygen is unstable at elevated temperatures and can be easily transformed in to O_2^- or O^-. There is an investigation which illustrates the formation of O_3^- on a metal oxide interacting with ozone at temperatures below 65ºC. It was shown that O_3^- may easily dissociate at the surface of the metal oxide layer by forming O^- [174]. It is supposed that the reaction of decomposition of ozone into O_2 and O gives rise to an increase in the O_3 sensitivity of the device because atomic oxygen O adsorbed at the semiconductor surface as O^{2-} or O^- induces a resistance increase [232]. Furthermore, O_3 adsorption in the form of O_3^- should lead to the formation of localised dipoles on the surface of the sensing film [174].

A number of techniques and analysis tools were utilised for the characterisation of the electrical, optical and structural properties of these devices. These include, UV-Vis Spectroscopy, Scanning Electron Microscopy (SEM), XRD and XPS.

8.2. In_2O_3 based devices

Thin films of In_2O_3 were deposited using the VTE technique at various different fabrication parameters; pressure, deposition rate, layer thickness, substrate temperature. However, there was little success in achieving a workable or usable ozone sensor due to the poor conductivity of the metal oxide layer.

Films prepared via In_2O_3 powder and In source in an oxygen rich environment at deposition rates ranging from 0.1nm/s – 1.4nm/s and having thickness of 40nm – 200nm yielded no improvement in the characteristics of the final film.

Initial results of films fabricated from mixtures of In_2O_3, SnO_2 and ZnO showed promising results and were further investigated.

It was found that the mixing of these materials and simultaneous evaporation from a molybdenum boat yielded workable ozone sensing layers. The optimization of the fabrication process and parameters were investigated. It was found that decreasing the

thickness of the sensing layer yielded a significant increase in the performance of the sensing device (sensitivity, response time and recovery time). It was also noted that increasing the deposition rate of the source material from the molybdenum boat from 0.1nm/s to 1.4nm/s resulted in a significant increase in the response of the device. However, the drawback was that the stability of the device was negatively affected, the sensor failed to return to a stable baseline reading after ozone had been switched off.

To understand the nature of the sensing films, the surfaces of the sensing layers were examined via SEM analysis. There were varying degrees of porosity, grain size and uniformity observed for varying the deposition rate of the oxide layer. From these SEM images it can be seen that higher deposition rates result in more porous layers. SEM image of the 0.6-0.8nm/s layer showed to have relatively porous and uniform structure.

Extensive XPS analysis of these various sensor samples (wide and narrow scans) was carried out in an attempt to better understand the increases in sensor performance. From these results it can be seen that there are slight shifts in the binding energies of the metal oxide components which is known to have an effect on the sensitivity of the devices. Also of particular interest from these results is the presence and shape of the O 1s peaks and the corresponding performance of the sensing layer. Asymmetric O 1s peak shape observed in this research leads to suspect of the existence of several different oxygen species on the surface of the sample. It has been suggested that these peaks may correspond to lattice oxygen and to one or more adsorbed species on the surface [12]. Oxygen species responsible for the asymmetric shape may be weakly bound to the surface.

From this analysis it was found that the parameters which result in most reliable and usable ozone sensor were for a 40nm thick sensing layer deposited at a rate of 0.6-0.8nm/s.

In a further attempt to improve on the performance of the sensing devices, the molar percentages of the source materials were changed slightly. As above these sensor samples were extensively analysed and it was found that slight variations in the source materials yields a significant change in the performance of the sensing device. Again, as above,

extensive XPS analysis was used as a means of understanding this shift in sensor performance.

8.3. NbO_2 based devices

It is important to note that for this material the deposition rate may be increased significantly from that of the In_2O_3 based devices. In this case it was found, similar to the In_2O_3 based sensors that decreasing the thickness of the sensing layer while increasing the deposition rate results in an increase in sensitivity of the device. However, this increase in sensitivity is coupled with a decrease in the sensor response and recovery times. Therefore there is a trade-off between maximising sensitivity while reducing the response and recovery times of the devices.

The optical properties of the niobium oxide layer were investigated. The optical energy gaps for as-deposited and exposed to 3ppm ozone films were determined from the high absorption regions of the fundamental edges using the Mott and Davis Model. From the optical absorbance spectra it was shown that from wavelength in the range 340nm – 1000nm the effect of ozone exposure manifested itself as a change in the optical density of the film. This change in optical density is associated with changes in the optical band gap.

8.4. Concluding Remarks

As discussed earlier, at high temperatures, typically > 100ºC oxygen molecules are dissociated by the chemisorption process. In this process oxygen is connected via a dipole binding to the surface atoms of the semiconductor. Under these elevated temperatures, electrons are removed from the surface of the oxide layer via a charge transfer mechanism, which is followed by the formation of chemical bonds with the semiconductor surface atoms.

For room temperature ozone detection a critical requirement is the catalytic activity of the oxide reaction of ozone decomposition, atomic oxygen is adsorbed on the oxide surface as O^{2-} or O^{-} which causes the resistivity of an n-type sensing layer to increase. At these low temperatures, oxygen molecules are adsorbed via the physisorption process. This process is accomplished via weak van der Waals forces [135].

It has been stated that where a metal-oxide semiconducting gas sensor is used at temperatures below 100ºC, additional equipment is required [135], such as the use of UV [161] light illumination.

The sensitivity/performance of the oxide layer depends strongly on layer thickness and oxygen vacancies. The sensitivity of the metal oxide sensor is directly influenced by the size of the oxygen induced depletion layer at the surface of the film, relative to the thickness of the bulk semiconductor.

Also studied and found to have a significant impact on sensor performance is the porosity of the deposited oxide layer. For porous layers, gases are able to gain access beyond the surface of the sensing layer, thereby allowing the gas sensing reaction to take place at the surface of individual grains, at grain-grain boundaries and even at the interface between grains and the underlying electrodes. SEM analysis of sensing layers supports this case, with the best performing sensors showing high porosity. From this work it has been found that increasing the deposition rate increases the porosity of the deposited sensing layer. Increasing the deposition rate of the gas sensitive layer has been shown to increase the concentration of oxygen vacancies of the sensitive layer. As can be seen from previous analysis and discussions (section 7.10) the intensity of the higher binding energy O1s

component measures the concentration of oxygen vacancies. When the intensity of this component is greater than that of the lower binding energy component there is a large oxygen deficient state at the surface. SEM images of layers deposited at 0.1nm/s are seen to be tightly packed and compact, thereby restricting the gas from penetrating into the sensing layer and reducing the surface area of the sensing layer, which results in reduced sensitivity.

Using the optimal fabrication processes and techniques outlined in this section it was found that variations of the molar percentages of the source materials have a significant effect on the sensitivity, response and recovery times. XPS Analysis was used to provide a further insight into the concentrations of materials found on the surface of the deposited metal oxide layers.

The majority of metal oxide based ozone gas sensors in the literature operate at elevated temperatures (Table 3.4). In general gas sensors working at these high temperatures use the volume effect concerning the diffusion and desorption of gas molecules. Therefore, they require a heating element to be incorporated into the design. Ideally the sensor would operate at room temperature, eliminating the need for a heating element. Operating the sensor at room temperature has the following advantages;

- Ease of implementation into portable applications
- More user friendly
- Reduced power consumption
- Reduced cost of fabrication and operation

8.5. Suggestions for Future Work

There are a large number of publications reporting on the excellent individual gas sensing performance of metal oxide based gas sensors. It is perhaps surprising then that there are so few of these devices used in real applications. The reason for which is that the results from the publications are mainly obtained by measuring the signals of laboratory samples in unrealistic working environments (in the absence of temperature variation, humidity and interfering gases, etc.).

The standard spectroscopic investigations are mostly performed under conditions far removed from that of real working environments, namely, in ultra-high vacuums (UHV), low temperatures, preconditioning of the samples at elevated temperatures, quenching and exposing to high concentrations of reactive gases, conducted on simplified systems (measurement of powders, crystals and thin films).

Future work would include further investigations into the reliability and repeatability of the sensing layers. Also of particular interest would be the fabrication of the sensing layers via different techniques such as sputtering and sol-gel methods, in an attempt to gain more control over the precise thickness and deposition parameters of the sensing layer.

The influence of the relative humidity as an interfering parameter on the performance of the sensors at different operating temperatures should be studied.

Regarding senor properties a further study of the selectivity against reducing as well as other oxidizing gases needs to be investigated.

The influence of the addition of noble metals such as Pt, Pd or other metal oxides to In_2O_3 based thin films on the gas sensing properties should be studied, as small amounts of such additives have been shown to improve gas sensitivity and reduce the operating temperature [200, 201].

Furthermore, the developed electronic control section of ozone sensing devices should be miniaturized to further decrease energy consumption and thereby making the integration of such device into portable devices a more attractive and obtainable prospect.

References:

1. Demarne, V., et al., *Domestic gas detection system using two SnO2 integrated sensors.* Sensors and Actuators B: Chemical, 1994. **19**(1-3): p. 658-660.
2. Grasdepot, F., et al., *Domestic gas sensor with micromachined optical tunable filter.* Sensors and Actuators B: Chemical, 1996. **36**(1-3): p. 377-380.
3. Kwon, C.H., et al., *Thick-film zinc-oxide gas sensor for the control of lean air-to-fuel ratio in domestic combustion systems.* Sensors and Actuators B: Chemical, 1995. **25**(1-3): p. 610-613.
4. Pulles, T. and D. Heslinga, *On the variability of air pollutant emissions from gas-fired industrial combustion plants.* Atmospheric Environment, 2004. **38**(23): p. 3827-3838.
5. Redondo, R. and J.G. Yélamos, *Determination of CO2 origin (natural or industrial) in sparkling bottled waters by 13C/12C isotope ratio analysis.* Food Chemistry, 2005. **92**(3): p. 507-514.
6. Stamate, E., et al., *IR and UV gas absorption measurements during NOx reduction on an industrial natural gas fired power plant.* Fuel, 2010. **89**(5): p. 978-985.
7. Chaudhari, G.N., et al., *Detection of liquid petroleum gas using mixed nanosized tungsten oxide-based thick film semiconductor sensor.* Talanta, 2006 **69**: p. 187 - 191.
8. Kadu, A.V., G.N. Jagtap, and G.N. Chaudhari, *Studies on the preparation and ethanol gas sensing properties of spinel Zn0.6Mn0.4Fe2O4 nanomaterials.* Current Applied Physics, 2009. **9**: p. 1246 - 1251.
9. Kumar, V., et al., *Copper doped SnO2 nanowires as highly sensitive H2S gas sensor.* Sensors and Actuators B: Chemical, 2009. **B**(138): p. 587 - 590.
10. Lee, S.C., et al., *Novel SnO2 based gas sensors promoted with metal oxides for the detection of dichloromethane.* Sensors and Actuators B: Chemical, 2009. **B**(138): p. 446-452.
11. Sberveglieri, G., *Recent developments in semiconducting thin film gas sensors.* Sensors and Actuators B, 1995. **B**(23): p. 103 - 109.
12. Correia Pires, J.M.A., *Thin Films For Gas Sensors*, in *Departamento de Fisica*. 2003, Universidade do Minho. p. 232.
13. Szilágyi, I.M., et al., *Gas Sensing Selectivity of Hexagonal and Monoclinic WO3 to H2S.* Solid State Sciences, 2010. **12**(11): p. 1857-1860.
14. Wang, C.-T., D.-L. Lai, and M.-T. Chen, *Synthesis of iron-doped vanadium-tin oxide nanocrystallites for CO gas sensing.* Materials Letters. **64**(1): p. 65-67.
15. Zheng, K., et al., *The properties of ethanol gas sensor based on Ti doped ZnO nanotetrapods.* Materials Science and Engineering: B. **166**(1): p. 104-107.
16. Becher, C., et al., *The detection of evaporating hazardous material released from moving sources using a gas sensor network.* Sensors and Actuators B: Chemical, 2010. **2**(146): p.5133-520.

17. Pearton, S.J., et al., *Recent advances in wide bandgap semiconductor biological and gas sensors.* Progress in Materials Science. **55**(1): p. 1-59.
18. www.epa.ie.
19. Kim, K., et al., *Fabrication and characterization of Ga-doped ZnO nanowire gas sensor for the detection of CO.* Thin Solid Films, 2009. **518**(4): p. 1190-1193.
20. Ahn, M.W., et al., *On-chip fabrication of ZnO-nanowire gas sensor with high gas sensitivity.* Sensors and Actuators B: Chemical, 2009. **138**(1): p. 168-173.
21. Carotta, M.C., et al., *ZnO gas sensors: A comparison between nanoparticles and nanotetrapods-based thick films.* Sensors and Actuators B: Chemical, 2009. **137**(1): p. 164-169.
22. Xu, H., et al., *A novel method for improving the performance of ZnO gas sensors.* Sensors and Actuators B: Chemical, 2006. **114**(1): p. 301-307.
23. Rao, G.S.T. and D. Tarakarama Rao, *Gas sensitivity of ZnO based thick film sensor to NH3 at room temperature.* Sensors and Actuators B: Chemical, 1999. **55**(2-3): p. 166-169.
24. Korotcenkov, G. and B.K. Cho, *Thin film SnO2-based gas sensors: Film thickness influence.* Sensors and Actuators B: Chemical, 2009. **142**(1): p. 321-330.
25. Vilaseca, M., et al., *Development and application of micromachined Pd/SnO2 gas sensors with zeolite coatings.* Sensors and Actuators B: Chemical, 2008. **133**(2): p. 435-441.
26. Wang, H.C., Y. Li, and M.J. Yang, *Fast response thin film SnO2 gas sensors operating at room temperature.* Sensors and Actuators B: Chemical, 2006. **119**(2): p. 380-383.
27. Choe, Y.-S., *New gas sensing mechanism for SnO2 thin-film gas sensors fabricated by using dual ion beam sputtering.* Sensors and Actuators B: Chemical, 2001. **77**(1-2): p. 200-208.
28. Korotchenkov, G.S., S.V. Dmitriev, and V.I. Brynzari, *Processes development for low cost and low power consuming SnO2 thin film gas sensors (TFGS).* Sensors and Actuators B: Chemical, 1999. **54**(3): p. 202-209.
29. Wagner, T., et al., *Gas sensor based on ordered mesoporous In2O3.* Thin Solid Films, 2009. **517**(22): p. 6170-6175.
30. Oprea, A., et al., *Transport and gas sensing properties of In2O3 nanocrystalline thick films: A Hall effect based approach.* Sensors and Actuators B: Chemical, 2009. **139**(2): p. 322-328.
31. Korotcenkov, G., et al., *Gas-sensing characteristics of one-electrode gas sensors based on doped In2O3 ceramics.* Sensors and Actuators B: Chemical, 2004. **103**(1-2): p. 13-22.
32. Korotcenkov, G., et al., *In2O3 films deposited by spray pyrolysis as a material for ozone gas sensors.* Sensors and Actuators B: Chemical, 2004. **99**(2-3): p. 297-303.
33. Korotcenkov, G., et al., *In2O3 films deposited by spray pyrolysis: gas response to reducing (CO, H2) gases.* Sensors and Actuators B: Chemical, 2004. **98**(2-3): p. 122-129.
34. Gurlo, A., et al., *Grain size control in nanocrystalline In2O3 semiconductor gas sensors.* Sensors and Actuators B: Chemical, 1997. **44**(1-3): p. 327-333.

35. Abhijith, N., *Semiconducting Metal Oxide Gas Sensors: Development and Related Instrumentation*, in *Department of Instrumentation*. 2006: Bangalore. p. 112.
36. Rubin, B.M., *The History of Ozone. The Schonbein Period, 1839 - 1868.* Bull. Hist. Chem., 2001. **26**(1): p. 40 - 56.
37. Rakitskaya, T.L., et al., *Catalysts for sanitary air cleaning from ozone.* Catalysis Today, 1999. **53**: p. 703 - 713.
38. Khurana, A., *Ozone Treatment for prevention of microbial growth in air conditioning systems*, in *Graduate School*. 2003, University of Florida: Florida. p. 94.
39. Gordon, G., *The chemistry and reactions of ozone in our environment.* Progress in Nuclear Energy, 1995. **29**(Supplement 1): p. 89 - 96.
40. Magara, Y., M. Itoh, and T. Morioka, *Application of ozone to water treatment and power consumption of ozone generating systems.* Progress in Nuclear Energy, 1995. **29**(Supplement 1): p. 175-182.
41. Manojlovic, D., et al., *Removal of phenol and chlorophenols from water by new ozone generator.* Desalination, 2007. **213**: p. 116-122.
42. Wang, K., et al., *Decomposition of two haloacetic acids in water using UV radiation, ozone and advanced oxidation processes.* Journal of Hazardous Materials, 2009. **162**: p. 1243 - 1248.
43. Ying-hui, Y., M. Jun, and H. Yan-jun, *Degradation of 2, 4 dichlorophenoxyacetic acid in water by ozone hydrogen peroxide process.* Journal of Environmental Sciences, 2006. **18**(6): p. 1043 - 1049.
44. Manttari, M., et al., *Membrane filtration and ozone treatment of biologically treated effluents from the pulp and paper industry.* Journal of Membrane Science, 2008. **309**: p. 112 - 119.
45. Roncero, M.B., et al., *TCF bleaching of wheat straw pulp using ozone and xylanase. Part A paper quality assessment.* Bioresource Technology, 2003. **87**: p. 305 - 314.
46. Oyama, S.T., *Chemical and Catalytic Properties of ozone.* Catal. Rev. Sci. Eng, 2000. **42**(3): p. 279 - 322.
47. Bocci, V.A., *Scientific and Medical Aspects of Ozone Therapy. State of the Art.* Archives of Medical Research, 2006. **37**(4): p. 425-435.
48. Bocci, V., *Is it true that ozone is always toxic? The end of a dogma.* Toxicology and Applied Pharmacology, 2006. **216**(3): p. 493-504.
49. Mahfoudh, A., et al., *Biocidal action of ozone-treated polystyrene surfaces on vegetative and sporulated bacteria.* Applied Surface Science. 2010. **256**(10): p. 3063-3072.
50. Johansson, E., R. Claesson, and J.W.V. van Dijken, *Antibacterial effect of ozone on cariogenic bacterial species.* Journal of Dentistry, 2009. **37**(6): p. 449-453.
51. Finch, G.R. and D.W. Smith, *Ozone dose-response ofEscherichia coli in activated sludge effluent.* Water Research, 1989. **23**(8): p. 1017-1025.
52. Bromley, W.G., *Ozone used to control bacteria.* Tribology International, 1977. **10**(1): p. 38-38.

53. Lin, Y.-C. and S.-C. Wu, *Effects of ozone exposure on inactivation of intra- and extracellular enterovirus 71.* Antiviral Research, 2006. **70**(3): p. 147-153.
54. Becker, S., et al., *Effect of ozone on susceptibility to respiratory viral infection and virus-induced cytokine secretion.* Environmental Toxicology and Pharmacology, 1998. **6**(4): p. 257-265.
55. Carpendale, M.T.F. and J.K. Freeberg, *Ozone inactivates HIV at noncytotoxic concentrations.* Antiviral Research, 1991. **16**(3): p. 281-292.
56. Shinriki, N., et al., *Mechanism of inactivation of tobacco mosaic virus with ozone.* Water Research, 1988. **22**(7): p. 933-938.
57. Bolton, D.C., Y.C. Zee, and J.W. Osebold, *The biological effects of ozone on representative members of five groups of animal viruses.* Environmental Research, 1982. **27**(2): p. 476-484.
58. Meunier, L., S. Canonica, and U. von Gunten, *Implications of sequential use of UV and ozone for drinking water quality.* Water Research, 2006. **40**(9): p. 1864-1876.
59. Dhandapani, B. and S.T. Oyama, *Gas phase ozone decomposition catalysts.* Applied Catalysis B: Environmental, 1997. **11**(2): p. 129-166.
60. Application, O.R.a., *Application of Ozone in Disinfection (AIR)*, Omniscient Treatment Technologies Pvt. Ltd: Hingna.
61. Mudway, I.S. and F.J. Kelly, *Ozone and the lung: a sensitive issue.* Molecular Aspects of Medicine, 2000. **21**(1-2): p. 1-48.
62. Lin, S., et al., *Ambient ozone concentration and hospital admissions due to childhood respiratory diseases in New York State, 1991-2001.* Environmental Research, 2008. **108**(1): p. 42-47.
63. Koenig, J.Q., *Effect of Ozone on Respiratory Responses in Subjects with Asthma.* Environmental Health Perspectives, 1995. **103**(2): p. 103-105.
64. Balmes, J.R., *The Role of Ozone Exposure in the Epidemiology of Asthma.* Environmental Health Perspectives, 1993. **101**(4): p. 219-224.
65. Gent, J.F., et al., *Association of Low-level Ozone and Fine Particles With Respiratory Symptoms in Children With Asthma.* JAMA, 2003. **290**(14): p. 1859-1867.
66. McDonnell, W.F., et al., *Long-Term Ambient Ozone Concentration and the Incidence of Asthma in Nonsmoking Adults: The Ahsmog Study.* Environmental Research, 1999. **80**(2): p. 110-121.
67. Stenfors, N., et al., *Effect of ozone on bronchial mucosal inflammation in asthmatic and healthy subjects.* Respiratory Medicine, 2002. **96**(5): p. 352-358.
68. Parodi, S., et al., *Ozone air pollution and daily mortality in Genoa, Italy between 1993 and 1996.* Public Health, 2005. **119**(9): p. 844-850.
69. Goldberg, M.S., *Short term exposure to ambient ozone increases mortality in the United States.* Evidence-Based Healthcare and Public health, 2005. **9**(3): p. 206-208.
70. Yang, Z. and S.W. Ballinger, *Environmental contributions to cardiovascular disease: Particulates and ozone.* Drug Discovery Today: Disease Mechanisms, 2005. **2**(1): p. 71-75.

71. Horrigan, B.J., *Study links ozone exposure and mortality rates.* EXPLORE: The Journal of Science and Healing, 2005. **1**(2): p. 82-85.
72. O'Neill, M.S., D. Loomis, and V.H. Borja-Aburto, *Ozone, area social conditions, and mortality in Mexico City.* Environmental Research, 2004. **94**(3): p. 234-242.
73. Kim, S.-Y., et al., *Determining the threshold effect of ozone on daily mortality: an analysis of ozone and mortality in Seoul, Korea, 1995-1999.* Environmental Research, 2004. **94**(2): p. 113-119.
74. Weschler, C.J., *Ozone's Impact on Public Health: Contributions from Indoor Exposures to Ozone and Products of Ozone-Initiated Chemistry.* Environmental Health Perspectives, 2006. **114**: p. 1489-1496.
75. Hubbell, B.J., et al., *Health-Related Benefits of Attaining the 8-Hr Ozone Standard.* Environmental Health Perspectives, 2005. **113**(1): p. 73-82.
76. Weschler, C.J., *Ozone in indoor Environment Concentration and Chemistry.* Indoor Air, 2000. **10**(4): p. 269-288.
77. Nazaroff, W.W., C.J. Weschler, and R.L. Corsi, *Indoor air chemistry and physics.* Atmospheric Environment, 2003. **37**(39-40): p. 5451-5453.
78. Singer, B.C., et al., *Indoor secondary pollutants from cleaning product and air freshener use in the presence of ozone.* Atmospheric Environment, 2006. **40**(35): p. 6696-6710.
79. Weschler, C.J., *Indoor/outdoor connections exemplified by processes that depend on an organic compound's saturation vapor pressure.* Atmospheric Environment, 2003. **37**(39-40): p. 5455-5465.
80. Weschler, C.J., *New Directions: Ozone-initiated reaction products indoors may be more harmful than ozone itself.* Atmospheric Environment, 2004. **38**(33): p. 5715-5716.
81. Weschler, C.J., *Changes in indoor pollutants since the 1950s.* Atmospheric Environment, 2009. **43**(1): p. 153-169.
82. Weschler, C.J. and H.C. Shields, *Potential reactions among indoor pollutants.* Atmospheric Environment, 1997. **31**(21): p. 3487-3495.
83. Weschler, C.J. and H.C. Shields, *Indoor ozone/terpene reactions as a source of indoor particles.* Atmospheric Environment, 1999. **33**(15): p. 2301-2312.
84. Wolkoff, P., *Photocopiers and indoor air pollution.* Atmospheric Environment, 1999. **33**: p. 2129 - 2130.
85. Wainman, T., et al., *Ozone and Limonene in Indoor Air: A source of submicrom Particle Exposure.* Environmental Health Perspectives, 2000. **108**(12): p. 1139-1145.
86. Franklin, M. and J. Schwartz, *The Impact of Secondary Particles on the Association between Ambient Ozone and Mortality.* Environmental Health Perspectives, 2008. **116**(4): p. 453-458.
87. van Zelm, R., et al., *European characterization factors for human health damage of PM10 and ozone in life cycle impact assessment.* Atmospheric Environment, 2008. **42**(3): p. 441-453.
88. Zhang, Y., et al., *Ozone and Daily Mortality in Shanghai, China.* Environmental Health Perspectives, 2006. **114**(8): p. 1227-1232.

89. Bell, M.L., R.D. Peng, and F. Dominici, *The Exposure Response Curve for Ozone and Risk of Mortality and the Adequacy of Current Ozone Regulations.* Environmental Health Perspectives, 2006. **114**(4): p. 532-536.
90. Kunkel, D.A., et al., *Passive reduction of human exposure to indoor ozone.* Building and Environment. **45**(2): p. 445-452.
91. Weschler, C.J. and J.C. Little, *Chemical and physical factors that influence pollutant dynamics in indoor atmospheric environments.* Atmospheric Environment, 2007. **41**(15): p. 3109-3110.
92. Park, Y.H., et al., *Sterilization effects of ozone decay time in acidic water against Bacillus atrophaeus endospores.* New Biotechnology, 2009. **25**(Supplement 1): p. S198-S198.
93. Takayama, M., et al., *Ozone generation by dielectric barrier discharge for soil sterilization.* Thin Solid Films, 2006. **506-507**: p. 396-399.
94. Pichat, P., et al., *Purification/deodorization of indoor air and gaseous effluents by TiO2 photocatalysis.* Catalysis Today, 2000. **63**(2-4): p. 363-369.
95. Tizaoui, C. and M.J. Slater, *The Design of an Industrial Waste-Water Treatment Process Using Adsorbed Ozone on Silica Gel.* Process Safety and Environmental Protection, 2003. **81**(2): p. 107-113.
96. Hao, Z., et al., *Supported gold catalysts used for ozone decomposition and simultaneous elimination of ozone and carbon monoxide at ambient temperature.* Applied Catalysis B: Environmental, 2001. **33**(3): p. 217-222.
97. Heisig, C., W. Zhang, and S.T. Oyama, *Decomposition of ozone using carbon-supported metal oxide catalysts.* Applied Catalysis B: Environmental, 1997. **14**(1-2): p. 117-129.
98. Riegel, J., H. Neumann, and H.M. Wiedenmann, *Exhaust gas sensors for automotive emission control.* Solid State Ionics, 2002. **152-153**: p. 783-800.
99. Francioso, L., et al., *Linear temperature microhotplate gas sensor array for automotive cabin air quality monitoring.* Sensors and Actuators B: Chemical, 2008. **134**(2): p. 660-665.
100. Pijolat, C., et al., *Gas detection for automotive pollution control.* Sensors and Actuators B: Chemical, 1999. **59**(2-3): p. 195-202.
101. Funazaki, N., et al., *Application of semiconductor gas sensor to quality control of meat freshness in food industry.* Sensors and Actuators B: Chemical, 1995. **25**(1-3): p. 797-800.
102. Perera, A., et al., *Evaluation of fish spoilage by means of a single metal oxide sensor under temperature modulation.* Sensors and Actuators B: Chemical, 2010. **146**(2): p. 477-482.
103. Li, C., et al., *Gas sensor array for blueberry fruit disease detection and classification.* Postharvest Biology and Technology. **55**(3): p. 144-149.
104. Di Natale, C., et al., *Lung cancer identification by the analysis of breath by means of an array of non-selective gas sensors.* Biosensors and Bioelectronics, 2003. **18**(10): p. 1209-1218.
105. Pennazza, G., et al., *Melanoma Volatile Fingerprint with a Gas Sensor Array: In Vivo and In Vitro Study.* Procedia Chemistry, 2009. **1**(1): p. 995-998.

106. Kanazawa, E., et al., *Metal oxide semiconductor N2O sensor for medical use.* Sensors and Actuators B: Chemical, 2001. **77**(1-2): p. 72-77.
107. Bitter, F., B. Müller, and D. Müller, *Estimation of odour intensity of indoor air pollutants from building materials with a multi-gas sensor system.* Building and Environment. **45**(1): p. 197-204.
108. Massie, C., et al., *Design of a portable optical sensor for methane gas detection.* Sensors and Actuators B: Chemical, 2006. **113**(2): p. 830-836.
109. Srivastava, A.K., *Detection of volatile organic compounds (VOCs) using SnO2 gas-sensor array and artificial neural network.* Sensors and Actuators B: Chemical, 2003. **96**(1-2): p. 24-37.
110. Chung, W.-Y. and S.-J. Oh, *Remote monitoring system with wireless sensors module for room environment.* Sensors and Actuators B: Chemical, 2006. **113**(1): p. 64-70.
111. Pohle, R., et al., *Fire detection with low power fet gas sensors.* Sensors and Actuators B: Chemical, 2007. **120**(2): p. 669-672.
112. Chen, S.-J., et al., *Fire detection using smoke and gas sensors.* Fire Safety Journal, 2007. **42**(8): p. 507-515.
113. Zhuiykov, S., *Novel sensor-actuator device for early detection of fire.* Sensors and Actuators A: Physical, 2008. **141**(1): p. 89-96.
114. Jerger, A., et al., *New applications of tin oxide gas sensors: II. Intelligent sensor system for reliable monitoring of ammonia leakages.* Sensors and Actuators B: Chemical, 2002. **81**(2-3): p. 301-307.
115. Chung, W.-Y. and D.-D. Lee, *Real time multi-channel gas leakage monitoring system using CPLD chip.* Sensors and Actuators B: Chemical, 2001. **77**(1-2): p. 186-189.
116. Abbaspour, M. and N. Mansouri, *City hazardous gas monitoring network.* Journal of Loss Prevention in the Process Industries. **18**(4-6): p. 481-487.
117. Grossel, S.S., *Hazardous gas monitoring: a guide for semiconductor and other hazardous occupancies (2000): Logan T. White, Noyes Publications/William Andrew Publishing, 13 Eaton Avenue, Norwich, NY 13815, 206 pages, $85.00.* Journal of Loss Prevention in the Process Industries, 2002. **15**(3): p. 249-250.
118. Mutschall, D. and E. Obermeier, *A capacitive CO2 sensor with on-chip heating.* Sensors and Actuators B: Chemical, 1995. **25**(1-3): p. 412-414.
119. Ishihara, T., S. Sato, and Y. Takita, *Capacitive-type sensors for the selective detection of nitrogen oxides.* Sensors and Actuators B: Chemical, 1995. **25**(1-3): p. 392-395.
120. Hagleitner, C., et al., *Smart single chip gas sensor microsystem.* Nature, 2001. **414**: p. 293-296.
121. Ishihara, T. and S. Matsubara, *Capacitive Type Gas Sensors.* Journal of Electroceramics, 1998. **2**(4): p. 215-228.
122. Albert, K.J., et al., *Cross Reactive Chemical Sensor Arrays.* Chemical Reviews, 2000. **100**: p. 2595-2626.
123. Pearce, T.C., et al., *Handbook of Machine Olfaction*. 2003: WILEY-VCH Verlag GmbH & Co. KGaA, Weinheim. 630.

124. Schaller, E., J.O. Bosset, and F. Escher, *Electronic Noses and Their Applications to Food.* Lebensm.-Wiss. u. -Technol., 1998. **31**: p. 305-316.
125. Drafts, B., *Acoustic Wave Technology Sensors.* IEEE Transactions on Microwave Theory and Techniques, 2001. **49**(4): p. 795-802.
126. Beck, K., et al., *Contactless surface acoustic wave gas sensor.* Sensors and Actuators A: Physical, 1999. **76**(1-3): p. 103-106.
127. Cheeke, J.D.N. and Z. Wang, *Acoustic wave gas sensors.* Sensors and Actuators B: Chemical, 1999. **59**(2-3): p. 146-153.
128. Déjous, C., et al., *A shear-horizontal acoustic plate mode (SH-APM) sensor for biological media.* Sensors and Actuators B: Chemical, 1995. **27**(1-3): p. 452-456.
129. Chang, K.-S., C.-K. Chang, and C.-Y. Chen, *A surface acoustic wave sensor modified from a wireless transmitter for the monitoring of the growth of bacteria.* Sensors and Actuators B: Chemical, 2007. **125**(1): p. 207-213.
130. Dubey, V.N. and R.M. Crowder, *A dynamic tactile sensor on photoelastic effect.* Sensors and Actuators A: Physical, 2006. **128**(2): p. 217-224.
131. Kim, H.-K., S. Lee, and K.-S. Yun, *Capacitive tactile sensor array for touch screen application.* Sensors and Actuators A: Physical, 2011. **165**(1): p. 2-7.
132. Grate, J.W., *Acoustic Wave Microsensor Arrays for Vapor Sensing.* Chemical Reviews, 2000. **100**: p. 2627-2648.
133. Wilson, D.M., et al., *Chemical Sensors for Portable, Handheld Field Instruments.* IEEE Sensors Journal, 2001. **1**(4): p. 256-274.
134. Eisele, I., T. Doll, and M. Burgmair, *Low power gas detection with FET sensors.* Sensors and Actuators B: Chemical, 2001. **78**(1-3): p. 19-25.
135. Majdeddin, A., *Wide band gap materials and devices for NOx, H_2 and 0_2 gas sensing applications.* 2008, Informationstechnik der Technischen Universitat llmenau: llmenau. p. 275.
136. Arshak, K., et al., *A review of gas sensors employed in electronic nose applications.* Sensor Review, 2004. **24**(2): p. 181-198.
137. Caiteanu, D., et al., *Growth of oxide films for optical gas sensor applications.* Applied Surface Science, 2005. **252**: p. 4582-4586.
138. Capone, S., et al., *Solid State Gas Sensors: State of the Art and Future Activities.* Journal of Optoelectronics and Advanced Materials 2003. **5**(5): p. 1335-1348.
139. Mari, C.M. and G.B. Barbi, *Gas Sensors - Principles, Operation and Developments*, ed. G. Sberveglieri. Vol. 329. 1992, Dordrecht: Kluwer Academic Publishers.
140. Kim, T.S., et al., *Sensing characteristics of dc reactive sputtered WO3 thin films as an NOx gas sensor.* Sensors and Actuators B: Chemical, 2000. **62**(2): p. 102-108.
141. Dirksen, J.A., K. Duval, and T.A. Ring, *NiO thin-film formaldehyde gas sensor.* Sensors and Actuators B: Chemical, 2001. **80**(2): p. 106-115.
142. Wöllenstein, J., et al., *Cobalt oxide based gas sensors on silicon substrate for operation at low temperatures.* Sensors and Actuators B: Chemical, 2003. **93**(1-3): p. 442-448.
143. Simon, I., et al., *Micromachined metal oxide gas sensors: opportunities to improve sensor performance.* Sensors and Actuators 2001. **B**(73): p. 1-26.

144. Barsan, N., D. Koziej, and U. Weimar, *Metal oxide-based gas sensor research: How to?* Sensors and Actuators B: Chemical, 2007. **121**(1): p. 18-35.
145. Fischerauer, A., C. Schwarzmuller, and G. Fischerauer. *Substrate Influence on the Characteristics of Interdigital Electrode Gas Sensors*. in *2009 6th International Multi-Conference on Systems, Signals and Devices*. 2009. Djerba.
146. Qu, W., R. Green, and M. Austin, *Development of multifunctional sensors in thick film and thin film technology.* Measurement Science and Technology, 2000. **11**: p. 1111-1118.
147. Hausner, M., J. Zacheja, and J. Binder, *Multi electrode substrate for selectivity enhancment in air monitoring.* Sensors and Actuators, 1997. **B**(43): p. 11-17.
148. Jimenez, C., H.T. Sun, and W. Wlodarski. *Preparation of In_2O_3 thin films by sol-gel process for ozone sensing*. in *IEEE* 1997.
149. Frank, J., et al., *Ozone Sensing Using In_2O_3-Modified Ga_2O_3.* IEEE Sensors Journal, 2001. **1**(4): p. 318-321.
150. Wu, R.-J., et al., *Photoreduction measurement of ozone using Pt/TiO2-SnO2 material at room temperature.* Sensors and Actuators B: Chemical, 2007. **123**(2): p. 1077-1082.
151. Hofmann, T., et al., *Fluid characterization using sensor elements based on interdigitated electrodes.* Sensors and Actuators, 1996. **B**(37): p. 37-42.
152. Hahn, S., *SnO2 thick film sensors at ultimate limits: Performance at low O2 and H2O concentration; Size reduction by CMOS technology*, in *der Fakulatat fur Chemie und Pharmazie*. 2002, Eberhard-Karls-Universitat-Tubingen: Tubingen. p. 162.
153. Kim, S.-R., et al., *Ozone sensing properties of In2O3-based semiconductor thick films.* Sensors and Actuators B: Chemical, 2000. **66**(1-3): p. 59-62.
154. Takada, T., *Chemical Sensor Technology*. Ozone detection by In_2O_3 thin film gas sensor. Vol. 2. 1989, Tokyo: Kodansha.
155. Becker, T., et al., *Ozone detection using low-power-consumption metal-oxide gas sensors.* Sensors and Actuators A: Physical, 1999. **74**(1-3): p. 229-232.
156. Qu, W. and W. Wlodarski, *A thin-film sensing element for ozone, humidity and temperature.* Sensors and Actuators B: Chemical, 2000. **64**(1-3): p. 42-48.
157. Mcgrath, M.M., *Silicon based gas sensor production*, in *Electronic and Computer Engineering Department*. 1999, University of Limerick: Limerick.
158. Sberveglieri, G., et al., *A new technique for the preparation of highly sensitive hydrogen sensors based on SnO_2 (Bi_2O_3) thin films.* Sensors and Actuators, 1991. **B**(5): p. 253-255.
159. Licari, J.J., *Hybrid microcircuit technology handbook; materials, processes, design and test*, ed. p. Ridge. 1988, New Jersey: Noyes Publications.
160. Suchea, M., et al., *Metal oxide thin films as sensing layers for ozone detection.* Analytica Chimica Acta, 2006. **573-574**: p. 9-13.
161. Kiriakidis, G., et al., *Ozone Sensing Properties of Polycrystalline Indium Oxide Films at Room Temperature.* Phys. Stat. Sol., 2001. **a**(185): p. 27-32.
162. Maissel, L. and R. Glang, *Handbook of Thin Film Technology*, ed. L. Maissel and R. Glang. 1979, New York: McGraw Hill, Inc.

163. Cantalini, C., et al., *NO2 response of In2O3 thin film gas sensors prepared by sol-gel and vacuum thermal evaporation techniques.* Sensors and Actuators B: Chemical, 2000. **65**(1-3): p. 101-104.
164. Chopra, K.L., *Thin Film Phenomena*, ed. K.L. Chopra. 1979, New York: R.E. Kreinger Publishing Company.
166. Wlodarski, W., et al. *Sol-gel Prepared In_2O_3 Thin Films for Ozone Sensing*. in *1997 International Conference on Solid State Sensors and Actuators*. 1997. Chicago.
167. Atashbar, M.Z., et al., *Investigation on ozone-sensitive In2O3 thin films.* Thin Solid Films, 1999. **354**(1-2): p. 222-226.
168. Zhou, J., *Indium Tin Oxide (ITO) Deposition, Patterning, and Shottky Contact Fabrication*, in *Department of Microelectronic Engineering*. 2005, Rochester Institute of Technology: New York. p. 89.
169. Doll, T., et al., *Conductivity and work function ozone sensors based on indium oxide.* Sensors and Actuators B: Chemical, 1998. **49**(1-2): p. 63-67.
170. Faglia, G., et al., *Electrical and structural properties of RGTO-In2O3 sensors for ozone detection.* Sensors and Actuators B: Chemical, 1999. **57**(1-3): p. 188-191.
171. Gurlo, A., et al., *In2O3 and MoO3-In2O3 thin film semiconductor sensors: interaction with NO2 and O3.* Sensors and Actuators B: Chemical, 1998. **47**(1-3): p. 92-99.
172. Baba Ali, E., et al., *In_2O_3 deposited by reactive evaporation of indium in oxygen atmosphere - influence of post-annealing treatment on optical and electrical properites.* Materials Chemistry and Physics, 2002. **73**: p. 78-85.
173. Baratto, C., et al., *Iron-doped indium oxide by modified RGTO deposition for ozone sensing.* Sensors and Actuators B: Chemical, 2006. **118**(1-2): p. 221-225.
174. Ivanovskaya, M., A. Gurlo, and P. Bogdanov, *Mechanism of O3 and NO2 detection and selectivity of In2O3 sensors.* Sensors and Actuators B: Chemical, 2001. **77**(1-2): p. 264-267.
175. Miyata, T., T. Hikosaka, and T. Minami, *Ozone gas sensors with high sensitivity using Zn2In2O5-MgIn2O4 multicomponent oxide thin films.* Surface and Coatings Technology, 2000. **126**(2-3): p. 219-224.
177. Hattori, A., et al., *Ozone sensor made by dip coating method.* Sensors and Actuators A: Physical, 1999. **77**(2): p. 120-125.
178. Wu, R.-J., et al., *Photoreduction measurement of ozone using Pt/TiO2-SnO2 material at room temperature.* Sensors and Actuators B: Chemical, 2007. **123**(2): p. 1077-1082.
179. Berry, L. and J. Brunet, *Oxygen influence on the interaction mechanisms of ozone on SnO2 sensors.* Sensors and Actuators B: Chemical, 2008. **129**(1): p. 450-458.
180. Korotcenkov, G., et al., *Effect of air humidity on gas response of SnO2 thin film ozone sensors.* Sensors and Actuators B: Chemical, 2007. **122**(2): p. 519-526.
181. Bendahan, M., et al., *Characterization of ozone sensors based on WO3 reactively sputtered films: influence of O2 concentration in the sputtering gas, and working temperature.* Sensors and Actuators B: Chemical, 2004. **100**(3): p. 320-324.

182. Aguir, K., C. Lemire, and D.B.B. Lollman, *Electrical properties of reactively sputtered WO3 thin films as ozone gas sensor.* Sensors and Actuators B: Chemical, 2002. **84**(1): p. 1-5.
183. Cantalini, C., et al., *Investigation on the O3 sensitivity properties of WO3 thin films prepared by sol-gel, thermal evaporation and r.f. sputtering techniques.* Sensors and Actuators B: Chemical, 2000. **64**(1-3): p. 182-188.
184. Katsarakis, N., Bender, M., Cimalla, V., Gagaoudakis, E., Kiriakidis, G., *Ozone sensing properties of DC-sputtered, c-axis oriented ZnO films at room temperature.* Sensors and Actuators, 2003. **B**(96): p. 76-81.
185. Kenankis, G., et al, *Ozone sensing properties of ZnO nanostructures grown by the aqueous chemical growth technique.* Sensors and Actuators, 2007. **B**(124): p. 187-191
186. Williams, D.E., *Semiconducting oxides as gas-sensitive resistors.* Sensors and Actuators, 1999. **B**(57): p. 1-16.
187. Choi, W.K., et al., *H_2 gas sensing characteristics of SnO_x sensors fabricated by a reactive ion-assisted deposition with/without and activator layer.* Sensors and Actuators, 1997. **B**(40): p. 21-27.
188. Twomey, K., *A Novel Thick/Thin Film Humidity Sensor with Associated System Level Electronics*, in *Department of Electronics and Computer Engineering*. 2002, University of Limerick: Limerick.
189. Miura, N., et al, *Novel solid-state manganese oxide-based reference electrode for YSZ-based oxygen sensors.* Sensors and Actuators 2011. **B**(152): p. 261-266.
190. Wang, C., *Metal organic chemical vapor deposition of indium oxide for ozone sensing*, in *Erlangung des akademischen Grades eines*. 2009, Albert-Ludwigs_Universitat Freiburb: Freiburg. p. 158.
191. Rothschild, A. and Y. Komem, *Numerical computation of chemisorption isotherms for device modelling od semiconductor gas sensors.* Sensors and Actuators, 2003. **B**(93): p. 362-369.
192. Guérin, J., K. Aguir, and M. Bendahan, *Modeling of the conduction in a WO3 thin film as ozone sensor.* Sensors and Actuators B: Chemical, 2006. **119**(1): p. 327-334.
193. Geistlinger, H., *Electron theory of thin-film gas sensors.* Sensors and Actuators, 1993. **B**(17): p. 47-60.
194. Natarajan, G., et al, *Influence of oxygen depletion layer on the properties of tin oxide gas-sensing films fabricated by atomic layer deposition.* Applied Physics A, 2009. **95**(3): p. 621-627
195. Barsan, N. and U. Weimar, *Conduction Model of Metal Oxide Gas Sensors.* Journal of Electroceramics, 2001. **7**: p. 143-167.
196. Ogawa, H., M. Nishikawa, and A. Abe, *Hall Measurement Studies and Electrical conduction model of tin oxide ultra thin particle films.* Journal of Applied Physics, 1982. **53**: p. 4448-4455.
197. Xu, C., et al., *Grain size effects on gas sensitivity of porous tin oxide based elements.* Sensors and Actuators, 1991. **3**(B): p. 147-155.
198. You, L., et al, *Highly sensitive NO_2 sensor based on monodispersed WO_3 nanoparticles.* IMCS 2012, The 14th International Meeting on Chemical Sensors.

199. Teoh, L.G., et al, *High Sensitivity Semiconductor NO_2 Gas Sensor Based on Mesoporous WO_3 Thin Film.* Electrochemical and Solid-State Letters, 2003. **6**(8): p. 108-111.
200. Korotcenkov, G., Cho, B.K. *Ozone measuring: What can limit application of SnO_2-based conductometric gas sensors?*. Sensors and Actuators, 2012. **B**(161): p. 28-44
201. Korotcenkov, G., Cho, B.K. *Instability of metal oxide-based conductometric gas sensors and approaches to stability improvement.* Sensors and Actuators, 2011. **B**(156): p. 527-538
202. Ishida, H., et al., *Odor source localization in the clean room by an autonomous mobile sensing system.* Sensors and Actuators, 1996. **B**(33): p. 115-121.
203. Lilienthal, A., et al. *Sensing odour sources in indoor environments without a constant airflow by a mobile robot.* in *IEEE Int. Conf. Robotics Automat.* . 2000. Seoul Korea.
204. Shapira, Y., S.M. Cox, and D. Lichtman, *Chemisorption, photodesorption and conductivity measurements on ZnO surfaces.* Surface Science 1976. **54**(1): p. 43-59.
205. Comini, E., G. Fagli, and G. Sberveglieri, *UV light activation of tin oxide thin films for NO_2 sensing at low temperatures.* Sensors and Actuators, 2001. **B**(78): p. 73-77.
206. Min, Y., *Properties and Sensor Performance of Zinc Oxide Thin Films*, in *Department of Materials Science and Engineering*. 2003, Massachusetts Institute of Technology: Massachusetts. p. 152.
207. White, N.M. and J.D. Turner, *Thick Film Sensors: Past, Present and Future.* Measurement Science and Technology, 1997. **8**(1).
208. Korostynska, O., *Development of a personal gamma-radiation sensor using thin/thick film technologies*, in *Electronic and Computer Engineering Department*. 2003, University of Limerick: Limerick. p. 245.
209. Lynch, C., *To Design and Fabricate a Capacitive Sensor*, in *Electronic and Computer Engineering Department*. 2001, University of Limerick: Limerick.
210. Stuart, R.V., *Vacuum Technology, Thin Films and Sputtering*. 1983, New York: Academic Press.
211. Perrem, R.L., *Thin Film Strain Gauge - An Investigation into the Properties of the Mixed Oxide V_2O_5-Bi_2O_3*, in *Electronic and Computer Engineering Department*. 1993, University of Limerick: Limerick.
212. Cohen, M.H., H. Fritzsche, and S.R. Ovshinsky, *Simple Band Model For Amorphous Semiconducing Alloys.* Physical Review Letters, 1969. **22**: p. 1065 - 1068.
213. Davis, E.A. and N.F. Mott, *Electronic Properties in non-crystalline materials, Second Edition*. 2nd ed. 1979, Oxford, London: Clarendon Press.
214. Urbach, F., *The long wavelength edge of photographic sensitivity and of the electronics of solids.* Physical Review 1953. **92**: p. 1324.
215. Jonscher, A.K., *Electronic properties of amorphous dielectric films.* Thin Solid Films, 1967. **1**: p. 213-234.

216. Prudenziati, M., *Handbook of Sensors and Actuators. Thick Film Sensors*. 1994, Amsterdam: Elseiver.
217. Anwar, M., et al, *The Electrical properties of amorphous thin films of Al-In_2O_3-Al Structure deposited by thermal evaporation.* Rom. Journ. Phys., Vol 50, Nos. 7-8: p. 763-784. Bucharest (2005).
218. Tsuruta, S., *Apparatus for Sterilisation with Ozone and Ultraviolet-Ray Radiation*, in *Pat, K. T*, J. Pat., Editor. 1988: Japan.
219. Atanassova, E., et al., *Influence of γ-radiation on thin Ta_2O_5-Si structures.* Microelectronics Journal, 2001. **32**: p. 553-562.
220. Moore, E., *Filler Enhanced Conducting Polymer Composite Enose Sensors for Use in Biomarker and Bacteria Detection*, in *Electronic and Computer Engineering Department*. 2007, University of Limerick: Limerick. p. 250.
221. Eranna, G., et al., *Oxide Materials for Development of Integrated Gas Sensors - A Comprehensive Review.* Critical Reviews in Solid State and Materials Sciences, 2004. **29**(3): p. 111-188.
222. Dutaive, M.S., R. Lalauze, and C. Pijolat, *Sintering catalytic effects and defect chemistry in polycrystalline tin oxide.* Sensors and Actuators, 1995. **B**(26/27): p. 38-44.
223. Mandeles, A. and C. Christofides, *Physics, Chemistry and Technology of Solid State Gas Sensor Devices*. 1993, New York: John Wiley & Sons, Inc.
224. Kiriakidis, G., et al, *Ultra-low gas sensing utilizing metal oxide thin films. Vacuum*, 2012. **86**(5): p. 495-506.
225. Zhou, Y., et al., *Preparation and characterisation of porous Nb_2O_5 nanoparticles.* Materials Research Bulletin, 2007. **MRB-3856**.
226. Gimon-Kinsel, M.E. and K.J. Balkus, *Pulsed Laser Deposition of Mesoporous niobium oxide thin films and application as chemical sensors.* Microporous and Mesoporous Materials, 1999. **28**: p. 113-123.
227. Ozer, N., D.G. Chen, and C.M. Lambert, *Preparation and Properties of spin-coated Nb_2O_5 films by the sol-gel Process for electrochromic applications.* Thin Solid Films, 1996. **277**: p. 162-168.
228. Sieber, L., et al., *Formation of self-organised Niobium porous on Niobium.* Electrochemsitry Communications, 2005. **7**: p. 97-100.
229. Viswanathamurthi, P., et al., *Preparation and morphology of niobium oxide fibres by electrospinning.* Chemical Physics Letters, 2003. **374**: p. 79-84.
230. Williams, D.E., *Semiconducing oxides as gas sensitive resistors.* Sensors and Actuators, 1999. **B**(57): p. 1-16.
231. Zakrzewska, K., *Mixed oxides as gas sensors.* Thin Solid Films, 2001. **391**: p. 229-238.
232. Takada, T., Suzuki, M., Nakane, M., , Sensors and Actuators, 1993. **B**(13).
234. Korotcenkov, G., Brinzari, V., Cerneavschi, A., Ivanov, M., Golovanov, V., Cornet, A., Morante, J., Cabot, A., Arbiol, J., *The influence of film structure on In_2O_3 gas response.* Thin Solid Films, 2004. **460**: p. 315-323.
235. Kiriakidis, G., et al. *Highly sensitive InO_x Ozone sensing films on flexible substrates.* Journal of Sensors, 2009. Article ID 727893, p. 5

236. Kim, Y.S., et al., *Effect of substrate temperature on the bonded states of indium tin oxide thin films deposited by plasma enhanced chemical vapor deposition.* Thin Solid Films, 2003. **426**(1): p. 124-131.
237. Wahab, R., et al., *Low temperature solution synthesis and characterisation of ZnO nano-flowers.* Materials Research Bulletin, 2007. **42**: p. 1640-1648.
238. Li, S.Y., et al., *Low temperature synthesized Sn doped indium oxide nanowires.* Nanotechnology, 2005. **16**(4): p. 451-457.
239. Du, Y., et al., *Structural and optical properties of nanophase zinc oxide.* Applied Physics A: Materials Science and Processing, 2003. **76**(2): p. 171-176.
240. Kiriakidis, G., et al, *Ultra-low gas sensing utilizing metal oxide thin films. Vacuum*, 2012. **86**(5): p. 495-506.
241. Chambon, L. et al, *A metallic oxide gas sensor array for selective detection of Co and NH3 gases.* Sensors and Actuators, 1999. **B**(60): p. 138-147
242. Chambon, L. et al, *Investigation, for NH3 gas sensing applications, of the Nb2O5 semiconducting oxide in the presence of interferent species such as oxygen and humidity.* Sensors and Actuators, 1997. **B**(45): p. 107-114
243. Seiyama, T. and Kagawa, S., *Study on a detector for gaseous components using semiconductive thin films. Analytical Chemistry*, 1996. 38: p. 1069-1073
244. Chambon, L. et al, *A model for the response of Nb2O5 sensors to CO and NH3 gases.* Sensors and Actuators, 1997. **B**(43): p. 60-64
245. Eagashira, M. et al, *Trimethylamine Sensor based on semiconductive metal oxide for detection of fish freshness.* Sensors and Actuators, 1990. **B**(1): p. 108-113
246. Zhu, J., et al, *A new automotive air/fuel sensor based on TiO2-Doped Nb2O5 thin film by ion-beam-enhanced deposition.* Sensors and Actuators, 2001. **B**(32): p. 209-213

List Of Publications

International Journals:

1. O. Korostynska, K. Arshak, G. Hickey, E. Forde, "Ozone and gamma radiation sensing properties of In2O3:ZnO:SnO2 thin films", Microsystem Technologies, Vol. 14, Is. 4-5, pp. 557-566, Apr. 2008.
2. K. Arshak, G. Hickey, E. Forde, J. Harris, "Ozone sensing properties of thermally evaporated In_2O_3 based thin films" NANO: Brief Reports and Reviews, Vol 3, No. 217, 2008
3. O. Korostynska, K. Arshak, G. Hickey, "Gamma radiation and ozone sensing using mixed oxides thin films", NANO: Brief Reports and Reviews, Vol. 3, No. 4, pp. 209–215, 2008.

Peer-reviewed Conferences:

1. K. Arshak, G. Hickey, E. Forde, J. Harris, "Development of a room temperature thin film In_2O_3, ZnO, SnO_2 ozone sensor". In proceedings of the ISIE 2007, IEEE International Symposium on Industrial Electronics. Vigo, Spain.
2. K. Arshak, G. Hickey, E. Forde, J. Harris, "Ozone sensing properties of NbO_2 thin films for health and safety applications", SAS 2008, IEEE Sensors Applications Symposium. Atlanta, GA, February 12-14, 2008
3. K. Arshak, O. Korostynska, G. Hickey, "Gamma radiation and ozone sensing using mixed oxides thin films", ISNEPP 2007, Nanotechnology in Environmental Protection and Pollution, 11-13 Dec 2007, Ft. Lauderdale, FL, USA.
4. K. Arshak, O. Korostynska, G. Hickey, "Gamma radiation and ozone sensing properties of In2O3:ZnO:SnO2 thin films", SPIE Conf. on "Smart Sensors, Actuators and MEMS", Microtechnologies for the New Millennium, Gran Canaria 2-4 May 2007, Proc. SPIE Vol. 6589, 658916.
5. K. Arshak, G. Hickey, E. Forde, J. Harris, " Development of novel room temperature ozone sensors for health and safety applications", ISSE 2007, 30th International Spring Seminar on Electronics Technology, 9-13 May 2007, Cluj-Napoca, Romania

Other Publications:

1. K. Arshak, O. Korostynska, G. Hickey, "Simultaneous sensing of ozone levels and gamma radiation in a hand-held device", SPIE Newsroom 2007, DOI: 10.1117/2.1200708.0817.